

Universidade de São Paulo
Instituto de Astronomia, Geofísica e Ciências Atmosféricas
Departamento de Astronomia

Estudos numéricos de difusão e amplificação de campos magnéticos em plasmas astrofísicos turbulentos

*Numerical studies of diffusion and amplification
of magnetic fields in turbulent astrophysical plasmas*

Reinaldo Santos de Lima

Orientadora: Profa. Dra. Elisabete M. de Gouveia Dal Pino

São Paulo

2013

Reinaldo Santos de Lima

Estudos numéricos de difusão e amplificação de campos magnéticos em plasmas astrofísicos turbulentos

*Numerical studies of diffusion and amplification
of magnetic fields in turbulent astrophysical plasmas*

Tese apresentada ao Departamento de Astronomia do Instituto de Astronomia, Geofísica e Ciências Atmosféricas da Universidade de São Paulo como requisito parcial à obtenção do título de **Doutor em Ciências**.

Sub-área de concentração: Astrofísica.

Orientadora: Profa. Dra. Elisabete M. de Gouveia Dal Pino

Versão Corrigida. O original encontra-se disponível na Unidade.

São Paulo

2013

Aos meus pais Alfredo e Edite.

Acknowledgments

I am grateful to everyone who helped me, directly or not, in accomplishing this thesis.

I am indebted to the Universidade de São Paulo (USP) and, in particular, to the Astronomy Department of the Instituto de Astronomia, Geofísica e Ciências Atmosféricas (IAG), for supporting me as a graduate student.

I acknowledge FAPESP (07/04551-0) and CAPES (3979/08-3) for the financial support which made possible the development of this work.

I would like to acknowledge my advisor Bete, who always guided me with a lot of disposal, optimism, and patience. I am deeply indebted with all her help and encouragement. *Thanks for all the knowledge and enthusiasm you transmitted me!*

I acknowledge the professors of the Astronomy Department, in special the ones who participated directly of my scientific formation through their courses: Ademir Salles de Lima, Antonio Mário Magalhães, Elisabete de Gouveia Dal Pino, Gastão Bierrenbach, Laerte Sodre, Roberto Costa, Ronaldo Eustaquio, Silvia Rossi.

I acknowledge the staff of the Astronomy Department for all their support, in special: Aparecida Neusa (Cida), Conceição, Marina Freitas, Regina Iacovelli, Ulisses Manzo, who were always so attentive, flexible, and nice with me.

I acknowledge the staff of the IAG, in special the very efficient secretaries of the Graduation Office: Ana Carolina, Lilian, Marcel Yoshio, and Rosemary Feijó.

Thanks to my group colleagues for discussing my work, sharing their knowledge, their incentive and friendship: Behrouz Khiali, Cláudio Melioli, Fernanda Geraissate, Grzegorz Kowal, Gustavo Guerrero, Gustavo Rocha, Luis Kadowaki, Márcia Leão, Maria Soledad, and María Victoria.

Thanks to Grzegorz Kowal for sharing his numerical code, which was used in the numerical simulations of this thesis.

I acknowledge Prof. Diego Falceta for helping me many times, and for making my start in numerical simulations smoother.

I acknowledge Prof. Alex Lazarian for his co-advising and collaboration. I am sincerely grateful to the University of Wisconsin (UW) at Madison, in special the Astronomy Department, for the kind hospitality during my six months visit to the Prof. Alex's group, in 2009. I am also grateful to Prof. Alex's students at that time for their hospitality and for the scientific discussions: Andrey Beresnyak, Blakesley Bhurkhart, and Thiem Hoang.

I am enormously indebted to Prof. Jungyeon Cho. His frequent advices about my numerical simulations allowed me to progress much faster in my research. He also helped me in many practical aspects of my stay in Madison.

Thanks to all the friends and colleagues I made in IAG during the last years, specially the ones I spent more time together: Aiara Lobo Gomes, Alan Carmo, Alberto Krone, Alessandro Moisés, Bruno Dias, Bruno Mota, Carlos Augusto Braga, Cyril Escolano, Daiane Breves, Diana Gama, Douglas Barros, Edgar Ramirez, Fernanda Urrutia, Felipe Andrade Santos, Felipe Oliveira (Lagosta), Fellipy Silva, Frederick Poidevin, Gleidson (Cabra), Juan Carlos Pineda, Luciene Coelho, Marcela Pacheco (Pupi), Marcio Avellar, Marcus Vinícius Duarte, Miguel Andres Paez (Cachorron), Raul Puebla (Compadre), Thiago Almeida (Zé Colméia), Thiago Junqueira (Gerson), Thiago Matheus (Monange), Thiago Triumpho, Tatiana Zapata, Thais Silva (Thais Bauer), Thaise Rodrigues, Tiago Ricci, Oscar Cavichia, Paulo Jakson, Pedro Beaklini, Rafael Kimura, Rafael Santucci, Silvio Fiorentin (Punk), Ulisses Machado, Vinicius Busti, Xavier Haubois.

Thanks to all the good friends I made in the university, for their positive influence: Daniel Cruz (Frisê), Dylene Agda, Breno Raphaldini, Everton Medeiros, Fausto Martins, Helen Soares, Jessé Américo, Marcelo Caetano (Pará), Ricardo Aloisio, Sandra (Sukita), Suryendrani Baptistuta, Zahra Sadre.

I also would like to acknowledge to these great heart people I met in Madison: Alhaji N'jai, Anand Narayanan, Christine Ondzigh-Assoume, Francisca Reyes, Linda Vakunta, Mrs. Susan Becker, and Mr. Rad Becker. *Thanks so much for all you made for me.*

I am enormously grateful to all my family, for their invaluable support and love: my father Alfredo, my mother Edite, my sisters Sheila and Aline, my brother-in-law Rafael, my nephews Ian, Luan, Lana, and Larissa, and my uncle Dinho.

I acknowledge María Victoria for all her love, comprehension, and the enormous help during the final phase of this thesis. *Thank you for being by my side in all the situations!*

Abstract

In this thesis we investigated two major issues in astrophysical flows: the transport of magnetic fields in highly conducting fluids in the presence of turbulence, and the turbulence evolution and turbulent dynamo amplification of magnetic fields in collisionless plasmas.

The first topic was explored in the context of star-formation, where two intriguing problems are highly debated: the requirement of magnetic flux diffusion during the gravitational collapse of molecular clouds in order to explain the observed magnetic field intensities in protostars (the so called “magnetic flux problem”) and the formation of rotationally sustained protostellar discs in the presence of the magnetic fields which tend to remove all the angular momentum (the so called “magnetic braking catastrophe”). Both problems challenge the ideal MHD description, usually expected to be a good approximation in these environments. The ambipolar diffusion, which is the mechanism commonly invoked to solve these problems, has been lately questioned both by observations and numerical simulation results. We have here investigated a new paradigm, an alternative diffusive mechanism based on fast magnetic reconnection induced by turbulence, termed turbulent reconnection diffusion (TRD). We tested the TRD through fully 3D MHD numerical simulations, injecting turbulence into molecular clouds with initial cylindrical geometry, uniform longitudinal magnetic field and periodic boundary conditions. We have demonstrated the efficiency of the TRD in decorrelating the magnetic flux from the gas, allowing the infall of gas into the gravitational well while the field lines migrate to the outer regions of the cloud. This mechanism works for clouds starting either in magnetohydrostatic equilibrium or initially out-of-equilibrium in free-fall. We

estimated the rates at which the TRD operate and found that they are faster when the central gravitational potential is higher. Also we found that the larger the initial value of the thermal to magnetic pressure ratio (β) the larger the diffusion process. Besides, we have found that these rates are consistent with the predictions of the theory, particularly when turbulence is trans- or super-Alfvénic. We have also explored by means of 3D MHD simulations the role of the TRD in protostellar disks formation. Under ideal MHD conditions, the removal of angular momentum from the disk progenitor by the typically embedded magnetic field may prevent the formation of a rotationally supported disk during the main protostellar accretion phase of low mass stars. Previous studies showed that an enhanced microscopic diffusivity of about three orders of magnitude larger than the Ohmic diffusivity would be necessary to enable the formation of a rotationally supported disk. However, the nature of this enhanced diffusivity was not explained. Our numerical simulations of disk formation in the presence of turbulence demonstrated the efficiency of the TRD in providing the diffusion of the magnetic flux to the envelope of the protostar during the gravitational collapse, thus enabling the formation of rotationally supported disks of radius ~ 100 AU, in agreement with the observations.

The second topic of this thesis has been investigated in the framework of the plasmas of the intracluster medium (ICM). The amplification and maintenance of the observed magnetic fields in the ICM are usually attributed to the turbulent dynamo action which is known to amplify the magnetic energy until close equipartition with the kinetic energy. This is generally derived employing a collisional MHD model. However, this is poorly justified *a priori* since in the ICM the ion mean free path between collisions is of the order of the dynamical scales, thus requiring a collisionless-MHD description. We have studied here the turbulence statistics and the turbulent dynamo amplification of seed magnetic fields in the ICM using a single-fluid collisionless-MHD model. This introduces an anisotropic thermal pressure with respect to the direction of the local magnetic field and this anisotropy modifies the MHD linear waves and creates kinetic instabilities. Our collisionless-MHD model includes a relaxation term of the pressure anisotropy due to the feedback of the mirror and firehose instabilities. We performed 3D numerical simulations of forced transonic turbulence in a periodic box mimicking the turbulent ICM, assuming

different initial values of the magnetic field intensity and different relaxation rates of the pressure anisotropy. We showed that in the high β plasma regime of the ICM where these kinetic instabilities are stronger, a fast anisotropy relaxation rate gives results which are similar to the collisional-MHD model in the description of the statistical properties of the turbulence. Also, the amplification of the magnetic energy due to the turbulent dynamo action when considering an initial seed magnetic field is similar to the collisional-MHD model, particularly when considering an instantaneous anisotropy relaxation. The models without any pressure anisotropy relaxation deviate significantly from the collisional-MHD results, showing more power in small-scale fluctuations of the density and velocity field, in agreement with a significant presence of the kinetic instabilities; however, the fluctuations in the magnetic field are mostly suppressed. In this case, the turbulent dynamo fails in amplifying seed magnetic fields and the magnetic energy saturates at values several orders of magnitude below the kinetic energy. It was suggested by previous studies of the collisionless plasma of the solar wind that the pressure anisotropy relaxation rate is of the order of a few percent of the ion gyrofrequency. The present study has shown that if this is also the case for the ICM, then the models which best represent the ICM are those with instantaneous anisotropy relaxation rate, i.e., the models which revealed a behavior very similar to the collisional-MHD description.

Resumo

Nesta tese, investigamos dois problemas chave relacionados a fluidos astrofísicos: o transporte de campos magnéticos em plasmas altamente condutores na presença de turbulência, e a evolução da turbulência e amplificação de campos magnéticos pelo dínamo turbulento em plasmas não-colisionais.

O primeiro tópico foi explorado no contexto de formação estelar, onde duas questões intrigantes são intensamente debatidas na literatura: a necessidade da difusão de fluxo magnético durante o colapso gravitacional de nuvens moleculares, a fim de explicar as intensidades dos campos magnéticos observadas em proto-estrelas (o denominado “problema do fluxo magnético”), e a formação de discos proto-estelares sustentados pela rotação em presença de campos magnéticos, os quais tendem a remover o seu momento angular (a chamada “catástrofe do freamento magnético”). Estes dois problemas desafiam a descrição MHD ideal, normalmente empregada para descrever esses sistemas. A difusão ambipolar, o mecanismo normalmente invocado para resolver estes problemas, vem sendo questionada ultimamente tanto por observações quanto por resultados de simulações numéricas. Investigamos aqui um novo paradigma, um mecanismo de difusão alternativo baseado em reconexão magnética rápida induzida pela turbulência, que denominamos reconexão turbulenta (TRD, do inglês *turbulent reconnection diffusion*). Nós testamos a TRD através de simulações numéricas tridimensionais MHD, injetando turbulência em nuvens moleculares com geometria inicialmente cilíndrica, permeadas por um campo magnético longitudinal e fronteiras periódicas. Demonstramos a eficiência da TRD em desacoplar o fluxo magnético do gás, permitindo a queda do gás no poço de potencial gravitacional, enquanto as linhas de campo migram para as regiões externas da nuvem. Este mecanismo funciona tanto

para nuvens inicialmente em equilíbrio magneto-hidrostático, quanto para aquelas inicialmente fora de equilíbrio, em queda livre. Nós estimamos as taxas em que a TRD opera e descobrimos que são mais rápidas quando o potencial gravitacional é maior. Também verificamos que quanto maior o valor inicial da razão entre a pressão térmica e magnética (β), mais eficiente é o processo de difusão. Além disto, também verificamos que estas taxas são consistentes com as previsões da teoria, particularmente quando a turbulência é trans- ou super-Alfvénica. Também exploramos por meio de simulações MHD 3D a influência da TRD na formação de discos proto-estelares. Sob condições MHD ideais, a remoção do momento angular do disco progenitor pelo campo magnético da nuvem pode evitar a formação de discos sustentados por rotação durante a fase principal de acreção proto-estelar de estrelas de baixa massa. Estudos anteriores mostraram que uma super difusividade microscópica aproximadamente três ordens de magnitude maior do que a difusividade ôhmica seria necessária para levar à formação de um disco sustentado pela rotação. No entanto, a natureza desta super difusividade não foi explicada. Nossas simulações numéricas da formação do disco em presença de turbulência demonstraram a eficiência da TRD em prover a difusão do fluxo magnético para o envelope da proto-estrela durante o colapso gravitacional, permitindo assim a formação de discos sustentados pela rotação com raios ~ 100 UA, em concordância com as observações.

O segundo tópico desta tese foi abordado no contexto dos plasmas do meio intra-aglomerado de galáxias (MIA). A amplificação e manutenção dos campos magnéticos observados no MIA são normalmente atribuídas à ação do dínamo turbulento, que é conhecidamente capaz de amplificar a energia magnética até valores próximos da equipartição com a energia cinética. Este resultado é geralmente derivado empregando-se um modelo MHD colisional. No entanto, isto é pobremente justificado *a priori*, pois no MIA o caminho livre médio de colisões íon-íon é da ordem das escalas dinâmicas, requerendo então uma descrição MHD não-colisional. Estudamos aqui a estatística da turbulência e a amplificação por dínamo turbulento de campos magnéticos sementes no MIA, usando um modelo MHD não-colisional de um único fluido. Isto introduz uma pressão térmica anisotrópica com respeito à direção do campo magnético local. Esta anisotropia modifica as ondas MHD lineares e cria instabilidades cinéticas. Nosso modelo MHD não-colisional

inclui um termo de relaxação da anisotropia devido aos efeitos das instabilidades *mirror* e *firehose*. Realizamos simulações numéricas 3D de turbulência trans-sônica forçada em um domínio periódico, mimetizando o MIA turbulento e considerando diferentes valores iniciais para a intensidade do campo magnético, bem como diferentes taxas de relaxação da anisotropia na pressão. Mostramos que no regime de plasma com altos valores de β no MIA, onde estas instabilidades cinéticas são mais fortes, uma rápida taxa de relaxação da anisotropia produz resultados similares ao modelo MHD colisional na descrição das propriedades estatísticas da turbulência. Além disso, a amplificação da energia magnética pela ação do dínamo turbulento quando consideramos um campo magnético semente, é similar ao modelo MHD colisional, particularmente quando consideramos uma relaxação instantânea da anisotropia. Os modelos sem qualquer relaxação da anisotropia de pressão mostraram resultados que se desviam significativamente daqueles do MHD colisional, mostrando mais potências nas flutuações de pequena escala da densidade e velocidade, em concordância com a presença significativa das instabilidades cinéticas nessas escalas; no entanto, as flutuações do campo magnético são, em geral, suprimidas. Neste caso, o dínamo turbulento também falha em amplificar campos magnéticos sementes e a energia magnética satura em valores bem abaixo da energia cinética. Estudos anteriores do plasma não-colisional do vento solar sugeriram que a taxa de relaxação da anisotropia na pressão é da ordem de uma pequena porcentagem da giro-frequência dos íons. O presente estudo mostrou que, se este também é o caso para o MIA, então os modelos que melhor representam o MIA são aqueles com taxas de relaxação instantâneas, ou seja, os modelos que revelaram um comportamento muito similar à descrição MHD colisional.

Contents

Acknowledgments	vii
Abstract	xi
Resumo	xv
1 Introduction	1
2 MHD turbulence: diffusion and amplification of magnetic fields	7
2.1 Kinetic and fluid descriptions of a plasma	8
2.2 Basic MHD equations	12
2.2.1 Linear modes	15
2.3 MHD turbulence: an overview	17
2.3.1 The hydrodynamic case	18
2.3.2 Alfvénic turbulence, weak cascade	19
2.3.3 Strong cascade	21
2.3.4 Compressible MHD turbulence	21
2.4 The role of MHD turbulence on magnetic field diffusion during star-forming processes	23
2.4.1 Mechanism of fast magnetic reconnection in the presence of turbulence	26
2.4.2 Magnetic diffusion due to fast reconnection	30
2.5 Magnetic field amplification and evolution in the turbulent intracluster medium (ICM)	33
2.5.1 Turbulent dynamos in astrophysics	35

2.5.2	The small-scale turbulent dynamo	37
2.5.3	Saturation condition of the magnetic fields in SSDs	39
2.5.4	Collisionless MHD model for the ICM	40
2.5.5	CGL-MHD waves and instabilities	42
2.5.6	Kinetic instabilities feedback on the pressure anisotropy	44
3 Removal of magnetic flux from clouds via turbulent reconnection diffusion		
		47
3.1	Numerical Model	48
3.2	Turbulent magnetic field diffusion in the absence of gravity	50
3.2.1	Initial Setup	50
3.2.2	Notation	52
3.2.3	Results	52
3.2.4	Effects of Resolution on the Results	56
3.3	“Reconnection diffusion” in the presence of gravity	57
3.3.1	Numerical Approach	57
3.3.2	Results	61
3.3.3	Effects of Resolution on the Results	65
3.3.4	Magnetic Field Expulsion Revealed	65
3.4	Discussion of the results: relations to earlier studies	72
3.4.1	Comparison with Heitsch et al. (2004): Ambipolar Diffusion Versus Turbulence and 2.5-dimensional Versus Three-dimensional	72
3.4.2	Transient De-correlation of Density and Magnetic Field	74
3.4.3	Relation to Shu et al. (2006): Fast Removal of Magnetic Flux Dur- ing Star Formation	74
3.5	Turbulent magnetic diffusion and turbulence theory	76
3.6	Accomplishments and limitations of the present study	78
3.6.1	Major Findings	78
3.6.2	Applicability of the Results	79
3.6.3	Magnetic Field Reconnection and Different Stages of Star Formation	80

3.6.4	Unsolved Problems and further Studies	81
3.7	Summary	82
4	The role of turbulent magnetic reconnection in the formation of rotationally supported protostellar disks	85
4.1	Introduction	86
4.2	Numerical Setup and Initial Disk Conditions	89
4.3	Results	91
4.4	Comparison with the work of Seifried et al.	97
4.4.1	Further calculations	99
4.5	Effects of numerical resolution on the turbulent model	107
4.6	Discussion	110
4.6.1	Our approach and alternative ideas	110
4.6.2	Present result and bigger picture	113
4.7	Conclusions	114
5	Turbulence and magnetic field amplification in collisionless MHD: an application to the ICM	117
5.1	Numerical methods and setup	118
5.1.1	Thermal relaxation model	118
5.1.2	Numerics	119
5.1.3	Reference units	120
5.1.4	Initial conditions and parametric choice	120
5.2	Results	122
5.2.1	The role of the anisotropy and instabilities	124
5.2.2	Magnetic versus thermal stresses	129
5.2.3	PDF of Density	131
5.2.4	The turbulence power spectra	132
5.2.5	Turbulent amplification of seed magnetic fields	137
5.3	Discussion	145

5.3.1	Consequences of assuming one-temperature approximation for all species	147
5.3.2	Limitations of the thermal relaxation model	148
5.3.3	Comparison with previous studies	149
5.3.4	Implications of the present study	152
5.4	Summary and Conclusions	152
6	Conclusions and Perspectives	157
	Bibliography	163
A	Numerical MHD <i>Godunov</i> code	177
A.1	Code units	177
A.2	MHD equations in conservative form	178
A.3	The collisionless MHD equations	180
A.4	Magnetic field divergence	181
A.5	Source terms	181
A.6	Turbulence injection	182
B	Diffusion of magnetic field and removal of magnetic flux from clouds via turbulent reconnection	183
C	The role of turbulent magnetic reconnection in the formation of rotationally supported protostellar disks	185
D	Disc formation in turbulent cloud cores: is magnetic flux loss necessary to stop the magnetic braking catastrophe or not?	187
E	Magnetic field amplification and evolution in turbulent collisionless MHD: an application to the intracluster medium	189

List of Figures

2.1	<i>Upper plot:</i> Sweet–Parker model of reconnection. The outflow is limited by a thin slot Δ , which is determined by Ohmic diffusivity. The other scale is an astrophysical scale $L_x \gg \Delta$. <i>Middle plot:</i> reconnection of weakly stochastic magnetic field according to LV99. The model that accounts for the stochasticity of magnetic field lines. The outflow is limited by the diffusion of magnetic field lines, which depends on field line stochasticity. <i>Low plot:</i> an individual small-scale reconnection region. The reconnection over small patches of magnetic field determines the local reconnection rate. The global reconnection rate is substantially larger as many independent patches come together. From Lazarian et al. (2004).	28
2.2	Schematic representation of two interacting turbulent eddies each one carrying its own magnetic flux tube. The turbulent interaction causes an efficient mixing of the gas of the two eddies, as well as fast magnetic reconnection of the two flux tubes which leads to diffusion of the magnetic field (extracted from Lazarian 2011).	31
2.3	Folded structure of the magnetic field at the saturated state of the SSD (Extracted from Schekochihin et al. 2004).	40
2.4	Mechanism of the firehose instability. (Extracted from Treumann & Baumjohann 1997).	43
2.5	Satellite measurements across a mirror-unstable region. (Extracted from Treumann & Baumjohann 1997).	44

3.1	<p>(x, y)-plane showing the initial configuration of the z component of the magnetic field B_z (<i>left</i>) and the density distribution (<i>right</i>) for the model B2 (see Table 3.1). The centers of the plots correspond to $(x, y) = (0, 0)$.</p>	51
3.2	<p>Evolution of the <i>rms</i> amplitude of the Fourier modes $(k_x, k_y) = (\pm 1, \pm 1)$ of $\langle B_z \rangle_z$ (upper curves) and $\langle B_z \rangle_z / \langle \rho \rangle_z$ (lower curves). The curves for $\langle B_z \rangle_z$ were multiplied by a factor of 10. All the curves were smoothed to make the visualization clearer.</p>	53
3.3	<p><i>Left</i>: evolution of the ratio of the averaged magnetic field over the averaged density (more left) and of the ratio of the averaged passive scalar over the averaged density (more right) within a distance $R = 0.25L$ from the central z-axis. The values have been subtracted from their characteristic values $\bar{B}/\bar{\rho}$ in the box. <i>Right</i>: evolution of the <i>rms</i> amplitude of the Fourier modes $(k_x, k_y) = (\pm 1, \pm 1)$ of $\langle \Phi \rangle_z$ (upper curves) and $\langle \Phi \rangle_z / \langle \rho \rangle_z$ (lower curves). The curves for Φ were multiplied by a factor of 10. All the curves were smoothed to make the visualization clearer.</p>	54
3.4	<p>Distribution of $\langle \rho \rangle_z$ vs. $\langle B_z \rangle_z$ for model B2 (see Table 3.1), at $t = 0$ (left) and $t = 10$ (center). <i>Right</i>: correlation between fluctuations of the strength of the magnetic field (δB) and density ($\delta \rho$).</p>	54
3.5	<p><i>Left</i>: distribution of $\langle \rho \rangle_z$ vs. $\langle \Phi \rangle_z$ for model B2 (see Table 3.1), at $t = 0$ (most left) and $t = 10$ (most right). <i>Right</i>: correlation between fluctuations of the passive scalar field ($\delta \Phi$) and density ($\delta \rho$).</p>	55
3.6	<p>Comparison between models of different resolution: B2, B2l, and B2h (Table 3.1). It presents the same quantities as in Figure 3.2.</p>	57
3.7	<p>Model C2 (see Table 3.2). <i>Top row</i>: logarithm of the density field; <i>bottom row</i>: B_z component of the magnetic field. <i>Left column</i>: central xy, xz, and yz slices of the system projected on the respective walls of the cubic computational domain, in $t = 0$; <i>middle and right columns</i>: the same for $t = 3$ (middle) and $t = 8$ (right).</p>	59

-
- 3.8 Evolution of the equilibrium models for different gravitational potential. The top row shows the time evolution of $\langle B_z \rangle_{0.25} / \bar{B}_z$ (*left*), $\langle \rho \rangle_{0.25} / \bar{\rho}$ (*middle*), and $(\langle B_z \rangle_{0.25} / \langle \rho \rangle_{0.25}) / (\bar{\rho} / \bar{B}_z)$ (*right*). The other plots show the radial profile of $\langle B_z \rangle_z$ (*upper panels*), $\langle \rho \rangle_z$ (*middle panels*), and $\langle B_z \rangle_z / \langle \rho \rangle_z$ (*bottom panels*) for the different values of A in $t = 0$ (magneto-hydrostatic solution with β constant, see Table 3.2) and $t = 8$. Error bars show the standard deviation. All models have initial $\beta = 1.0$ 66
- 3.9 Evolution of the equilibrium models for different turbulent driving. The top row shows the time evolution of $\langle B_z \rangle_{0.25} / \bar{B}_z$ (*left*), $\langle \rho \rangle_{0.25} / \bar{\rho}$ (*middle*), and $(\langle B_z \rangle_{0.25} / \langle \rho \rangle_{0.25}) / (\bar{\rho} / \bar{B}_z)$ (*right*). The bottom row shows the radial profile of $\langle B_z \rangle_z$ (*left*), $\langle \rho \rangle_z$ (*middle*), and $\langle B_z \rangle_z / \langle \rho \rangle_z$ (*right*) for each value of the turbulent velocity V_{rms} , in $t = 0$ (magneto-hydrostatic solution with β constant) and $t = 8$. Error bars show the standard deviation. All models have initial $\beta = 1.0$. See Table 3.2. 67
- 3.10 Evolution of the equilibrium models for different degrees of magnetization (plasma $\beta = P_{\text{gas}} / P_{\text{mag}}$). The top row shows the time evolution of $\langle B_z \rangle_{0.25} / \bar{B}_z$ (*left*), $\langle \rho \rangle_{0.25} / \bar{\rho}$ (*middle*), and $(\langle B_z \rangle_{0.25} / \langle \rho \rangle_{0.25}) / (\bar{\rho} / \bar{B}_z)$ (*right*). The other plots show the radial profile of $\langle B_z \rangle_z$ (*upper panels*), $\langle \rho \rangle_z$ (*middle panels*), and $\langle B_z \rangle_z / \langle \rho \rangle_z$ (*bottom panels*) for each value of β , in $t = 0$ (magneto-hydrostatic solution with β constant) and $t = 8$. Error bars show the standard deviation of the data. See Table 3.2. 68
- 3.11 Comparison between the model C2 (turbulent diffusivity) and resistive models without turbulence (see Table 3.4). All the cases have analogous parameters. 69
- 3.12 Comparison of the time evolution of $\langle B_z \rangle_{0.35}$ between models C1, C3, C4, C5, C6, and C7 (see Table 3.2) and resistive models without turbulence (see Table 3.4). 69

3.13	Evolution of models which start in non-equilibrium. The top row shows the time evolution of $\langle B_z \rangle_{0.25} / \bar{B}_z$ (<i>left</i>), $\langle \rho \rangle_{0.25} / \bar{\rho}$ (<i>middle</i>), and $(\langle B_z \rangle_{0.25} / \langle \rho \rangle_{0.25}) / (\bar{\rho} / \bar{B}_z)$ (<i>right</i>), for runs with (thick lines) and without (thin lines) injection of turbulence. The other plots show the radial profile of $\langle B_z \rangle_z$ (<i>upper panels</i>), $\langle \rho \rangle_z$ (<i>middle</i>), and $\langle B_z \rangle_z / \langle \rho \rangle_z$ (<i>right</i>) for different values of β , at $t = 8$, for runs with and without turbulence. Error bars show the standard deviation. See Table 3.3.	70
3.14	Comparison of the time evolution of $\langle B_z \rangle_{0.25}$ (<i>left</i>), $\langle \rho \rangle_{0.25}$ (<i>middle</i>), and $\langle B_z \rangle_{0.25} / \langle \rho \rangle_{0.25}$ (<i>right</i>) between models with different resolutions: C2, C2l, C2h (Table 3.2) and D2, D2l, D2h (Table 3.3).	71
4.1	Face-on (top) and edge-on (bottom) density maps of the central slices of the collapsing disk models listed in Table 4.1 at a time $t = 9 \times 10^{11}$ s (≈ 0.03 Myr). The arrows in the top panels represent the velocity field direction and those in the bottom panels represent the magnetic field direction. From left to right rows it is depicted: (1) the pure hydrodynamic rotating system; (2) the ideal MHD model; (3) the MHD model with an anomalous resistivity 10^3 times larger than the Ohmic resistivity, i.e. $\eta = 1.2 \times 10^{20}$ cm ² s ⁻¹ ; and (4) the turbulent MHD model with turbulence injected from $t = 0$ until $t = 0.015$ Myr. All the MHD models have an initial vertical magnetic field distribution with intensity $B_z = 35 \mu\text{G}$. Each image has a side of 1000 AU.	93
4.2	Three-dimensional diagrams of snapshots of the density distribution for the <i>turbulent</i> model of disk formation in the rotating, magnetized cloud core computed by SGL12. From left to right: $t = 10.000$ yr; 20.000 yr; and 30.000 yr. The side of the external cubes is 1000 AU.	94

-
- 4.3 Radial profiles of the: (i) radial velocity v_R (top left), (ii) rotational velocity v_ϕ (top right); (iii) inner disk mass (bottom left); and (iv) vertical magnetic field B_z , for the four models of Figure 4.3 at time $t \approx 0.03$ Myr). The velocities were averaged inside cylinders centered in the protostar with height $h = 400$ AU and thickness $dr = 20$ AU. The magnetic field values were also averaged inside equatorial rings centered in the protostar. The standard deviation for the curves are not shown in order to make the visualization clearer, but they have typical values of: $2 - 4 \times 10^4$ cm s $^{-1}$ (for the radial velocity), $5 - 10 \times 10^4$ cm s $^{-1}$ (for the rotational velocity), and $100 \mu\text{G}$ (for the magnetic field). The vertical lines indicate the radius of the sink accretion zone. 95
- 4.4 Disk formation in the rotating, magnetized cloud cores analysed by SGL12. Three cases are compared: an ideal MHD system, a resistive MHD system, and an ideal turbulent MHD system. Right row panels depict the time evolution of the total mass (gas + accreted gas onto the central sink) within a sphere of $r=1000$ AU (top panel), the magnetic flux (middle panel), and the mass-to-flux ratio normalized by the critical value averaged within $r=1000$ AU (bottom panel). Left row panels depict the same quantities for $r=100$ AU, i.e., the inner sphere that involves only the region where the disk is build up as time evolves. Middle row panels show the same quantities for the intermediate radius $r=500$ AU. We note that the little bumps seen on the magnetic flux and μ diagrams for $r=100$ AU are due to fluctuations of the turbulence whose injection scale (~ 1000 AU) is much larger than the disk scale. 100
- 4.5 Mass-to-magnetic flux ratio μ , normalized by its initial value $\mu_0(M)$, plotted against the mass, for (i) $r = 100$ AU (left), (ii) $r = 500$ AU (middle), and (iii) $r = 1000$ AU (right). $\mu_0(M)$ is the value of μ for the initial mass M : $\mu_0(M) = \{M/[B_0\pi R_0^2(M)]\} / \{0.13/\sqrt{G}\}$, where B_0 is the initial value of the magnetic field and $R_0(M)$ is the initial radius of the sphere containing the mass M . The initial conditions are the same as in Figure 4.4. 103

-
- 4.6 Mean magnetic intensity as a function of bins of density, calculated for the models analyzed in SGL12 at $t = 30$ kyr. The statistical analysis was taken inside spheres of radius of 100 AU (left), 500 AU (middle), and 1000 AU (right). Cells inside the sink zone (i.e., radius smaller than 60 AU) were excluded from this analysis. For comparison, we have also included the results for the turbulent model *turbulent-512* which was simulated with a resolution twice as large as the model *turbulent-256* presented in SGL12 (see also the Section 4.5). 105
- 4.7 Comparison between the radial profiles of the high resolution turbulent model *turbulent-512* with the models presented in SGL12 (for which the resolution is 256^3). Top left: radial velocity v_R . Top right: rotational velocity v_ϕ . Bottom left: inner disk mass. Bottom right: vertical magnetic field B_z . The numerical data are taken at time $t \approx 0.03$ Myr. The velocities were averaged inside cylinders centered in the protostar with height $h = 400$ AU and thickness $dr = 20$ AU. The magnetic field values were also averaged inside equatorial rings centered in the protostar. The vertical lines indicate the radius of the sink accretion zone for all models except *turbulent-512* for which the the sink radius of the accretion zone is half of that value. . . 109
- 5.1 Central XY plane of the cubic domain showing the density (left column) and the magnetic intensity (right column) distributions for models of Table 5.1 with initial moderate magnetic field ($\beta_0 = 200$) and different values of the anisotropy relaxation rate ν_S , at $t = t_f$. Top row: model A2 (with $\nu_S = 0$, corresponding to the standard CGL model with no constraint on anisotropy growth); middle row: model A1 ($\nu_S = \infty$, corresponding to instantaneous anisotropy relaxation to the marginal stability condition); bottom row: model Amhd (collisional MHD with no anisotropy). The remaining initial conditions are all the same for the three models (see Table 5.1). 123

5.2	The panels show two-dimensional normalized histograms of $A = p_{\perp}/p_{\parallel}$ versus $\beta_{\parallel} = p_{\parallel}/(B^2/8\pi)$ for models starting with moderate magnetic fields (models A with $\beta_0 = 200$) and the model B1 with strong magnetic field (with $\beta_0 = 0.2$ (see Table 5.1). The histograms were calculated considering snapshots every $\Delta t = 1$, from $t = 2$ until the final time step t_f indicated in Table 5.1 for each model. The continuous gray lines represent the thresholds for the linear firehose ($A = 1 - 2\beta_{\parallel}^{-1}$, lower curve) and mirror ($A = 1 + \beta_{\perp}^{-1}$, upper curve) instabilities, obtained from the kinetic theory. The dashed gray line corresponds to the linear mirror instability threshold obtained from the CGL-MHD approximation ($A/6 = 1 + \beta_{\perp}^{-1}$).	126
5.3	Maps of the anisotropy $A = p_{\perp}/p_{\parallel}$ distribution at the central slice in the XY plane at the the final time t_f for a few models A and B of Table 5.1. .	127
5.4	Central slice in the XY plane of the domain showing distributions of the maximum growth rate γ_{max} (normalized by the initial ion gyrofrequency Ω_{i0}) of the firehose (left column) and mirror (right column) instabilities for models A2 and A3 (with $\beta_0 = 200$ and different values of the anisotropy relaxation rate ν_S). The expressions for the maximum growth rates are given by Equations (2.50), with a maximum value given by $\gamma_{max}/\Omega_i = 1$. Data are taken at the the final time t_f for each model, indicated in Table 5.1.	129
5.5	The same as Figure 5.4, for models A4 and A5.	130
5.6	Normalized histogram of $\log \rho$. Left: models starting with $\beta_0 = 200$. Right: models starting with $\beta_0 = 0.2$. The histograms were calculated using one snapshot every $\Delta t = 1$, from $t = 2$ until the final time t_f indicated in Table 5.1.	131
5.7	Two-dimensional normalized histograms of $\log \rho$ versus $\log B$. Left: collisionless model A2 with null anisotropy relaxation rate. Right: collisional MHD model Amhd. The histograms were calculated using snapshots every $\Delta t = 1$, from $t = 2$ until the final time t_f indicated in Table 5.1. See more details in Section 5.2.3.	132

5.8	Power spectra of the velocity $P_u(k)$ (top row), magnetic field $P_B(k)$ (middle row), and density $P_\rho(k)$ (bottom row), multiplied by $k^{5/3}$. Left column: models A, with initial $\beta_0 = 200$. Right column: models B, with $\beta_0 = 0.2$. Each power spectrum was averaged in time considering snapshots every $\Delta t = 1$, from $t = 2$ to the final time step t_f indicated in Table 5.1.	134
5.9	Ratio between the power spectrum of the compressible component $P_C(k)$ and the total velocity field $P_u(k)$, for the same models as in Figure 5.8 (see Table 5.1 and Section 5.2.4 for details).	135
5.10	l_\perp vs l_\parallel obtained from the structure function of the velocity field (Eq. 5.5). The axes are scaled in cell units.	136
5.11	Ratio between the power spectrum of the magnetic field $P_B(k)$ and the velocity field $P_u(k)$ for the same models as in Figure 5.8 (see Table 5.1 and Section 5.2.4 for details).	137
5.12	Time evolution of the magnetic energy $E_M = B^2/2$ for the models starting with a weak (seed) magnetic field, models C1, C2, C3, C4, and Cmhd, from Table 5.1. The left and right panels differ only in the scale of E_M . This is shown in a log scale in the top panel and in a linear scale in the bottom panel. The curves corresponding to models C2 and C3 are not visible in the right panel.	138
5.13	Magnetic field power spectrum multiplied by $k^{5/3}$ for the same models presented in Figure 5.12, from $t = 2$ at every $\Delta t = 2$ (dashed lines) until the final time indicated in Table 5.1 (solid lines). The velocity field power spectrum multiplied by $k^{5/3}$ at the final time is also depicted for comparison (dash-dotted line).	139

List of Tables

2.1	Scaling laws, anisotropy, and energy spectra for different models of incompressible MHD turbulence	22
2.2	Typical plasma parameters inferred from observations of the ICM	34
2.3	Plasma and turbulence parameters estimated for the ICM	35
3.1	Parameters of the Simulations in the Study of Turbulent Diffusion of Magnetic Flux without Gravity.	52
3.2	Parameters for the Models with Gravity Starting at Magneto-hydrostatic Equilibrium with Initial Constant β	60
3.3	Parameters for the Models with Gravity Starting Out-of-equilibrium, with Initially Homogeneous Fields.	60
3.4	Parameters for the 2.5-dimensional Resistive Models with Gravity Starting with Magneto-hydrostatic Equilibrium and Constant β	61
4.1	Summary of the models	92
5.1	Parameters of the simulated models	122
5.2	Space and time averages (upper lines) and standard deviations (lower lines) for the models A which have moderate initial magnetic fields ($\beta_0 = 200$).	142
5.3	Space and time averages (upper lines) and standard deviations (lower lines) for models B which have initial strong magnetic field ($\beta = 0.2$).	143
5.4	Space and time averages (upper lines) and standard deviations (lower lines) for models C which have initial very weak (seed) magnetic field.	144

Chapter 1

Introduction

Magnetic fields and turbulence are known to be present in astrophysical flows of every scale: stellar interiors and surfaces, molecular clouds, the warm and the hot phase of the interstellar medium (ISM) of the Milk Way, the ISM of external galaxies, and the intracluster medium (ICM). The specific role played by these two ingredients in different branches of astrophysics is still highly debated, but it is generally regarded as important.

In particular, for the interstellar medium and star formation, the role of turbulence has been discussed in many reviews (see Elmegreen & Scalo 2004; McKee & Ostriker 2007). The opinion regarding the role of magnetic fields in these environments varies from being absolutely dominant in the processes (see Tassis & Mouschovias 2005; Galli et al. 2006) to moderately important, as in the turbulence dominated models of star formation (see Padoan et al. 2004).

In most of the astrophysical environments, these two fundamental phenomena (magnetism and turbulence) are intrinsically related. The large scale dynamics of these environments is commonly described by the magnetohydrodynamic (MHD) theory, which links the evolution of the magnetic fields and the bulk motions of the gas. In this theory, the gas suffers a force perpendicular to the magnetic field (the Lorentz force), at the same time the magnetic field lines are dragged and distorted by the gas motions perpendicular to them; that is, the magnetic field and the gas perform work on each other through motions normal to the magnetic field lines.

One central concept regarding the evolution of the magnetic field in the MHD theory is that, in the limit in which the electrical resistivity in the plasma is negligible, each fluid element stays confined on the same imaginary field line over the system evolution. Expressed in another way, the flux of the magnetic field \mathbf{B} across a lagrangian closed circuit does not change, for any configuration the system can assume. This matter-magnetic field coupling is called “flux freezing” or “frozen-in” condition and the MHD theory in this limit is called *ideal MHD*.

The frozen-in condition is usually thought as a good approximation for an MHD flow characterized by a large value of the dimensionless parameter the *magnetic Reynold's number* Rm (whose definition is given in Chapter 2, Equation 2.12). When $Rm \gg 1$, the time-scale for the diffusion of the large scale (i.e., the scale of the flow) magnetic field through the gas is much larger than the dynamical times of the flow. In general, typical flows in the ISM and ICM have huge values of Rm .

In star formation media, where Rm is generally high, without considering diffusive mechanisms that can violate this flux freezing, one faces problems attempting to explain many observational facts. For example, simple estimates show that if all the magnetic flux remains well coupled with the material that collapses to form a star in molecular clouds, then the magnetic field in a protostar should be several orders of magnitude higher than the one observed in T-Tauri stars (this is the “magnetic flux problem”, see Galli et al. 2006 and references therein, for example).

In late phases of the star-forming process, another difficulty arises to explain the observed protostellar disks. Theoretically, the flux freezing prevents the formation of rotationally supported disks around protostars, in contradiction with the observations. This is because flux freezing causes the loss of the angular momentum of the collapsing cloud via the torques exerted by the magnetic field lines torsioned by the differentially rotating gas. This problem is known as the “magnetic braking catastrophe”.

Does magnetic field remain absolutely frozen-in within high Rm flows? The answer to this question affects the description of numerous essential processes in the interstellar and intergalactic gas. A mechanism based on magnetic reconnection was proposed in Lazarian (2005) as a way of breaking the frozen-in condition and removing magnetic flux from

gravitating clouds, e.g. from star-forming clouds. That work referred to the reconnection model of Lazarian & Vishniac (1999) and Lazarian et al. (2004) for the justification of the concept of fast magnetic reconnection in the presence of turbulence. Through this diffusion process, that we call "turbulent reconnection diffusion" or TRD (Santos-Lima et al. 2010, 2012, 2013a; Leao et al. 2013), we will demonstrate in this thesis that it is possible to solve both the magnetic flux transport and the magnetic braking catastrophe problems in star formation.

Another consequence from the MHD approximation is the ability of a driven turbulent flow to amplify the magnetic fields until close equipartition between kinetic and magnetic energies (Schekochihin et al. 2004). That is, once a weak magnetic field seed is present, turbulent motions of the gas will "stretch" and "fold" the field lines until the magnetic forces become dynamically important. In this equilibrium situation, the magnetic fields have correlation lengths of the order of the largest scales of the turbulent motions. This process is referred as turbulent dynamo or small-scale dynamo, and is a powerful mechanism to amplify seed magnetic fields.

Although the origin of the seed fields is still a matter of discussion (see Grasso & Rubinstein 2001), the above turbulent dynamo scenario is amply accepted as the mechanism responsible for amplifying and sustaining the observed magnetic fields in the ICM (de Gouveia Dal Pino et al. 2013). This picture is supported by MHD simulations of galaxies merger showing the amplification of the magnetic field in the surround intergalactic medium (Kotarba et al. 2011).

However, the applicability of the standard MHD model (and turbulent dynamo) to the magnetized plasma of the intracluster media of galaxies needs to be revised. In these environments, the hypothesis of local thermodynamical equilibrium behind the MHD theory is not fulfilled due to the low collisionality of the gas there. Different gas temperatures (or pressures) can develop in the directions along and perpendicular to the local magnetic. Such an anisotropic pressure is known to develop electromagnetic kinetic instabilities whose feedback on the plasma can relax the difference between the pressure components. A modified MHD model should be used, which takes into account the development and effects of an anisotropic pressure. Such models have been referred in the literature as col-

collisionless MHD, or anisotropic MHD, or kinetic MHD models. How the turbulent dynamo and the turbulence itself in these models compares with the more explored (collisional) MHD approach is a new topic of research (Kowal et al. 2011) and will be also explored here in depth in the framework of the intracluster medium (Santos-Lima et al. 2013b).

As remarked, this thesis focuses on the investigation of two main issues. One is to test the turbulent reconnection diffusion mechanism (TRD) originally proposed by Lazarian (2005) in the context of star-formation processes. For this aim, we have performed 3D MHD numerical simulations of high Rm turbulent flows modeling interstellar clouds in different phases of star-formation. We found that turbulent reconnection diffusion was able to break the frozen in condition and to diffuse the magnetic fields, in consistency with the observational requirements.

The second subject is the investigation of the turbulent dynamo amplification of seed magnetic fields and the turbulence statistics in the ICM using collisionless MHD models and comparing with the more explored collisional MHD approach. An MHD numerical code was modified for this purpose and employed for performing 3D simulations of driven turbulence with in an ICM-like domain. We found that the results are sensitive to the rate at which the kinetic instabilities relax the pressure anisotropy of the system. For values of this rate which are suitable to the conditions of the ICM, the overall behavior of the turbulent flow, as well as the dynamo amplification of seed magnetic fields do not seem to deviate significantly from the results obtained with the collisional MHD model. Despite the limitations in our model, this result has the importance of giving support to the employment of a collisional MHD description for studying the turbulence in the ICM (Santos-Lima et al. 2013b).

The thesis is organized in the following way: Chapter 2 is devoted to present the theoretical grounds which support the investigation of both subjects. We first present the collisional MHD equations and its limit of validity. Since our focus are turbulent flows, we also present an overview about MHD turbulence. Then, we briefly discuss the magnetic flux transport problem in the framework of star formation and the proposed mechanism of turbulent reconnection diffusion (TRD) for solving it. Next, we briefly describe the conditions of the ICM and the turbulent dynamo magnetic field amplification in the

context of collisional MHD, as currently investigated. Finally we present the collisionless MHD model which we use to model the ICM. In Chapter 3, we present the results of our numerical studies of TRD in molecular clouds collapsing gravitationally (Santos-Lima et al. 2010). In Chapter 4, we present the results of our numerical studies of the effects of TRD on the formation of rotating protostellar disks (Santos-Lima et al. 2012, 2013a). In Chapter 5 we discuss the results obtained from the collisionless MHD description of the evolution of the turbulence and the dynamo amplification of seed fields in the ICM (Santos-Lima et al. 2013b). Finally, in Chapter 6 we summarize the results of this thesis and present our perspectives.

The numerical methods of the codes employed in the simulations presented are briefly described in Appendix A. The results presented in Chapters 3 and 4 have been published in refereed journals and the articles are reproduced in the Appendices B, C, and D. The results presented in Chapter 5 are in an article just submitted to publication, which is reproduced in the Appendix E. Complementary material can be also found in Leão, de Gouveia Dal Pino, Santos-Lima et al. (2012); and de Gouveia Dal Pino, Leão, Santos-Lima et al. (2012).

Chapter 2

MHD turbulence: diffusion and amplification of magnetic fields

The magnetohydrodynamics (MHD) theory describes the evolution of electrically conducting fluids and magnetic fields, in mutual interaction. These magnetic fields can have origin in electrical currents internal or external to the fluid volume in question. The MHD theory has a broad range of applicability in astrophysics because most of the astrophysical environments are composed by fluids with some degree of electrical conduction, and in addition they are observed to be pervaded by magnetic fields (see Chapter 1). The intrinsic complexity of the interaction fluid - magnetic field in MHD flows is increased by turbulence present in the astrophysical fluids, like the ISM and ICM. In particular, the turbulence is sometimes fundamental to understand the evolution of the magnetic fields in these fluids. Since MHD is actually a macroscopic description of plasmas, in this chapter, we start by presenting the basic concepts of plasmas, then we present the collisional MHD equations justifying their applicability range and next an overview of MHD turbulence. We then discuss the problem of magnetic field diffusion in the framework of star formation and a potential mechanism for solving it, the turbulent reconnection diffusion. Finally, we discuss turbulence in the context of the ICM and argue that a collisional MHD description is unsuitable in this case and then present a collisionless MHD model which better describes the ICM plasma.

2.1 Kinetic and fluid descriptions of a plasma

In a broad definition, plasma is a gas fully or partially ionized permeated by magnetic fields. Most of the astrophysical environments are filled by plasmas. In fact, more than 90% of the visible matter in the Universe is believed to be in a plasma state (e.g. de Gouveia Dal Pino 1995, and refs. therein; Goedbloed & Poedts 2004). For simplicity, we will restrict our attention to non-relativistic gases obeying the Maxwell-Boltzmann statistics, where quantum effects are negligible.

In a plasma, the charged particles in motion produce electrical currents and electromagnetic fields. These fields in turn, exert forces on the particles themselves. Therefore, a complete description of the system (particles and electromagnetic fields) involves the knowledge of the position and velocity of every particle, which is obviously impossible.

However, a statistical description of the plasma is still possible. For this, the plasma is required to behave like an almost ideal gas: the electrostatic interaction energy between particles must be small compared to their kinetic energy. For a plasma composed by electrons of charge $-e$ and positive ions of charge Ze , this condition is expressed by

$$k_B T \gg e^2 / \bar{r} \sim e^2 N^{-1/3}, \quad (2.1)$$

where T is the temperature of the plasma, k_B the Boltzmann constant, $\bar{r} \sim N^{-1/3}$ is the average distance between particles and N is the total number of particles per volume. This condition is more commonly expressed in terms of the Debye length λ_D , defined as

$$\lambda_D^2 = \frac{k_B T}{4\pi \left[\sum_s N_s (Z_s e)^2 \right]}, \quad (2.2)$$

where the summation is over the species denoted by the subscript s ($s = i, e$, for ions and electrons respectively). Using $\lambda_D \sim (k_B T / 4\pi N e^2)^{1/2}$, the condition for the almost ideal gas behavior is

$$e^2 N^{-1/3} / k_B T \sim \bar{r}^2 / 4\pi \lambda_D^2 \ll 1. \quad (2.3)$$

The above condition states the existence of many particles inside a sphere of radius λ_D , the ‘‘Debye sphere’’. Physically, the Debye length λ_D has the meaning of the distance

at which an electrical charge is screened by oppositely charged particles in the plasma. Over volumes with radii $\lambda \gg \lambda_D$, the plasma is quasi-neutral: $|ZeN_i - eN_e| \ll 1$. This is one of the fundamental properties of the plasma, the macroscopic quasi-neutrality.

Under this circumstance, the thermodynamic equilibrium properties of a plasma can be obtained from the statistical mechanics, as in the case of neutral gases, and the out-of-equilibrium phenomena can be described by kinetic theory.

In the kinetic theory, each species s of the plasma is described by a distribution function $f_s(t, \mathbf{r}, \mathbf{v})$ in the position \mathbf{r} and velocity \mathbf{v} spaces. The evolution of each distribution function is given by the Boltzmann transport equation (Landau & Lifshitz 1980):

$$\frac{\partial f_s}{\partial t} + \mathbf{v} \cdot \frac{\partial f_s}{\partial \mathbf{r}} + \frac{e_s}{m_s} \left(\mathbf{E} + \frac{1}{c} \mathbf{v} \times \mathbf{B} \right) \cdot \frac{\partial f_s}{\partial \mathbf{v}} = C(f_s), \quad (2.4)$$

where m_s is the particle mass, c is the speed of light, and $C(f_s)$ is the collisional term that includes the interactions with all the other species (also neutral species). The electromagnetic forces on the left-hand side are self-consistently obtained from the Maxwell equations with source terms (charge and current densities) calculated by the distribution function of all the species. However, they are “macroscopic” fields, in the sense that they are averaged over a large volume compared to the particles distances, but small compared to Debye length. The fluctuating components of the electromagnetic fields, eliminated by the averaging, are responsible for the random scattering of the particles. This random scattering is represented by $C(f_s)$ and leads the system to relax to thermodynamic equilibrium. It is responsible for the increase of entropy.

Although the kinetic approach provides a more complete description of a plasma, its intrinsic complexity makes it very hard to employ it in the study of the large scale plasma dynamics. In this sense, the commonly adopted simplification comes from the fluid approximation.

In a fluid model, the plasma is described by a set of macroscopic fields, like: density, temperature, and velocity field. These fields can be formally defined as statistical moments of the particles velocity. The equations of evolution for these fields can be obtained by taking successively high order velocity moments of the Boltzmann equation. This chain of equations composes the so called moments hierarchy. The evolution for each moment

depends on higher order moments, and, of course, on the electromagnetic fields. The electromagnetic fields, in turn, are obtained from the Maxwell equations, with the source terms determined by the velocity moments.

The advantage of the fluid approach comes from restricting the number of moments describing the plasma, by stopping the moments hierarchy at some level. The highest moment is then considered as null, or modeled in terms of the lower moments, that is, the macroscopic variables. This is the closure of the moment hierarchy.

Depending on the problem characteristics and formulation, the fluid description may be an one-fluid, a two-fluid, or many-fluid. In the one-fluid description, one set of macroscopic variables represent all the species of the plasma. In the two- or many-fluid description, two or more sets of macroscopic variables are employed.

For astrophysical plasmas which are the focus of this work, a macroscopic fluid description is generally more appropriate because of the large scales involved. In the next section, we present the basic MHD equations which describe the one-fluid model for the plasma, together with the assumptions necessary for its validity. Before, we will introduce a few time and space scales, which are important for defining the plasma regime.

The mentioned process of screening of an electrical charge inside the plasma occurs at a time-scale related to the inverse of the plasma frequency ω_{ps}

$$\omega_{ps} = \left(\frac{4\pi N_s Z_s^2 e^2}{m_s} \right)^{1/2}. \quad (2.5)$$

This is the harmonic frequency at which the species oscillate when the quasi-neutrality is perturbed. Due to the difference in masses, $\omega_{pe} \gg \omega_{pi}$ that is, the electrons move faster. The plasma can be considered quasi-neutral for processes having frequencies ω larger than $\approx \omega_{pe}$.

Next, let us consider the frequency $\omega_{s1,s2}$ of collisions between the species $s1$ and $s2$. The collisionality regime of a plasma depends on the frequency ω of variation of the electromagnetic fields appearing in the Boltzmann equation (2.4). In the limiting case where $\omega \ll \omega_{s1,s2}$ for any $s1, s2$, the plasma is considered collisionless, and the right-hand side of the equation (2.4) is not important. Collisions are also considered unimportant if the mean-free-path of the particles are large compared to the distances at

which the fields vary. In the opposite limit, when the collision frequencies are higher than the frequencies of the processes under consideration, the species have time to relax to the local thermodynamical equilibrium and their distribution functions are well approximated by the Maxwell-Boltzmann distribution.

Other important scales are introduced by the presence of the magnetic field in the plasma. In the presence of a magnetic field of intensity B , the particles orbit the magnetic field lines with the Larmor frequency Ω_s , given by:

$$\Omega_s = \frac{Z_s e B}{m_s c}. \quad (2.6)$$

The radius of this orbit is the Larmor radius $R_s = \frac{v_\perp}{\Omega_s}$ where v_\perp is the component of the particle velocity perpendicular to the magnetic field line.

2.2 Basic MHD equations

Here we describe the basic equations for the simplest MHD model which describes a plasma as one-fluid model. The time and spatial scales described by this basic model must be larger than the times associated with the Larmor and plasma frequencies of the species, and the scales of the Debye length and Larmor radius of the species. This model is non-relativistic and assumes the plasma to be in local thermodynamical equilibrium: that is, the collision rate between particles is assumed to be faster than the frequency of the macroscopic phenomena, and the mean-free-path of the particles smaller than the macroscopic lengths.

When convenient, we will point the modifications on the equations in specific physical situations.

The plasma is macroscopically described by eight fields: a mass density ρ , a scalar pressure p or temperature T , three components of the velocity \mathbf{u} , and three components of the magnetic field \mathbf{B} . These fields are evolved by a set of eight equations, the MHD equations. In the absence of external forces, the basic MHD equations in differential form are (see, for example, de Gouveia Dal Pino 1995):

- The continuity equation describing the conservation of mass:

$$\frac{\partial \rho}{\partial t} + \nabla \cdot (\rho \mathbf{u}) = 0. \quad (2.7)$$

- Equation of motion describing the momentum evolution:

$$\rho \left(\frac{\partial}{\partial t} + \mathbf{u} \cdot \nabla \right) \mathbf{u} = -\nabla p + \frac{1}{c} \mathbf{J} \times \mathbf{B} + \rho \nu \nabla^2 \mathbf{u} + \rho \left(\zeta + \frac{1}{3} \nu \right) \nabla \nabla \cdot \mathbf{u}, \quad (2.8)$$

where c is the light speed, \mathbf{J} is the current density given by the Ampère's law

$$\mathbf{J} = \frac{c}{4\pi} \nabla \times \mathbf{B}, \quad (2.9)$$

ν and ζ are the coefficients of kinematic viscosity (shear and bulk viscosity, respectively). Normally $\nu \gg \zeta$. In the absence of the Lorentz force $(\mathbf{J} \times \mathbf{B})/c$, this equation is called the *Navier-Stokes equation*. Observe that the electric field term (Maxwell's displacement current) is not included in the last equation. It comes from the assumption of non-relativistic regime.

- Faraday's law or induction equation, describing the magnetic field evolution:

$$\frac{\partial \mathbf{B}}{\partial t} = \nabla \times (\mathbf{u} \times \mathbf{B}) + \eta \nabla^2 \mathbf{B}. \quad (2.10)$$

where $\eta = c^2/(4\pi\sigma)$ is the Ohmic magnetic diffusivity and σ is the electrical conductivity given by

$$\sigma = \frac{n_e e^2 \tau_{ei}}{m_e}, \quad (2.11)$$

where n_e and m_e are the electron density and mass, respectively, and τ_{ei} is the time interval between electron-ion collisions. In the limit $\eta = 0$, the induction equation describes the evolution of the magnetic field in the *ideal* MHD approach.

The relative importance between the term advecting the magnetic field and the dissipative term is given by the magnetic Reynold's number

$$Rm = \frac{LU}{\eta}, \quad (2.12)$$

where L is now the characteristic scale of variation of the magnetic field, and U is the characteristic velocity of the system. When $Rm \gg 1$ (which is the case of most astrophysical flows) the ideal MHD approach is adopted.

In this situation, the magnetic flux Φ_B through some surface S fixed to the fluid particles is conserved:

$$\frac{d\Phi_B}{dt} = \frac{d}{dt} \int_S \mathbf{B} \cdot \hat{\mathbf{n}} dS = 0. \quad (2.13)$$

with $\hat{\mathbf{n}}$ the unitary vector normal to the surface.

This induction equation can have a more general form, accounting for special physical situations, with more terms appearing in the rhs. One term we should mention is the Biermann battery term

$$-\frac{c}{n_e^2 e} (\nabla n_e) \times (\nabla p_e), \quad (2.14)$$

which can generate seed magnetic fields in the plasma (see Section 2.4), important in the context of origin of the cosmic magnetic fields.

When the plasma is weakly ionized, a term accounting for the *Ambipolar Diffusion* effect is usually invoked as dissipative mechanism (which in astrophysics is particularly important during star-formation processes). This term is given by:

$$\nabla \times \left\{ \frac{(\mathbf{J} \times \mathbf{B}) \times \mathbf{B}}{c\gamma_{in}\rho\rho_i} \right\} \quad (2.15)$$

where ρ_i is the mass density of the ions ($\ll \rho$), and γ_{in} is the rate of momentum exchange between ions and neutrals (see for example Shu et al. 1983).

- Equation of energy conservation:

$$\frac{\partial e}{\partial t} + \nabla \cdot \mathbf{q} = 0, \quad (2.16)$$

with the energy density e given by

$$e = \frac{1}{2}\rho u^2 + \frac{B^2}{8\pi} + w,$$

where w is the internal energy of the gas, given by the relation $w = p/(\gamma - 1)$ (assuming the equation of ideal gas with the adiabatic exponent γ), and the energy flux vector \mathbf{q} is given by¹

$$\mathbf{q} = \left(e + p + \frac{B^2}{4\pi} \right) \mathbf{u} + \frac{\eta}{c} \mathbf{J} \times \mathbf{B} - \frac{\mathbf{u} \cdot \mathbf{B}}{4\pi} \mathbf{B} - \rho\nu \sum_i \left(\frac{\partial u_i}{\partial x_k} + \frac{\partial u_k}{\partial x_i} - \frac{2}{3} \delta_{ik} \nabla \cdot \mathbf{u} \right) v_i \mathbf{e}_k.$$

Depending on the problem, several further simplifications can be done. For example, we can consider the scalar pressure p given simply by the equation of state of a politropic gas:

$$p = A\rho^\gamma \quad (2.17)$$

where A is in general a function of the entropy S .

Another simplification, usually adopted when the flow is subsonic (i.e., when u is much smaller than the sound speed $c_s = \sqrt{\gamma p/\rho}$) is to assume incompressibility: $\nabla \cdot \mathbf{u} \approx 0$.

¹We note that in this work we are not considering radiative cooling or heat conduction, which can be important in many astrophysical situations (see however comments on these issues in Chapters 5 and 6).

The dimensionless number which characterizes the compressibility of a flow is the sonic Mach number

$$M_S = \frac{U}{c_s}. \quad (2.18)$$

When $M_S > 1$, the flow is said *supersonic*, when $M_S = 1$ it is *trans-sonic*, and when $M_S \approx 1$ it is *subsonic*.

The set of collisional MHD equations above will be employed in most of the studies undertaken in this thesis. In particular, in Chapters 3 and 4 they will be used to describe the gravitational collapse of turbulent interstellar clouds and protostellar disk formation, respectively.

2.2.1 Linear modes

Considering the collisional ideal MHD equations in the adiabatic regime (i.e. with constant entropy which implies no radiative cooling, viscosity or resistivity), a linear analysis in an homogeneous background reveals the existence of three propagating waves: the Alfvén, fast and slow magnetosonic waves. The propagating velocities of these three waves are respectively (de Gouveia Dal Pino 1995):

$$v_A = \left(\frac{B^2}{4\pi\rho} \right)^{1/2} \cos\theta \quad (2.19)$$

$$c_f = \left\{ \frac{(c_s^2 + v_A^2) + \sqrt{(c_s^2 + v_A^2)^2 - 4c_s^2v_A^2 \cos^2\theta}}{2} \right\}^{1/2} \quad (2.20)$$

$$c_s = \left\{ \frac{(c_s^2 - v_A^2) + \sqrt{(c_s^2 + v_A^2)^2 - 4c_s^2v_A^2 \cos^2\theta}}{2} \right\}^{1/2} \quad (2.21)$$

where θ is the angle between the direction of propagation of the wave and the local magnetic field \mathbf{B} .

The Alfvén wave is incompressible (it implies no change in density), while the fast and slow magnetosonic modes are compressible.

An useful dimensionless number characterizing the regime of an MHD flow is the Alfvénic Mach number

$$M_A = \frac{U}{v_A}. \quad (2.22)$$

When $M_A > 1$, the flow is called *super-Alfvénic*, otherwise *sub-Alfvénic*. In the intermediary case, the flow is called *trans-Alfvénic*.

In Section 2.5 below, we will see how these modes are modified when considering a collisionless MHD model.

2.3 MHD turbulence: an overview

The notion of a turbulent flow is associated with a random or chaotic velocity field in space and time. This randomness arises when the velocity field evolution is strongly non-linear. In opposition, a flow is called laminar when it has an organized or deterministic velocity field, again in space and time (see for example, Landau & Lifshitz 1959).

Consider, for example, a hydrodynamic incompressible flow ($\nabla \cdot \mathbf{u} = 0$). The equation describing the evolution of the velocity field is

$$\frac{\partial \mathbf{u}}{\partial t} + (\mathbf{u} \cdot \nabla) \mathbf{u} = -\frac{1}{\rho} \nabla p + \nu \nabla^2 \mathbf{u}. \quad (2.23)$$

The advection term in the left-hand side shows the intrinsic non-linearity of the equation. On the right-hand side we have the viscous force $\nu \nabla^2 \mathbf{u}$ which has the effect of damping “irregularities” in the velocity field. When viscosity dominates, the flow tends to be laminar; when the non-linear term dominates, turbulence can develop. The relative importance between these two terms is estimated by the Reynolds number Re of the flow

$$Re = \frac{LU}{\nu}, \quad (2.24)$$

where L is the characteristic scale of changes in the velocity field, and U is the characteristic speed of the flow. The higher Re , the more unstable to perturbations is the flow. That is, at very high Re ($Re \gg 1$), a flow probably develops turbulence.

Turbulence is ubiquitous in astrophysical environments as it follows from theoretical considerations based on the high Reynolds numbers of astrophysical flows and is strongly supported by studies of spectra of the interstellar electron density fluctuations (see Armstrong, Rickett, & Spangler 1995; Chepurnov & Lazarian 2010), as well as of HI (Lazarian 2009 for a review and references therein; Chepurnov et al. 2010) and CO lines (see Padoan et al. 2009).

No complete quantitative theory on turbulence exists yet, but many important qualitative results are known. Keeping this in mind, the physical quantities in the arguments and results presented below are to be considered in order of magnitude. We first introduce some results and hypotheses about hydrodynamical turbulence theory and extend them to the more general MHD case.

2.3.1 The hydrodynamic case

A turbulent flow can be depicted as a superposition of eddies of several scales. For eddies of a given scale l a speed u_l is associated. A Reynolds number can be attributed to the eddies of each scale: $Re_l = u_l l / \nu$. The biggest eddies are produced by the largest scales L of the flow and have speeds U . These eddies are unstable (high Re_l) and produce a number of smaller eddies with smaller speeds. This process of cascading of kinetic energy (Richardson cascade) to smaller eddies continue, until the size and speed of the eddies are such that the molecular viscosity dominates ($Re_l \sim 1$) and their kinetic energy is dissipated into heat (Landau & Lifshitz 1959).

The scale L of the largest eddies is called the *external* or *injection* scale of the turbulence. The scale l_ν for which the motions are dissipated by the viscosity is called the *internal* or *dissipative* scale.

In the situation in which a source of energy and momentum stirs the fluid generating the largest eddies continually and this cascade proceeds in the statistically steady state, the turbulence is said to be fully developed. We will focus on this case here, instead of the transition to turbulence or of the decaying of turbulence. The constant energy injection rate will be denoted by ϵ (with dimension of energy per mass per time).

Kolmogorov's 1941 theory (K41) assumes that at a very high Re , the statistical properties of the eddies of scales l ($L \gg l \gg l_\nu$) are homogeneous and isotropic: they do not depend on the mean velocity of the flow or the specific characteristic of the mechanism injecting turbulence. Also, they do not depend on the dissipation mechanism. This range of scales is called the *inertial range*. Using self-similarity and dimensional arguments, the following relation is satisfied in the inertial range:

$$u_l \propto (\epsilon l)^{1/3}, \quad (2.25)$$

(Kolmogorov and Obukhov's scaling law, 1941). This law is interpreted in the following way: the energy $\sim u_l^2$ contained in eddies of all scales $< l$ is dissipated (after cascading until the dissipation scale) in the turnover time l/u_l , at a rate ϵ (equal to the energy injection rate in the cascade).

From dimensional arguments, or using the Kolmogorov law at the end of the inertial range, the dissipative scale l_ν is given by

$$l_\nu \sim (\nu^3/\epsilon)^{1/4}, \quad (2.26)$$

(Kolmogorov, 1941).

One is usually interested in characterize the inertial range by the knowledge of the amount of energy carried by eddies at each scale. This energy distribution is usually represented in the Fourier space by the energy spectrum $E(k)$. Thus, $E(k)dk$ represents the energy of the eddies of the scale $l \sim 1/k$. For the incompressible hydrodynamic turbulence, the energy spectrum following from the Kolmogorov law is:

$$E(k) \propto k^{-5/3}. \quad (2.27)$$

2.3.2 Alfvénic turbulence, weak cascade

Now we will consider the situation when magnetic fields are present.

If the magnetic fields are not dynamically important at the injection scale L , that is, $M_A = U/v_A \gg 1$, turbulence at these scales will be essentially hydrodynamic. As cascade of energy proceeds, the eddy velocities will reduce until $u_l \sim v_A$ at the scale l_A . Using Kolmogorov's law, $l_A \sim LM_A^{-3}$. Henceforth, we will consider the scales $l < l_A$.

The presence of a mean magnetic field introduces a preferential direction and so the hypothesis of isotropy of the hydronamic turbulence should be abandoned. The eddies in incompressible MHD turbulence are formed by Alfvén wave packets. The velocity parallel to the magnetic field lines associated to eddies of any length l_{\parallel} is obviously the v_A given by the local mean magnetic field. The local magnetic field felt by an eddy of scale l is the magnetic field averaged over a scale a few times greater than l . It should be remembered that for an Alfvén wave, the fluctuations in velocity and magnetic field are $u^2 = b^2/4\pi\rho$. Therefore, the fluctuating magnetic field energy contained in eddies of scales smaller than l is $b_l^2 \sim \rho u_l^2$.

The cascade of energy is considered to occur by the non-linear interaction of Alfvén wave packets traveling in opposite directions which are colliding. From this interaction,

energy is transferred to smaller scales. This interaction is assumed to occur between eddies of the same scale.

This cascade proceeds until the end of the inertial range. For the hydrodynamic case, we defined the viscous dissipation scale l_ν as the one for which the associated Reynolds number Re_l achieves unity. Now we define the resistive dissipation scale l_η as that for which the associated magnetic Reynolds number $Rm_l \equiv lu_l/\eta$ is of the order of unity. The inertial range has scales $L \gg l \gg \max(l_\nu, l_\eta)$.

If the non-linear interaction between the Alfvén wave packets is assumed to be weak, that is, a large number of collisions is required for the energy of a single wave packet to be transferred to smaller scales, the turbulence is called *weak*.

The non-linearity can be measured as the ratio between the collision crossing time of the wave packets $\sim l_\parallel/v_A$ (inverse of the linear frequency of the eddies) and the turnover time of the eddie $\sim l_\perp/u_{l\perp}$ (the inverse of the non-linear frequency associated with the eddies). The non-linearity parameter $\chi(l_\perp)$ is defined as

$$\chi(l_\perp) = \frac{l_\parallel}{v_A} \frac{u_{l\perp}}{l_\perp}. \quad (2.28)$$

For the hypothesis of weak turbulence to be valid, it is necessary that at the injection scale $U < v_A$.

By assuming the transfer of energy in the cascading process as being spatially isotropic ($l_\parallel \sim l_\perp$), Iroshnikov (1963) and Kraichnan (1965) (IK) derived the scaling law $u_l \propto l^{1/4}$. The corresponding energy spectrum is $E(k) \propto k^{-3/2}$, known as the Iroshnikov-Kraichnan spectrum. With this scaling law, $\chi(l_\perp) \sim l_\perp^{1/4}$, and the hypothesis of weak turbulence keeps consistent for all the inertial range.

However, more recent observational and numerical evidences have shown that the transfer of energy in weak MHD turbulence is much faster in the direction perpendicular to the magnetic field, being therefore anisotropic. The predicted scaling from new theories (Goldreich & Sridhar 1997, Ng & Bhattacharjee 1997) is

$$u_l \propto l_\perp^{1/2}, \quad (2.29)$$

corresponding to an energy spectrum $E(k) \propto k^{-2}$. Practically all the energy is transferred in the perpendicular direction.

This last scaling law results in $\chi(l_\perp) \sim l_\perp^{-1/2}$. If turbulence is weak at the injection scale, it will become *strong* at the scale l_{strong} for which $\chi \sim 1$, given by

$$l_{strong} \sim LU^2/v_A^2 = LM_A^{-2}, \quad (2.30)$$

if the inertial range is sufficiently broad.

2.3.3 Strong cascade

The strong turbulence is treated phenomenologically with the assumption of the *critical balance*: $\chi \sim 1$ through the cascade (Goldreich & Sridhar 1995, GS95 hereafter). The GS95 theory predicts a scaling law and energy spectrum

$$u_l \propto l_\perp^{1/3}, \quad (2.31)$$

$$E(k_\perp) \propto k_\perp^{-5/3}, \quad (2.32)$$

and an anisotropy scale-dependence for the eddies:

$$l_\parallel \propto l_\perp^{2/3}, \quad (2.33)$$

which means that the smaller eddies have shapes more elongated in the direction of the local mean magnetic field.

Numerical simulations support the above scale dependent anisotropy for strong MHD turbulence (Cho & Vishniac 2000, Maron & Goldreich 2001, Cho et al. 2002, Beresnyak & Lazarian 2010, Beresnyak 2011); however, sometimes the energy spectra are better approximated by the Iroshnikov-Kraichnan spectrum $E(k) \propto k_\perp^{-3/2}$ rather than by the Kolmogorov spectrum $E(k) \propto k_\perp^{-5/3}$ (Maron & Goldreich 2001, Müller, Biskamp & Grappin 2003, Müller & Grappin 2005, Mason, Cattaneo & Boldyrev 2008), and the matter of strong MHD turbulence is still debated (see for example Boldyrev 2005, 2006).

Bellow, Table 2.1 summarizes some results from theories of incompressible turbulence.

2.3.4 Compressible MHD turbulence

If $M_S > 1$ at the injection scale, compressible modes can also be produced in the plasma. The weak turbulence treatment of compressible MHD for fast and Alfvén waves suggests

Table 2.1: Scaling laws, anisotropy, and energy spectra for different models of incompressible MHD turbulence

Theory	u_l	$E(k)$	anisotropy	scales range
Hydrodynamic (K41)	$\propto l^{1/3}$	$\propto k^{-5/3}$	no	$L > l > l_A$
Weak, isotropic (IK)	$\propto l^{1/4}$	$\propto k^{-3/2}$	no	-
Weak, anisotropic	$\propto l_{\perp}^{1/2}$	$\propto k_{\perp}^{-2}$	(only perpendicular cascade)	$l_A > l > l_{strong}$
Strong, anisotropic (GS95)	$\propto l_{\perp}^{1/3}$	$\propto k_{\perp}^{-5/3}$	$l_{\parallel} \propto l_{\perp}^{2/3}$	$l_{strong} > l > \max(l_{\nu}, l_{\eta})$

that only a small amount of energy is transferred from magnetosonic fast waves to Alfvén waves at large k_{\parallel} models (Chandran 2006).

Cho & Lazarian (2003) performed numerical simulations of strong turbulence and analysed the energy spectrum and anisotropy relation for each mode (Alfvén, slow, and fast) separately. They found that: (i) the Alfvén modes follow the GS95 energy spectrum $E(k_{\perp}) \propto k_{\perp}^{-5/3}$ and the anisotropy scale dependence $l_{\parallel} \sim l_{\perp}^{2/3}$; (ii) the slow mode also follows the GS95 energy spectrum and the anisotropy relation when β is high, and a steeper spectrum for highly compressible and low β regime; and (iii) the fast modes show an isotropic cascade with the energy spectrum $E(k) \propto k^{-3/2}$. Besides, in these numerical simulations (Cho & Lazarian 2002, 2003) the coupling between the Alfvén mode and the compressible modes was verified to be weak.

Therefore, the picture of the Alfvén wave cascade from the incompressible MHD theory is not expected to change when compressive modes are present. Nonetheless, this is still an open research topic.

Despite the fact that MHD turbulence is still a theory in construction, several phenomena in astrophysics, such as magnetic field diffusion and dynamo amplification rely on it. In the next paragraphs of this chapter and all along this thesis, the theoretical grounds discussed in this section will be invoked in different contexts.

2.4 The role of MHD turbulence on magnetic field diffusion during star-forming processes

As remarked before, the role played by MHD turbulence in the ISM and star formation is still highly debated, but generally regarded as important. This has been discussed in many reviews (see Elmegreen & Scalo 2004; McKee & Ostriker 2007) and in general magnetic field dynamics is regarded as dominant (see Tassis & Mouschovias 2005; Galli et al. 2006) or at least moderately important, as in super-Alfvénic models of star formation (see Padoan et al. 2004).

The vital question that frequently permeates these debates is the diffusion of the magnetic field. The conductivity of most of the astrophysical fluids is high enough to make the Ohmic diffusion negligible on the scales involved which means that the “frozen-in” approximation is a good one for many astrophysical environments. However, without considering diffusive mechanisms that can violate the flux freezing, one faces problems attempting to explain many observational facts. For example, simple estimates assuming magnetic flux conservation show that if all the magnetic flux is brought together with the material that collapses to form a star in molecular clouds, then the magnetic field in a protostar should be several orders of magnitude higher than the one observed in T-Tauri

stars (this is the “magnetic flux problem”, see Galli et al. 2006 and references therein).²

To address the problem of the magnetic field diffusion both in the partially ionized ISM and in molecular clouds, researchers usually appeal to the ambipolar diffusion concept (see Mestel & Spitzer 1956; Shu 1983). The idea of the ambipolar diffusion (see Eq. 2.15) is very simple and may be easily exemplified in the case of gas collapsing to form a star. As the magnetic field acts on charged particles of the gas only, it does not directly affect neutrals. Neutrals move under the gravitational pull but are scattered by collisions with ions and charged dust grains which are coupled with the magnetic field. The resulting flow dominated by the neutrals will be unable to drag the magnetic field lines and these will diffuse away through the infalling matter. This process of ambipolar diffusion becomes faster as the ionization ratio decreases and therefore, becomes more important in poorly ionized cloud cores.

Shu et al. (2006) have explored the accretion phase in low-mass star formation and concluded that there should exist an effective diffusivity about four orders of magnitude larger than the Ohmic diffusivity in order to allow an efficient magnetic flux transport to occur. They have argued that ambipolar diffusion could work, but only under rather special circumstances like, for instance, considering particular dust grain sizes. In other words, currently it is unclear if ambipolar diffusion is really high enough to solve the

²This point can be further illustrated by the use of the induction equation in its ideal form. One can rewrite Eq. (2.10), neglecting the resistive term in the following way: $\frac{\partial \mathbf{B}}{\partial t} = -\mathbf{B}(\nabla \cdot \mathbf{v}) + (\mathbf{B} \cdot \nabla)\mathbf{v} - (\mathbf{v} \cdot \nabla)\mathbf{B}$. Using the continuity Equation (2.7) one obtains

$$\frac{d}{dt} \left(\frac{\mathbf{B}}{\rho} \right) = \left(\frac{\mathbf{B}}{\rho} \cdot \nabla \right) \mathbf{v}.$$

From this equation, it is easy to see that if a cloud permeated by an uniform magnetic field has velocity gradients in the direction perpendicular to \mathbf{B} (in the parallel direction the plasma motion does not affect the magnetic field), the final $|\mathbf{B}|$ will scale with the final density ρ inside the cloud. For collapse in arbitrary geometries, the evolution of $|\mathbf{B}|$ with the density of the cloud can be parameterized as $|\mathbf{B}| \propto \rho^\kappa$ (e.g. Crutcher 2005). For example, for collapse parallel to the field lines, $\kappa = 0$. When the magnetic field is initially weak and does not impose a preferred direction on the collapse, it can proceed spherically symmetric in which case the relation $\kappa = 2/3$ is predicted, provided that there is flux conservation (e.g. Mestel 1966).

magnetic flux transport problem in collapsing flows.

Does magnetic field remain absolutely frozen-in within highly ionized astrophysical fluids? The answer to this question affects the description of numerous essential processes in the interstellar and even in the intergalactic gas.

First, one has to note that Richardson’s diffusion in turbulent flows (Richardson 1926; Lesieur 1990) indicates that the particles suffer spontaneous stochasticity, as a consequence there is an explosive separation into larger and larger turbulent eddies that cause an efficient turbulent diffusion in the flow. An important implication of this result is that magnetic flux conservation in turbulent fluids is violated! It is only stochastically conserved, as claimed by Eyink (2011).

Magnetic reconnection was appealed in Lazarian (2005) as a way of removing magnetic flux from gravitating clouds, e.g. from star-forming clouds. That work referred to the reconnection model of Lazarian & Vishniac (1999) and Lazarian et al. (2004) for the justification of the concept of fast magnetic reconnection in the presence of turbulence. The advantage of the scheme proposed by Lazarian (2005) was that robust removal of magnetic flux can be accomplished both in partially and fully ionized plasma, with only marginal dependence on the ionization state of the gas³. The concept of “turbulent reconnection diffusion” (TRD) introduced in Lazarian (2005) is relevant to our understanding of many basic astrophysical processes. In particular, it suggests that the classical textbook description of molecular clouds supported both by hourglass magnetic field and turbulence is not self-consistent (see Leão et al. 2012). Indeed, turbulence is expected to induce “reconnection diffusion” which should enable fast magnetic field removal from the cloud. However, in the absence of numerical confirmation of the fast reconnection, the scheme of magnetic flux removal through “reconnection diffusion” as opposed to ambipolar diffusion stayed somewhat speculative.

Fortunately, it has been shown numerically (see Kowal et al. 2009, 2012) that three-dimensional magnetic reconnection in turbulent fluids is indeed fast, following the predictions of Lazarian & Vishniac (1999). Motivated by this result, we present in Chapter 3

³The rates were predicted to depend on the reconnection rate, which according to Lazarian et al. (2004) very weakly depends on the ionization degree of the gas.

numerical studies aiming to gain understanding of the diffusion of magnetic field induced by turbulence. We will apply this study to interstellar clouds and compare “reconnection diffusion” with the ambipolar diffusion as described in Heitsch et al. (2004). The latter study reported the enhancement of ambipolar diffusion in the presence of turbulence which raised the question on how important is the simultaneous action of turbulence and ambipolar diffusion and whether turbulence alone, i.e. without any effect from ambipolar diffusion, can equally well induce de-correlation of magnetic field and density.

What are the laws that govern *magnetic field diffusion* in turbulent magnetized fluids? Could these laws affect our understanding of basic interstellar and star formation processes? These are the questions that we will address in Chapter 3 and 4. We will explore an alternative way of decreasing the magnetic flux-to-mass ratio without appealing to ambipolar diffusion. We claim that since turbulence in astrophysics is really ubiquitous, our results should be widely applicable.

2.4.1 Mechanism of fast magnetic reconnection in the presence of turbulence

The dynamical response of magnetic fields in turbulent fluids, as we discussed above, depends on the ability of magnetic fields to change their topology via reconnection. We know from observations that magnetic field reconnection may be both fast and slow. Indeed, a slow phase of reconnection is necessary in order to explain the accumulation of free energy associated with the magnetic flux that precedes eruptive flares in magnetized coronae. Thus it is important to identify the conditions for the reconnection to be fast. Different mechanisms prescribe different necessary requirements for this to happen.

The problem of magnetic reconnection is most frequently discussed in terms of solar flares. However, this is a general basic process underlying the dynamics of magnetized fluids in general. If the magnetic field lines in a turbulent fluid do not easily reconnect, the properties of the fluid should be dominated by intersecting magnetic flux tubes which are unable to pass through each other. Such fluids cannot be simulated with the existing codes as magnetic flux tubes readily reconnect in the numerical simulations which are

currently very diffusive compared to the actual astrophysical flows.

The famous Sweet-Parker model of reconnection (Sweet 1958; Parker 1958; see Figure 2.1, upper panel) produces reconnection rates which are smaller than the Alfvén velocity by a square root of the Lundquist number, i.e. by $S^{-1/2} \equiv (L_x V_A / \eta)^{-1/2}$, where L_x in this case is the length of the current sheet and η is the magnetic diffusivity. Astrophysical values of S can be as large as 10^{15} or 10^{20} , thus this scheme produces reconnection at a rate which is negligible for most of the astrophysical circumstances. If Sweet–Parker were the only model of reconnection it would have been possible to show that MHD numerical simulations do not have anything to do with real astrophysical fluids. Fortunately, fast reconnection is possible.

The first model of fast reconnection proposed by Petschek (1964) assumed that magnetic fluxes get into contact not along the astrophysically large scales of L_x , but instead over a scale comparable to the resistive thickness δ , forming a distinct X-point, where magnetic field lines of the interacting fluxes converge at a sharp point to the reconnection spot. The stability of such a reconnection geometry in astrophysical situations is an open issue. At least for uniform resistivity, this configuration was proven to be unstable and to revert to a Sweet–Parker configuration (Biskamp, 1986; Uzdensky & Kulsrud, 2000).

Recent years have been marked by the progress in understanding some of the key processes of reconnection in astrophysical plasmas. In particular, a substantial progress has been obtained by considering reconnection in the presence of the Hall-effect (Shay et al., 1998, 2004). The condition for which the Hall-MHD term becomes important for the reconnection is that the ion skin depth δ_{ion} becomes comparable with the Sweet-Parker diffusion scale δ_{SP} . The ion skin depth is a microscopic characteristic and it can be viewed as the gyroradius of an ion moving at the Alfvén speed, i.e. $\delta_{\text{ion}} = V_A / \omega_{ci}$, where ω_{ci} is the cyclotron frequency of an ion. For the parameters of the ISM (see Table 1 in Draine & Lazarian 1998), the reconnection is collisional (see further discussion in Yamada et al. 2006).

To deal with both collisional and collisionless plasma Lazarian & Vishniac (1999, henceforth LV99) proposed a model of fast reconnection in the presence of weak turbulence where magnetic field back-reaction is extremely important.

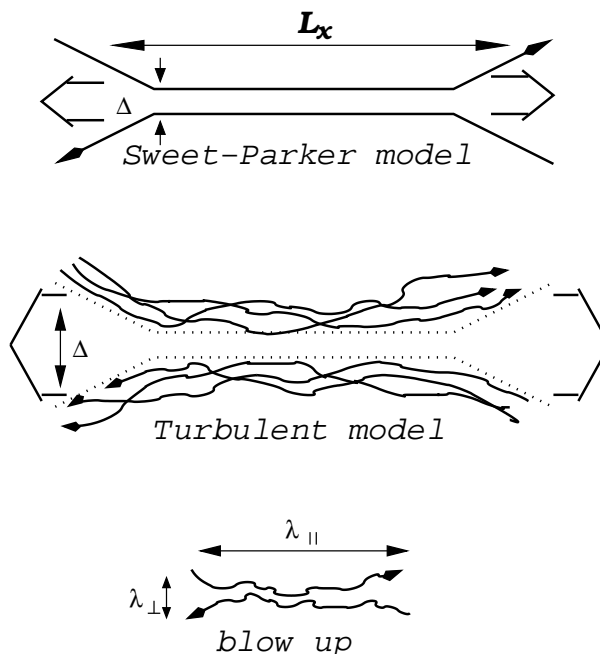


Figure 2.1: *Upper plot*: Sweet–Parker model of reconnection. The outflow is limited by a thin slot Δ , which is determined by Ohmic diffusivity. The other scale is an astrophysical scale $L_x \gg \Delta$. *Middle plot*: reconnection of weakly stochastic magnetic field according to LV99. The model that accounts for the stochasticity of magnetic field lines. The outflow is limited by the diffusion of magnetic field lines, which depends on field line stochasticity. *Low plot*: an individual small-scale reconnection region. The reconnection over small patches of magnetic field determines the local reconnection rate. The global reconnection rate is substantially larger as many independent patches come together. From Lazarian et al. (2004).

The middle and bottom panels of Figure 2.1 illustrate the key components of the LV99 model⁴. The reconnection events happen on small scales λ_{\parallel} where magnetic field lines get into contact. As the number of independent reconnection events that take place

⁴The cartoon in Figure 2.1 is an idealization of the reconnection process as the actual reconnection region also includes reconnected open loops of magnetic field moving oppositely to each other. Nevertheless, the cartoon properly reflects the role of the three-dimensionality of the reconnection process, the importance of small-scale reconnection events, and the increase of the outflow region compared to the Sweet–Parker scheme.

simultaneously is $L_x/\lambda_{\parallel} \gg 1$ the resulting reconnection speed is not limited by the speed of individual events on the scale λ_{\parallel} . Instead, the constraint on the reconnection speed comes from the thickness of the outflow reconnection region Δ , which is determined by the magnetic field wandering in a turbulent fluid. The model is intrinsically three dimensional⁵ as both field wandering and simultaneous entry of many independent field patches, as shown in Figure 2.1, are three-dimensional effects. In the LV99 model the magnetic reconnection speed becomes comparable with V_A when the scale of magnetic field wandering Δ becomes comparable with L_x .⁶

For a quantitative description of the reconnection, one should adopt a model of MHD turbulence (see Iroshnikov 1963; Kraichnan 1965; Dobrowolny et al. 1980; Shebalin et al. 1983; Montgomery & Turner 1981; Higdon 1984, and also Section 2.3). Most important for magnetic field wandering is the Alfvénic component. Adopting the GS95 (see Section 2.3.3) scaling of the Alfvénic component of MHD turbulence extended to include the case of weak turbulence, LV99 predicted that the reconnection speed in a weakly turbulent magnetic field is

$$V_R = V_A(l/L_x)^{1/2}(v_l/V_A)^2 \quad (2.34)$$

where the level of turbulence is parameterized by the injection velocity v_l ; the combination $V_A(v_l/V_A)^2$ is the velocity of the largest strong turbulent eddies V_{strong} , i.e., the velocity at the scale at which the Alfvénic turbulence transfers from the weak to the strong regimes. Thus Equation (2.34) can also be rewritten as $V_R = V_{\text{strong}}(l/L_x)^{1/2}$; $v_l < V_A$ and l is the turbulence injection scale.

The scaling predictions given by Equation (2.34) have been tested successfully by three-dimensional MHD numerical simulations in Kowal et al. (2009). This stimulates us to adopt the LV99 model as a starting point for our discussion of magnetic reconnection.

⁵Two-dimensional numerical simulations of turbulent reconnection in Kulpa-Dybel et al. (2009) show that the reconnection is not fast in this case.

⁶Another process that is determined by magnetic field wandering is the diffusion of energetic particles perpendicular to the mean magnetic field. Indeed, the coefficient of diffusion perpendicular to the magnetic field in the Milky Way is just an order of unity less than the coefficient of diffusion parallel to the magnetic field (see Giacalone & Jokipii 1999, and references therein).

How can λ_{\parallel} be determined? In the LV99 model, as many as $L_x^2/\lambda_{\perp}\lambda_{\parallel}$ localized reconnection events take place, each of which reconnects the flux at the rate $V_{\text{rec, local}}/\lambda_{\perp}$, where $V_{\text{rec, local}}$ is the velocity of local reconnection events at the scale λ_{\parallel} . The individual reconnection events contribute to the global reconnection rate, which in three dimensions becomes a factor of L_x/λ_{\parallel} larger, i.e.,

$$V_{\text{rec, global}} \approx L_x/\lambda_{\parallel} V_{\text{rec, local}}. \quad (2.35)$$

The local reconnection speed, conservatively assuming that the local events are happening at the Sweet–Parker rate, can be easily obtained by identifying the local resistive region δ_{SP} with λ_{\perp} and using the relations between λ_{\parallel} and λ_{\perp} that follow from the MHD turbulence model. The corresponding calculations in LV99 provided the local reconnection rate $v_l S^{-1/4}$. Substituting this local reconnection speed in Equation (2.35) one estimates the global reconnection speed, which is larger than V_A by a factor $S^{1/4}$. As a result, one has to conclude that the reconnection is fast in presence of turbulence and is not sensitive to the resistivity.

In this work, we will address problems which are relevant to the reconnection in a partially ionized, weakly turbulent gas. The corresponding model of reconnection was proposed in Lazarian et al. (2004, henceforth LVC04). The extensive calculations summarized in Table 1 in LVC04 show that the reconnection for realistic circumstances varies from $0.1V_A$ to $0.03V_A$, i.e., is also fast, which should enable fast diffusion arising from turbulent motions.

The fact that magnetic fields reconnect fast in turbulent fluids ensures that the large-scale dynamics that we can reproduce well with numerical codes is not compromised by the difference in reconnection processes in the computer and in astrophysical flows. This motivates our present study in which we investigate diffusion processes in turbulent magnetized fluids via three-dimensional simulations.

2.4.2 Magnetic diffusion due to fast reconnection

A natural consequence of the fast reconnection in turbulent flows is that it provides an efficient way by which magnetic flux can diffuse through the turbulent eddies, particularly

when the turbulence is super-Alfvénic. The theoretical grounds of this “reconnection diffusion” mechanism in turbulent flows have been described in detail in several recent reviews (Lazarian 2005; Lazarian 2011; Lazarian et al. 2011; de Gouveia Dal Pino et al. 2011; 2012; Eyink et al. 2011).

Figure 2.36 shows a schematic representation of how interacting turbulent eddies can mix the gas and exchange parts of their magnetic flux tubes (through reconnection) favoring their diffusion. This theory predicts a turbulent reconnection diffusivity η_t which is much larger than the Ohmic diffusivity at the turbulent scales (Lazarian 2005; Santos-Lima et al. 2010; Lazarian 2006; 2011; Lazarian et al. 2012; Leão et al. 2012):

$$\begin{aligned} \eta_t &\sim l_{inj} v_{turb} && \text{if } v_{turb} \geq v_A , \\ \eta_t &\sim l_{inj} v_{turb} \left(\frac{v_{turb}}{v_A} \right)^3 && \text{if } v_{turb} < v_A , \end{aligned} \quad (2.36)$$

where $l_{inj} = L/k_f$ and $v_{turb} = v_{rms}$. The relations above indicate that the ratio $(v_{turb}/v_A)^3$ is important only in a regime of sub-Alfvénic turbulence, i.e. with the Alfvénic Mach number $M_A \leq 1$. We also notice that when $v_{turb} \geq v_A$ the predicted diffusivity is similar to Richardson’s turbulent diffusion coefficient, as one should expect.

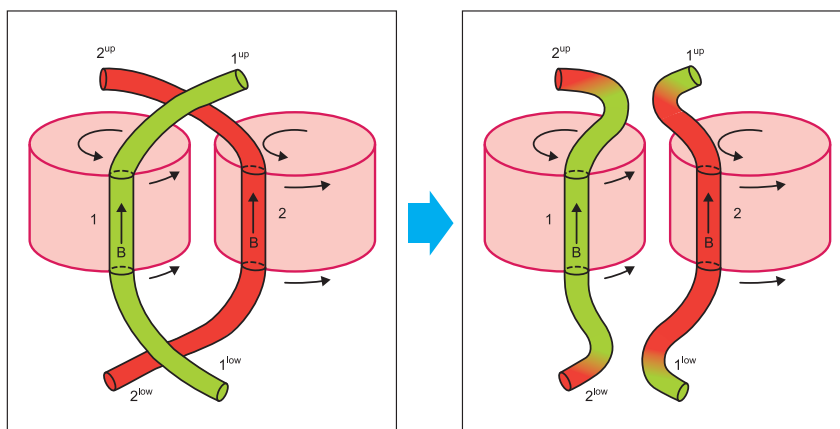


Figure 2.2: Schematic representation of two interacting turbulent eddies each one carrying its own magnetic flux tube. The turbulent interaction causes an efficient mixing of the gas of the two eddies, as well as fast magnetic reconnection of the two flux tubes which leads to diffusion of the magnetic field (extracted from Lazarian 2011).

Visualization of turbulent diffusion of heat or any passive scalar field is easy within the GS95 model, which can be interpreted as a model of Kolmogorov cascade perpendicular to the local direction of the magnetic field (LV99 and more discussion in Section 2.3 above). The corresponding eddies are expected to advect heat similarly to the case of the hydrodynamic heat advection. The corresponding visualization of the magnetic field diffusion is more involved. Every time that magnetic field lines intersect each other, they change their configuration draining free energy from the system. In the presence of self-gravity this may mean the escape of magnetic field which is a “light fluid” from the self-gravitating gaseous “heavy fluid”. Naturally, if the turbulence gets very strong the system gets unbound and then the mixing of magnetic field and gas, rather than their segregation is expected. In Chapters 3 and 4 we will test these ideas numerically.

2.5 Magnetic field amplification and evolution in the turbulent intracluster medium (ICM)

The ICM is turbulent and magnetized (see for example Govoni & Ferreti 2004; Ensslin & Vogt 2005). Understanding how the magnetic fields evolve in connection with the turbulent motions of the plasmas permeating the ICM inevitably involves the turbulent dynamo amplification of these fields. This is a broad and active topic of research. Excellent reviews on the subject can be found in Brandenburg & Subramanian (2005); Brandenburg et al. (2012), Schekochihin et al. (2007), and de Gouveia Dal Pino et al. (2013).

The large scale dynamics of the magnetized plasma in the ICM, commonly links the evolution of the observed magnetic fields and the bulk motions of the gas. In this context, one of the most important outcomes from the MHD approximation is the ability of a driven turbulent flow to amplify the magnetic fields until close equipartition between kinetic and magnetic energies (Schekochihin et al. 2004). That is, once a magnetic field seed is present, turbulence will stretch and fold the field lines until the magnetic forces become dynamically important. In this equilibrium situation, the magnetic fields have correlation lengths of the order of the largest scales of the turbulence. While the origin of the seed fields is still a matter of discussion (Grasso & Rubinstein 2001), the above turbulent dynamo scenario is amply accepted as the mechanism responsible for amplifying and sustaining the observed magnetic fields in the ICM (de Gouveia Dal Pino et al. 2013). This picture is supported by MHD simulations of galaxy mergers, showing the amplification of the magnetic field in the intergalactic medium (Kotarba et al. 2011).

However, examining more carefully the typical physical conditions in the ICM (see Tables 2.3 and 2.2), it seems that the applicability of the standard collisional MHD approximation to the description of the turbulence and the dynamo magnetic field amplification there should be revised. This is due to the small collision frequency of the protons compared to the frequencies of the turbulent motions and to the gyrofrequency of these particles around the field lines. The typical time and distance scales involved are: (i) for the injection scales of the turbulence: $\tau_{turb} = l_{turb}/v_{turb} \sim 100$ Myr considering $l_{turb} \sim 500$

kpc and $v_{turb} \sim 10^3 \text{ km s}^{-1}$ (e.g. Lazarian 2006a); (ii) for the proton-proton (electron-electron) collision: $\tau_{pp} \sim 30 \text{ Myr}$ ($\tau_{ee} \sim 1 \text{ Myr}$) and the mean free path is $l_{pp} \sim 30 \text{ kpc}$ ($l_{ee} \sim 1 \text{ kpc}$); (iii) for the proton (electrons) gyromotion: $\tau_{cp} \sim 10^3 \text{ s}$ ($\tau_{ce} \sim 1 \text{ s}$) and the Larmor radius $l_{ci} \sim 10^5 \text{ km}$ ($l_{ce} \sim 10^3 \text{ km}$). This makes the proton-proton collision rates negligible, disabling the thermalization of the energy of their motions in the different directions (see more details in Section 2.1), if we consider only binary collisions. As a consequence the particles velocity distributions parallel and perpendicular (gyromotions) to the magnetic field lines are decoupled.

Table 2.2: Typical plasma parameters inferred from observations of the ICM

Parameter	Notation	Value
Particle density	n	$2 \times 10^{-3} \text{ cm}^{-3}$
Temperature	T	10 keV
Magnetic field	B	$1 \mu\text{G}$

Under these circumstances, a kinetic description of the collisionless plasma should be invoked. The unavoidable occurrence of temperature (and thermal pressure) anisotropy is known from kinetic theory to trigger electromagnetic instabilities (see, for instance Kulsrud 1983). These electromagnetic fluctuations in turn, redistribute the pitch angles of the particles, decreasing the temperature anisotropy (Gary 1993). This instability feedback is observed in the collisionless plasma of the magnetosphere and the solar wind (Marsch 2006 and references therein), in laboratory experiments (Keiter 1999), and kinetic simulations (e.g. Tajima et al. 1977; Tanaka 1993; Gary et al. 1997, 1998, 2000; Qu et al. 2008). On the other hand, a fluid-like model is desirable for studying the large scale plasma phenomena in the ICM, as well as the evolution of turbulence and magnetic fields there.

Fortunately, it is possible to describe a collisionless plasma still using an MHD model with some constraints. The simplest *collisionless* MHD approximation is the CGL-MHD model (Chew, Goldberger & Low 1956; see Section 2.5.4). A modified CGL-MHD model taking into account the anisotropy constraints due to kinetic instabilities has been used

Table 2.3: Plasma and turbulence parameters estimated for the ICM

Parameter	Notation	Value
Debye length	λ_D	$1.7 \times 10^6 \left(\frac{n_p}{10^{-3} \text{ cm}^{-3}} \right)^{-1/2} \left(\frac{T_p}{10 \text{ keV}} \right)^{1/2} \text{ cm}$
Largest scales of the turbulence	l_{turb}	500 kpc
Turbulent velocity (at the l_{turb})	v_{turb}	10^8 cm/s
Thermal velocity (e,p)	$v_{Te, Tp} = (kT_{e,p}/m_{e,p})^{1/2}$	$4.2 \times 10^9 / 9.8 \times 10^7 \left(\frac{T_{e,p}}{10 \text{ keV}} \right)^{1/2} \text{ cm/s}$
Alfven velocity	$v_A = B/(4\pi n_p m_p)^{1/2}$	$6.9 \times 10^6 \left(\frac{B}{1 \mu \text{ G}} \right) \left(\frac{n_p}{10^{-3} \text{ cm}^{-3}} \right)^{-1/2} \text{ cm/s}$
Thermal to magnetic energy ratio	$\beta = 8\pi n k T / B^2$	$8.0 \times 10^2 \left(\frac{n}{2 \times 10^{-3} \text{ cm}^{-3}} \right) \left(\frac{T}{10 \text{ keV}} \right) \left(\frac{B}{1 \mu \text{ G}} \right)^{-2}$
Sonic Mach number	$M_S \sim v_{turb}/v_{Tp}$	$1.0 \left(\frac{v_{turb}}{10^8 \text{ cm/s}} \right) \left(\frac{T_p}{10 \text{ keV}} \right)^{-1/2}$
Alfvénic Mach number	$M_A = v_{turb}/v_A$	$14.0 \left(\frac{v_{turb}}{10^8 \text{ cm/s}} \right) \left(\frac{B}{1 \mu \text{ G}} \right)^{-1} \left(\frac{n_p}{10^{-3} \text{ cm}^{-3}} \right)^{1/2}$
Turbulence cascade time	$\tau_{turb} = l_{turb}/v_{turb}$	$1.5 \times 10^{16} \left(\frac{l_{turb}}{500 \text{ kpc}} \right) \left(\frac{v_{turb}}{10^8 \text{ cm/s}} \right)^{-1} \text{ s}$
Larmor period (e,p)	$\tau_{ce, cp}$	$3.6 \times 10^{-1} / 6.6 \times 10^2 \left(\frac{B}{1 \mu \text{ G}} \right)^{-1} \text{ s}$
Collision time (ee,pp)	$\tau_{ee, pp} = 1/\nu_{ee, pp}$	$1.7 \times 10^{13} / 10^{15} \left(\frac{n_{e,p}}{10^{-3} \text{ cm}^{-3}} \right)^{-1} \left(\frac{\ln \Lambda}{20} \right)^{-1} \left(\frac{T_{e,p}}{10 \text{ keV}} \right)^{3/2} \text{ s}$
Turbulent diffusivity	$\eta_{turb} \sim v_{turb} l_{turb}$	$1.5 \times 10^{32} \left(\frac{v_{turb}}{10^8 \text{ cm/s}} \right) \left(\frac{l_{turb}}{500 \text{ kpc}} \right) \text{ cm}^2/\text{s}$
Kinematic viscosity ¹	ν	$9.6 \times 10^{30} \left(\frac{n_p}{10^{-3} \text{ cm}^{-3}} \right)^{-1} \left(\frac{\ln \Lambda}{20} \right)^{-1} \left(\frac{T_p}{10 \text{ keV}} \right)^{5/2} \text{ cm}^2/\text{s}$
Magnetic diffusivity ²	η_{Ohm}	$16 \left(\frac{\ln \Lambda}{20} \right) \left(\frac{T}{10 \text{ keV}} \right)^{-3/2} \text{ cm}^2/\text{s}$

¹ due to the ions viscosity.

² due to the Spitzer resistivity.

In all the formulas, the plasma is assumed to be fully ionized, constituted only by electrons and protons in charge neutrality.

for modeling the solar wind in numerical simulations (Samsonov et al. 2007; Chandran et al. 2011; Meng et al. 2012a,b).

In the next sections we describe briefly the fundamental grounds of the turbulent dynamo process in the context of the standard collisional MHD. Then, we discuss a fluid model which better describes a collisionless plasma like the ICM, i.e., a collisionless MHD model.

2.5.1 Turbulent dynamos in astrophysics

As stressed above, the turbulent dynamo is a process by which turbulent flows of conducting fluids amplify seed magnetic fields. The theory of turbulent dynamos provides a

plausible physical explanation for the origin and maintenance of the observed magnetic fields in different astrophysical media.

The magnetic fields in astrophysical objects can be divided into two classes: large-scale fields, which have coherent scales of the size of the astrophysical object, and small-scale fields, with scales associated to the turbulence of the system. Both magnetic field classes can be dynamically important.

Large-scale dynamos (LSDs) are generated when statistical symmetries of the turbulence are broken by large-scale asymmetries of the system such as a density stratification, differential rotation and shear (Vishniac & Cho 2001; Käpylä et al 2008, Beresnyak 2012). Turbulent flows possessing perfect statistical isotropy cannot generate large-scale magnetic fields. The so-called twist-stretch-fold mechanism introduced by Vainshtein & Zeldovich (1972) was conceived for generating large-scale fields.

Large-scale dynamos can also be referred to as mean-field dynamos since the field evolution can be obtained from the mean field theory, namely, by averaging the governing equations, particularly the induction equation. LSDs can be excited by helical turbulence and are expected to generate magnetic fields in astrophysical sources such as the sun and stars, accretion disks, and disk galaxies.

Small-scale dynamos (SSDs) on the other hand, can be excited by homogeneous and isotropic turbulence and are believed to be a key dynamo process, for instance, in the ICM (Subramanian et al. 2006). They are based on the fact that three-dimensional, random (in space and time) velocity fields are able to amplify small-scale magnetic fluctuations due to the random stretching of the field lines.

It should be noted that in general mean-field theories for LSD treat the small-scale magnetic fluctuations as perturbations of the mean field originated by the turbulence. Therefore, such small-scale fields disappears in the absence of the mean-field, and they are different from the small-scale fields generated by the SSD.

SSDs are faster than LSDs in most astrophysical environments and the magnetic energy grows in the beginning exponentially up to equipartition with the kinetic energy at the eddy turnover timescale of the smallest eddies (Subramanian 1998). Later, it grows linearly at the turnover timescale of the larger eddies (Beresnyak 2012), with the largest

scales of the resulting field being a fraction of the outer scale of the turbulence. Both time scales are typically much shorter than the age of the system. For instance, in the case of galaxy clusters, the typical scale and velocity of the turbulent eddies are around 100 kpc and 100 km/s, respectively, implying a growth time $\sim 10^8$ yr which is much smaller than the typical ages of such systems. This means that SSDs should operate and are actually crucial to explaining the observed magnetic fields on the scales of tens of kiloparsecs in the intracluster media. Besides, according to Subramanian et al. (2006), it would be hard to explain magnetic fields on larger scales in such environments because the conditions for LSD action are probably absent.

2.5.2 The small-scale turbulent dynamo

Three-dimensional laminar flows with chaotic trajectories can have dynamo action if the magnetic Reynolds number Rm is above a certain critical value $R_{m,c}$. Batchelor 1950 realized that this amplification of the magnetic fluctuations would occur as a consequence of the random stretching of the field lines and would occur exponentially at the rate of strain of the flow.

In a turbulent flow, while the magnetic field is dynamically weak ($M_A \ll 1$) and the turbulence is Kolmogorov-like, the highest rate of strain $\sim \delta u_l/l \sim l^{-2/3}$ occurs at the viscous scale l_ν . Therefore, the fastest amplification would occur at this scale.

The repeated random stretching and shearing of the magnetic field by the flow produces magnetic field structures with reversals in small scales (limited by the resistive dissipation), giving origin to a “folded” structure of the field. An analytical demonstration of this dynamo property of a laminar random flow and of the formation of this magnetic field folded structure can be found in Zel’dovich et al. (1984) and Schekochihin et al. (2007).

This dynamo property of random flows is the base of the SSD mechanism. Following Maron et al. (2004), we describe below a heuristic model for the growth of the magnetic field due to the action of the SSD.

Consider a flow with the turbulence injected at the scale l_f with velocity u_f , with

timescale $t_f = l_f/u_f$. While the magnetic field is weak, turbulence is essentially hydrodynamic, and we can use the Kolmogorov scale relations.

This model is based on the assumption that, at a given time, there is only one scale where the magnetic field is being amplified. This scale will be designed by l_s , the shearing scale. The speed in this scale is u_s , and its dynamical timescale $t_s = l_s/u_s$. The magnetic field is amplified at a rate $\gamma \sim t_s^{-1}$, and dissipated at the resistive scale l_η , where the growth is counterbalanced by the resistive diffusivity, $t_s \sim l_\eta^2/\eta$. Hence,

$$l_\eta \sim (\eta t_s)^{1/2} \sim l_f Rm^{-1/2} (t_s/t_f)^{1/2}. \quad (2.37)$$

During this stage when the magnetic field is dynamically unimportant, the eddies of the viscous scale amplify the field more quickly, and therefore $l_s = l_\nu$, and the growth rate of the field is $\gamma \sim t_s^{-1} \sim t_\nu^{-1}$. Going to smaller scales, the field decreases in a rate similar to the exponential. At the end of this stage, the field is strong enough for affecting the eddies at the shearing scale, $B^2/8\pi \sim \frac{1}{2}\rho u_\nu^2$. The field structures have lengths $\sim l_\nu$ and reversal scales $\sim l_\eta$.

Now the magnetic field starts to be strong enough to become dynamically important. It is supposed that for $l < l_s$ the velocity is too weak to shear and amplify the field. For $l > l_s$ the velocities are weakly affected and turbulence remains Kolmogorov. The shearing scale is then the smallest scale (= highest rate of strain) capable to deform the field, $\frac{1}{2}\rho u_s^2 = B^2/8\pi$. The field evolution is given by

$$\frac{d}{dt} \left(\frac{B^2}{8\pi} \right) \sim \frac{u_s}{l_s} \frac{B^2}{8\pi} \sim \frac{1}{2} \rho \frac{u_s^3}{l_s} \sim \epsilon, \quad (2.38)$$

where ϵ is the constant energy flux of the Kolmogorov cascade. The previous equation states that at the scale l_s , a significative fraction of the energy of the cascade is converted into magnetic energy. Solving the previous equation with $B^2/8\pi = \frac{1}{2}\rho u_\nu^2$ in $t = 0$ gives

$$\frac{B^2}{8\pi} = \frac{1}{2}\rho u_\nu^2 + \epsilon t \quad (2.39)$$

and $(t_s/t_f) = B^2/(4\pi\rho u_f^2)$. As expected, the time and scale of shearing grows during the non-linear stage. At the same time, the folded structures are elongated (with lengths of the order of the stretching scale l_s) and are “enlarged” (the reversal scales are of

the order of the resistive scale l_η , which increases because the stretching rate decreases: $l_s \sim u_s^3/\epsilon \sim \epsilon^{1/2}t^{3/2}$, and $l_\eta \sim (\eta t_s)^{1/2} \sim (\eta t)^{1/2}$.

When $t \sim t_f \sim (l_f/u_f)$, a dynamical time of the turbulence, the shear scale achieves the forcing scale and $B^2/8\pi \sim \rho u_f^2/2$. At this point, the growth ceases when the shearing in every scale is suppressed by the field.

2.5.3 Saturation condition of the magnetic fields in SSDs

In the description of the SSD of the previous session, the magnetic Prandtl number was assumed $Pr_m > 1$.

This number is given by the ratio between the magnetic Reynolds number (Rm) and the Reynolds number Re . In a turbulent flow, $Re = v_{rms}/k_{inj}\nu$, while $Rm = v_{rms}/k_{inj}\eta$, where v_{rms} is the root mean square of the turbulent velocity, ν is the kinematic viscosity and η is the magnetic diffusivity, so that $Pr_m = Rm/Re = \nu/\eta$.

Typical values of Pr_m , Rm , and Re for astrophysical systems have been compiled by Brandenburg & Subramanian (2005) using the microscopic (Spitzer) values for both the magnetic resistivity and the kinematic viscosity. In most of the cases Re and Rm are very large because of the large scales involved in astrophysical systems, and Pr_m is generally different from 1. For partially ionized gas, one finds that (e.g., Brandenburg & Subramanian 2005) $Pr_m < 1$ in dense environments, such as stars (for which $Pr_m \sim 10^{-4}$) and accretion disks. In these cases $l_\eta > l_\nu$, where l_η corresponds to the scale at which the turbulent magnetic fields diffuse and l_ν corresponds to the scale where turbulence dissipates. While $Pr_m > 1$ in small density environments, such as galaxies ($Pr_m \sim 10^{14}$) and clusters of galaxies, implying $l_\eta < l_\nu$.

The different regimes above will determine the scale at which an SSD saturates. For instance, for a system with $Pr_m \gg 1$ and $Re \sim 1$, Schekochihin et al. (2004) have found that the SSD spreads most of the magnetic energy over the sub-viscous range and piles up at the magnetic resistive scales resulting in a very folded magnetic field structure. However, this does not seem to be the case when $Re \gg 1$.

For systems with $Pr_m \gg 1$ and $Re \gg 1$ (typical of galaxies and clusters), numerical

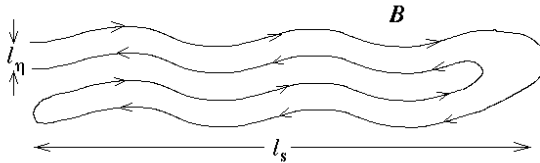


Figure 2.3: Folded structure of the magnetic field at the saturated state of the SSD (Extracted from Schekochihin et al. 2004).

simulations indicate that both folded and non-folded magnetic field structures should coexist (Brandenburg & Subramanian 2005).

Consistent with the results shown in the previous paragraph, for systems with $Pr_m \sim 1$ (implying $Re = Rm$), numerical studies by Haugen et al. (2003, 2004) have shown that the magnetic field correlation lengths at the saturated state are of the order of $1/6$ of the velocity correlation scales and therefore much larger than the magnetic resistive scale.

For systems with $Pr_m \ll 1$ and $Re \gg 1$ (as one expects in the case of stars and accretion disks), since $k_\eta \ll k_\nu$ most of the energy is dissipated resistively leaving very little kinetic energy to be cascaded and terminating the kinetic energy cascade earlier than in the case of a system with $Pr_m = 1$.

2.5.4 Collisionless MHD model for the ICM

As mentioned in the beginning of this section, the ion-ion collision time in the ICM is comparable to the dynamical timescales of the turbulence. This makes the application of a standard (collisional) MHD formulation inappropriate in this case. A way to solve this problem is to apply a kinetic description for the ICM, however, such an approach is not appropriate either for studying the large scale phenomena in these environments and, in particular, the evolution of the turbulence and magnetic fields.

Fortunately, it is possible to formulate a fluid approximation for collisionless plasmas, namely, a collisionless-MHD approach. The low rate of collisions in the fluid leads to anisotropy of the thermal pressure. In this case, it is possible to assume a double Maxwellian velocity distribution of the particles in the directions parallel and perpendic-

ular to the local magnetic field which result in distinct pressure terms in both directions. The pressure tensor Π_P assumes the gyrotropic form:

$$\Pi_P = p_\perp \mathbf{I} + (p_\parallel - p_\perp) \mathbf{b}\mathbf{b}, \quad (2.40)$$

where \mathbf{I} is the unitary dyadic tensor and $\mathbf{b} = \mathbf{B}/B$.

The simplest collisionless-MHD approximation that introduces this pressure anisotropy in the MHD formulation was first proposed by Chew, Goldberger & Low (Chew et al. 1956), the so called CGL-MHD model. In this model, the evolution of the two components of the pressure tensor are given by the conservation of the magnetic moment of the particles and the conservation of the total entropy of the gas. The CGL closure is also called the double-adiabatic law. The formal derivation from the statistical moments of the Vlasov-Maxwell equations can be found, for example, in Kulsrud (1983).

The CGL-MHD equations are:

$$\frac{d\rho}{dt} = -\rho \nabla \cdot \mathbf{u} \quad (2.41)$$

$$\rho \frac{d\mathbf{u}}{dt} = -\nabla_\perp p_\perp - \nabla_\parallel p_\parallel + \frac{p_\parallel - p_\perp}{B} \nabla_{\mathbf{b}} B + \frac{1}{4\pi} (\nabla \times \mathbf{B}) \times \mathbf{B} \quad (2.42)$$

$$\frac{d\mathbf{B}}{dt} = -\mathbf{B}(\nabla \cdot \mathbf{u}) + (\mathbf{B} \cdot \nabla) \mathbf{u} \quad (2.43)$$

$$\frac{d}{dt} \left(\frac{p_\perp}{\rho B} \right) = 0 \quad \frac{d}{dt} \left(\frac{p_\parallel B^2}{\rho^3} \right) = 0 \quad (2.44)$$

where $\nabla_\parallel = \mathbf{b}(\mathbf{b} \cdot \nabla)$ and $\nabla_\perp = \nabla - \mathbf{b}(\mathbf{b} \cdot \nabla)$ are the gradients in the parallel and perpendicular direction (to the local magnetic field).

First, we observe that the CGL-MHD equations have no diffusive terms, in analogy with the ideal MHD equations. Second, we wrote the momentum equation in such a way as to identify the peculiar force arising from the pressure anisotropy (the rhs term containing the difference between the pressure components in Equation 2.42). This force is along the field lines and, when is dominant over the other terms (regions of curvature of the magnetic field and high β) then: (a) when $p_\perp \gg p_\parallel$, the gas is pushed to lower magnetic intensity regions, being trapped there (mirror effect); (b) when $p_\parallel \gg p_\perp$, the gas is pushed to the side of increasing magnetic intensity, being able to stretch the field lines with this motion.

2.5.5 CGL-MHD waves and instabilities

Linear perturbation analysis of the CGL-MHD equations reveals three waves, analogous to the Alfvén, slow and fast magnetosonic MHD waves (described in Section 2.2). These waves, however, can have imaginary frequencies for sufficiently high degrees of the pressure anisotropy. The corresponding dispersion relations can be found in Kulsrud (1983). For convenience, we reproduce here these relations (as in Hau & Wang 2007):

$$\left(\frac{\omega}{k}\right)_a^2 = \left(\frac{B^2}{4\pi\rho} + \frac{p_\perp}{\rho} - \frac{p_\parallel}{\rho}\right) \cos^2 \theta, \quad (2.45)$$

$$\left(\frac{\omega}{k}\right)_{f,s}^2 = \frac{b \pm \sqrt{b^2 - 4c}}{2}, \quad (2.46)$$

where $\cos \theta = \mathbf{k} \cdot \mathbf{B}/B$ (being \mathbf{k} the wavevector of the perturbation) and

$$b = \frac{B^2}{4\pi\rho} + \frac{2p_\perp}{\rho} + \left(\frac{2p_\parallel}{\rho} - \frac{p_\perp}{\rho}\right) \cos^2 \theta,$$

$$c = -\cos^2 \theta \left[\left(\frac{3p_\parallel}{\rho}\right)^2 \cos^2 \theta - \frac{3p_\parallel}{\rho} b + \left(\frac{p_\perp}{\rho}\right)^2 \sin^2 \theta \right].$$

The dispersion relation for the transverse (Alfvén) mode $(\omega/k)_a^2$ coincides with that obtained from the kinetic theory (in the limit when the Larmor radius goes to zero) and does not change when heat conduction is added to the system (see Kulsrud 1983); the criterium for the instability (named firehose instability), in terms of $A = p_\perp/p_\parallel$ and $\beta_\parallel = p_\parallel/(B^2/8\pi)$ is in this case

$$A < 1 - 2\beta_\parallel^{-1}. \quad (2.47)$$

However, for the compressible modes $(\omega/k)_{f,s}^2$ (which include the mirror unstable modes), the linear dispersion relation of the CGL-MHD equations is known to deviate from the kinetic theory. The mirror instability criterium is

$$A/6 > 1 + \beta_\perp^{-1}, \quad (2.48)$$

while the one derived from the kinetic theory is

$$A > 1 + \beta_\perp^{-1}, \quad (2.49)$$

where $\beta_\perp = p_\perp/(B^2/8\pi)$ in the last two expressions.

Taking into account the finite Larmor radius effects, Meng et al. (2012a) (see also Hall 1979, 1980, 1981) give the following expressions for the the maximum growth rate γ_{max} (normalized by the ion gyrofrequency Ω_i) of the firehose and kinetic mirror instabilities:

$$\frac{\gamma_{max}}{\Omega_i} = \begin{cases} \frac{1}{2} \frac{(1 - A - 2\beta_{\parallel}^{-1})}{\sqrt{A - 1/4}} & \text{(firehose),} \\ \frac{4\sqrt{2}}{3\sqrt{5}} \sqrt{A - 1 - \beta_{\perp}^{-1}} & \text{(mirror),} \end{cases} \quad (2.50)$$

which are achieved for $k^{-1} \sim l_{ci}$, the ion Larmor radius. These expressions are valid for the case of $|A - 1| \ll 1$ and $\beta_{\parallel, \perp} \gg 1$.

Figures 2.4 and 2.5 illustrate the behavior of these instabilities. In Figure 2.4, the firehose instability results from the unbalance between a higher centrifugal force (in the particles reference frame) $F_R = p_{\parallel}/R$ exerted by the gas on the curved (R is the local curvature radius) magnetic field line due to the parallel streaming of the particles, against the ‘‘centripetal forces’’ $F_B = B^2/4\pi R$ (Lorentz curvature force) and $F_{p\perp} = p_{\perp}/R$. In Figure 2.5, the thick arrows show the direction of the mirror forces, which trap the gas in zones of small magnetic field intensity.

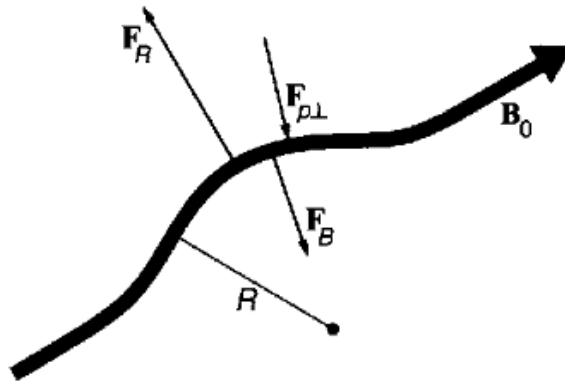


Figure 2.4: Mechanism of the firehose instability. (Extracted from Treumann & Baumjohann 1997).

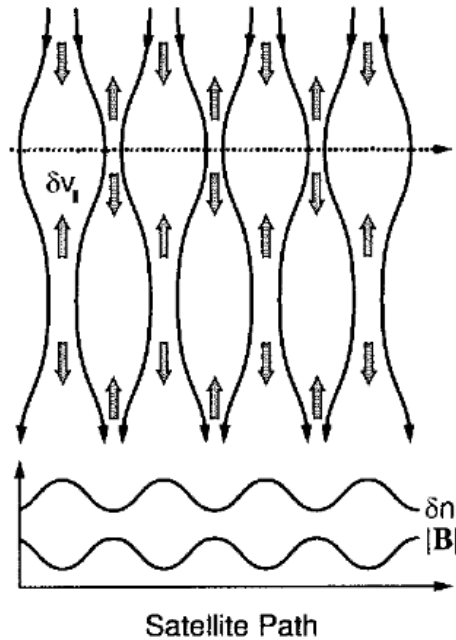


Figure 2.5: Satellite measurements across a mirror-unstable region. (Extracted from Treumann & Baumjohann 1997).

2.5.6 Kinetic instabilities feedback on the pressure anisotropy

Measurements from weakly collisional plasmas, as those in the solar wind and the earth's magnetosphere have demonstrated that the kinetic instabilities driven by pressure anisotropy are able to induce the pitch angle scattering of plasma particles, thus decreasing the resulting anisotropy. Besides all the available *in situ* cosmic plasma observations (Marsch 2006 and references therein), further motivation for the choice of our relaxation model is based on the fact that, regardless of the differences in collisionless plasma regimes and the anisotropy instabilities, analytical models (Hall 1979, 1980, 1981), quasi-linear calculations (Yoon & Seough 2012; Seough & Yoon 2012), PIC simulations (Tajima et al. 1977; Tanaka 1993; Gary et al. 1997, 1998, 2000; Le et al. 2010; Nishimura et al. 2002; Qu et al. 2008; Riquelme et al. 2012), as well as laboratory experiments (Keiter 1999) evidence the existence of saturation of the temperature anisotropy at some level, originated from the microscopic instabilities. In particular, constraints on the anisotropy due to the mirror and firehose instabilities have been clearly detected from solar wind protons (see for

example Hellinger et al. 2006; Bale et al. 2009) and α -particles (Maruca et al. 2012).

Based on this phenomenology, the numerical studies on turbulence about the ICM presented in Chapter 5 employ the one-fluid CGL-MHD model modified to take into account the anisotropy relaxation due to the feedback of the kinetic instabilities. The equations of this model can be written in conservative form (which is convenient for our conservative numerical code described in Appendix A):

$$\frac{\partial}{\partial t} \begin{bmatrix} \rho \\ \rho \mathbf{u} \\ \mathbf{B} \\ e \\ A(\rho^3/B^3) \end{bmatrix} + \nabla \cdot \begin{bmatrix} \rho \mathbf{u} \\ \rho \mathbf{u} \mathbf{u} + \Pi_P + \Pi_B \\ \mathbf{u} \mathbf{B} - \mathbf{B} \mathbf{u} \\ e \mathbf{u} + \mathbf{u} \cdot (\Pi_P + \Pi_B) \\ A(\rho^3/B^3) \mathbf{u} \end{bmatrix} = \begin{bmatrix} 0 \\ \mathbf{f} \\ 0 \\ \mathbf{f} \cdot \mathbf{v} + \dot{w} \\ \dot{A}_S(\rho^3/B^3) \end{bmatrix}, \quad (2.51)$$

where Π_P is the gyrotropic pressure (eq. 2.40) and Π_B is the magnetic stress tensor:

$$\Pi_B = (B^2/8\pi)\mathbf{I} - \mathbf{B}\mathbf{B}/4\pi, \quad (2.52)$$

In the source terms, \mathbf{f} represents an external bulk force responsible for driving the turbulence (see details in Section 5.1.2), \dot{w} gives the rate of change of the internal energy $w = (p_\perp + p_\parallel/2)$ of the gas due to heat conduction and radiative cooling, and \dot{A}_S gives the rate of change of A due to microphysical processes.

Following previous works (Denton et al. 1994; see also Pudovkin et al. 1999; Samsonov & Pudovkin 2000; Samsonov et al. 2001; Meng et al. 2012a), whenever the plasma satisfies the firehose (Eq. 2.47) or kinetic mirror instability criteria (Eq. 2.49), we impose the following pressure anisotropy relaxation condition:

$$\left(\frac{\partial p_\perp}{\partial t} \right)_S = -\frac{1}{2} \left(\frac{\partial p_\parallel}{\partial t} \right)_S = -\nu_S (p_\perp - p_\perp^*), \quad (2.53)$$

where p_\perp^* is the value of p_\perp for the marginally stable state (which is obtained from the equality in Equations 2.47 and 2.49 for each instability and with the conservation of the thermal energy w).

It is not clear yet how the saturation and isotropization timescales are related to the local physical parameters. Some authors claim that the values of ν_S are of the order of the

maximum growth rate of each instability γ_{max} , which in turn is a fraction of the ion Larmor frequency $\gamma_{max}/\Omega_i \sim 10^{-2} - 10^{-1}$ (see Gary et al. 1997, 1998, 2000). In the ICM, the frequency Ω_i is very large compared to the frequencies that we resolve numerically. This implies that $\nu_S \rightarrow \infty$ would be a good approximation, or in other words, the relaxation to the marginal values would be instantaneous (which is similar to the “hardwalls” employed in Sharma et al. 2006). However, it is not clear yet whether the extreme low density and weak magnetic fields of the ICM would result in isotropization timescales as fast as these. Therefore, we have also tested, for comparison, finite values for ν_S which are $\ll \Omega_i$ (see Section 5.3).

In Chapter 5 we will discuss the results of numerical simulations where we applied the collisionless MHD model above to conditions suitable for the ICM aiming to explore both the turbulent dynamo amplification of seed magnetic fields and the overall evolution of the MHD turbulence in this environment.

Chapter 3

Removal of magnetic flux from clouds via turbulent reconnection diffusion

The diffusion of astrophysical magnetic fields in conducting fluids in the presence of turbulence depends on whether magnetic fields can change their topology via reconnection in highly conducting media. Recent progress in understanding fast magnetic reconnection in the presence of turbulence is reassuring that the magnetic field behavior in computer simulations and turbulent astrophysical environments is similar, as far as magnetic reconnection is concerned. This makes it meaningful to perform MHD simulations of turbulent flows in order to understand the diffusion of magnetic field in astrophysical environments. Our studies of magnetic field diffusion in turbulent medium reveal interesting new phenomena. First of all, our three-dimensional MHD simulations initiated with anti-correlating magnetic field and gaseous density exhibit at later times a de-correlation of the magnetic field and density, which corresponds well to the observations of the interstellar media. While earlier studies stressed the role of either ambipolar diffusion or time-dependent turbulent fluctuations for de-correlating magnetic field and density, we get the effect of *permanent* de-correlation with one fluid code, i.e. without invoking ambipolar diffusion. In addition, in the presence of gravity and turbulence, our three-dimensional simulations

show the decrease of the magnetic flux-to-mass ratio as the gaseous density at the center of the gravitational potential increases. We observe this effect both in the situations when we start with equilibrium distributions of gas and magnetic field and when we follow the evolution of collapsing dynamically unstable configurations. Thus the process of turbulent magnetic field removal should by TRD be applicable both to quasi-static subcritical molecular clouds and cores and violently collapsing supercritical entities. The increase of the gravitational potential, as well as the magnetization of the gas increases the segregation of the mass and magnetic flux in the saturated final state of the simulations, supporting the notion that the reconnection-enabled diffusivity relaxes the magnetic field + gas system in the gravitational field to its minimal energy state. This effect is expected to play an important role in star formation, from its initial stages of concentrating interstellar gas to the final stages of the accretion to the forming protostar.

We have drawn the theoretical grounds on turbulent reconnection diffusion (TRD) Section 2.4. This Chapter is organized as follows: In Section 3.1, we describe the numerical model employed. In Section 3.2, we present the results concerning the diffusion of magnetic field in a setup without external gravitational forces. In Section 3.3, we present the results of our numerical simulations of diffusion of magnetic field in the presence of a gravitational field. In Section 3.4, we discuss our results and compare with previous works. In Section 3.6, we discuss the accomplishments and limitations of our present study. In Section 3.5, we discuss our findings in the context of strong turbulence theory, and finally in Section 3.7, we summarize our conclusions.

3.1 Numerical Model

The systems studied numerically in this work is described by the resistive MHD equations, assuming an isothermal equation of state (see also Section 2.2):

$$\frac{\partial \rho}{\partial t} + \nabla \cdot (\rho \mathbf{u}) = 0 \quad (3.1)$$

$$\rho \left(\frac{\partial}{\partial t} + \mathbf{u} \cdot \nabla \right) \mathbf{u} = -c_s^2 \nabla \rho + (\nabla \times \mathbf{B}) \times \mathbf{B} - \rho \nabla \Psi + \mathbf{f} \quad (3.2)$$

$$\frac{\partial \mathbf{B}}{\partial t} = \nabla \times (\mathbf{u} \times \mathbf{B}) + \eta_{\text{Ohm}} \nabla^2 \mathbf{B} \quad (3.3)$$

plus the divergenceless condition for the magnetic field $\nabla \cdot \mathbf{B} = 0$. The spatial coordinates are given in units of a typical length L_* . The density ρ is normalized by a reference density ρ_* , and the velocity field \mathbf{u} by a reference velocity U_* . The constant sound speed c_s is also given in units of U_* , and the magnetic field \mathbf{B} is measured in units of $U_* \sqrt{4\pi\rho_*}$. The uniform Ohmic resistivity η_{Ohm} is given in units of $U_* L_*$. In our numerical calculations we will use both non-zero and zero values of η_{Ohm} . In the latter case, the calculations will include only numerical resistivity. Time t is measured in units of L_*/U_* . The external gravitational potential Ψ is given in units of U_*^2 . The source term \mathbf{f} is a random force term responsible for injection of turbulence.

The above equations are solved inside a three-dimensional box with periodic boundary conditions. We use a shock-capturing Godunov-type scheme with an HLL solver (see, for example, Kowal et al. 2007; Falceta-Gonçalves et al. 2008). Time integration is performed with the Runge-Kutta method of second order. Unless we say explicitly the opposite, we assume $\eta_{\text{Ohm}} = 0$.

We employ an isotropic, non-helical, solenoidal, delta correlated in time forcing \mathbf{f} . This forcing acts in a thin shell around the wave number $k_f = 2.5(2\pi/L)$, that is, the scale of turbulence injection l_{inj} that is about 2.5 times smaller than the box size L (in all the simulations, we choose $L = 1$ in code units). In most of the experiments, the *rms* velocity V_{rms} induced by turbulence in the box is close to unity (in code units). Therefore, in these cases, the turnover time of the energy-carrying eddies (or the turbulent timescale t_{turb}) is $t_{\text{turb}} \sim l_{\text{inj}}/v_{\text{turb}} \sim (L/2.5)/V_{\text{rms}} \approx 0.4$ units of time in code units.

We note that for our present purposes we use an one-fluid approximation, which does not include ambipolar diffusion. This choice is appropriate for approximating a fully ionized gas. One may argue that the code describes also the dynamics of partially ionized gas, but on the scales where ions and neutrals are strongly coupled, i.e., on scales larger than the scale of ambipolar diffusion (see discussion in Lazarian et al. 2004).

3.2 Turbulent magnetic field diffusion in the absence of gravity

Observations of different regions of the diffuse ISM compiled by Troland & Heiles (1986) indicate that magnetic fields and density are not straightforwardly correlated. These observations motivated Heitsch et al. (2004) to perform 2.5-dimensional numerical calculations in the presence of both ambipolar diffusion and turbulence. As remarked in Chapter 2, the results in Heitsch et al. (2004) also indicated de-correlation of magnetic field and density¹ and one may wonder whether ambipolar diffusion is always required to de-correlate magnetic field and density or if, otherwise, to what extent the concept of “turbulent ambipolar diffusion” introduced in Heitsch et al. (2004) is useful (see also Zweibel 2002). To address these issues we performed three-dimensional simulations of magnetic diffusion in the absence of ambipolar diffusion effects.

3.2.1 Initial Setup

The magnetic field is assumed to have initially only the component in the z -direction. The initial configuration of the magnetic and density fields are:

$$B_z(x, y) = B_0 + B_1 \cos\left(\frac{2\pi}{L}x\right) \cos\left(\frac{2\pi}{L}y\right) \quad (3.4)$$

$$\rho(x, y) = \rho_0 - \frac{1}{c_s^2} \left\{ B_0 B_1 \cos\left(\frac{2\pi}{L}x\right) \cos\left(\frac{2\pi}{L}y\right) + 0.5 [B_1 \cos\left(\frac{2\pi}{L}x\right) \cos\left(\frac{2\pi}{L}y\right)]^2 \right\}, \quad (3.5)$$

where $(x, y) = (0, 0)$ is the center of the x, y -plane. Boundary conditions are periodic.

This initial magnetic field configuration has an uniform component B_0 plus an harmonic perturbation of amplitude B_1 . The density field is distributed in such a way that

¹We feel that the constrained geometry of the simulations in Heitsch et al. (2004) (where the magnetic field was assumed to be perpendicular to the plane of the two-dimensional turbulence, so that there were no reconnection) weakened the comparison of their set up with effects in the magnetized ISM, but this point is beyond the scope of our present discussion.

the gas pressure, given by the isothermal equation of state $p = c_s^2 \rho$, equilibrates exactly the magnetic pressure, giving a magneto-hydrostatic solution. We choose the parameters $B_1 = 0.3$, $\rho_0 = 1$ and $c_s = 1$ in all our simulations. Figure 3.1 illustrates these initial fields when $B_0 = 1.0$.

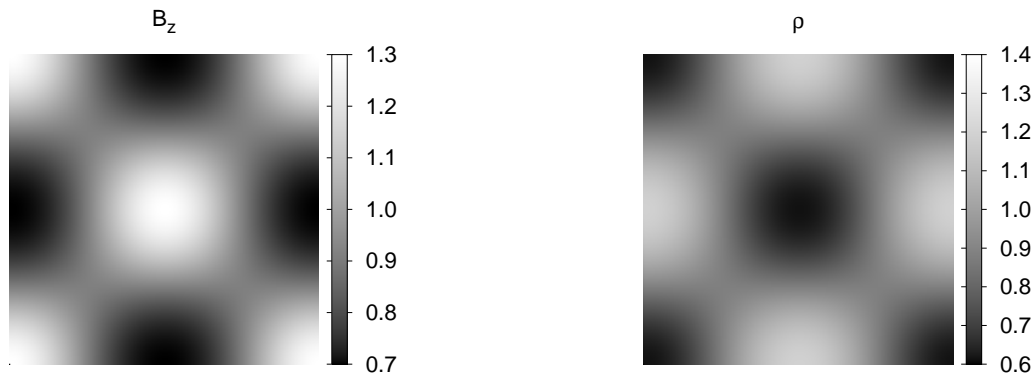


Figure 3.1: (x, y) -plane showing the initial configuration of the z component of the magnetic field B_z (*left*) and the density distribution (*right*) for the model B2 (see Table 3.1). The centers of the plots correspond to $(x, y) = (0, 0)$.

We should remark that the simulations presented in Heitsch et al. (2004) do not start at the equilibrium, like ours. There is no pressure term in their equation for the evolution of the momentum of the ions to counterbalance the magnetic pressure. In addition, in their work the ion-density field is kept constant in time and space.

Another difference between our setup and that in Heitsch et al. (2004) is that our parameter B_1 is assumed to be the same for all the models studied, and not a fraction of B_0 . Also, the amplitude of the perturbation of the homogeneous component of the density field is a free parameter in Heitsch et al. (2004), while here it is constrained by the imposed equilibrium between gas and magnetic pressures.

In addition, we introduce a passive scalar field Φ initially identical to B_z . The parameters of our relevant simulations are presented in Table 3.1.

In these simulations we keep the random velocity approximately constant, i.e., $V_{\text{rms}} \approx 0.8$ for all the models after one time step. Therefore, all these models are slightly subsonic.

Table 3.1: Parameters of the Simulations in the Study of Turbulent Diffusion of Magnetic Flux without Gravity.

Model	B_0	l_{inj}	V_{rms}	t_{turb}	$\eta_{\text{turb}} - B_z$	$\eta_{\text{turb}} - \Phi$	Resolution
B1	0.5	0.4	0.8	0.5	0.18(0.03)	0.19(0.02)	256^3
B2	1.0	0.4	0.8	0.5	0.09(0.02)	0.14(0.02)	256^3
B3	1.5	0.4	0.8	0.5	0.10(0.02)	0.08(0.02)	256^3
B4	2.0	0.4	0.8	0.5	0.13(0.02)	0.11(0.02)	256^3
B2l	1.0	0.4	0.8	0.5	0.15(0.02)	0.11(0.02)	128^3
B2h	1.0	0.4	0.8	0.5	0.10(0.01)	0.13(0.02)	512^3

3.2.2 Notation

Hereafter, the quantities within brackets with subscript “ $R = 0.25L$ ”: $\langle \cdot \rangle_{R=0.25L}$, or simply “0.25”: $\langle \cdot \rangle_{0.25}$ will denote averages inside a cylinder with main-axis in the z -direction centered in the computational box, with radius $R = 0.25L$, while a subscript “ z ”: $\langle \cdot \rangle_z$ will denote an average over the z -direction. An overbar means the average of some quantity inside the entire box.

3.2.3 Results

Figure 3.2 shows the evolution of the amplitude of the mode that is identical to the initial harmonic perturbation of the magnetic field (i.e., the *rms* of the amplitude of the Fourier modes $(k_x, k_y) = (\pm 1, \pm 1)$), for $\langle B_z \rangle_z$ and $\langle B_z \rangle_z / \langle \rho \rangle_z$. Most right plot in Figure 3.3 shows the evolution of the amplitude of the same mode for $\langle \Phi \rangle_z$ and $\langle \Phi \rangle_z / \langle \rho \rangle_z$. All the curves presented were smoothed in order to make the visualization clearer. We see that the decay of the magnetic field occurs at a similar rate to that of the passive field. The mode decays nearly exponentially at roughly the same rate for most of the models. Only the model B1 ($B_0 = 0.5$) exhibits a higher decay rate. This may be due to the large scale field reversals that are common in super-Alfvénic turbulence. Table 3.1 shows the fitted values (and the uncertainty) of η_{turb} in the curves corresponding to the evolution of the amplitude

of the modes for $\langle B_z \rangle_z$. The fitted curve is $\exp\{-k^2 \eta_{\text{turb}} t\}$, where $k^2 = k_x^2 + k_y^2 = 2$ is the square of the module of the corresponding wave-vector. We observe that the decay of the amplitude of the modes of $\langle B_z \rangle_z$ is not continuous but saturates at a value that is naturally maintained by the turbulence (in Figure 3.2 it occurs after about $t = 6$).

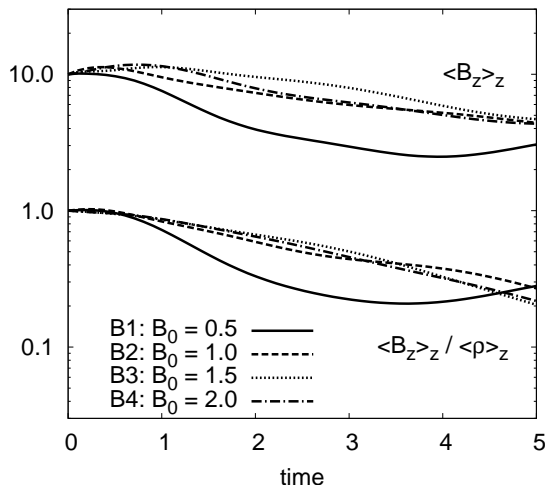


Figure 3.2: Evolution of the *rms* amplitude of the Fourier modes $(k_x, k_y) = (\pm 1, \pm 1)$ of $\langle B_z \rangle_z$ (upper curves) and $\langle B_z \rangle_z / \langle \rho \rangle_z$ (lower curves). The curves for $\langle B_z \rangle_z$ were multiplied by a factor of 10. All the curves were smoothed to make the visualization clearer.

The diffusion of B/ρ on large scales was also observed in Heitsch et al. (2004) for two-fluid simulations and there it was associated with the difference between the velocity field of the ions and neutrals, at small scales. However, here we observe a similar effect, but in one-fluid simulations, which is suggestive that turbulence rather than the details of the microphysics are responsible for the diffusion.

Left and center panels of Figure 3.4 shows the distribution of $\langle \rho \rangle_z$ versus $\langle B_z \rangle_z$ for the model B2 ($B_0 = 1.0$) at the initial configuration ($t = 0$) and after 10 time steps. We see in this projected view that the initial magnetic flux-to-mass relation is quickly spread and, in contrast with the $\Phi - \rho$ distribution (see Figure 3.5), we do not see any tendency for the magnetic field and density to become correlated.

To give a quantitative measure of the evolution of the flux-to-mass relation in the

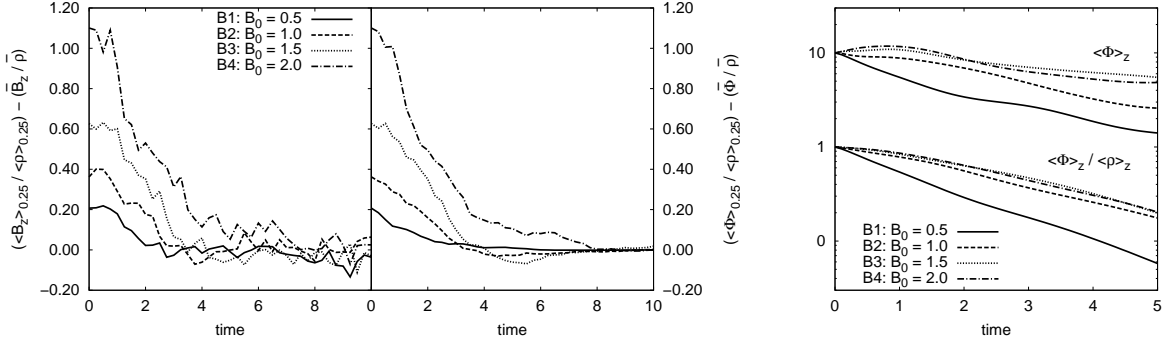


Figure 3.3: *Left*: evolution of the ratio of the averaged magnetic field over the averaged density (more left) and of the ratio of the averaged passive scalar over the averaged density (more right) within a distance $R = 0.25L$ from the central z -axis. The values have been subtracted from their characteristic values $\bar{B}/\bar{\rho}$ in the box. *Right*: evolution of the rms amplitude of the Fourier modes $(k_x, k_y) = (\pm 1, \pm 1)$ of $\langle \Phi \rangle_z$ (upper curves) and $\langle \Phi \rangle_z / \langle \rho \rangle_z$ (lower curves). The curves for Φ were multiplied by a factor of 10. All the curves were smoothed to make the visualization clearer.

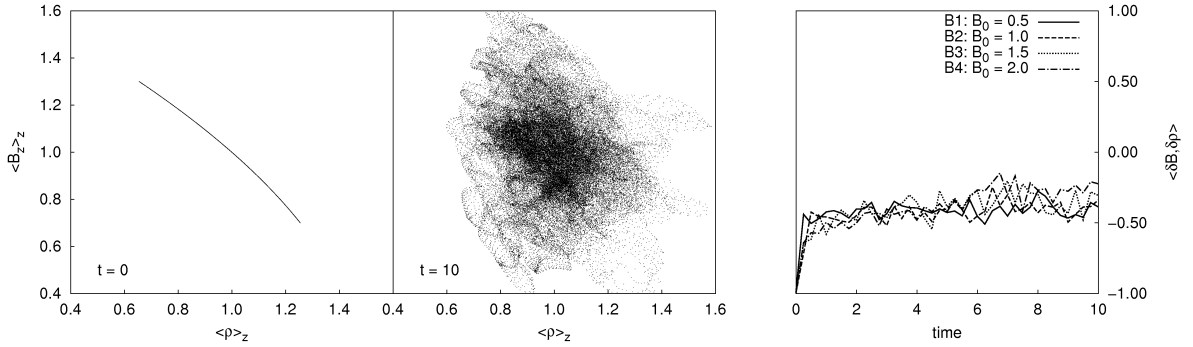


Figure 3.4: Distribution of $\langle \rho \rangle_z$ vs. $\langle B_z \rangle_z$ for model B2 (see Table 3.1), at $t = 0$ (left) and $t = 10$ (center). *Right*: correlation between fluctuations of the strength of the magnetic field (δB) and density ($\delta \rho$).

models, let us consider $\langle \delta B, \delta \rho \rangle$, the correlation between fluctuations of the magnetic

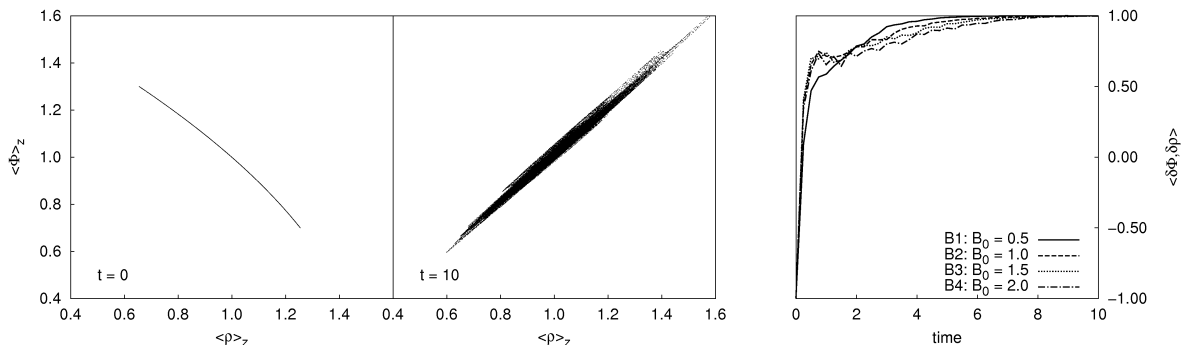


Figure 3.5: *Left*: distribution of $\langle \rho \rangle_z$ vs. $\langle \Phi \rangle_z$ for model B2 (see Table 3.1), at $t = 0$ (most left) and $t = 10$ (most right). *Right*: correlation between fluctuations of the passive scalar field ($\delta \Phi$) and density ($\delta \rho$).

field δB and density $\delta \rho$, defined by

$$\langle \delta B, \delta \rho \rangle = \frac{\int (B - \bar{B})(\rho - \bar{\rho}) d^3x}{\sqrt{\int (B - \bar{B})^2 d^3x} \sqrt{\int (\rho - \bar{\rho})^2 d^3x}}. \quad (3.6)$$

Right panel of Figure 3.4 shows the evolution of $\langle \delta B, \delta \rho \rangle$ (see right side of Figure 3.5 for the evolution of $\langle \delta \Phi, \delta \rho \rangle$ which is similarly defined). Differently from the passive scalar field that quickly becomes correlated to the density field, the magnetic field keeps a residual anti-correlation with it.

A more careful analysis of our results indicates that the correlation between magnetic field intensity and density depends on the Mach number M_s . For example, when we calculate the correlation $\langle \delta B, \delta \rho \rangle$ using the turbulent models (study of diffusion of passive scalar fields, see Appendix A in Santos-Lima et al. 2010), we find weak positive correlations for the supersonic models and negative correlations for the subsonic ones. These correlations increase with M_s . Thus, the anti-correlation detected in Figure 3.4 can be due to the slightly subsonic regime of the turbulence. These correlations and anti-correlations at this level cannot be excluded by the observational data as discussed, e.g., in Troland & Heiles (1986). We shall address this issue in more detail elsewhere.

To summarize, the results of Figures 3.2 and 3.4 suggest that the turbulence can substantially change the flux-to-mass ratio B/ρ without any effect of ambipolar diffusion.

The diffusion of the magnetic flux occurs in a rate similar to the rate of the turbulent diffusion of heat (passive scalar), even for sub-Alfvénic turbulence.

As remarked in Section 2.4.1, we should emphasize that the efficient turbulent diffusion of magnetic field that we are observing in the simulations above is due to fast magnetic reconnection because otherwise, if the tangled magnetic lines by turbulence were not reconnecting, then they would be behaving like a Jello-type substance and this would make the diffusive transport of magnetic flux very inefficient (contrary to what is observed in the simulations). The issue of magnetic reconnection was avoided in Heitsch et al. (2004) due to the settings in which magnetic field was assumed perpendicular to the plane of the fluid motions. Magnetic reconnection, however, is an effect that is present within any realistic three-dimensional setup.

3.2.4 Effects of Resolution on the Results

To convince the reader that the above results are not being affected by numerical effects, we ran one of the models (model B2) with increased and decreased resolutions (models B2h and B2l, respectively, see Table 3.1). Figure 3.6 compares the same quantities presented in Figure 3.2 for these models. We do not observe significant difference between them. Thus, we can expect that the results presented for the models with resolution of 256^3 are robust.

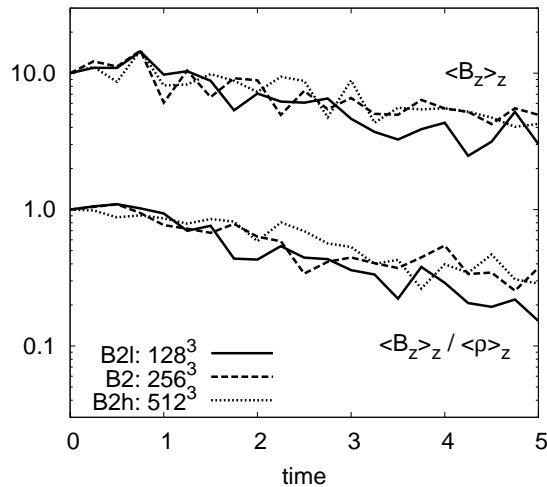


Figure 3.6: Comparison between models of different resolution: B2, B2l, and B2h (Table 3.1). It presents the same quantities as in Figure 3.2.

3.3 “Reconnection diffusion” in the presence of gravity

The “reconnection diffusion” of magnetic field in the absence of gravity can represent the magnetic field dynamics in diffuse interstellar gas where cloud self-gravity is not important. In molecular clouds, clumps and accretion disks, the diffusion of magnetic field should happen in the presence of gravity. We study this process below.

3.3.1 Numerical Approach

In order to get an insight into the magnetic field diffusion in a turbulent fluid immersed in a gravitational potential, we have performed experiments in the presence of a gravitational potential with cylindrical symmetry Ψ , given in cylindrical coordinates (R, ϕ, z) by:

$$\Psi(R \leq R_{\max}) = -\frac{A}{R + R_*} \quad (3.7)$$

$$\Psi(R > R_{\max}) = -\frac{A}{R_{\max} + R_*} \quad (3.8)$$

where $R = 0$ is the center of the (x, y) -plane, and we fixed $R_* = 0.1L$ and $R_{\max} = 0.45L$ ($L = 1$ is the size of the computational box, as remarked in Section 3.1). We assume a relatively high value of R_* in order to limit the values of the gravitational force and prevent the system to be initially Parker–Rayleigh–Taylor unstable. We assume an outer cut-off R_{\max} on the gravitational force to ensure the cylindrical symmetry while using periodic boundary conditions.

In one class of experiments, we start the simulation with a magneto-hydrostatic equilibrium with $\beta = P_{\text{gas}}/P_{\text{mag}} = c_s^2\rho/(B^2/8\pi)$ constant. The initial density and magnetic fields are, respectively,

$$\rho(R) = \rho_0 \exp \left\{ (\Psi(R_{\max}) - \Psi(R))/c_s^2(1 + \beta^{-1}) \right\} \quad (3.9)$$

$$B_z(R) = c_s \sqrt{2\beta^{-1}\rho(R)}. \quad (3.10)$$

Figure 3.7 illustrates this initial configuration for one of the studied models (model C2, see Table 3.2).

We restricted our experiments to the trans-sonic case $c_s = 1$ (in most of the experiments, we keep $V_{\text{rms}} \approx 0.8$, see Table 3.2). We also fixed $\rho_0 = 1$. The turbulence is injected at $t = 0$ and we follow the evolution of $\langle B_z \rangle_R$ and $\langle \rho \rangle_R$ for eight time steps. Table 3.2 lists the parameters used for these experiments. $\bar{\rho}$ and \bar{B}_z represent the average of the density and magnetic field over the entire box. $V_{A,i}$ refers to the initial Alfvén speed of the system. The *rms* velocity of the system V_{rms} is measured after the turbulence is well-developed.

We have also performed experiments starting out of equilibrium, with homogeneous fields: the system starts in free fall. We leave the system to evolve for eight time steps applying turbulence from the very beginning. For a comparison, we have also performed these experiments without turbulence. The initial uniform magnetic field is parallel to the z -direction for these models. Table 3.3 lists the parameters for these runs. The listed values of β refer to the initial conditions.

Concerning the diffusion of the magnetic field, in order to provide a quantitative comparison between the models, we have also performed simulations with similar initial conditions to the models presented in Table 3.2, but without turbulence and with the

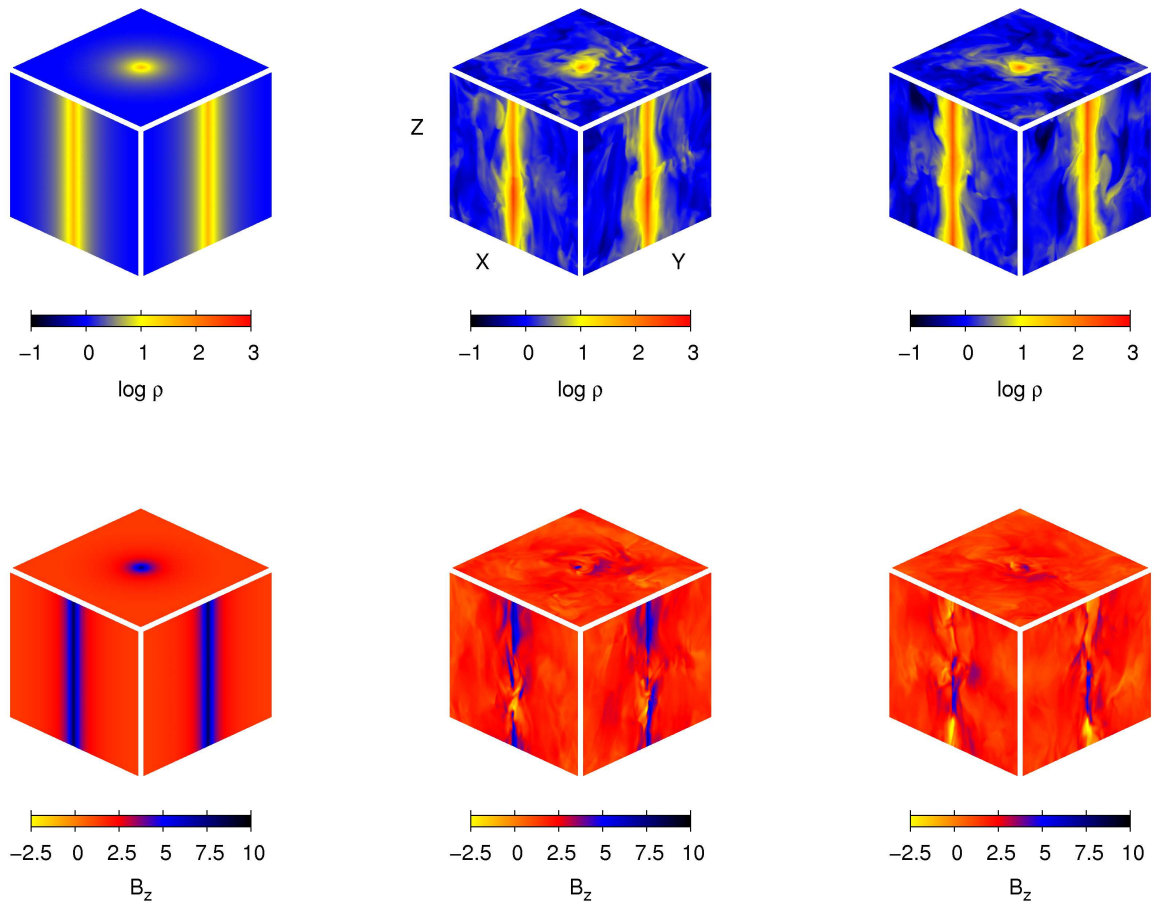


Figure 3.7: Model C2 (see Table 3.2). *Top row*: logarithm of the density field; *bottom row*: B_z component of the magnetic field. *Left column*: central xy , xz , and yz slices of the system projected on the respective walls of the cubic computational domain, in $t = 0$; *middle and right columns*: the same for $t = 3$ (middle) and $t = 8$ (right).

explicit presence of Ohmic diffusivity η_{Ohm} in the induction equation. As these models have perfect symmetry in the z -direction, we simulated only a plane cutting the z -axis, that is, they are 2.5-dimensional simulations. We use a resolution comparable to the turbulent three-dimensional models. Table 3.4 lists the parameters for these runs. We simulated a three-dimensional model equivalent to the model E7r1, and we found exact agreement in the time evolution of the magnetic flux distribution (not shown). Therefore, we can believe that in this case these 2.5-dimensional simulations give results which are

Table 3.2: Parameters for the Models with Gravity Starting at Magneto-hydrostatic Equilibrium with Initial Constant β .

Model	β^1	$V_{A,i}$	A^2	$\bar{\rho}$	\bar{B}_z	V_{rms}	t_{turb}	η_{turb}	$\eta_{\text{turb}}/V_{\text{rms}}l_{\text{inj}}$	Resolution
C1	1.0	1.4	0.6	1.26	1.59	0.8	0.5	≈ 0.005	≈ 0.015	256^3
C2	1.0	1.4	0.9	1.52	1.74	0.8	0.5	≈ 0.01	≈ 0.03	256^3
C3	1.0	1.4	1.2	1.95	1.98	0.8	0.5	≈ 0.03	≈ 0.09	256^3
C4	1.0	1.4	0.9	1.52	1.74	1.4	0.3	$\approx 0.10 - 0.20$	$\approx 0.18 - 0.36$	256^3
C5	1.0	1.4	0.9	1.52	1.74	2.0	0.2	≈ 0.30	≈ 0.37	256^3
C6	3.3	0.8	0.9	2.40	1.20	0.8	0.5	≈ 0.02	≈ 0.06	256^3
C7	0.3	2.4	0.9	1.18	2.66	0.8	0.5	≈ 0.01	≈ 0.03	256^3
C2l	1.0	1.4	0.9	1.52	1.74	0.8	0.5	128^3
C2h	1.0	1.4	0.9	1.52	1.74	0.8	0.5	512^3

¹ Initial β parameter for the plasma: $\beta = P_{\text{gas}}/P_{\text{mag}}$

² The parameter A for the strength of gravity (see Equations 3.7 and 3.8) is given in units of $c_s^2 L$.

Table 3.3: Parameters for the Models with Gravity Starting Out-of-equilibrium, with Initially Homogeneous Fields.

Model	β	$V_{A,i}$	A	$\bar{\rho}$	\bar{B}_z	V_{turb}	Resolution
D1	1.0	1.4	0.9	1.0	1.41	0.8	256^3
D1a	1.0	1.4	0.9	1.0	1.41	0.0	256^3
D2	3.3	0.8	0.9	1.0	0.77	0.8	256^3
D2a	3.3	0.8	0.9	1.0	0.77	0.0	256^3
D3	0.3	2.4	0.9	1.0	2.45	0.8	256^3
D3a	0.3	2.4	0.9	1.0	2.45	0.0	256^3
D1l	1.0	1.4	0.9	1.0	1.41	0.8	128^3
D1h	1.0	1.4	0.9	1.0	1.41	0.8	512^3

equivalent to three-dimensional simulations.

Table 3.4: Parameters for the 2.5-dimensional Resistive Models with Gravity Starting with Magneto-hydrostatic Equilibrium and Constant β .

Model	β	A	η_{Ohm}	Resolution
E1r0	1.0	0.6	0.005	256^2
E1r1	1.0	0.6	0.01	256^2
E2r1	1.0	0.9	0.01	256^2
E2r2	1.0	0.9	0.02	256^2
E2r3	1.0	0.9	0.03	256^2
E2r4	1.0	0.9	0.05	256^2
E3r1	1.0	1.2	0.01	256^2
E3r2	1.0	1.2	0.02	256^2
E3r3	1.0	1.2	0.03	256^2
E4r2	1.0	0.9	0.10	256^2
E4r3	1.0	0.9	0.20	256^2
E5r3	1.0	0.9	0.30	256^2
E6r1	3.3	0.9	0.01	256^2
E6r2	3.3	0.9	0.02	256^2
E6r3	3.3	0.9	0.03	256^2
E7r1	0.3	0.9	0.01	256^2

3.3.2 Results

Evolution of the Equilibrium Distribution

Top row of Figure 3.8 shows the evolution of $\langle B_z \rangle_{0.25}$ (*left*), $\langle \rho \rangle_{0.25}$ (*middle*), and $\langle B_z \rangle_{0.25} / \langle \rho \rangle_{0.25}$ (*right*), normalized by the respective characteristic values inside the box (\bar{B}_z , $\bar{\rho}$ and $\bar{B}_z / \bar{\rho}$), for the models C1, C2, and C3 ($\beta = 1$). We compare the evolution of these quantities for different strengths of gravity A , maintaining the other parameters identical. The central magnetic flux reduces faster the higher the value of A . The flux-to-mass ratio has similar behavior. The other plots of Figure 3.8 show the profile of the quantities $\langle B_z \rangle_z$ (*upper*

panels), $\langle \rho \rangle_z$ (*middle panels*), and $\langle B_z \rangle_z / \langle \rho \rangle_z$ (*bottom panels*) along the radius R , each column corresponding to a different value of A both for $t = 0$ (in magneto-hydrostatic equilibrium and constant β) and for $t = 8$. We see the deepest decay of the magnetic flux toward the central region for the highest value of A at $t = 8$.

In Figure 3.9, we compare the rate of the “reconnection diffusion” when we change the turbulent velocity and maintain the other parameters identical as in models C2, C4 and C5. An inspection of the left panel shows that the central magnetic flux $\langle B_z \rangle_{0.25}$ decreases faster for the two highest turbulent velocities. Fluctuations are higher in the cases with higher velocity. The central density however, gets smaller for the highest turbulent velocity. This is explained by the fact that the dynamic pressure is higher for the largest velocities. The central flux-to-mass ratio $\langle B_z \rangle_{0.25} / \langle \rho \rangle_{0.25}$ decays for the two smallest velocities. However, for the largest velocity, it is not clear if this ratio decreases or not. Looking at the middle graph of Figure 3.9 (*bottom row*), we see that the central density decreases for the highest forcing. This is indicative that the turbulence driving overcomes the gravitational potential making the system less bound.

Top row of Figure 3.10 compares the evolution of $\langle B_z \rangle_{0.25}$ (*left*), $\langle \rho \rangle_{0.25}$ (*middle*), and $\langle B_z \rangle_{0.25} / \langle \rho \rangle_{0.25}$ (*right*), normalized by the characteristic average values inside the box (\bar{B}_z , $\bar{\rho}$ and $\bar{B}_z / \bar{\rho}$), for models C2, C6, and C7 with different β . Both the central magnetic flux and the flux-to-mass ratio decreases faster for the less magnetized model ($\beta = 3.3$). The other plots of Figure 3.10 show the radial profile of the quantities $\langle B_z \rangle_z$ (*upper panels*), $\langle \rho \rangle_z$ (*middle panels*), and $\langle B_z \rangle_z / \langle \rho \rangle_z$ (*bottom panels*) for each model. We can again observe a lower value of the flux in the central region (relative to the external regions) for the highest values of β at the time step $t = 8$. The contrast between the central and the more external values for the flux-to-mass ratio is quite different for the three models, being higher for the more magnetized models. This is expected, as turbulence brings the system in the state of minimal energy. The effect of varying magnetization in some sense is analogous to the effect of varying gravity. The equilibrium flux-to-mass ratio is larger in both the case of higher gravity and higher magnetization. The physics is simple, the lighter fluid (magnetic field) gets segregated from the heavier fluid (gas).

All in all, we clearly see that turbulence substantially influences the quasi-static evo-

lution of magnetized gas in the gravitational potential. The system in the presence of turbulence relaxes faster to its minimum potential energy state. This explains the change of the flux-to-mass ratio, which for years was a problem to deal with invoking ambipolar diffusion.

Equilibrium Models: Comparison of Magnetic Diffusivity and Resistivity Effects

In terms of the removal of the magnetic field from quasi-static clouds, does the effect of “reconnection diffusion” act similar to the effect of diffusion induced by resistivity? To address this question, we have performed a series of simulations with enhanced Ohmic resistivity (see models of Table 3.4).

In Figure 3.11, we compare the evolution of $\langle B_z \rangle_R$ (at different radius) for model C2 of Table 3.2 with similar resistive models without turbulence of Table 3.4, with different values of Ohmic diffusivity η_{Ohm} . The decay seems initially faster and comparable with the highest value of η_{Ohm} ($\eta_{\text{Ohm}} = 0.05$). But after this initial phase, the turbulent model (C2) seems to have a behavior similar to the resistive models with η_{Ohm} between 0.01 and 0.02.

Figure 3.12 compares the turbulent models C1, C3, C4, C5, C6, and C7 of Table 3.2 with similar resistive models of Table 3.4. After roughly one time step, the model C1 (weaker gravitational field) seems to be consistent with a value of η_{Ohm} between 0.005 or lesser, while the model C3 (stronger gravitational field) seems to be consistent with $\eta_{\text{Ohm}} \approx 0.03$. These results show that the effective turbulent magnetic diffusivity is sensitive to the strength of the gravitational field.

The resistive simulations with increasing η_{Ohm} values are more comparable with models with increasing turbulent velocity. The model C4 (with smaller turbulent velocity) seems to be consistent with the resistive model with $\eta_{\text{Ohm}} = 0.10$. The model C5 (with larger turbulent velocity) seems to be more comparable with the model with $\eta_{\text{Ohm}} \sim 0.30$ (or higher), however, in this case we cannot associate a representative value of η_{Ohm} due to the very quick diffusion which occurs even before $t = 1$, when the turbulence becomes

well developed.

The turbulent curve for the less magnetized model (C6) seems to follow the resistive curve with $\eta_{\text{Ohm}} = 0.02$, while the more magnetized model (C7) is comparable to the resistive model with $\eta_{\text{Ohm}} \approx 0.01$. This result indicates that the effective turbulent diffusivity is also sensitive to the strength of the magnetic field.

In summary, the results above indicate a correspondence between the two different effects. In other words, the turbulent magnetic diffusion may mimic the effects of Ohmic diffusion of magnetic fields in gravitating clouds. However, we should keep in mind that the physics of turbulent diffusion and Ohmic resistivity is different. Thus this analogy should not be overstated.

Evolution of Non-equilibrium Models

Figure 3.13 shows the same set of comparisons as in Figure 3.10 for the models D1, D2, and D3 of Table 3.3 — these models have started out of the equilibrium with a homogeneous density and magnetic field in a free fall system. Besides the runs with turbulence, we also present, for comparison, the evolution for the systems without turbulence (models D1a, D2a, and D3a). The strong oscillations seen in the evolution of the central magnetic flux and density for these models (which are more pronounced in the models without turbulence) are acoustic oscillations, since the time for the virialization of these systems is larger than the simulated period. We note that the initial flux-to-mass ratio does not change in the cases without turbulence. We also observe similar trends as in Figure 3.10: the higher the value of β , the faster the decrease of the central magnetic flux relative to the mean flux into the box. We also note that the radial profile of the flux-to-mass ratio for the turbulent models crosses the mean value for the models without turbulence at nearly the same radius. This is due to the fact that the effective gravity potential in all these simulations acts up to this radius approximately.

This set of simulations shows that the change of mass-to-flux ratio can happen at the time scale of the gravitational collapse of the system and therefore, turbulent diffusion of magnetic field is applicable also to dynamic situations, e.g., to the formation of

supercritical cores.

3.3.3 Effects of Resolution on the Results

As in the case of the study presented in Section 3.2, we would like to know how the results shown in this section are sensitive to changes in resolution. Again, we ran some models employing higher resolution and we inspected the changes in the results concerned.

Figure 3.14 compares the evolution of some of the quantities studied through this section for models C2l and C2h — which are identical to C2, except by the lower (C2l) and higher resolution (C2h, see Table 3.2). It shows no significant difference between these models. Figure 3.14 also depicts the evolution of the same quantities for the models D1, D1l, and D1h. Both models have the same parameters as in model D1, but model D1h (D1l) has higher (lower) resolution (see Table 3.3). Again, we see no disagreement between the models.

Therefore, the results presented in this section are not expected to change with an increase in resolution.

3.3.4 Magnetic Field Expulsion Revealed

Both in the case of equilibrium and non-equilibrium we observe a substantial change of the mass-to-flux ratio. Even our experiments with no turbulence injection confirm that this process arises from the action of turbulence. As a result, in all the cases with gravity the turbulence allows magnetic field to escape from the dense core which is being formed in the center of the gravitational potential.

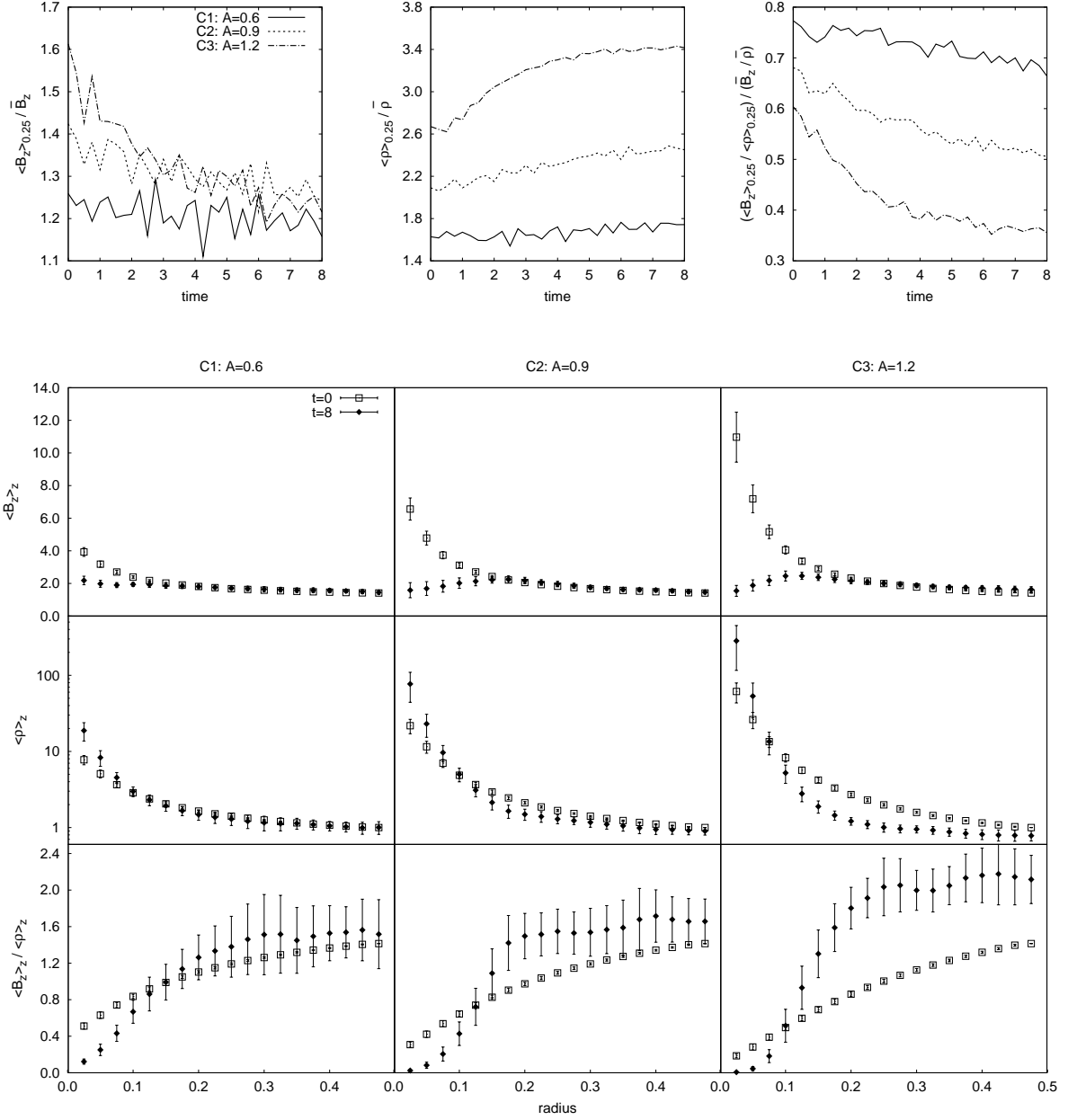


Figure 3.8: Evolution of the equilibrium models for different gravitational potential. The top row shows the time evolution of $\langle B_z \rangle_{0.25} / \bar{B}_z$ (*left*), $\langle \rho \rangle_{0.25} / \bar{\rho}$ (*middle*), and $(\langle B_z \rangle_{0.25} / \langle \rho \rangle_{0.25}) / (\bar{B}_z / \bar{\rho})$ (*right*). The other plots show the radial profile of $\langle B_z \rangle_z$ (*upper panels*), $\langle \rho \rangle_z$ (*middle panels*), and $\langle B_z \rangle_z / \langle \rho \rangle_z$ (*bottom panels*) for the different values of A in $t = 0$ (magneto-hydrostatic solution with β constant, see Table 3.2) and $t = 8$. Error bars show the standard deviation. All models have initial $\beta = 1.0$.

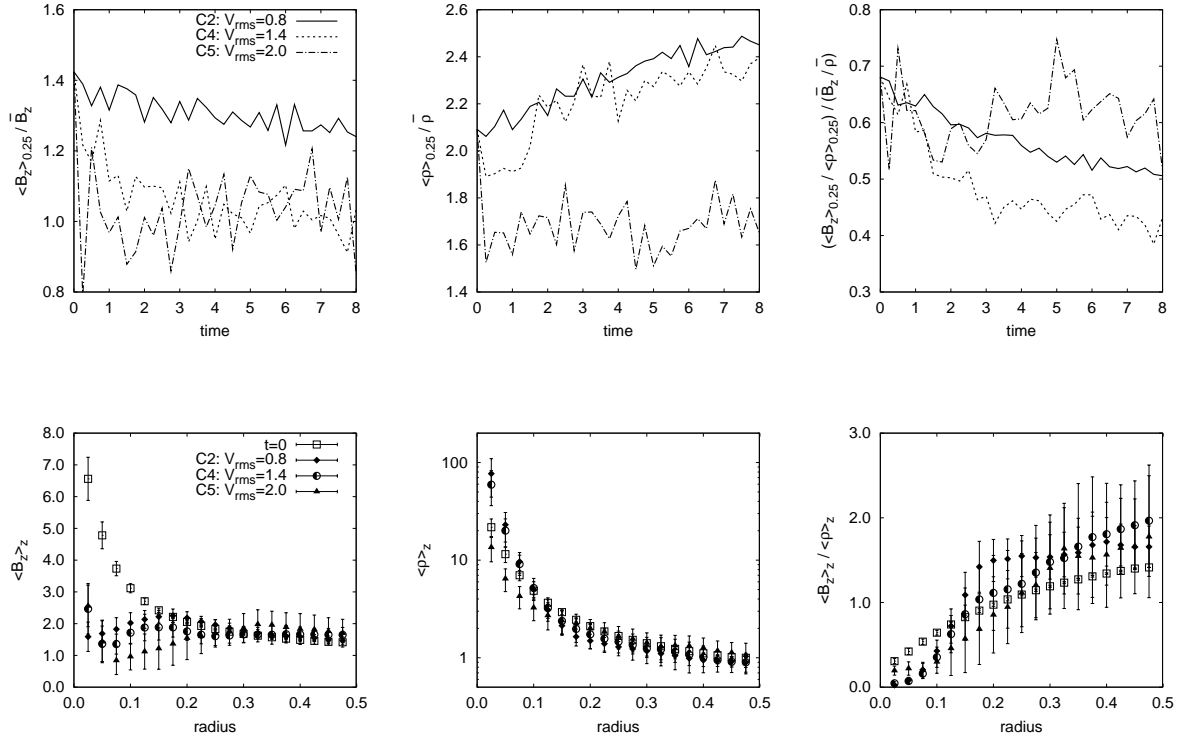


Figure 3.9: Evolution of the equilibrium models for different turbulent driving. The top row shows the time evolution of $\langle B_z \rangle_{0.25} / \bar{B}_z$ (*left*), $\langle \rho \rangle_{0.25} / \bar{\rho}$ (*middle*), and $(\langle B_z \rangle_{0.25} / \langle \rho \rangle_{0.25}) / (\bar{B}_z / \bar{\rho})$ (*right*). The bottom row shows the radial profile of $\langle B_z \rangle_z$ (*left*), $\langle \rho \rangle_z$ (*middle*), and $\langle B_z \rangle_z / \langle \rho \rangle_z$ (*right*) for each value of the turbulent velocity V_{rms} , in $t = 0$ (magneto-hydrostatic solution with β constant) and $t = 8$. Error bars show the standard deviation. All models have initial $\beta = 1.0$. See Table 3.2.

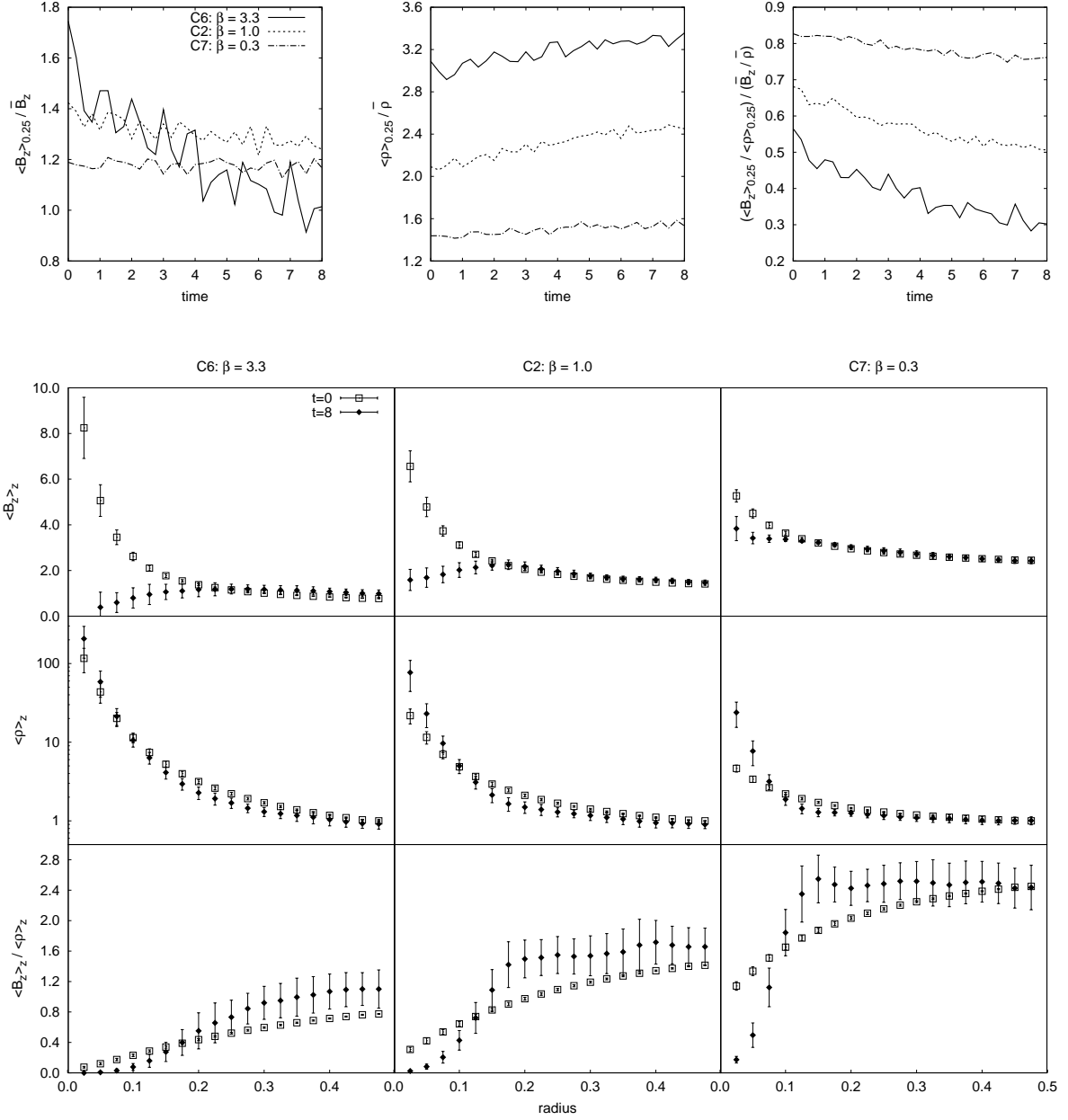


Figure 3.10: Evolution of the equilibrium models for different degrees of magnetization (plasma $\beta = P_{\text{gas}}/P_{\text{mag}}$). The top row shows the time evolution of $\langle B_z \rangle_{0.25} / \bar{B}_z$ (left), $\langle \rho \rangle_{0.25} / \bar{\rho}$ (middle), and $(\langle B_z \rangle_{0.25} / \langle \rho \rangle_{0.25}) / (\bar{\rho} / \bar{B}_z)$ (right). The other plots show the radial profile of $\langle B_z \rangle_z$ (upper panels), $\langle \rho \rangle_z$ (middle panels), and $\langle B_z \rangle_z / \langle \rho \rangle_z$ (bottom panels) for each value of β , in $t = 0$ (magneto-hydrostatic solution with β constant) and $t = 8$. Error bars show the standard deviation of the data. See Table 3.2.

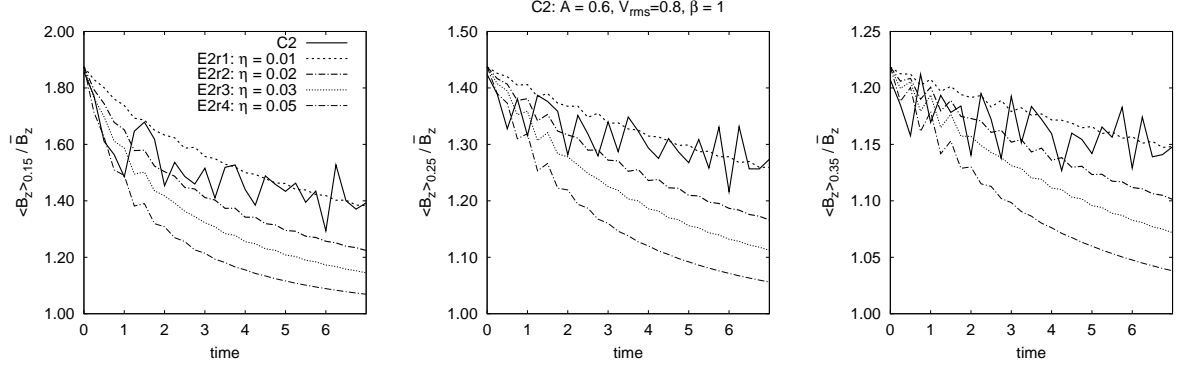


Figure 3.11: Comparison between the model C2 (turbulent diffusivity) and resistive models without turbulence (see Table 3.4). All the cases have analogous parameters.

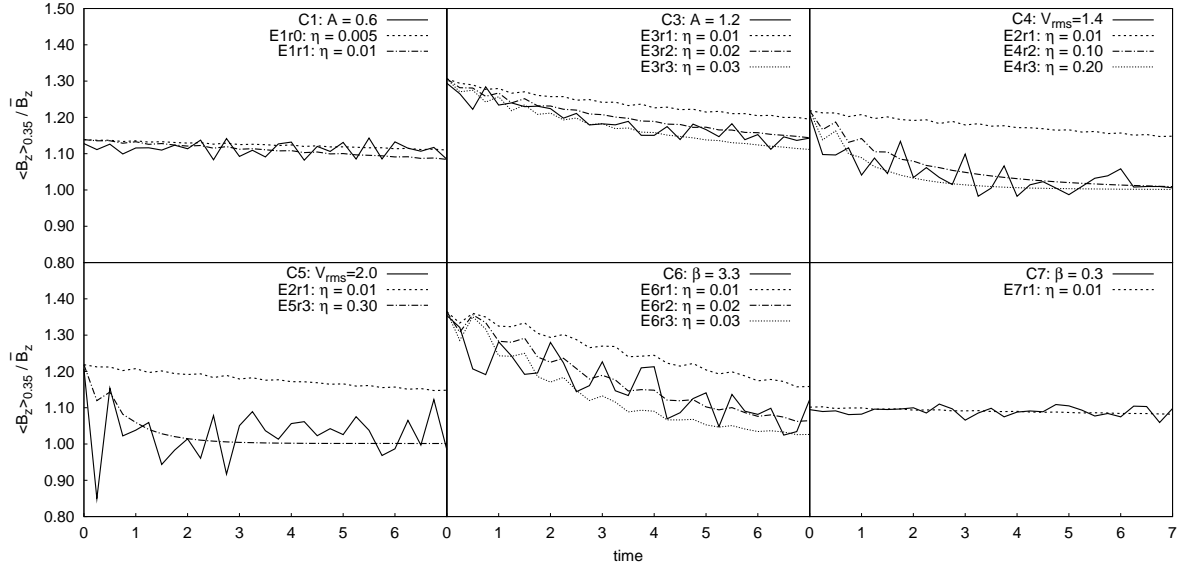


Figure 3.12: Comparison of the time evolution of $\langle B_z \rangle_{0.35}$ between models C1, C3, C4, C5, C6, and C7 (see Table 3.2) and resistive models without turbulence (see Table 3.4).

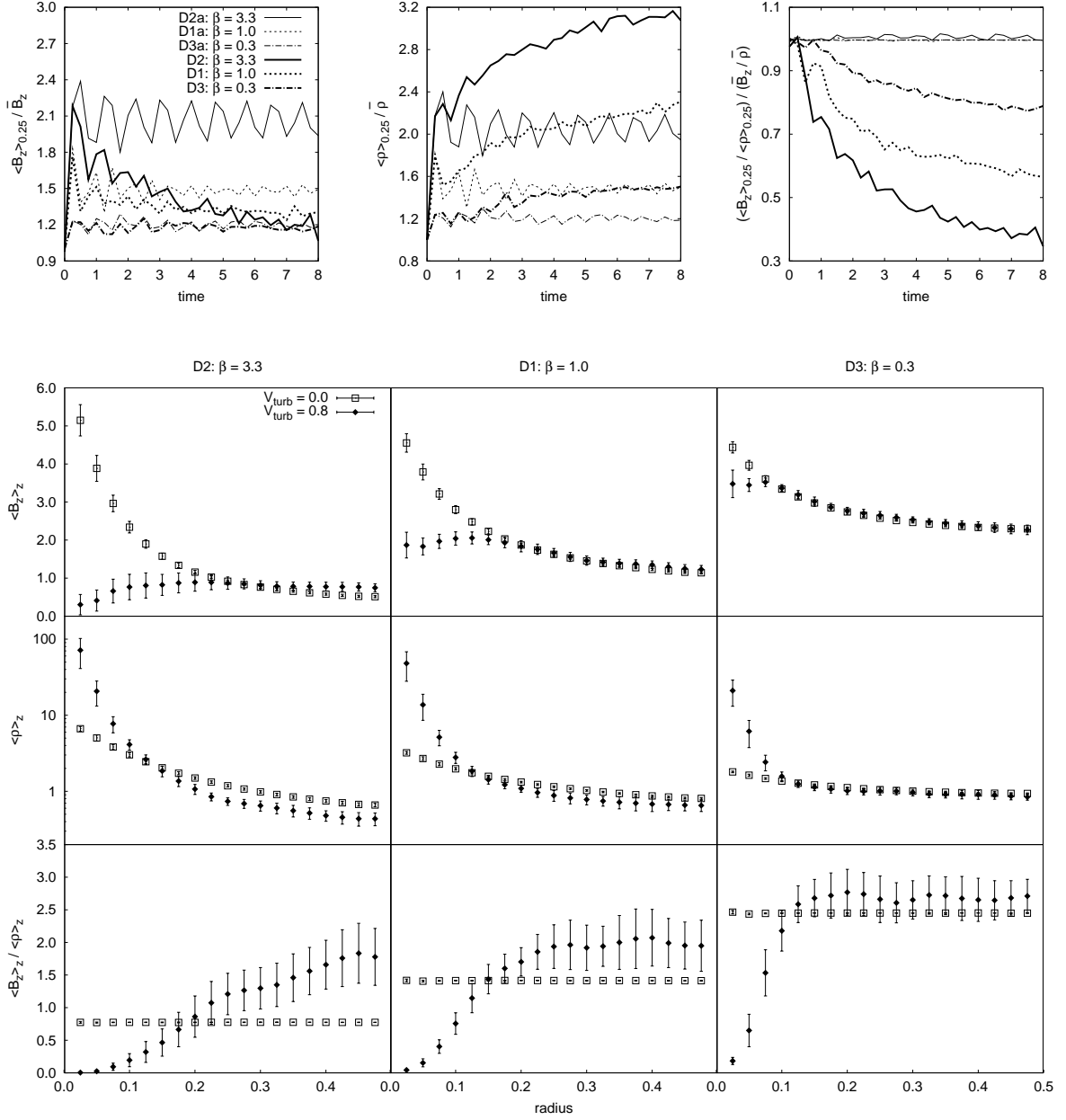


Figure 3.13: Evolution of models which start in non-equilibrium. The top row shows the time evolution of $\langle B_z \rangle_{0.25} / \bar{B}_z$ (left), $\langle \rho \rangle_{0.25} / \bar{\rho}$ (middle), and $(\langle B_z \rangle_{0.25} / \langle \rho \rangle_{0.25}) / (\bar{\rho} / \bar{B}_z)$ (right), for runs with (thick lines) and without (thin lines) injection of turbulence. The other plots show the radial profile of $\langle B_z \rangle_z$ (upper panels), $\langle \rho \rangle_z$ (middle), and $\langle B_z \rangle_z / \langle \rho \rangle_z$ (right) for different values of β , at $t = 8$, for runs with and without turbulence. Error bars show the standard deviation. See Table 3.3.

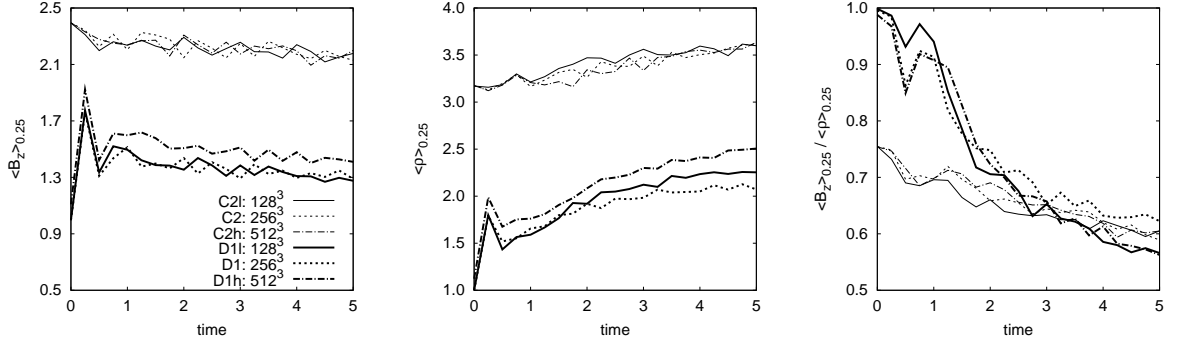


Figure 3.14: Comparison of the time evolution of $\langle B_z \rangle_{0.25}$ (*left*), $\langle \rho \rangle_{0.25}$ (*middle*), and $\langle B_z \rangle_{0.25} / \langle \rho \rangle_{0.25}$ (*right*) between models with different resolutions: C2, C2l, C2h (Table 3.2) and D2, D2l, D2h (Table 3.3).

3.4 Discussion of the results: relations to earlier studies

Through this work we have performed the comparison of our results with the study by Heitsch et al. (2004). Below, we provide yet another outlook of the connection of that study with the present work. We also discuss the work by Shu et al. (2006), which was the initial motivation of our study of the diffusion of magnetic field in the presence of gravity.

3.4.1 Comparison with Heitsch et al. (2004): Ambipolar Diffusion Versus Turbulence and 2.5-dimensional Versus Three-dimensional

In view of the astrophysical implications, the comparison between our results and those of Heitsch et al. (2004) calls for the discussion on how ambipolar diffusion and turbulence interact to affect the magnetic field diffusivity. In particular, Heitsch et al. (2004) claim that a new process “turbulent ambipolar diffusion” (see also Zweibel 2002) acts to induce fast magnetic diffusivity.

At the same time, our results do not seem to exhibit less magnetic diffusivity than those of Heitsch et al. (2004) in spite of the fact that we do not have ambipolar diffusion. How can this be understood? We propose the following explanation. In the absence of ambipolar diffusion, the turbulence propagates to smaller scales making small-scale interactions possible. On the other hand, ambipolar diffusion affects the turbulence, increasing the damping scale. As a result, the ambipolar diffusion acts in two ways, in one to increase the small-scale diffusivity of the magnetic field, in another is to decrease the turbulent small-scale diffusivity and these effects essentially compensate each other².

²A possible point of confusion is related to the difference of the physical scales involved. If one associates the scale of the reconnection with the thickness of the Sweet–Parker layer, then, indeed, the ambipolar diffusion scale is much larger and therefore the reconnection scale gets irrelevant. However, within the LV99 model of reconnection, the scale of reconnection is associated with the scale of magnetic

In other words, if we approximate the turbulent diffusivity by $(1/3)V_{\text{inj}}L_{\text{inj}}$, where V_{inj} and L_{inj} are the injection velocity and the injection scale for strong MHD turbulence (see LV99, Lazarian 2006b), respectively, the ambipolar diffusivity acting on small scales will not play any role and the diffusivity will be purely “turbulent”. If, however, the ambipolar diffusion coefficient is larger than $V_{\text{inj}}L_{\text{inj}}$, then the Reynolds number of the steered flow may become small for strong MHD turbulence to exist and the diffusion is purely ambipolar in this case. We might speculate that this leaves little, if any, parameter space for the “turbulent ambipolar diffusion” when turbulence and ambipolar diffusion synergetically enhance diffusivity, acting in unison. This point should be tested by three-dimensional two-fluid simulations exhibiting both ambipolar diffusion and turbulence.

In view of our findings one may ask whether it is surprising to observe the “turbulent reconnection diffusion” of magnetic field being independent of ambipolar diffusion. We can appeal to the fact well known in hydrodynamics, namely, that in a turbulent fluid the diffusion of a passive contaminant does not depend on the microscopic diffusivity. In the case of high microscopic diffusivity, the turbulence provides mixing down to a scale l_1 at which the microscopic diffusivity both, suppresses the cascade and ensures efficient diffusivity of the contaminant. In the case of low microscopic diffusivity, turbulent mixing happens down to a scale $l_2 \ll l_1$, which ensures that even low microscopic diffusivity is sufficient to provide efficient diffusion. In both cases the total effective diffusivity of the contaminant is turbulent, i.e. is given by the product of the turbulent injection scale and the turbulent velocity. This analogy is not directly applicable to ambipolar diffusion, as this is a special type of diffusion and magnetic fields are different from passive contaminants. However, we believe that our results show that to some extent the concept of turbulent diffusion developed in hydrodynamics carries over (due to fast reconnection) to magnetized fluid.

field wandering. The corresponding scale depends on the turbulent velocity and is not small.

3.4.2 Transient De-correlation of Density and Magnetic Field

Magneto-sonic waves are known to create transient changes of the density and magnetic field correlation. In the case of turbulence the situation is less clear, but the research in the field suggests that the decomposition of the turbulent motions into basic MHD modes is meaningful and justified even for high amplitude motions (Cho et al. 2003a). Thus the claim in Passot & Vázquez-Semadeni (2003) that even in the limit of ideal MHD, turbulence can *transiently* affect the magnetic field and density correlations is justified. However, the process discussed in this work is different in the sense that the de-correlation we describe here is *permanent* and it will not disappear if the turbulence dissipates. In a sense, as we showed above, “turbulent reconnection diffusion” is similar to the ambipolar and Ohmic diffusion. It is a dissipative diffusion process, which does require non-zero resistivity, although this resistivity can be infinitesimally small for the LV99 model of fast reconnection in the presence of turbulence (see Section 2.4.1).

3.4.3 Relation to Shu et al. (2006): Fast Removal of Magnetic Flux During Star Formation

As discussed in Shu et al. (2006), the sufficiency of the ambipolar diffusion efficiency for explaining observational data of accreting protostars is questionable. At the same time, they found that the required dissipation is about 4 orders of magnitude larger than the expected Ohmic dissipation. Thus they appealed to the hyper-resistivity concept in order to explain the higher dissipation of magnetic field.

We feel, however, that the hyper-resistivity idea is poorly justified (see criticism of it in Lazarian et al. 2004 and Kowal et al. 2009). At the same time, fast three-dimensional “reconnection diffusion” can provide the magnetic diffusivity that is adequate for fast removing of the magnetic flux. This is what, in fact, was demonstrated in the present set of numerical simulations.

It is worth mentioning that, unlike the actual Ohmic diffusivity, “reconnection diffusion” does not transfer the magnetic energy directly into heat. The lion share of the energy is being released in the form of kinetic energy, driving turbulence (see LV99). If

the system is initially laminar, this potentially result in flares of reconnection and the corresponding diffusivity. This is in agreement with LV99 scheme where a more intensive turbulence should induce more intensive turbulent energy injection and lead to the unstable feeding of the energy of the deformed magnetic field. However, the discussion of this effect is beyond the scope of the present work.

Similar to Shu et al. (2006), we expect to observe the heating of the media. Indeed, although we do not expect to have Ohmic heating, the kinetic energy released due to magnetic reconnection is dissipated locally and therefore we expect to observe heating in the medium. Our setup for gravity can be seen as a toy model representing the situation in Shu et al. (2006). In the broad sense, our work confirms that a process of magnetic field diffusion that does not rely on ambipolar diffusion is efficient.

We accept that our setup assuming an axial gravitational field is a very simple and ignores complications that could arise from using a nearly spherical potential of the self-gravitating cloud. The periodic boundary conditions give super-stability to the system, and do not allow inflow (or outflow) of material/magnetic field as we expect in a more realistic accretion process. However, our experiments can give us qualitative insights. They show that the turbulent diffusion of the magnetic field can remove magnetic flux from the central region, leading to a lower flux-to-mass ratio in regions of higher gravity compared with that of lower gravity.

We chose parameters to the simulations such that the system is not initially unstable to the Parker–Rayleigh–Taylor (PRT) instability. Although the PRT instability could be present in real accretion systems and could help to remove magnetic field from the core of gravitational systems, its presence would make the interpretation of the results more difficult and we wanted to analyze only the turbulence role in the removal of magnetic flux. However, it is possible that this instability had been also acting due to local changes of parameters due to the turbulent motion. To ensure that the transport of magnetic flux is being caused by injection of turbulence only, we stopped the injection after a few time steps in some experiments and left the system to evolve. When we did this, the changes in the profile of the magnetic field and the other quantities stopped.

We showed that the higher the strength of the gravitational force, the lower the flux-

to-mass ratio is in the central region (compared with the mean value in the computational domain). This could be understood in terms of the potential energy of the system. When the gravitational potential well is deeper, more energetically favorable is the pile up of matter near the center of gravity, reducing the total potential energy of the system. When the turbulence is increased, there is an initial trend to remove more magnetic flux from the center (and consequently more inflow of matter into the center), but for the highest value of the turbulent velocity in our experiments, there is a trend to remove material (together with magnetic flux) from the center, reducing the role of the gravity, due to the fact that the gravitational energy became small compared to the kinetic energy of the system. Our results also showed that when the gas is less magnetized (higher β , or higher values of the Alfvénic Mach number M_A), the reconnection diffusion of magnetic flux is more effective, but the central flux-to-mass ratio relative to external regions is smaller for more magnetized models (low β), compared to less magnetized models. That is, the contrast B/ρ between the inner and outer radius is higher for lower β (or M_A).

If the turbulent diffusivity of magnetic field may explain the results in Shu et al. (2006), one may wonder whether one can remove magnetic field by this way not only from the class of systems studied by Shu et al. (2006), but also from less dense systems. For instance, it is frequently assumed that only ambipolar diffusion is important for the evolution of subcritical magnetized clouds (Tassis & Mouschovias, 2005). Our study indicates that this conclusion may be altered in the presence of turbulence. This point, however, requires further careful study, which is beyond the scope of the present work. In the future, we intend to study a more realistic model, e.g., with open boundary conditions and more realistic gravitational potentials.

3.5 Turbulent magnetic diffusion and turbulence theory

As remarked in Chapter 2, the concept of “turbulent reconnection diffusion” is related to the LV99 model of fast reconnection which makes use of the model of strong turbulence

proposed by Goldreich & Sridhar (1995, henceforth GS95) the turbulence is being injected at the large scales with the injection velocity V_{inj} equal to the Alfvén velocity V_A (see Cho et al. 2003b for a review). The turbulent eddies mix up magnetic field mostly in the direction perpendicular to the local magnetic field thus forming a Kolmogorov-type picture in terms of perpendicular motions. Naturally, these eddies are as efficient as hydrodynamic eddies are expected in terms of heat advection. One also can visualize how such eddies can induce magnetic field diffusion.

It is important to note that the GS95 model deals with motions with respect to the *local* rather than mean magnetic field. Indeed, it is natural that the motions of the parcel of fluid are affected only by the magnetic field of the parcel and of the near vicinity, i.e., by local fields. At the same time, in the reference frame of the mean field, the local magnetic fields of different parcels vary substantially. Thus we do not expect to see a substantial anisotropy of the heat advection when $V_{\text{inj}} \sim V_A$.

It was noted in LV99 that one can talk about turbulent eddies perpendicular to the magnetic field only if the magnetic field can reconnect fast. The rates of reconnection predicted in LV99 ensured that the magnetic field changes topology over one eddy turnover period. If the reconnection were slow, the magnetic fields would form progressively complex structures consisting of unresolved knots, which would invalidate the GS95 model. The response of such a fluid to mechanical perturbations would be similar to “Jello”, making the turbulence-sponsored diffusion of magnetic field and heat impossible.

What happens when $V_{\text{inj}} < V_A$? In this case the turbulence at large scales is weak and therefore magnetic field mixing is reduced. Thus one may expect a partial suppression of magnetic diffusivity. However, as turbulence cascades the strength of interactions increases and at a scale $L_{\text{inj}}(V_{\text{inj}}/V_A)^2$ the turbulence gets strong. According to Lazarian (2006b), the diffusivity in this regime decreases by the ratio of $(V_{\text{inj}}/V_A)^3$, with the eddies of strong turbulence playing a critical role in the process. When we compare the turbulent diffusivity η_{turb} estimated for the sub-Alfvénic models described in Table 3.2 (see Section 3.3) with $L_{\text{inj}}V_{\text{turb}}(V_{\text{turb}}/V_A)^3$, we find that the values are roughly consistent with the predictions of Lazarian (2006b), although a more detailed study is required in this regard. For instance, we know that Lazarian (2006b) theory was not intended for

high Mach number turbulence.

All in all, we believe that the high diffusivity that we observe is related to the properties of strong magnetic turbulence. While the latter is still a theory which is subject to intensive study (see Boldyrev 2005, 2006; Beresnyak & Lazarian 2006, 2009a,b; Gogoberidze 2007), we believe that for the purpose of describing magnetic and heat diffusion the existing theory and the present model catch all the essential phenomena.

3.6 Accomplishments and limitations of the present study

3.6.1 Major Findings

This work presents several sets of simulations which deal with magnetic diffusion in turbulent fluids. Comparing our result on magnetic diffusion and that of heat, we see many similarities in these two processes. Our numerical testing in the work would not make sense if the astrophysical reconnection were slow. Indeed, the major criticism that can be directed to the work of turbulent diffusion of heat by Cho et al. (2003a) is that reconnection in their numerical simulations was fast due to high numerical diffusivity. With the confirmation of the LV99 model of turbulent reconnection by Kowal et al. (2009) one may claim that astrophysical reconnection is also generally fast and the differences between the computer simulations and astrophysical flows are not so dramatic as far as the reconnection is concerned.

The most important part of our study is the removal of magnetic fields from gravitationally bounded systems (see Section 3.3). Generally speaking, this is what one can expect on the energetic grounds. Magnetic field can be identified with a light fluid which is not affected by gravity, while the matter tends to fall into the gravitational potential³. Turbulence in the presence of magnetic reconnection helps “shaking off” matter from magnetic fields. In our simulations the gravitational energy was larger than the turbulent

³As a matter of fact, in our low β simulations, which we did not include in the work, we see clear signatures of the PRT instability.

energy. In the case when the opposite is true, the system is expected to get unbounded with turbulence mixing magnetic field in the same way it does in the absence of gravity (see Section 3.2).

It is important to note that in Section 3.3 we obtained the segregation of magnetic field and matter both in the case when we started with equilibrium distribution and in the case when the system was performing a free fall. In the case of non-equilibrium initial conditions the amount of flux removed from the forming dense core is substantially larger than in the case of the equilibrium magnetic field/density configurations (compare Figures 3.10 and 3.13). Nevertheless, the flux removal happens fast, essentially in one turnover of the turbulent eddies. In comparison, the effect of numerical diffusion for the flux removal in our simulations is marginal, and this is testified by the constant flux-to-mass ratio obtained in the simulations without turbulence (see Figure 3.13).

What is the physical picture corresponding to our findings? In the absence of gravity turbulence mixes up⁴ flux tubes with different magnetic flux-to-mass ratios decreasing the difference in this ratio. In the presence of gravity, however, it is energetically advantageous of flux tubes at the center of the gravitational potential to increase the mass-to-flux ratio. This process is enabled in highly conducting fluid by turbulence which induces “reconnection diffusion”.

3.6.2 Applicability of the Results

The diffusion of magnetic field in our numerical runs exhibits a few interesting features. First of all, according to Figure 3.4 one may expect to see a broad distribution of magnetic field intensity with density. This seems to be consistent with the measurements of magnetic field strength in diffuse media (Troland & Heiles, 1986).

The situation gets even more intriguing as we discuss magnetic field diffusion in the gravitational potential. It is tempting to apply these results to star formation process (see

⁴This mixing for Alfvénic modes happens mostly perpendicular to the local magnetic field for sub-Alfvénic and trans-Alfvénic turbulence (LV99). For super-Alfvénic turbulence the mixing is essentially hydrodynamic at large scales and the picture with motions perpendicular to the local magnetic field direction is restored at small scales (see discussion in Lazarian et al. 2004).

studies by Leão et al. 2009, 2012). There, molecular clouds are known to be either magnetically supercritical or magnetically subcritical (see Mestel & Ray 1985). If, however, the magnetic flux can be removed from the gravitating turbulent cloud in a timescale of about an eddy turnover time, then the difference between clouds with different initial magnetization becomes less important. The initially subcritical turbulent clouds can lose their magnetic flux via the turbulent diffusion to become supercritical.

An important point of the turbulent diffusion of the magnetic field is that it does not require gas to be weakly ionized, which is the requirement of the action of the ambipolar diffusion. Therefore, one may expect to observe gravitational collapse even of the highly ionized gas.

3.6.3 Magnetic Field Reconnection and Different Stages of Star Formation

“Reconnection diffusion” seems to be a fundamental process that accompanies all the stages of star formation. Our work shows (Section 3.2) that three-dimensional diffusion of magnetic field provides a wide distribution of the mass-to-flux ratios with some of the fluctuations having this ratio rather high. We believe that the diffusion of magnetic field described here is one the reasons for creation of zones of super-Alfvénic turbulence even for sub-Alfvénic driving (see Burkhart et al. 2009).

The regions of density concentration get gravitationally bound. One can associate such regions with GMCs. These entities are known to be highly turbulent and turbulent diffusion will proceed within them, providing a hierarchy of self-gravitating zones with different density and different mass-to-flux ratios. Some of those zones may be subcritical in terms of magnetic field and some of them may be supercritical. In subcritical magnetic cores the turbulent diffusion may proceed quasi-statically as we described in Section 3.3.2 and in the supercritical cores the turbulent diffusion may proceed as we described in Section 3.3.2. In both cases, we expect the removal of magnetic field from the self-gravitating cores. This process proceeds all the time, including the stage of the accretion disks.

Indeed, in the turbulent scenario of star formation it is usually assumed that at the initial stages of star formation the concentration of material happens due to gas moving along magnetic field lines (Mestel & Paris, 1984). This one-dimensional process requires rather long times of the accumulation of material. In contrast, the TRD allows for the much faster three-dimensional accumulation.

What is the relative role of the ambipolar diffusion and the TRD? This issue requires further studies. It is clear from the study by Shu et al. (2006) that in some situations the ambipolar diffusion may be not fast enough to explain the removal of magnetic fields from accretion disks. This is the case when we claim that the “reconnection diffusion” should dominate. At the same time, in cores with low turbulence, the ambipolar diffusion may dominate the reconnection diffusion. The exact range of the parameters for one or the other process to dominate should be defined by future research.

3.6.4 Unsolved Problems and further Studies

Our work has a clearly exploratory character. For instance, to simplify the interpretation of our results we studied the concentration of material in the given gravitational potential, ignoring self-gravity of the gas. This has been recently considered in another numerical study involving initially self-gravitating spherical clouds with embedded magnetic fields (Leão et al. 2012). The results of this study have confirmed the present ones. In particular, self-gravity also seems to favour the decoupling between the collapsing gas and the magnetic fields due to TRD. They also have demonstrated that turbulent reconnection diffusion of the magnetic flux is very effective and may allow the transformation of initially subcritical into supercritical cores (Leão et al. 2012). In addition, our study indicates that the highly magnetized gas in gravitational potential is subject to instabilities (Parker–Rayleigh–Taylor-type, Parker 1966) which drive turbulence and induce reconnection diffusion of magnetic field. This is another avenue that we intend to explore.

We have reported fast magnetic diffusion which happens at the rate of turbulent diffusion, but within the present set of simulations we did not attempt to precisely evaluate

the rate. Thus we did not attempt to test, e.g., the predictions in Lazarian (2006b) of the variations of the turbulent diffusion rate with the fluid magnetization for the passive scalar field. We also observed that while the magnetic field and the passive scalar field diffuse fast, there are differences in their diffusion arising, e.g., from magnetic field being associated with magnetic pressure. We have not attempted to quantify these differences in our work either.

3.7 Summary

Motivated by a vital problem of the dynamics of magnetic fields in astrophysical fluids, i.e., by the magnetic flux removal in star formation, in this work we have numerically studied the diffusion of magnetic field both in the absence and in the presence of gravitational potential. Our findings obtained on the basis of three-dimensional MHD numerical simulations can be briefly summarized as follows:

1. In the absence of gravitational potential the TRD removes strong anti-correlations of magnetic field and density that we impose at the start of our simulations. The system after several turbulent eddy turnover times relaxes to a state with no clear correlation between magnetic field and density, reminiscent of the observations of the diffuse ISM by Troland & Heiles (1986).

2. Our simulations that started with a quasi-static equilibrium in the presence of a gravitational potential, revealed that the turbulent diffusivity induces gas to concentrate at the center of the gravitational potential, while the magnetic field is efficiently pushed to the periphery. Thus the effect of the magnetic flux removal from collapsing clouds and cores, which is usually attributed to ambipolar diffusion effect, can be successfully accomplished without ambipolar diffusion, but in the presence of turbulence.

3. Our simulations that started in a state of dynamical collapse induced by an external gravitational potential showed that in the absence of turbulence, the flux-to-mass ratio is preserved for the collapsing gas. On the other hand, in the presence of turbulence, fast removal of magnetic field from the center of the gravitational potential occurs. This may explain the low magnetic flux-to-mass ratio observed in stars compared to the

corresponding ratio of the interstellar gas.

4. As an enhanced Ohmic resistivity to remove magnetic flux from cores and accretion disks has been appealed in the literature, e.g., by Shu et al. (2006), we have also compared models with a turbulent fluid and models without turbulence but with substantially enhanced Ohmic diffusivity. We have shown that, in terms of the magnetic flux removal, the reconnection diffusion can mimic the effect of an enhanced Ohmic resistivity.

Chapter 4

The role of turbulent magnetic reconnection in the formation of rotationally supported protostellar disks

The formation of protostellar disks out of molecular cloud cores is still not fully understood. Under ideal MHD conditions, the removal of angular momentum from the disk progenitor by the typically embedded magnetic field may prevent the formation of a rotationally supported disk during the main protostellar accretion phase of low mass stars. This has been known as the magnetic braking problem and the most investigated mechanism to alleviate this problem and help removing the excess of magnetic flux during the star formation process, the so called ambipolar diffusion (AD), has been shown to be not sufficient to weaken the magnetic braking at least at this stage of the disk formation. In this work, motivated by recent progress in the understanding of magnetic reconnection in turbulent environments, we appeal to the diffusion of magnetic field mediated by turbulent magnetic reconnection (TRD) as an alternative mechanism for removing magnetic flux. We investigate numerically this mechanism during the late phases of the protostellar disk formation and show its high efficiency. By means of fully 3D MHD simulations, we

show that the diffusivity arising from turbulent magnetic reconnection is able to transport magnetic flux to the outskirts of the disk progenitor at time scales compatible with the collapse, allowing the formation of a rotationally supported disk around the protostar of dimensions ~ 100 AU, with a nearly Keplerian profile in the early accretion phase. Since MHD turbulence is expected to be present in protostellar disks, this is a natural mechanism for removing magnetic flux excess and allowing the formation of these disks. This mechanism dismisses the necessity of postulating a hypothetical increase of the Ohmic resistivity as discussed in the literature. Together with our earlier work (described in Chapter 3) which showed that magnetic flux removal from molecular cloud cores is very efficient, this work calls for reconsidering the relative role of AD for the processes of star and planet formation.

4.1 Introduction

Circumstellar disks (with typical masses $\sim 0.1 M_{\odot}$ and diameters ~ 100 AU) are known to play a fundamental role in the late stages of star formation and also in planet formation. However, the mechanism that allows their formation and the decoupling from the surrounding molecular cloud core progenitor is still not fully understood (see, e.g., Krasnopolsky et al. 2011 for a recent comprehensive review). Former studies have shown that the observed embedded magnetic fields in molecular cloud cores, which imply magnetic mass-to-flux ratios relative to the critical value a few times larger than unity (Crutcher 2005; Troland & Crutcher 2008) are high enough to inhibit the formation of rotationally supported disks during the main protostellar accretion phase of low mass stars, provided that ideal MHD applies. This has been known as the magnetic braking problem (see e.g., Allen, Li, & Shu 2003; Galli et al. 2006; Price & Bate 2007; Hennebelle & Fromang 2008; Mellon & Li 2008).

In this situation, the angular momentum of the disk is transferred to the external medium (envelope) through torsional Alfvén waves (Machida et al. 2011). The magnetic braking timescale corresponds to the time necessary for extracting all the angular momentum of the disk. When the angular momentum of the disk is aligned with the uniform

magnetic field, the magnetic braking timescale is found to be

$$\tau_{\parallel} = \frac{\rho_d}{\rho_e} \frac{Z_d}{v_{A,e}} \equiv \left(\frac{\pi}{\rho_e} \right)^{1/2} \frac{M_d}{\Phi_B} \quad (4.1)$$

where ρ_d and ρ_e are the densities of the disk and envelope, respectively, Z_d the half-thickness of the disk, $v_{A,e}$ the Alfvén speed in the envelope, M_d the disk mass, and Φ_B its magnetic flux (Basu & Mouschovias 1994). Therefore, the magnetic braking becomes effective when the timescales of the system are large compared to τ_{\parallel} and this seems to be the case in observed systems if the magnetic flux is conserved..

Proposed mechanisms to alleviate this problem and help removing the excess of magnetic flux during the star formation process include non-ideal MHD effects such as ambipolar diffusion (AD) and, to a smaller degree, Ohmic dissipation effects. The AD, which was first discussed in this context by Mestel & Spitzer (1956), has been extensively investigated since then (e.g., Spitzer 1968; Nakano & Tademaru 1972; Mouschovias 1976, 1977, 1979; Nakano & Nakamura 1978; Shu 1983; Lizano & Shu 1989; Fiedler & Mouschovias 1992, 1993; Li et al. 2008; Fatuzzo & Adams 2002; Zweibel 2002). In principle, AD allows magnetic flux to be redistributed during the collapse in low ionization regions as the result of the differential motion between the ionized and the neutral gas. However, for realistic levels of core magnetization and ionization, recent work has shown that AD does not seem to be sufficient to weaken the magnetic braking in order to allow rotationally supported disks to form. In some cases, the magnetic braking has been found to be even enhanced by AD (Mellon & Li, 2009; Krasnopolsky & Königl, 2002; Basu & Mouschovias, 1995; Hosking & Whitworth, 2004; Duffin & Pudritz, 2009; Li et al., 2011).¹ These findings motivated Krasnopolsky et al. (2010) (see also Li et al. 2011) to examine whether Ohmic dissipation could be effective in weakening the magnetic braking. They claimed that in order to enable the formation of persistent, rotationally supported disks during the protostellar mass accretion phase a highly enhanced resistivity, or “hyper-resistivity” $\eta \gtrsim 10^{19} \text{ cm}^2\text{s}^{-1}$ of unspecified origin would be required. Although this value is somewhat

¹See however a recent work that investigates the effects of AD in the triggering of magneto-rotational instability in more evolved cold, proto-planetary disks where the fraction of neutral gas is much larger (Bai & Stone, 2011).

dependent on the degree of core magnetization, it implies that the required resistivity is a few orders of magnitude larger than the classic microscopic Ohmic resistivity values (Krasnopolsky et al., 2010).

On the other hand, Machida et al. (2010) (see also Inutsuka et al. 2010; Machida et al. 2011) performed core collapse three-dimensional simulations and found that, even with just the classical Ohmic resistivity, a tiny rotationally supported disk can form at the beginning of the protostellar accretion phase (see also Dapp & Basu 2010) and grow to larger, 100-AU scales at later times. They claim that the later growth of the circumstellar disk is caused by the depletion of the infalling envelope. As long as this envelope remains more massive than the circumstellar disk, the magnetic braking is effective, but when the circumstellar disk becomes more massive, then the envelope cannot brake the disk anymore. In their simulations, they assume an initially much denser core than in Krasnopolsky et al. work, which helps the early formation of a tiny rotating disk facilitated by the Ohmic diffusion in the central regions. But they have to wait for over 10^5 yr in order to allow a large-scale rotationally supported, massive disk to form (see discussion in Section 4.6). While this question on the effectiveness of the Ohmic diffusion in the early accretion phases of disk formation deserves further careful testing, we here investigate the mechanism of turbulent reconnection diffusion (TRD) which has been described in detail in Chapter 2 (Section 2.4; see also Chapter 3).

Before addressing this new mechanism, it is crucial to note that the concept of “hyper-resistivity” previously mentioned (see also Strauss 1986; Bhattacharjee & Hameiri 1986; Diamond & Malkov 2003) is not physically justified and therefore one cannot rely on it (see criticism in Kowal et al. 2009; Eyink, Lazarian, & Vishniac 2011). Therefore, the dramatic increase of resistivity is not justified.

We show below by means of 3D MHD numerical simulations that the TRD enables the transport of magnetic flux to the outskirts of the collapsing cloud core at time scales compatible with the collapse time scale, thus allowing the formation of a rotationally supported protostellar disk with nearly Keplerian profile.

In Section 4.2 we describe the numerical setup and initial conditions, in Section 4.3 we show the results of our three-dimensional (3D) MHD turbulent numerical simulations

of disk formation, and in Section 4.6, we discuss our results within a bigger picture of reconnection diffusion processes. Our summary is presented in Section 4.7.

4.2 Numerical Setup and Initial Disk Conditions

To investigate the formation of a rotationally supported disk due to turbulent reconnection diffusion, we have integrated numerically the following system of MHD equations ²:

$$\frac{\partial \rho}{\partial t} + \nabla \cdot (\rho \mathbf{u}) = 0 \quad (4.2)$$

$$\rho \left(\frac{\partial}{\partial t} + \mathbf{u} \cdot \nabla \right) \mathbf{u} = -c_s^2 \nabla \rho + \frac{1}{4\pi} (\nabla \times \mathbf{B}) \times \mathbf{B} - \rho \nabla \Psi + \mathbf{f} \quad (4.3)$$

$$\frac{\partial \mathbf{A}}{\partial t} = \mathbf{u} \times \nabla \times \mathbf{A} - \eta_{Ohm} \nabla \times \nabla \times \mathbf{A} \quad (4.4)$$

where ρ is the density, \mathbf{u} is the velocity, Ψ is the gravitational potential generated by the protostar, \mathbf{B} is the magnetic field, and \mathbf{A} is the vector potential with $\mathbf{B} = \nabla \times \mathbf{A} + \mathbf{B}_{ext}$ (where \mathbf{B}_{ext} is the initial uniform magnetic field). \mathbf{f} is a random force term responsible for the injection of turbulence. An isothermal equation of state is assumed with uniform sound speed c_s .

In order to compare our results with those of Krasnopolsky et al. (2010), we have considered the same initial conditions as in their setup.

Our code works with cartesian coordinates and vector field components. We started the system with a collapsing cloud progenitor with initial constant rotation (see below) and uniform magnetic field in the z direction.

Given the cylindrical symmetry of the problem, we adopted circular boundary conditions. Eight rows of ghost cells were put outside a inscribed circle in the xy plane. For the four outer rows of ghost cells, we adopted fixed boundary conditions in the radial direction in every time step, while for the four inner ghost cells, linear interpolation between the initial conditions and the values in the interior bound of the domain were applied for

²We note that these equations are similar to the set of collisional MHD equations employed in Chapter 3 (eqs. 3.1 - 3.3), except that we solve the induction equation here for the vector potential.

the density, velocity, and vector potential. With this implementation the vector potential \mathbf{A} has kept its initial null value. Although this produces some spurious noisy components of \mathbf{B} in the azimuthal and vertical directions in the boundaries, these are too far from the central regions of the domain to affect the disk evolution. In the z direction, we have applied the usual open boundary conditions (i.e., zero derivatives for all conservative quantities: density, momentum and potential vector). We found this implementation far more stable than using open boundary conditions in the x and y directions, or even in the radial direction. Besides, adopting *circular* rather than square boundaries prevented the formation of artificial spiral arms and *corners* in the disk.

For modeling the accretion in the central zone, the technique of sink particles was implemented in the code in the same way as described in Federrath et al. (2010). A central sink with accretion radius encompassing 4 cells was introduced in the domain. The gravitational force inside this zone has a smoothing spline function identical to that presented in Federrath et al. (2010). We do not allow the creation of sink particles elsewhere, since we are not calculating the self-gravity of the gas. We note that this accreting zone essentially provides a *pseudo* inner boundary for the system and for this reason the dynamical equations are not directly solved there where accretion occurs, although we assure momentum and mass conservation.

The physical length scales of the computational domain are 6000 AU in the x and y directions and 4000 AU in the z direction. A sink particle of mass $0.5 M_{\odot}$ is put in the center of the domain. At $t = 0$, the gas has a uniform density $\rho_0 = 1.4 \times 10^{-19} \text{ g cm}^{-3}$ and a sound speed of $c_s = 2.0 \times 10^4 \text{ cm s}^{-1}$ (which implies a temperature $T \approx 4.8\bar{\mu} \text{ K}$, where $\bar{\mu}$ is mean molecular weight in atomic units). The initial rotation profile is $v_{\Phi} = c_s \tanh(R/R_c)$ (as in Krasnopolsky et al. 2010), where R is the radial distance to the central z -axis, and the characteristic distance $R_c = 200 \text{ AU}$.

We employed a uniform resolution of 384x384x256 which for the chosen set of parameters implies that each cell has a physical size of 15.6 AU in each direction. The sink zone has an accretion radius of 62.5 AU. ³

³We note that in the two-dimensional simulations of Krasnopolsky et al. (2010), they use a non-uniform mesh with a maximum resolution of 0.2 AU in the central region. The employment of a non-uniform mesh

Although we are interested in the disk that forms inside a radius of approximately 400 AU around the central axis, we have carried out the simulations in a much larger region of 6000 AU in order to keep the dynamically important central regions of the domain free from any outer boundary effects.

4.3 Results

We performed simulations for four models which are listed in Table 1. Model *hydro* is a purely hydrodynamical rotating system. All the other models have the same initial (vertical) magnetic field with intensity $B_z = 35 \mu\text{G}$. In order to have a benchmark, in the model named *resistive* we included an *anomalous* high resistivity, with a magnitude about 3 orders of magnitude larger than the Ohmic resistivity estimated for the system, i.e., $\eta = 1.2 \times 10^{20} \text{ cm}^2 \text{ s}^{-1}$. According to the results of Krasnopolsky et al. (2010), this is nearly the ideal value that the magnetic resistivity should have in order to remove the magnetic flux excess of a typical collapsing protostar disk progenitor and allow the formation of a rotationally sustained disk. We have thus included this anomalous resistive model in order to compare with more realistic MHD models that do not appeal to this resistivity excess.

We have also considered an MHD model with turbulence injection (labeled as *turbulent* model in Table 1). In this case, we introduced in the cloud progenitor a solenoidal turbulent velocity field with a characteristic scale of 1600 AU and a Mach number $M_S \approx 4 - 5$ increasing approximately linearly from $t = 0$ until $t = 3 \times 10^{10} \text{ s}$ (or $\approx 3000 \text{ yr}$). These parameters result an estimated turbulent diffusivity which is of the order of the anomalous diffusivity employed in *resistive* model: $\eta_{turb} \sim V_{turb} L_{inj} \sim 10^{20} \text{ cm}^2 \text{ s}^{-1}$. The induced turbulent velocity field has been intentionally smoothed beyond a radius of 800 AU, by a factor $\exp\{-[R(\text{AU}) - 800]^2/400^2\}$, in order to prevent disruption of the cloud

could be advantageous in this problem, allowing a better resolution close the protostar. However, in the present work since we are dealing with turbulence injection in the evolving system, the use of a uniform mesh has the advantage of making the effects of numerical dissipation more uniform and therefore, the analysis of the turbulent evolution and behavior more straightforward.

at large radii. The injection of turbulence was stopped at $t = 4.5 \times 10^{11} \text{ s} \approx 0.015 \text{ Myr}$. From this time on, it naturally decayed with time, as one should expect to happen in a real system when the physical agent that injects turbulence in the cloud ceases to occur.

The last of the models (which is labeled as ideal MHD) has no explicit resistivity or turbulence injected so that in this case the disk evolves under an ideal MHD condition.

Table 4.1: Summary of the models

Model	B_0 (μG)	η_{Ohm} ($\text{cm}^2 \text{ s}^{-1}$)	η_{turb} ($\text{cm}^2 \text{ s}^{-1}$)
<i>hydro</i>	0	0	0
<i>resistive</i>	35	1.2×10^{20}	0
<i>turbulent</i>	35	0	$\sim 10^{20}$
<i>ideal MHD</i>	35	0	0

Figure 4.3 shows face-on and edge-on density maps of the central slice of the disk for the four models at $\approx 0.03 \text{ Myr}$. The arrows in the top panels represent the direction of the velocity field, while those in the bottom panels represent the direction of the magnetic field.

The pure hydrodynamical model in the left panels of Figure 4.3 clearly shows the formation of a high density torus structure within a radius $\approx 300 \text{ AU}$ which is typical of a Keplerian supported disk (see also Figure 4.3, top-right panel).

In the case of the ideal-MHD model (second row panels in Figure 4.3), the disk core is much smaller and a thin, low density outer part extends to the outskirts of the computational domain. The radial velocity component is much larger than in the pure hydrodynamical model. The bending of the disk in the core region is due to the action of the magnetic torques. As the poloidal field lines are dragged to this region by the collapsing fluid, large magnetic forces develop and act on the rotating flow. The resulting torque removes angular momentum from the inner disk and destroys its rotational support (see also Figure 4.3, upper panels).

The third column (from left) of panels in Figure 4.3 shows the resistive MHD model.

As in Model 1, a torus (of radius ≈ 250 AU) with a rotationally dominant velocity field is formed and is surrounded by a flat, low density disk up to a radius of ~ 500 AU. Compared to the ideal MHD model (second column), the structure of the magnetic field is much simpler and exhibits the familiar hourglass geometry.

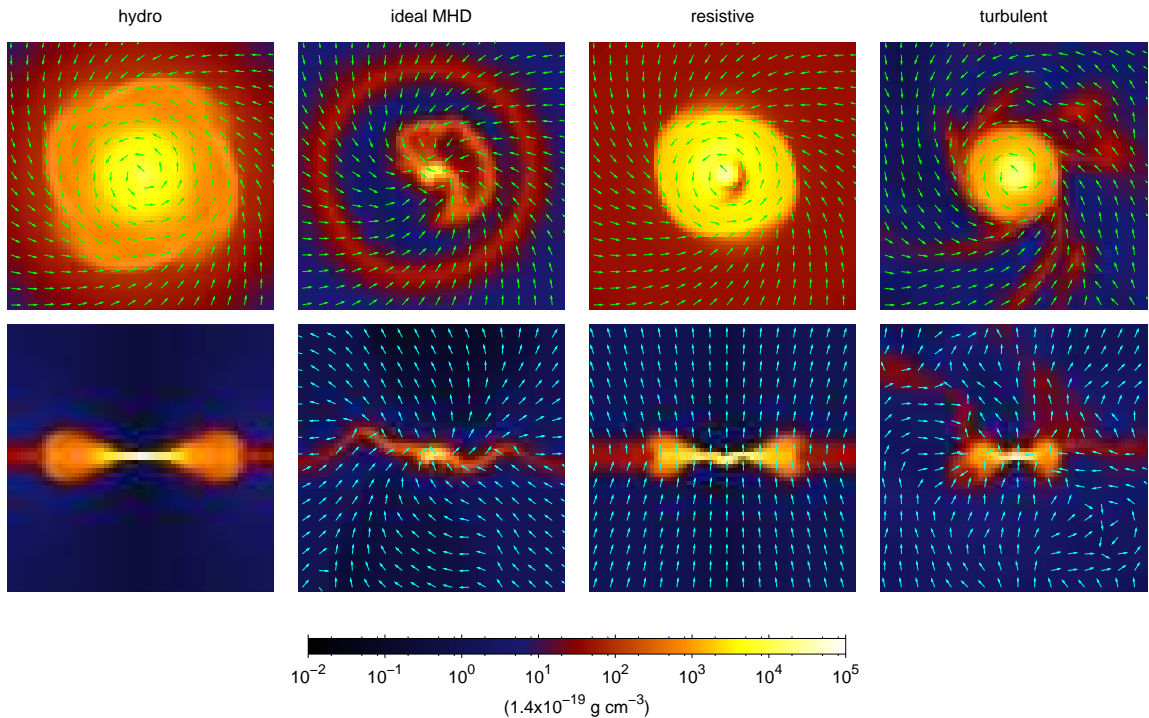


Figure 4.1: Face-on (top) and edge-on (bottom) density maps of the central slices of the collapsing disk models listed in Table 4.1 at a time $t = 9 \times 10^{11}$ s (≈ 0.03 Myr). The arrows in the top panels represent the velocity field direction and those in the bottom panels represent the magnetic field direction. From left to right rows it is depicted: (1) the pure hydrodynamic rotating system; (2) the ideal MHD model; (3) the MHD model with an anomalous resistivity 10^3 times larger than the Ohmic resistivity, i.e. $\eta = 1.2 \times 10^{20}$ cm² s⁻¹; and (4) the turbulent MHD model with turbulence injected from $t = 0$ until $t=0.015$ Myr. All the MHD models have an initial vertical magnetic field distribution with intensity $B_z = 35 \mu\text{G}$. Each image has a side of 1000 AU.

Figure 4.2 depicts three-dimensional diagrams of three snapshots of the turbulent

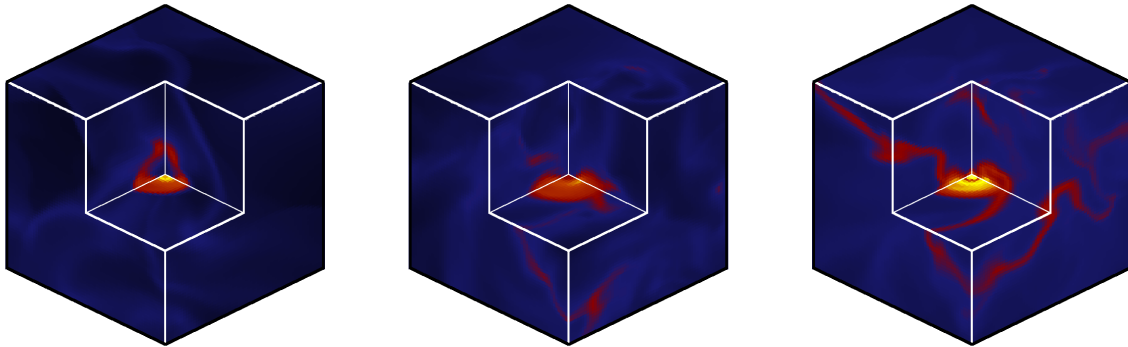


Figure 4.2: Three-dimensional diagrams of snapshots of the density distribution for the *turbulent* model of disk formation in the rotating, magnetized cloud core computed by SGL12. From left to right: $t = 10.000$ yr; 20.000 yr; and 30.000 yr. The side of the external cubes is 1000 AU.

model.

The last column (on the right of Figure 4.3) shows the ideal MHD model with injected turbulence (labeled *turbulent*). A high density disk arises in the central region within a radius of 150 AU surrounded by turbulent debris. From the simple visual inspection of the velocity field inside the disk one cannot say if it is rotationally supported. On the other hand, the distorted structure of the magnetic field in this region, which is rather distinct from the helical structure of the ideal MHD model, is an indication that magnetic flux is being removed by the turbulence in this case. The examination of the velocity and magnetic field intensity profiles in Figure 4.3 are more elucidative, as described below.

Figure 4.3 shows radial profiles of: (i) the radial velocity v_R (top left), (ii) the rotational velocity v_ϕ (top right); (iii) the inner disk mass (bottom left); and (iv) the vertical magnetic field B_z (bottom right) for the models of Figure 4.3. v_R and v_ϕ were averaged inside cylinders centered in the protostar with height $h = 400$ AU and thickness $dr = 20$ AU. Only cells with a density larger than 100 times the initial density of the cloud ($\rho_0 = 1.4 \times 10^{-19}$ g cm $^{-3}$) were taken into account in the average evaluation. The internal disk mass was calculated in a similar way, but instead of averaging, we simply summed the masses of the cells in the inner region. The magnetic field profiles were also

obtained from average values inside equatorial rings centered in the protostar with radial thickness $dr = 20$ AU.

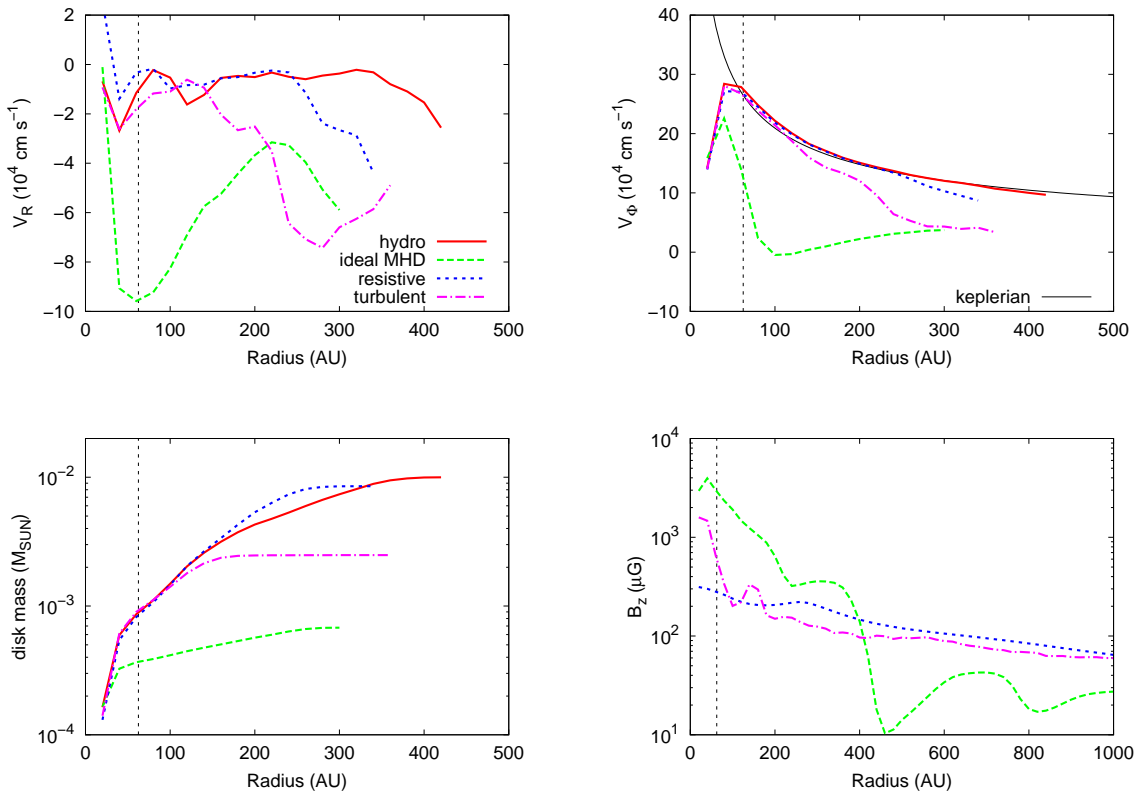


Figure 4.3: Radial profiles of the: (i) radial velocity v_R (top left), (ii) rotational velocity v_ϕ (top right); (iii) inner disk mass (bottom left); and (iv) vertical magnetic field B_z , for the four models of Figure 4.3 at time $t \approx 0.03$ Myr). The velocities were averaged inside cylinders centered in the protostar with height $h = 400$ AU and thickness $dr = 20$ AU. The magnetic field values were also averaged inside equatorial rings centered in the protostar. The standard deviation for the curves are not shown in order to make the visualization clearer, but they have typical values of: $2 - 4 \times 10^4$ cm s $^{-1}$ (for the radial velocity), $5 - 10 \times 10^4$ cm s $^{-1}$ (for the rotational velocity), and $100 \mu\text{G}$ (for the magnetic field). The vertical lines indicate the radius of the sink accretion zone.

For an ideal rotationally supported disk, the centrifugal barrier prevents the gas to

fall into the center. In this ideal scenario, the radial velocity should be null (at distances above the accretion sink zone). The top left panel of Figure 4.3 depicts the curves of the radial velocities for the four models. Above the central sink accretion zone ($R > 62.5$ AU), the hydrodynamical model (*hydro*) is the prototype of a rotationally supported disk, the radial velocity being smaller than the sound speed ($c_S = 2 \times 10^4$ cm s⁻¹) inside the formed disk. In the ideal MHD model, the effect of the magnetic flux braking partially destroys the centrifugal barrier and the radial (infall) velocity becomes very large, about three times the sound speed. The MHD model with anomalous resistivity instead, shows a very similar behavior to the hydrodynamical model due to the efficient removal of magnetic flux from the central regions. In the case of the turbulent model, although it shows a persisting non-null radial (infall) speed even above $R > 62.5$ AU this is much smaller than in the ideal MHD model, of the order of the sound speed where the disk forms (between the $R \approx 70$ AU and ≈ 150 AU).

The top right panel of Figure 4.3 compares the rotational velocities v_ϕ of the four models with the Keplerian profile $v_K = \sqrt{GM_*/R}$. All models show similar trends to the Keplerian curve (beyond the accreting zone), except the ideal MHD model. In this case, the strong suppression of the rotational velocity due to removal of angular momentum by the magnetic field to outside of the inner disk region is clearly seen, revealing a complete failure to form a rotationally supported disk. The turbulent MHD model, on the other hand, shows good agreement with the Keplerian curve at least inside the radius of ≈ 120 AU where the disk forms. Its rotation velocity profile is also very similar to the one of the MHD model with constant anomalous resistivity. Both models are able to reduce the magnetic braking effects by removing magnetic flux from the inner region and the resulting rotation curves of the formed disks are nearly Keplerian. In the resistive model, this is provided by the hyper-resistivity, while in the turbulent model is the turbulent reconnection that provides this diffusion.

The bottom right panel of Figure 4.3 compares the profiles of the vertical component of the magnetic field, B_z , in the equator of the four models of Figure 4.3. While in the ideal MHD model, the intensity and gradient of the magnetic field in the central regions are very large due to the inward advection of magnetic flux by the collapsing

material, in the anomalous resistive MHD model, the magnetic flux excess is completely removed from the central region resulting a smooth radial distribution of the field. In the turbulent model, the smaller intensity of the magnetic field in the inner region and smoother distribution along the radial direction compared to the ideal MHD case are clear evidences of the transport of magnetic flux to the outskirts of the disk due to turbulent reconnection diffusion (Santos-Lima et al. 2010; see also Chapter 3). We note however that, due to the complex structure which is still evolving, the standard deviation from the average value is very large in the turbulent model, with a typical value of $100 \mu\text{G}$ (and even larger for radii smaller than 100 AU) which accounts for the turbulent component of the field.

Finally, the bottom left panel of Figure 4.3 shows the mass of the formed disks in the four models, as a function of the radius. In the hydrodynamical and the MHD resistive models (*hydro* and *resistive*), the mass increases until $R \approx 250$ AU and ≈ 350 AU, respectively, and both have similar masses. The masses in the ideal MHD and the turbulent MHD models (*ideal MHD* and *turbulent*) increase up to $R \approx 150$ AU and ≈ 250 AU, respectively, and are smaller than those of the other models. Nonetheless the turbulent MHD disk has a total mass three times larger than that of the ideal MHD model.

4.4 Comparison with the work of Seifried et al.

The results just described in this Chapter (see also Santos-Lima et al. 2012) have been recently criticized in Seifried et al. (2012) (hereafter S+12) who performed AMR simulations of the collapse of a 100 solar mass turbulent cloud core permeated by a magnetic field (with 1.3 mG in the center and declining radially outwards with $R^{-0.75}$). They introduced sink particles in the cloud above a density threshold and detected the formation of several protostars around which Keplerian discs with typical sizes of up to 100 AU built up. Then, they examined a few mechanisms that could be potentially responsible for lowering the magnetic braking efficiency and thus, allowing for the formation of the Keplerian discs and concluded that none was necessary in their models, nor even reconnection diffusion.

They argued that the build up of the Keplerian disk was a consequence of the shear flow generated by the turbulent motions in the surroundings of the disk (which carry large amounts of angular momentum). The lack of coherent rotation in the turbulent velocity field would not allow the development of toroidal B components and toroidal Alfvén waves that could remove outward magnetic flux, in spite of the small values of the mass-to-flux ratio that they considered in their models (around $\mu \simeq 2 - 3$).

According to S+12, any effects like misaligned magnetic fields and angular momentum vectors, reconnection diffusion or any other non-ideal MHD effects seem not to be necessary. They conclude that “turbulence alone provides a natural and at the same time very simple mechanism to solve the magnetic braking catastrophe”.

S+12 conclusion above was based on the calculation of the mean mass-to-flux ratio within a sphere around the disk with a radius much larger than the disk (i.e., $r = 500$ AU). This ratio μ was computed taking the volume-weighted, mean magnetic field evaluated in this sphere, in combination with the sphere mass M , normalized by the critical value. They found that at these scales μ varies around a mean of 2 - 3 and is comparable with the initial value in the core (which is also the overall initial value in the massive cloud) and also to the MHD simulations without turbulence. However, they have also found that in some cases μ increases at smaller radius and eventually reaches values above 10 at radii ≤ 100 AU (i.e., nearly 5 times larger than the initial value). Therefore, S+12 detected flux transport within the Keplerian disk, at least in some of the disks formed. They did not consider that this could be due to transport arising from reconnection diffusion, because at these scales the velocity structures are already well ordered in their models. Thus S+12 concluded that numerical diffusion was the possible source of flux loss. In the following paragraphs, we put this conclusion to scrutiny and argue that the increase seen in S+12 is *real* and due to reconnection diffusion, in agreement with both theoretical expectation and the results described in the former sections of this thesis (see also Santos-Lima et al. 2013a).

4.4.1 Further calculations

Let us go back to our results reported in Section 4.3. Focusing on the formation of a Keplerian disk in a turbulent cloud core with a single sink, we clearly found flux loss during the process of the disk build up, as indicated from the analysis of Figure 4.3. We found that the ideal MHD model is unable to produce a rotationally supported disk due to the magnetic flux excess that accumulates in the central regions, while the MHD model with artificially enhanced resistivity produces a nearly-Keplerian disk with dimension, radial and rotational velocities, and mass similar to the pure hydrodynamical model, and the turbulent model also produces a nearly-Keplerian disk, but less massive and smaller ($r \simeq 100$ AU), in agreement with the observations.

Considering the three MHD disk formation models investigated in Figure 4.3 (i.e., an ideal collapsing cloud core with no turbulence, a highly resistive core with no turbulence, and an ideal turbulent core), Figure 4.4 shows the time evolution of the gas mass, the average magnetic flux and the mean mass-to-magnetic flux ratio, μ , which was calculated employing the same Equation (1) of S+12, for these three models. These quantities were computed within a sphere surrounding the central region for three different radii: a large one ($r=1000$ AU), which encompasses the large scale envelope where the disc is build up (similarly as in S+12), an intermediate ($r=500$ AU), and a small one ($r=100$ AU) which corresponds to the region where the disc is later formed.

Figure 4.4 shows that our turbulent model starts with an average $\mu \simeq 0.2$ and finishes with $\mu \simeq 0.5$ within $r = 1000$ AU (see Figure 4.4, bottom right panel). Therefore, as in S+12, this result suggests no significant variations in μ . Besides, these values reveal no significant changes with respect to the ideal MHD model either. However, the values of both, the turbulent and the ideal MHD model at this scale, are also comparable to those of the resistive model where we clearly know that *there is* large magnetic flux loss.

How to interpret these results then? When averaging over the whole sphere of radius $r = 1000$ AU around the disk/system, the real value of μ at the small disk scales ($r \leq 100$ AU) is hindered by the computed overall values in the envelope. Therefore, it is not enough to compute this average value to conclude that there is no flux loss in the process

The role of turbulent magnetic reconnection
in the formation of rotationally supported protostellar disks

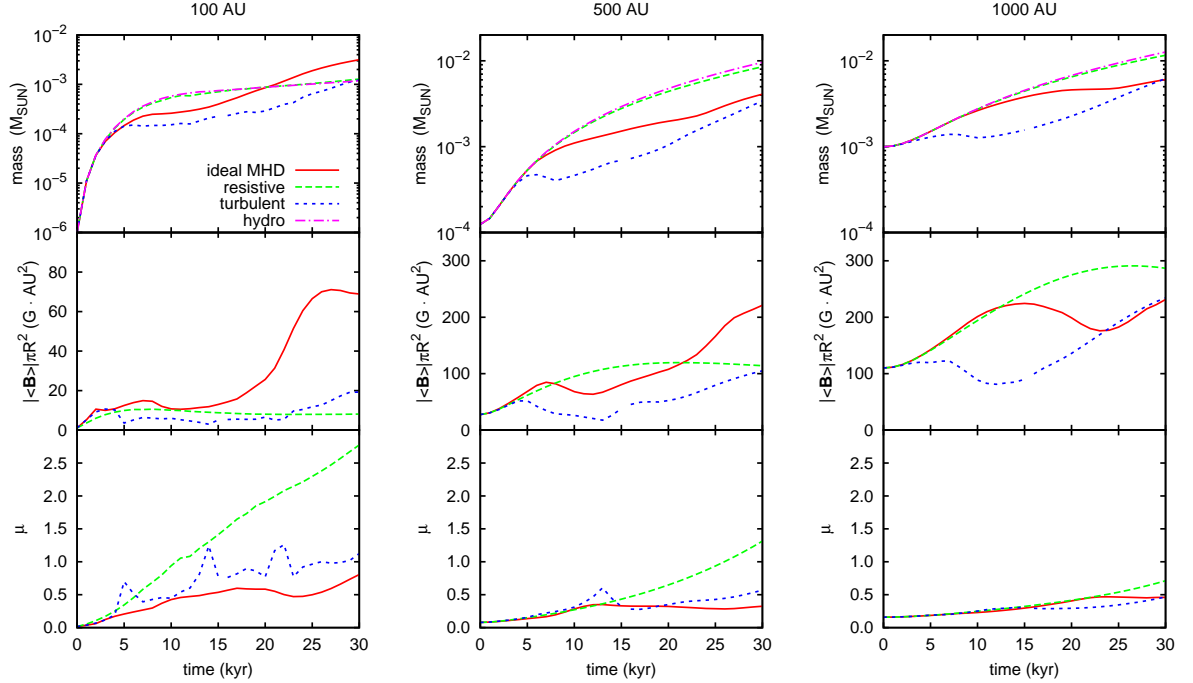


Figure 4.4: Disk formation in the rotating, magnetized cloud cores analysed by SGL12. Three cases are compared: an ideal MHD system, a resistive MHD system, and an ideal turbulent MHD system. Right row panels depict the time evolution of the total mass (gas + accreted gas onto the central sink) within a sphere of $r=1000$ AU (top panel), the magnetic flux (middle panel), and the mass-to-flux ratio normalized by the critical value averaged within $r=1000$ AU (bottom panel). Left row panels depict the same quantities for $r=100$ AU, i.e., the inner sphere that involves only the region where the disk is build up as time evolves. Middle row panels show the same quantities for the intermediate radius $r=500$ AU. We note that the little bumps seen on the magnetic flux and μ diagrams for $r=100$ AU are due to fluctuations of the turbulence whose injection scale (~ 1000 AU) is much larger than the disk scale.

of the disk build up.

As we decrease the radius of the sphere at which the average μ is computed, we clearly see that the magnetic flux of the turbulent model becomes comparable to that of the resistive model (see middle panels of Figure 4.4), specially at the scale of the Keplerian disk build up ($r \simeq 100$ AU) and, in consequence, there is an increase of μ with time in the turbulent model with respect to the ideal MHD model. The final value of $\mu \simeq 1$ within the disk region, therefore, nearly 5 times larger than the initial value in the whole cloud.

Thus, similarly to S+12, there is no significant variations of μ with time when considering its average over the whole sphere that contains both the turbulent envelope and the disk/sink. But, in the final state the resulting value of μ within the disk is larger than the initial value in the cloud. A similar trend is also found for the non-turbulent *resistive* MHD model, where the imposed explicit artificial resistivity leads to magnetic flux loss which in turn allows the build up of the Keplerian disk. These results clearly indicate that a nearly constant value of the average value of μ with time over the whole disk+envelope system is not a powerful diagnostic to conclude that there is no significant magnetic flux transport in protostellar disk formation (as suggested by S+12).

When examining the ideal MHD model, there is one important point to remark. μ , which should be expected to be constant with time in an isolated system, is also slightly growing within $r \simeq 100$ AU in this model.⁴ This is due to the adopted open boundaries in the system and to the volume averaging of the magnetic flux. To understand this behavior, we must inspect the time evolution of both the mass and the average magnetic flux in the system which are shown in the top and middle diagrams of Figure 4.4, respectively. Actually, in all models the total mass (envelope/disk plus accreted gas into the sink) increases with time due to a continuous mass aggregation to the system entering through the open boundaries. Also, there is a growing of the magnetic flux with time which is at least in part due to a continuous injection of magnetic field lines into the system through the open boundaries. Both effects, i.e., the increase in mass and magnetic flux could compensate each other and produce a nearly constant μ with time. However, there is

⁴At the larger radii this variation is hindered by averaging over larger scales as discussed.

another effect to be noticed. The magnetic flux in the middle diagrams of Figure 4.4 was not computed within a *comoving* (accreting) volume with the gas, but at a fixed sphere radius. If we had followed a fixed amount of accreting gas with time then, we would have obtained a constant number of magnetic field lines and therefore, a constant magnetic flux within this comoving volume in the ideal MHD case. This is in practice very difficult to compute from the simulations because of the complex geometry of the turbulent magnetic field lines. However, the key point here is not to obtain the exact value of the magnetic flux for the ideal MHD or the other models in a comoving volume, but to realize that at the scale of the disk build up (~ 100 AU), the magnetic flux of the turbulent MHD model, which is initially comparable to that of the ideal MHD model, decreased to a value similar to that of the resistive model at the time that the disk has formed ($\sim 25,000$ to $30,000$ yr), as indicated by the middle left panel of Figure 4.4. This is a clear indication of the removal of magnetic flux from the disk build up region to its surrounds in the turbulent model.

To help to better clarify the analyses above, we have also plotted in Figure 4.5 μ as a function of the mass for the three different regions considered in Figure 4.4. Each $\mu(M)$ in Figure 4.5 has been normalized by its initial value:

$$\mu_0(M) = \left[\frac{M}{B_0 \pi R_0^2(M)} \right] / \left[0.13 / \sqrt{G} \right], \quad (4.5)$$

where B_0 is the initial value of the magnetic field and $R_0(M)$ is the initial radius of the sphere containing the mass M). These diagrams provide a way to evaluate μ in comoving parcels with the gas. Inside 100 AU, Figure 4.5 shows that in the turbulent model $\mu(M)$ is larger than in the ideal MHD model and comparable to the resistive model at the largest masses. This indicates a smaller amount of magnetic flux in the turbulent and resistive models inside the disk region. As we go to the larger radii, μ becomes more and more comparable in the three models, in consistency with the results of Figure 4.4.

Therefore, based on the results above, we conclude that the flux loss (and the increase of μ within the disk) in our turbulent models is REAL and is due to the action of reconnection diffusion, as discussed in detail in SGL12 (see also Santos-Lima et al. 2010, Lazarian 2011, de Gouveia Dal Pino et al. 2012, Lazarian et al. 2012, Leão et al. 2012).

The role of turbulent magnetic reconnection
in the formation of rotationally supported protostellar disks

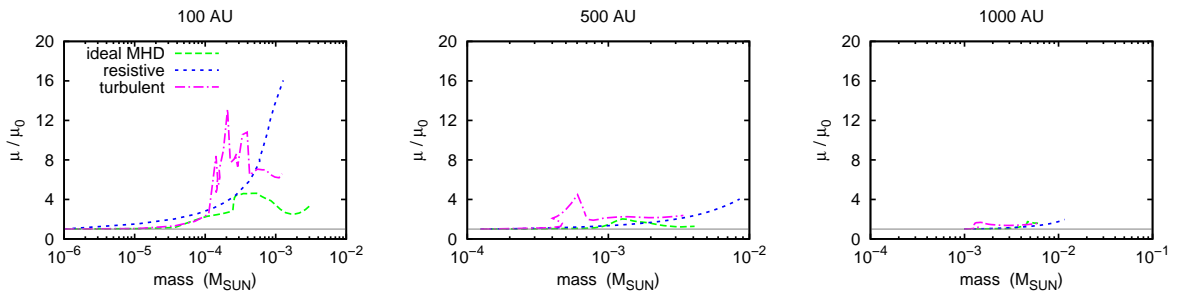


Figure 4.5: Mass-to-magnetic flux ratio μ , normalized by its initial value $\mu_0(M)$, plotted against the mass, for (i) $r = 100$ AU (left), (ii) $r = 500$ AU (middle), and (iii) $r = 1000$ AU (right). $\mu_0(M)$ is the value of μ for the initial mass M : $\mu_0(M) = \{M/[B_0\pi R_0^2(M)]\} / \{0.13/\sqrt{G}\}$, where B_0 is the initial value of the magnetic field and $R_0(M)$ is the initial radius of the sphere containing the mass M . The initial conditions are the same as in Figure 4.4.

We must note that the flux transport by TRD is faster where turbulence is stronger and faster. This is a fundamental prediction from LV99 fast reconnection theory which was numerically tested in Chapter 3 (see also Santos-Lima et al. 2010 and Section 4.5). In our turbulent simulations, while the disk is built up by the accretion of the turbulent gas in the envelope that surrounds the sink, reconnection diffusion is fast and causes magnetic flux loss at the same time that it allows the turbulent shear to build up a Keplerian profile in this *collapsing* material. This means that the material that formed the Keplerian disk out of the accretion of the turbulent envelope *has already lost magnetic flux* when it reaches its final state and that is why the final value of μ is much larger within the disk radius (≤ 100 AU). In other words, the mass-to-flux ratio increase that is detected in the final Keplerian disk is due to removal of magnetic flux from the highly turbulent envelope material while this material was accreting and building up the disk, i.e., *before* the final state. After the Keplerian disk is formed (in $r \leq 100$ AU), the operation of reconnection diffusion inside this region decreases because turbulent structures are smaller and slower there. Fortunately, in terms of magnetic breaking, high values of reconnection diffusion are no longer needed because the magnetic field flux excess has been already removed during the accreting phase and disk build up.

As a result, the argument given by S+12 that reconnection diffusion could not explain the increase of μ in their tests within the disk scales because the fluid is no longer turbulent there, is not correct.

We have also plotted the magnetic field B versus the density ρ in different times as in S+12 and found variations which are significant as we decrease the radius where the average of B and ρ are computed, in consistency with the results of Figures 4.4 and 4.5 and the discussion above. Figure 4.6 shows these plots for 30,000 yr within spheres of radii equal 100, 500, and 1000 AU. At the 1000 AU scale, both the ideal and the turbulent MHD models are comparable and follow approximately the $B \propto \rho^{0.5}$ trend, as in S+12. However, as we go to the smaller scales and specially to the 100 AU scale, the two models clearly loose this correlation, similar to the resistive model in all scales. This effect in the resistive model is clearly a natural consequence of the diffusion of the magnetic field from the inner denser regions to the less dense envelope regions. The turbulent model tends to follow the same trend: we note that for a given density, the magnetic field is smaller in the resistive model than in the turbulent model which in turn, has a smaller magnetic field than in the ideal model (see left panel in Figure 4.6), in consistence with the previous results. In the case of the MHD model, the nearly constant magnetic field with density at the 100 AU scale is due to the effect of the geometry. At this scale, the built up disk dominates, but the averaging is performed over the whole sphere that encompasses the region. This includes also the very light material above and below the disk which has magnetic field intensities as large as those of the high density material in the disk. (The same effect explains also the larger magnetic field intensities in the low density tail at the 500 and 1000 AU scale diagrams – middle and right panels, specially for the ideal MHD model.) The geometry at 100 AU obviously also affects the turbulent model in the same way, however we have found from the simulations that in this case the amount of low density gas carrying high intensity magnetic field below and above the disk is smaller than in the ideal MHD case. This is because in this case the loss of the $B - \rho$ correlation at the 100 AU scale is also affected by the diffusion of the magnetic field as in the resistive model, in consistence with the analyses of Figures 4.4 and 4.5.

Although the initial conditions above are different from those in S+12, the build up

The role of turbulent magnetic reconnection
in the formation of rotationally supported protostellar disks

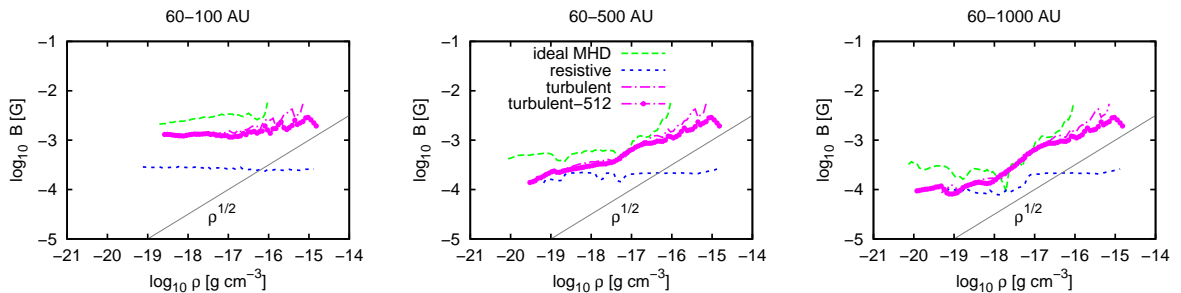


Figure 4.6: Mean magnetic intensity as a function of bins of density, calculated for the models analyzed in SGL12 at $t = 30$ kyr. The statistical analysis was taken inside spheres of radius of 100 AU (left), 500 AU (middle), and 1000 AU (right). Cells inside the sink zone (i.e., radius smaller than 60 AU) were excluded from this analysis. For comparison, we have also included the results for the turbulent model *turbulent-512* which was simulated with a resolution twice as large as the model *turbulent-256* presented in SGL12 (see also the Section 4.5).

of the Keplerian disks by the accretion of the turbulent envelope around the sinks is quite similar to our setup, so that we can perform at least qualitative comparisons between the results. In particular, both models consider initially supercritical cores⁵, i.e., initial μ larger than unity. We remember that in Figures 4.4 and 4.5 only the values of μ corresponding to the accreted gas mass were plotted in order to allow an easier track of the mass and magnetic flux evolution of the disk and envelope material. Nonetheless, the total μ in our models are larger than unity when including the sink, as in S+12 models. Another important parameter in this analysis of magnetic flux transport is the initial ratio between the thermal and magnetic pressure of the gas, β , which is also similar in both models ($\beta \sim 0.1$ in the center of the cloud in the S+12 models, while $\beta \sim 0.6$ in the whole core of our models). As a matter of fact, we chose an initial value of β smaller than unity in the core in order to show that reconnection diffusion could be able to remove the magnetic flux excess even from an initially magnetically dominated gas and thus solve the magnetic braking problem. In the case of the S+12 models, it is possible that due to their

⁵Supercritical cores have a mass-to-magnetic flux ratio which is larger than the critical value at which the magnetic field force balances the gravitational force. Subcritical cores, satisfy the opposite condition.

setup, sink regions far from the center of the cloud do not have this constraint on β . In this case, such regions might not require, in principle, removal of magnetic flux to allow the formation of a rotating disk and thus this initial condition would naturally avoid the magnetic braking problem. However, when ingredients such as rotation and turbulence are introduced, the accreting history in the different sinks within this cloud may change completely depending on the relative strength of the turbulence and magnetic field. In this sense, the formation of a Keplerian disk is very sensitive to the *local* conditions of the region around the sink (rather than the global initial conditions of the entire cloud) and therefore, the track of the detailed evolution of the magnetic flux around each sink region at the scale of the disk build up would be required in order to evaluate the real evolution of μ around each sink. Such an analysis is missing in S+12 work.

Based on the discussion in the previous paragraphs, it is natural to assume that the increase in μ detected in some of the S+12 models within the disk radius is *real*, as in our model. This increase could be simply an evidence that flux loss was very efficient during the disk build up in the turbulent envelope around this sink. The fact that they find a final μ in the disk which is much larger than the initial value in the cloud suggests that even if numerical resistivity is operating in the inner regions, a substantial magnetic flux excess was removed by turbulent reconnection diffusion when the disk was still forming from the accreting envelope.

Regarding the potential role of the numerical resistivity, we can make some quantitative estimates. The relevant scales for the reconnection diffusion to be operative are the turbulent scales, from the injection to the dissipation scale, i.e., within the inertial range scales of the turbulence which are larger than the numerical viscous scale. In our simulations with a resolution of 256^3 this scale is approximately of 8 cells. To evaluate the relative role of the numerical dissipation on the evolution of the magnetic flux at scales near the dissipation range, we can compare the advection and the diffusion terms of the magnetic field induction equation at a given scale. Considering the magnetic flux variations of our turbulent model within a 100 AU scale at $t = 30$ kyr, we find that the ratio between these two terms, which gives the magnetic Reynolds number, is $R_m = LV/\eta_{Num} \sim 75$, where $L = 100$ AU and we have considered the radial infall velocity as a characteristic velocity

of the system in this region, $V \approx 0.5$ km/s (see Figure 4.7). The approximate numerical resistivity for our employed resolution is $\eta_{Num} \sim 10^{18} \text{cm}^2 \text{s}^{-1}$. Therefore, although present, the numerical dissipation was not the dominant ingredient driving the change of the magnetic flux inside 100 AU in the SGL12 turbulent model. Examining the case of the S+12 models with increase in μ , considering that their magnetic Reynolds number must be even larger at 100 AU (i.e., the numerical viscosity is even smaller) due to their higher resolution, then in their case there should be no significant magnetic flux removal either at 100 AU due to numerical resistivity because of the same arguments above.

Since the S+12 authors do not provide the details of the magnetic field, turbulence, and density intensity within their Keplerian disks, it is hard to argue whether there was some significant flux loss or not in the other cases that they investigated where no increase was detected in the averaged μ over a large volume. It is also possible that some of these disks developed in regions where the local magnetic fields were not strong enough to cause magnetic braking and prevent the growth of the Keplerian disk. In these cases, even if flux loss by reconnection diffusion is occurring it would be undetectable.

4.5 Effects of numerical resolution on the turbulent model

In Chapter 3 (see also Santos-Lima et al. 2010), we have performed a rigorous numerical test of the role of turbulent magnetic reconnection diffusion on the transport of magnetic flux in diffuse cylindrical clouds, considering periodic boundaries and different numerical resolutions between 128^3 and 512^3 . We found very similar results for all resolutions which revealed the importance of the diffusion mechanism above to remove magnetic flux from the inner denser to the outer less dense regions of the clouds.

The turbulent reconnection diffusion theory is based on the fact that in the presence of turbulence, magnetic reconnection becomes fast and independent of the Ohmic resistivity (at the scales where the magnetic Reynolds number R_m is $\gtrsim 1$). This is because there is an increase of the number of magnetic reconnection events boosted by the turbulence, in

according with Lazarian & Vishniac (1999) reconnection theory (which has been already tested numerically in Kowal et al. 2009, 2012). However, a common distrust in turbulent numerical simulations is that turbulence could be enhancing the numerical resistivity itself. This is unjustified, as proved by the careful numerical analysis performed in Kowal et al. (2009, 2012) and in Santos-Lima et al. (2010). If this were true, the turbulent reconnection rate would reduce whenever the resolution of the numerical experiment were increased, which is not the case. Besides, the turbulent reconnection diffusion coefficient, which is of the order of the Richardson hydrodynamical diffusion coefficient ($\eta_{turb} \simeq LV_{turb}$ for super-Alfvénic turbulence; see e.g., Lazarian 2011), is much larger than the numerical (or the Ohmic) diffusion coefficient at scales larger than the dissipation scales of the turbulence, so that the effects of turbulent reconnection diffusion on the magnetic flux transport are dominant over numerical diffusion at the relevant scales of the system.

Nonetheless, in order to provide more quantitative tests about the reliability of our models of Figure 4.3, we also have run a similar turbulent model but with a resolution twice as large, which is named *turbulent-512*. We also included in this model an explicit small Ohmic resistivity ($\eta_{Ohm} = 10^{17} \text{cm}^2 \text{s}^{-1}$) in order to speed up the numerical computation (this is however, comparable to the numerical viscosity for this resolution and much smaller than the turbulent diffusion coefficient, so that it does not influence the physical results of the problem). The computational domain in this model is cubic with 4000 AU of side, and the sink accretion radius is half of the value for the models in SGL12 (≈ 30 AU). In Figure 4.7, we present the radial profiles for the mean values of the radial and azimuthal velocities, the disk (+ envelope) mass, and the mean vertical magnetic field at $t = 30$ kyr for this model, which are compared with those of the Figure 4.3 models.

We clearly see that the results of the turbulent models for both resolutions are similar. The mass of the disk inside this radius is also identical in both models and slightly smaller for larger radii (in the envelope) in the higher resolution model. The vertical magnetic field is also slightly smaller for radii larger than 500 AU, but similar to the lower resolution model in the inner regions (except for some fluctuations due to the different sizes of the sinks, but which are not relevant for the present analysis). The infall velocity is generally smaller in the higher resolution model. Nonetheless, in this model, a slightly thinner disk

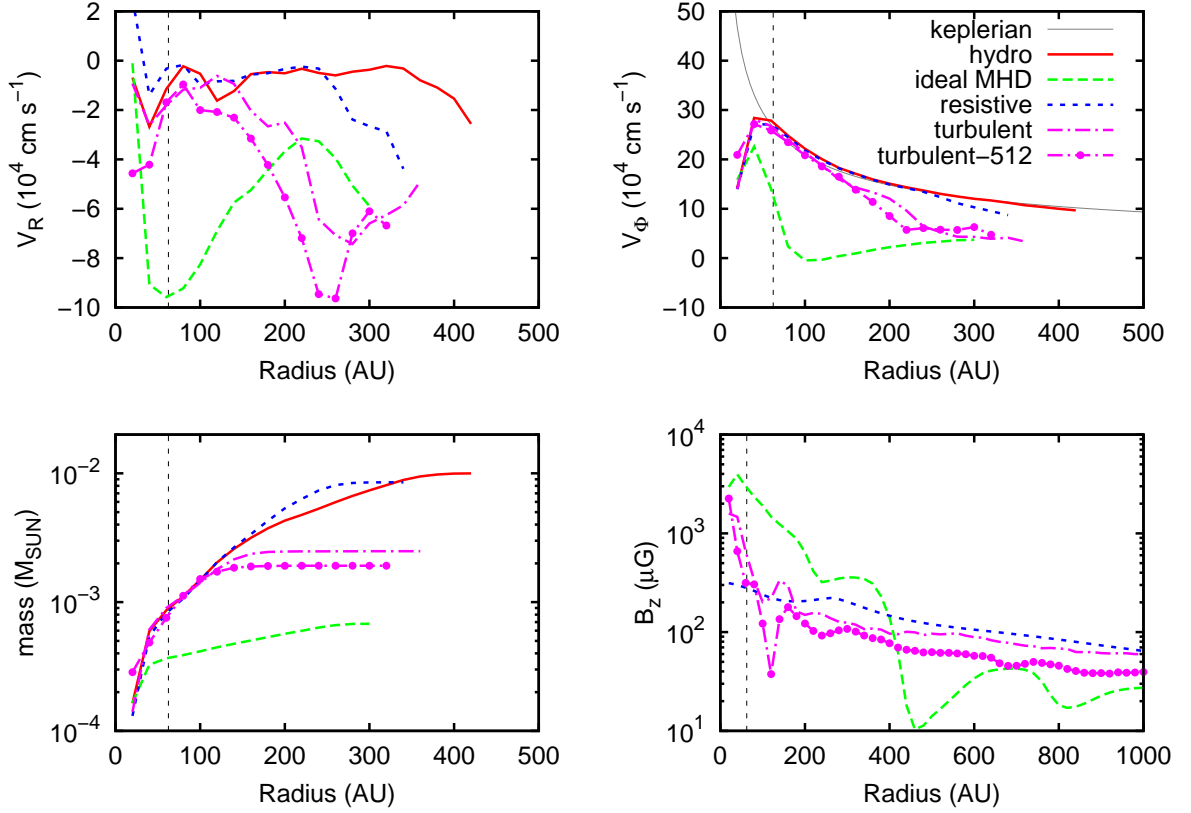


Figure 4.7: Comparison between the radial profiles of the high resolution turbulent model *turbulent-512* with the models presented in SGL12 (for which the resolution is 256^3). Top left: radial velocity v_R . Top right: rotational velocity v_ϕ . Bottom left: inner disk mass. Bottom right: vertical magnetic field B_z . The numerical data are taken at time $t \approx 0.03$ Myr. The velocities were averaged inside cylinders centered in the protostar with height $h = 400$ AU and thickness $dr = 20$ AU. The magnetic field values were also averaged inside equatorial rings centered in the protostar. The vertical lines indicate the radius of the sink accretion zone for all models except *turbulent-512* for which the the sink radius of the accretion zone is half of that value.

develops and if this velocity is averaged only over the higher density gas concentrated at smaller heights around the disk, then the infall velocity profile becomes very similar with that of the smaller resolution model. This also has to do with the fact that the turbulence in the model with lower resolution decays slightly faster, so that at the period of time considered in Figure 4.7, the model with lower resolution has reached already a more relaxed, non turbulent state. The similarity between the results of both turbulent models indicates that the lower resolution model of Figures 4.3 and 4.3 is reliable and therefore, can be employed in the analysis presented in this work.

4.6 Discussion

4.6.1 Our approach and alternative ideas

Shu et al. (2006) (and references therein) mentioned the possibility that the ambipolar diffusion can be substantially enhanced in circumstellar disks, but did not consider this as a viable solution. The subsequent paper of Shu et al. (2007) refers to the anomalous resistivity and sketches the picture of magnetic loops being reformed in the way of eventual removing magnetic flux. The latter process requires fast reconnection and we claim that in the presence of fast reconnection a more natural process associated with turbulence, i.e. magnetic reconnection diffusion can solve the problem.

Krasnopolsky et al. (2010) and Li et al. (2011) showed by means of 2D simulations that an effective magnetic resistivity $\eta \gtrsim 10^{19} \text{ cm}^2 \text{ s}^{-1}$ is needed for neutralizing the magnetic braking and enable the formation of a stable, rotationally supported, 100 AU-scale disk around a protostar. The origin of this enhanced resistivity is completely unclear and the value above is at least two to three orders of magnitude larger than the estimated ohmic diffusivity for these cores (e.g., Krasnopolsky et al. 2010). On the other hand, these same authors found that ambipolar diffusion, the mechanism often invoked to remove magnetic flux in star forming regions, is unable to provide such required levels of diffusivity (see also Li et al. 2011).

In this work, we have explored a different mechanism to remove the magnetic flux

excess from the central regions of a rotating magnetized collapsing core which is based on magnetic reconnection diffusion in a turbulent flow. Unlike the Ohmic resistivity enhancement, reconnection diffusion does not appeal to any hypothetical processes, but to the turbulence existing in the system and fast magnetic reconnection of turbulent magnetic fields. One of the consequences of fast reconnection is that, unlike resistivity, it conserves magnetic field helicity. This may be important for constructing self-consistent models of disks.

In order to compare our turbulent MHD model with other rotating disk formation models, we also performed 3D simulations of a pure hydrodynamical, an ideal MHD and a resistive MHD model with a hyper-resistivity coefficient $\eta \sim 10^{20} \text{ cm}^2 \text{ s}^{-1}$ (Figure 4.3). The essential features produced in these three models are in agreement with the 2D models of Krasnopolsky et al. (2010), i.e., the ideal MHD model is unable to produce a rotationally supported disk due to the magnetic flux excess that accumulates in the central regions, while the MHD model with artificially enhanced resistivity produces a nearly-Keplerian disk with dimension, mass, and radial and rotational velocities similar to the pure hydrodynamical model.

The rotating disk formed out of our turbulent MHD model exhibits rotation velocity and vertical magnetic field distributions along the radial direction which are similar to the resistive MHD model (Figure 4.3). These similarities indicate that the turbulent magnetic reconnection is in fact acting to remove the magnetic flux excess from the central regions, just like the ordinary enhanced resistivity does in the resistive model. We note, however, that the disk formed out of the turbulent model is slightly smaller and less massive than the one produced in the hyper-resistive model. In our tests the later has a diameter $\sim 250 \text{ AU}$, while the disk formed in the turbulent model has a diameter $\sim 120 \text{ AU}$ which is compatible with the observations.

The effective resistivity associated to the MHD turbulence in the turbulent model is approximately given by $\eta_{turb} \sim V_{turb} L_{inj}$, where V_{turb} is the turbulent rms velocity, and L_{inj} is the scale of injection of the turbulence ⁶. We have adjusted the values of L_{inj}

⁶We note however, that this value may be somewhat larger in the presence of the gravitational field (see L05, SX10)

and V_{turb} in the turbulent model employing turbulent dynamical times (L_{inj}/V_{turb}) large enough to ensure that the cloud would not be destroyed by the turbulence before forming the disk. We tested several values of η_{turb} and the one employed in the model presented in Figure 4.3 is of the same order of the magnetic diffusivity of the model with enhanced resistivity, i.e., $\eta_{turb} \sim V_{turb}L_{inj} \approx 10^{20} \text{ cm}^2 \text{ s}^{-1}$. Smaller values were insufficient to produce rotationally supported disks. Nonetheless, further systematic parametric study should be performed in the future.

As mentioned in Section 4.1, Machida et al. (2010, 2011) have also performed 3D MHD simulations of disk formation and obtained a rotationally supported disk solution when including only Ohmic resistivity (with a dependence on density and temperature obtained from the fitting of the resistivities computed in Nakano et al. 2002). However, they had to evolve the system much longer, about four times longer than in our turbulent simulation, in order to obtain a rotationally supported disk of 100-AU scale. In their simulations, a tiny rotationally supported disk forms in the beginning because the large Ohmic resistivity that is present in the very high density inner regions is able to dissipate the magnetic fields there. Later, this disk grows to larger scales due to the depletion of the infalling envelope. Their initial conditions with a more massive gas core (which has a central density nearly ten times larger than in our models) probably helped the formation of the rotating massive disk (which is almost two orders of magnitude more massive than in our turbulent model). The comparison of our results with theirs indicate that even though at late stages Ohmic, or more possibly ambipolar diffusion, can become dominant in the high density cold gas, the turbulent diffusion in the early stages of accretion is able to form a light and large rotationally supported disk very quickly, in only a few 10^4 yr.

Finally, we should remark that other mechanisms to remove or reduce the effects of the magnetic braking in the inner regions of protostellar cores have been also investigated in the literature recently. Hennebelle & Ciardi (2009) verified that the magnetic braking efficiency may decrease significantly when the rotation axis of the core is misaligned with the direction of the regular magnetic field. They claim that even for small angles of the order of $10 - 20^\circ$ there are significant differences with respect to the aligned case. Also, in a concomitant work to the present one, Krasnopolsky et al. (2011) have examined the

Hall effect on disk formation. They found that a Hall-induced magnetic torque can diffuse magnetic flux outward and generate a rotationally supported disk in the collapsing flow, even when the core is initially non-rotating, however the spun-up material remains too sub-Keplerian (Li et al., 2011).

Of course, in the near future, these mechanisms must be tested along with the just proposed turbulent magnetic reconnection and even with ambipolar diffusion, in order to assess the relative importance of each effect on disk formation and evolution. Nonetheless, since MHD turbulence is expected to be present in these magnetic cores (e.g., Ballesteros-Paredes & Mac Low 2002; Melioli et al. 2006; Leão et al. 2009; Santos-Lima et al. 2010, and references therein; see also Chapter 3), turbulent reconnection arises as a natural mechanism for removing magnetic flux excess and allowing the formation of these disks.

4.6.2 Present result and bigger picture

In this work we showed that the concept of reconnection diffusion successfully works in the formation of protostellar disks. Together with our earlier testing of magnetic field removal through reconnection diffusion from collapsing clouds this work supports a considerable change of the paradigm of star formation. Indeed, in the presence of reconnection diffusion, there is no necessity to appeal to ambipolar diffusion. The latter may still be important in low ionization, low turbulence environments, but, in any case, the domain of its applicability is seriously challenged.

The application of TRD concept to protostellar disk formation and, in a more general framework, to accretion disks in general, is natural as the disks are expected to be turbulent, enabling our appeal to LV99 model of fast reconnection. An important accepted source of turbulence in accretion disks is the well known magneto-rotational instability (MRI) (Chandrasekhar 1960, Balbus & Hawley 1991)⁷, but at earlier stages turbulence can be induced by the hydrodynamical motions associated with the disk formation. The application of the reconnection diffusion mechanism to already formed accretion disks will

⁷We note, however, that in the present study, we were in a highly magnetized disk regime, where the magneto-rotational instability is ineffective.

be investigated in detail elsewhere. It should be noted however that former studies of the injection of turbulence in accretion disks have shown that at this stage turbulence may be ineffective to magnetic flux diffusion outward (Rothstein & Lovelace, 2008).

4.7 Conclusions

Appealing to the LV99 model of fast magnetic reconnection and inspired by the successful demonstration of removal of magnetic field through turbulent reconnection diffusion from numerical models of molecular clouds in Santos-Lima et al. (2010; see also Chapter 3), we have performed numerical simulations and demonstrated that:

1. The concept of reconnection diffusion is applicable to the formation of protostellar disks with radius ~ 100 AU. The extension of this concept to accretion disks is foreseen.
2. In the gravitational field, reconnection diffusion mitigates magnetic breaking allowing the formation of protostellar disks.
3. The removal of magnetic field through turbulent reconnection diffusion is fast enough to explain observations without the necessity of appealing to enhanced fluid resistivity.

In Section 4.4.1, we have demonstrated that an analysis which is based solely on the computation of the average value of the mass-to-magnetic flux ratio (μ) over the whole envelope that surrounds a newly formed Keplerian disk, is not adequate to conclude that there is no significant magnetic flux loss in simulations of disk formation. This averaging masks significant real increases of μ in the inner regions where the disk is build up out of the turbulent envelope material that is accreting.

Actually, we have demonstrated that this is what happens on the build up of the Keplerian disk both, in our turbulent and resistive models, where magnetic flux loss has been detected. While the average μ computed over the large scale envelope/disk does remain nearly constant with time, the value of μ inside the formed Keplerian disk is 5 times larger than the initial value in the cloud core. Similarly, some of the disks formed in the turbulent S+12 models also revealed a value of μ 5 times larger within the disk than the initial cloud value, while the average μ over the whole envelope surrounding the

disk was nearly constant with time.

In our models we have found that the reduction of the magnetic braking efficiency during the building of the disk was due to the action of TRD; we suggest that the increase in μ found in S+12's disk is real and, as in our model, is caused by reconnection diffusion rather than numerical effects. While the shear flow generated by the turbulent motions in the surroundings of the disk (which carry large amounts of angular momentum) allows the build up of the rotationally supported disk, it also removes the magnetic flux excess due to fast turbulent reconnection, which otherwise may prevent the formation of the disk. During the build up of these disks out of turbulent envelopes around the sinks embedded in a massive cloud core (as in S+12 models), some envelopes may have strong local magnetic support (low local μ) which may prevent the Keplerian disk formation unless magnetic flux is removed, and some not. In the former case, we argue that reconnection diffusion is reducing the effect of the magnetic braking. In the latter case, even in the presence of magnetic flux loss induced by reconnection diffusion in the turbulent flow, its effect is marginal and therefore difficult to detect, because the magnetic field is dynamically unimportant.

Chapter 5

Turbulence and magnetic field amplification in collisionless MHD: an application to the ICM

As stressed in Chapter 2 (Section 2.5), the applicability of the standard collisional MHD model to the magnetized plasma of the intracluster medium (ICM) of galaxies can be questioned due to the collisionless nature of the gas. But a fully kinetic approach is not appropriate either for studying large scale phenomena, like the evolution of the turbulence and magnetic fields in these environments. Nevertheless, it is still possible to formulate a fluid approximation for collisionless plasmas, namely a collisionless-MHD description. In this case, we assume a double Maxwellian velocity distribution of the particles in both directions, parallel and perpendicular to the local magnetic field, which gives rise to an anisotropic thermal pressure. The forces arising from this anisotropy modify the standard Alfvén and magnetosonic waves and lead to the development of kinetic instabilities. Measurements of weakly collisional plasmas (like the solar wind and laboratory plasmas) as well as PIC simulations have demonstrated that these instabilities are able to saturate the pressure anisotropy.

In Section 2.5 we described the physical characteristics of the ICM. In this chapter, we present the results of our numerical studies of the evolution of the turbulence and the

magnetic fields in the ICM, employing a collisionless-MHD description with constraints on the pressure anisotropy as described in Chapter 2 (Section 2.5.6). In particular, we demonstrate that due to the saturation of the pressure anisotropy at the relevant large scales of the system, the turbulent dynamo amplification of seed magnetic fields and the overall magnetic field power spectrum evolution are similar to those found in a collisional MHD description of the ICM.

In Section 5.1 below we describe the numerical setup; in Section 5.2 we describe our numerical experiments and results; in Section 5.3 we discuss our results and the limitations of our model; in Section 5.4 we summarize our conclusions.

5.1 Numerical methods and setup

5.1.1 Thermal relaxation model

The simplest collisionless MHD description, the so called CGL-MHD model (see Section 2.5.4) neglects any heat conduction or radiative cooling mechanisms which is not a realistic assumption for the ICM. Combining Equations (2.44) we find that

$$w^* = \left[\left(\frac{B}{B_0} \right) A_0 + \frac{1}{2} \left(\frac{B}{B_0} \right)^{-2} \left(\frac{\rho}{\rho_0} \right)^2 \right] \frac{w_0^*}{(A_0 + 1/2)}, \quad (5.1)$$

where the subscripts 0 refer to the initial values in the Lagrangian fluid volume.

In the statistically steady state of the turbulence, the constant turbulent dissipation power leads to a secular increasing of the temperature of the gas which can lead to heat conduction and radiative losses. In order to deal with these effects in a simplified way, we employ a term \dot{w} that relaxes the specific internal energy $w^* = (p_\perp + p_\parallel/2)/\rho$ to the initial value w_0^* at a constant rate ν_{th} (see Brandenburg et al. 1995):

$$\dot{w} = -\nu_{th}(w^* - w_0^*)\rho. \quad (5.2)$$

Although simplistic, this approximation is useful for two reasons: (i) it allows the system to dissipate the turbulent power excess; and (ii) it helps to relax the local values of w^* which may become artificially high or low in the CGL-MHD formulation without constraints on the anisotropy growth (see discussion in Section 5.3.2).

5.1.2 Numerics

Equations (2.51) were evolved in a three-dimensional Cartesian box employing the code described in Appendix A.

The induction equation was integrated in its “uncurled” form. In the simulations presented in this research, no explicit diffusion term was used, except for model A2 (see Table 5.1) where an Ohmic dissipation term with a diffusivity $\eta \sim 10^{-4}$ (i.e., of the same order of the numerical diffusivity) was employed in order to prevent eventual negative values of the internal energy w . These can arise because the eventual diffusion of the magnetic energy, specially in the presence of very high spatial frequency instabilities, is not being explicitly taken into account in the energy equation. Nonetheless, numerical tests showed that the introduction of this diffusion term does not cause significant differences in the results for this model.

The pressure anisotropy relaxation was applied after each sub-time-step of the RK2 method, by transforming the conservative variables e and A in the primitive ones p_{\perp} and p_{\parallel} , calculating their relaxed values through Eq. (2.53) (using the same implicit method as in Meng et al. 2012b)¹ and then, reconstructing back the conservative variables.

A time-step constraint is considered due to the thermal relaxation (Eq. 5.2). At the end of each time-step, we estimate the minimum characteristic time of the thermal relaxation δt_{th} for the next time step as given by

$$\delta t_{th} = \min \left(\frac{w}{\dot{w}} \right), \quad (5.3)$$

where \dot{w} is the value calculated during the time-step and the minimum value is computed over the whole domain.

The next time-step is then taken as the minimum between $\epsilon_C \delta t_C$ and $\epsilon_{th} \delta t_{th}$ where, after performing several tests, we have chosen the following factors $\epsilon_C = 0.3$ and $\epsilon_{th} = 0.1$.

¹In the case $\nu_S = \infty$ (see Table 5.1), when the plasma is in the firehose (Eq. 2.47) or in the kinetic mirror instability (Eq. 2.49) regimes, this method simply replaces the pressures p_{\perp} and p_{\parallel} by the values given by the corresponding marginal stability criterium (while ensuring conservation of the internal energy $w = p_{\perp} + p_{\parallel}/2$).

5.1.3 Reference units

In the next sections, all the physical quantities are given in code units and can be easily converted in physical units using the reference physical quantities described below (see also Appendix A). We arbitrarily choose three representative quantities from which all the other ones can be derived: a length scale l_* (which is given by the computational box side), a density ρ_* (given by the initial ambient density of the system), and a velocity v_* (given by the initial sound speed in most of the models, but Model C3 for which the velocity unit is $0.3v_*$; see Table 5.1). For instance, with such representative quantities the physical time scale is given by the time in code units multiplied by l_*/v_* ; the physical energy density is obtained from the energy value in code units times $\rho_*v_*^2$, and so on. The magnetic field in code units is already divided by $\sqrt{4\pi}$, thus to obtain the magnetic field in physical units one has to multiply the value in code units by $v_*\sqrt{4\pi\rho_*}$.

5.1.4 Initial conditions and parametric choice

Table 5.1 lists the simulated models and their initial parameters.

In Table 5.1, $V_{A0} = B_0/\sqrt{\rho_0}$ is the Alfvén speed given by the initial intensity of the magnetic field directed along the x -axis. Initially, the gas pressure is isotropic for all the models with an isothermal sound speed $V_{S0} = \sqrt{p_0/\rho_0}$. The parameter β_0 is the initial ratio between the thermal pressure and the magnetic pressure ($\beta_0 = 2p_0/B_0^2$).

Turbulence was driven considering the same setup in all the models of Table 5.1. The injection scale is $l_{turb} = 0.4$. The power of injected turbulence ϵ_{turb} is kept constant and equal to unity. After $t = 1$ a fully turbulent flow develops in the system with an rms velocity v_{turb} close to unity. This implies a turbulent turn-over (or cascading) time $t_{turb} \approx 0.4$.

Models A, B and C in Table 5.1 are collisionless MHD models with initial moderate, strong, and very small (seed) magnetic fields, respectively. For models A and C the injected turbulence is initially super-Alfvénic, while for models B it is sub-Alfvénic.

Amhd, Bmhd, and Cmhd correspond to collisional MHD models, i.e., have no anisotropy in pressure. The set of equations describing these models is identical to those in Eq. (2.51),

but dropping the equation for the evolution of the anisotropy A and replacing the thermal energy by $w = 3p/2$ (which corresponds to a polytropic gas index $5/3$). Their corresponding dispersion relations are those from the usual collisional MHD approach (rather than Equations 2.45 and 2.46).

We have considered different values of the pressure anisotropy relaxation rate ν_S . Models with $\nu_S = \infty$ (i.e. with instantaneous relaxation rate) represent conditions for which the relaxation time $\sim \nu_S^{-1}$ is much shorter than the minimum time step δt_{min} that our numerical simulations are able to solve ($\delta t_{min} \sim 10^{-6}$). Previous studies (Gary et al. 1997, 1998, 2000) suggest that the rate ν_S should be of the order of a few percent of Ω_p , the proton gyrofrequency (see Section 5.3.2). If we consider typical physical conditions for the ICM, in order to convert the code units into physical units (see Section 5.1.3), we may take $l_* = 100$ kpc, $v_* = 10^8$ cm/s, and $\rho_* = 10^{-27}$ g/cm³ as characteristic values for the length scale, dynamical velocity and density of the ICM, respectively. This implies a characteristic time scale $t_* \sim 10^{15}$ s, while for models A in Table 5.1, the proton Larmor period is $\tau_{cp} \sim 10^3$ s. Using $\nu_S \sim 10^{-3}\tau_{cp}^{-1}$, we find $\nu_S^{-1} \sim 10^{-9}t_*$. Therefore, the models of Table 5.1 for which we assumed $\nu_S = \infty$ are very good approximations to the description of the direct effect of plasma instabilities at the large scale turbulent motions within the ICM. For comparison, we have also run models with no anisotropy relaxation, or $\nu_S = 0$, which thus behave like standard CGL-models.

We notice that the turbulence in the ICM is expected to be trans- or even subsonic, and the plasma beta is expected to be high ($\beta \sim 200$). Therefore, models A are possibly more representative of the typical conditions in the ICM.

In the following section we will start by describing the results for models A and B which have initial finite magnetic fields and therefore, reach a nearly steady state turbulent regime relatively rapidly after the injection of turbulence. Then, we will describe models C which start with seed magnetic fields and therefore, undergo a dynamo amplification of field due to the turbulence and take much longer to reach a nearly steady state.

Table 5.1: Parameters of the simulated models

Name	ν_S	ν_{th}	V_{A0}	V_{S0}	β_0	t_f	Resolution
A1	∞	5	0.3	1	200	5	512^3
A2	0	5	0.3	1	200	5	512^3
A3	10^1	5	0.3	1	200	5	512^3
A4	10^2	5	0.3	1	200	5	512^3
A5	10^3	5	0.3	1	200	5	512^3
A6	∞	0	0.3	1	200	5	512^3
A7	∞	0.5	0.3	1	200	5	512^3
A8	∞	50	0.3	1	200	5	512^3
Amhd	-	5	0.3	1	200	5	512^3
B1	∞	5	3.0	1	0.2	5	512^3
Bmhd	-	5	3.0	1	0.2	5	512^3
C1	∞	5	10^{-3}	1	2×10^6	40	256^3
C2	0	5	10^{-3}	1	2×10^6	40	256^3
C3	0	5	10^{-3}	0.3	2×10^5	40	256^3
C4	10^2	5	10^{-3}	1	2×10^6	40	256^3
Cmhd	-	5	10^{-3}	1	2×10^6	40	256^3

5.2 Results

Figure 5.1 depicts the density (left column) and the magnetic intensity (right column) distribution maps of the central slices for collisionless models with moderate initial magnetic fields A2 (top row), A1 (middle row), and Amhd (bottom row). All these models have $\beta_0 = 200$ and the same initial conditions, except for the anisotropy relaxation rate ν_S .

In the A2 model there is no constraint on the growth of the pressure anisotropy ($\nu_S = 0$). In this case, the kinetic instabilities that develop due to the anisotropic pressure are very strong at the smallest scales. This makes the density (and the magnetic field

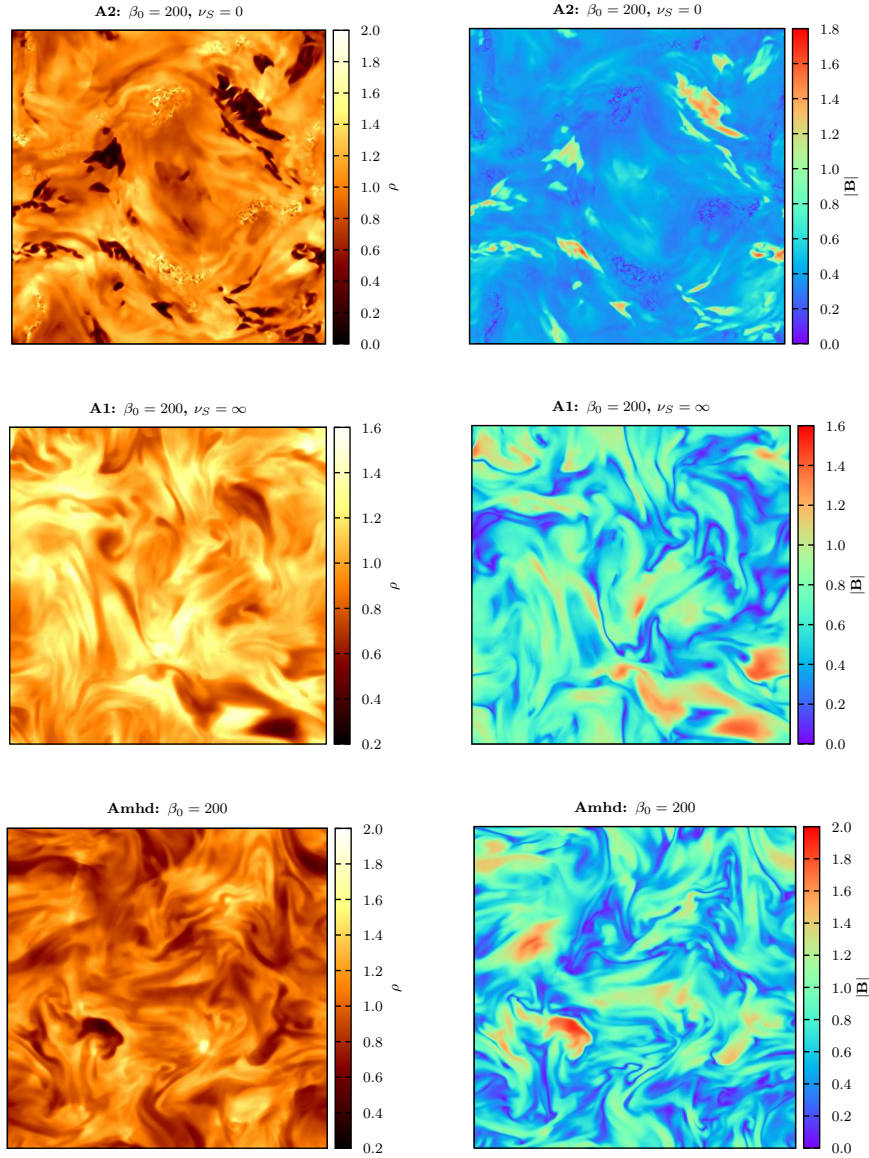


Figure 5.1: Central XY plane of the cubic domain showing the density (left column) and the magnetic intensity (right column) distributions for models of Table 5.1 with initial moderate magnetic field ($\beta_0 = 200$) and different values of the anisotropy relaxation rate ν_S , at $t = t_f$. Top row: model A2 (with $\nu_S = 0$, corresponding to the standard CGL model with no constraint on anisotropy growth); middle row: model A1 ($\nu_S = \infty$, corresponding to instantaneous anisotropy relaxation to the marginal stability condition); bottom row: model Amhd (collisional MHD with no anisotropy). The remaining initial conditions are all the same for the three models (see Table 5.1).

intensity) distribution in Figure 5.1 more “wrinkled” than in the standard (collisional) MHD case. On the other hand, in the A1 model where the isotropization of the thermal pressure due to the back reaction of the same kinetic instabilities is allowed to occur above a threshold, the developed density (and magnetic field intensity) structures are larger and more similar to those of the collisional MHD turbulent model Amhd.

In order to better quantify and understand the results evidenced by Figure 5.1 regarding the collisionless models without and with anisotropy growth constraints, in the next paragraphs of this Section we will present a statistical analysis of the physical variables of these turbulent models after they reach a steady state.

For models A1 to Bmhd in Table 5.1, the statistical analyses were performed by averaging data from snapshots taken every $\Delta t = 1$, from $t = 2$ until the final time step t_f indicated in Table 5.1. For the models with initial seed fields, C1 to Cmhd, the statistical analysis considered snapshots from $t = t_f - 10$ until t_f .

Averages and standard deviation of important physical quantities that will be discussed below are presented in Tables 5.2, 5.3, and 5.4.

Tables 5.2, 5.3, and 5.4 present one point statistics in space and time for the simulated models in Table 5.1. The averaged quantities are listed in the most left column. Each column presents the averages and below it the standard deviation, for each model. For the statistics, we considered snapshots spaced in time by $\Delta t = 1$, from $t = 2$ (Tables 5.2 and 5.3) or $t_f - 10$ (Table 5.4), until t_f (the t_f for each model is listed in Table 5.1). All the values are in code units and can be converted into physical units according to the prescription given in Section 5.1.3. The functional definitions (in terms of the code units) of the physical quantities listed are: $E_K = \rho u^2/2$, $E_M = B^2/2$, $E_I = (p_\perp + p_\parallel/2)$, $M_A = u\rho^{1/2}/B$, $M_S = u(3\rho)^{1/2}/(2p_\perp + p_\parallel)^{1/2}$. For the collisional MHD models, the following definitions are used: $E_I = 3p/2$, $M_S = u(\rho/p)^{1/2}$, $\beta_\parallel = \beta$.

5.2.1 The role of the anisotropy and instabilities

The injected turbulence produces shear and compression in the gas and in the magnetic field. Under the collisionless approximation, according to Eqs. (2.44) $A \propto B^3/\rho^2$, there-

fore, one should expect that compressions along the magnetic field lines, which keep B constant but make ρ to increase, cause a decrease of A , while compressions or shear perpendicular to the magnetic field lines, which make B to increase but keep either B/ρ or ρ constant, cause an increase of A . Therefore, even starting with $A = 1$, parcels of the gas with $A \neq 1$ will naturally develop. Inside these parcels, kinetic instabilities can be triggered which in turn will inhibit the growth of the anisotropy.

Figure 5.2 presents the distribution of the anisotropy A as a function of β_{\parallel} for the models with moderate initial magnetic field A1, A2, A3, A4, and A5 of Table 5.1. Model A2 ($\nu_S = 0$) has an A distribution that nearly follows a line with negative inclination in the log-log diagram. This is consistent with the derived A dependence in the CGL models given by $A \propto (\rho/B)\beta_{\parallel}^{-1}$ (when the initial conditions are homogeneous; see Eqs. 2.44). This model attains values of A spanning several orders of magnitude (from 10^{-2} to 10^3).

Model A1 ($\nu_S = \infty$), on the other hand, keeps A close to unity, varying by less than one order of magnitude.

Figure 5.2 also shows the distribution of A for the A3, A4, and A5 models which have bounded anisotropy with finite anisotropy relaxation rates ν_S (see Table 5.1). We see that in these cases, a fraction of the gas has A values out of the stable zone. The model with smaller anisotropy relaxation rate (model A3) obviously presents a larger fraction of gas inside the unstable zones. We also note that the higher the value of β_{\parallel} , the larger the linear growth rate of the instabilities and more gas is inside the unstable regions with $A < 1$. This is consistent with the CGL trend for which $A \propto \beta_{\parallel}^{-1}$.

Bottom right panel of Figure 5.2 shows the distribution of A versus β_{\parallel} for the model B1 with strong initial magnetic field (small $\beta_0 = 0.2$). We see that in this regime, B1 model has an A distribution inside the stable zone.

The spatial anisotropy distribution is illustrated in Figure 5.3 in two-dimensional maps that depict central slices of A in the XY-plane at the final time step for models A1, A2, A3, A4, A5 and B1. For the CGL model with moderate magnetic field ($\beta_0 = 200$), model A2, the A structures are thin and elongated. These small scale structures probably arise from the fast fluctuations driven by the kinetic instabilities (see Figure 5.2). For the model with strong magnetic field (small β_0), B1 model, the A structures are smoother. They are

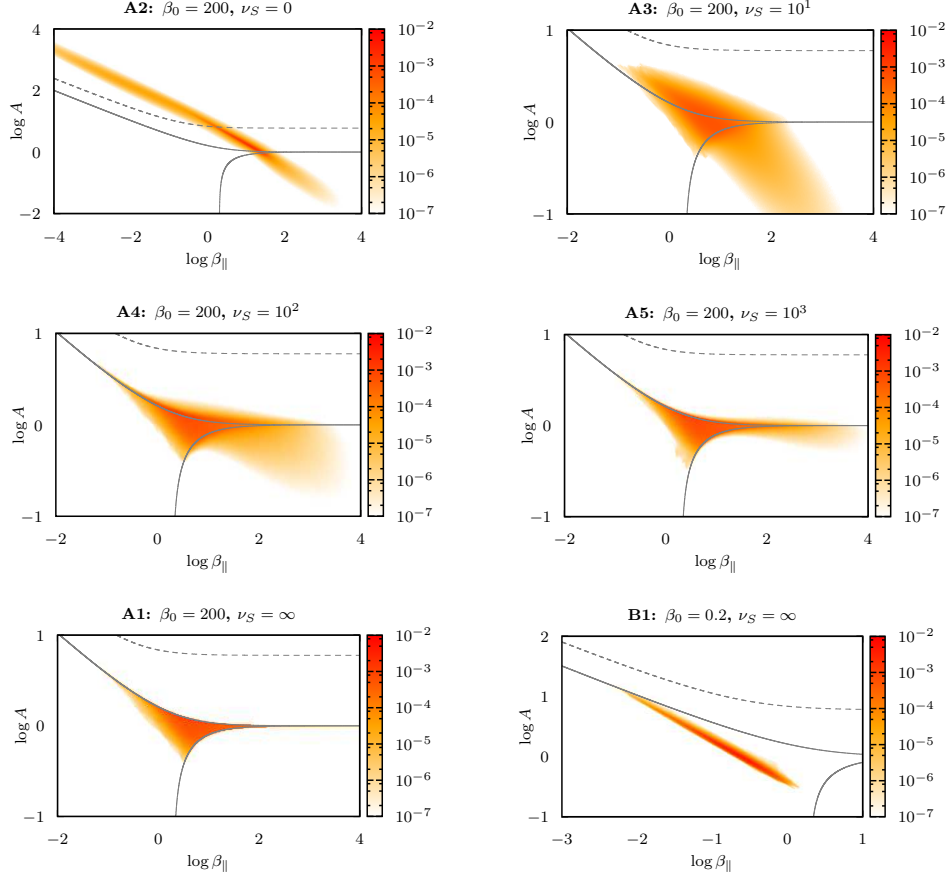


Figure 5.2: The panels show two-dimensional normalized histograms of $A = p_{\perp}/p_{\parallel}$ versus $\beta_{\parallel} = p_{\parallel}/(B^2/8\pi)$ for models starting with moderate magnetic fields (models A with $\beta_0 = 200$) and the model B1 with strong magnetic field (with $\beta_0 = 0.2$ (see Table 5.1)). The histograms were calculated considering snapshots every $\Delta t = 1$, from $t = 2$ until the final time step t_f indicated in Table 5.1 for each model. The continuous gray lines represent the thresholds for the linear firehose ($A = 1 - 2\beta_{\parallel}^{-1}$, lower curve) and mirror ($A = 1 + \beta_{\perp}^{-1}$, upper curve) instabilities, obtained from the kinetic theory. The dashed gray line corresponds to the linear mirror instability threshold obtained from the CGL-MHD approximation ($A/6 = 1 + \beta_{\perp}^{-1}$).

originated by small amplitude magnetic fluctuations (Alfvén waves) and also compression modes at the large scales. The map of model A1 also shows thin and elongated structures, but with lengths of the order of the turbulence scale.

As an illustration of the spatial distribution of the unstable gas, Figures 5.4 and 5.5

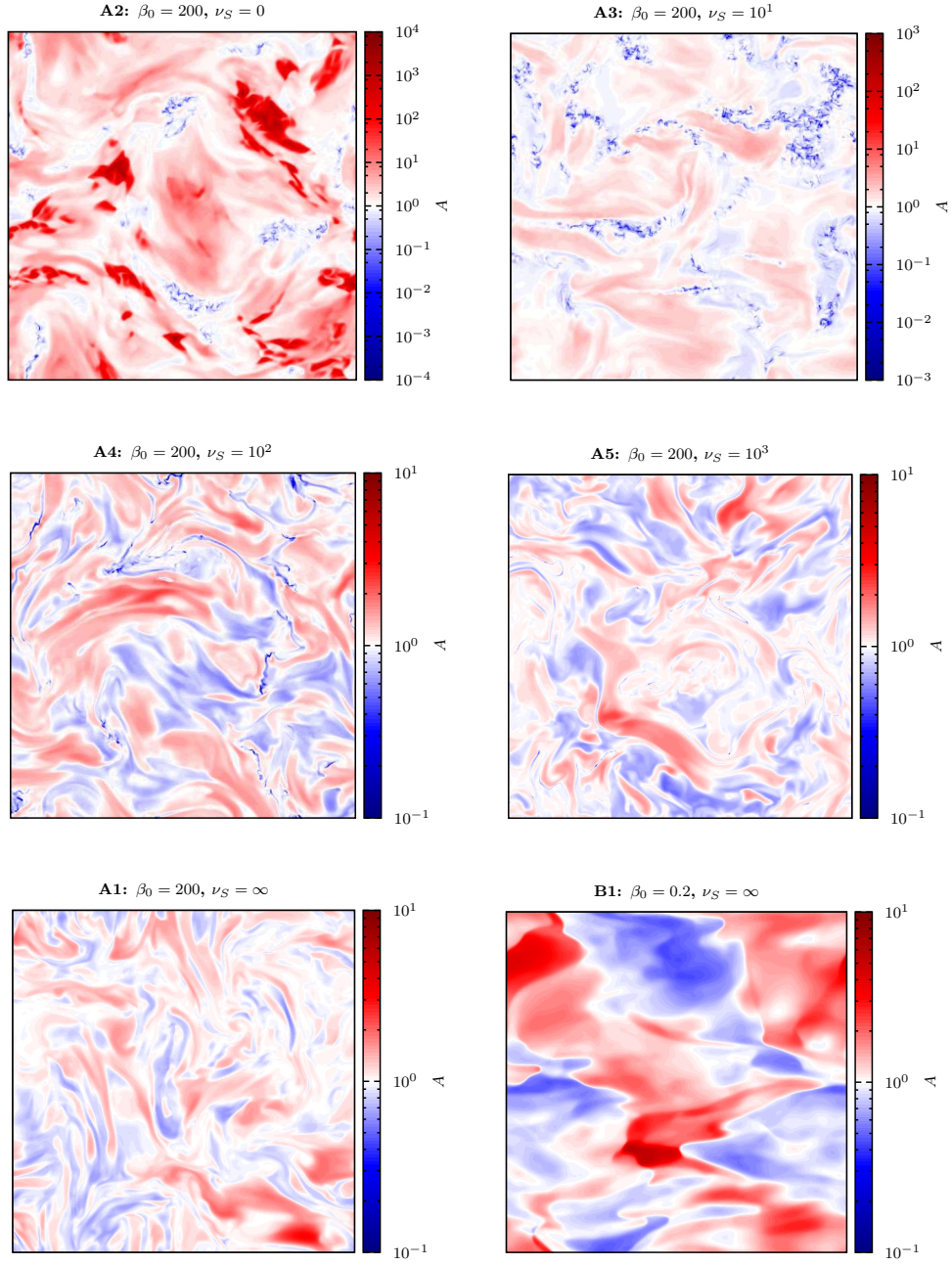


Figure 5.3: Maps of the anisotropy $A = p_{\perp}/p_{\parallel}$ distribution at the central slice in the XY plane at the the final time t_f for a few models A and B of Table 5.1.

depict maps of the maximum growth rate of both the firehose (left column) and the mirror (right column) instabilities given by Equations (2.50) for the models with moderate initial

magnetic field ($\beta_0 = 200$) and different anisotropy relaxation rates ν_S .² These maximum growth rates are normalized by the initial ion gyrofrequency Ω_{i0} and occur for modes with wavelengths of the order of the ion Larmor radius. First thing to note is that the mirror unstable regions have a larger volume filling factor than the firehose unstable regions for all the models in Figure 5.4. This is because the regions where the magnetic field is amplified have a large perpendicular pressure and this happens on most of the turbulent volume. Regions with an excess of parallel pressure arise when the magnetic intensity decays, like in regions with magnetic field reversals. The correspondence of the low intensity magnetic field with firehose unstable regions can be checked directly in model A2 by comparing the maps of Figures 5.4 and 5.1. The firehose unstable regions in models A2 and A3 in Figure 5.4 are small and fragmented; while in models A4 and A5 (in Figure 5.5), they are elongated (at lengths of the turbulent injection scale) and very thin (with thickness of the order of the dissipative scales) and are regions with magnetic field reversals and reconnection.

Also, from Figures 5.4 and 5.5 we see that most of the volume of models A2 and A3 are mirror unstable; for models A4 and A5, the mirror unstable regions are elongated but with much larger thickness than in the firehose unstable regions. We must remember that the criterium for the mirror unstable regions in Figures 5.4 and 5.5 is the kinetic one (Eq. 2.49) rather than the CGL-MHD criterium (Eq. 2.48) (see also Figure 5.2).

The spatial dimensions of the unstable regions in Figures 5.4 and 5.5 also reveal the maximum wavelength of the unstable modes which should develop inside the turbulent domain. In the models with finite anisotropy relaxation rate ν_S , the larger the value of ν_S the smaller the wavelength of the unstable modes. For realistic values of ν_S of the order of γ_{max} (the maximum frequency of the instabilities), there would have only unstable modes with wavelengths below the spatial dimensions we can resolve.

²We note that because Equations (2.50) have a validity limit as described in Section 2.5.5, we have corrected the growth rates to $\gamma_{max}/\Omega_i = 1$ when outside of the validity range. This limit is well justified by fully solutions of the dispersion relation obtained from the linearization of the Vlasov-Maxwell equation by Gary (1993; see Chapter 7).

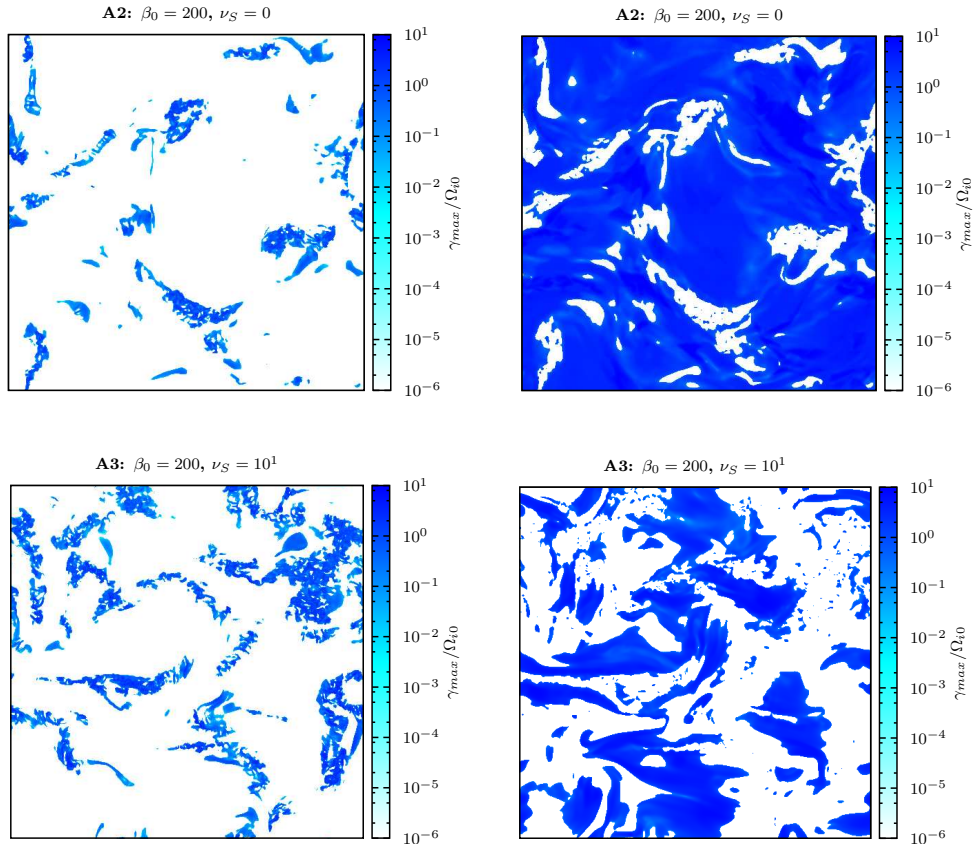


Figure 5.4: Central slice in the XY plane of the domain showing distributions of the maximum growth rate γ_{max} (normalized by the initial ion gyrofrequency Ω_{i0}) of the firehose (left column) and mirror (right column) instabilities for models A2 and A3 (with $\beta_0 = 200$ and different values of the anisotropy relaxation rate ν_S). The expressions for the maximum growth rates are given by Equations (2.50), with a maximum value given by $\gamma_{max}/\Omega_i = 1$. Data are taken at the the final time t_f for each model, indicated in Table 5.1.

5.2.2 Magnetic versus thermal stresses

The gyrotropic tensor gives the gas a larger (smaller) strength to resist against bending or stretching of the field lines if $A > 1$ ($A < 1$). This higher or smaller strength comes from the parallel anisotropic force

$$f_A = (p_{\parallel} - p_{\perp})\nabla_{\parallel} \ln B, \quad (5.4)$$

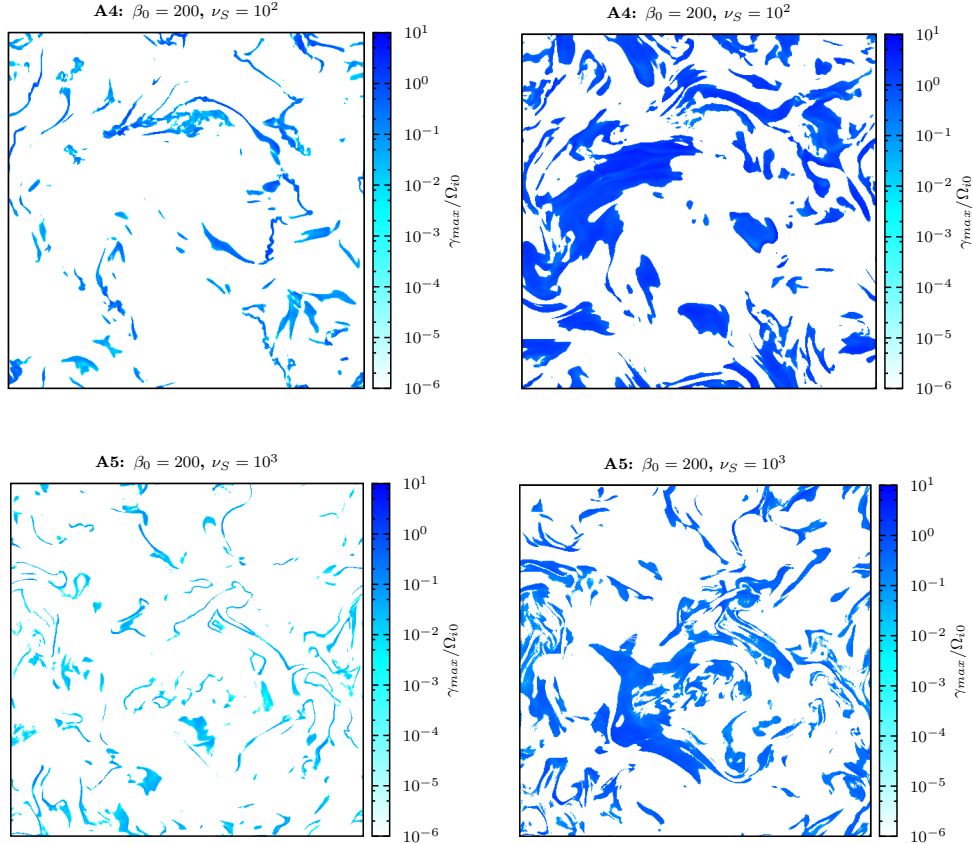


Figure 5.5: The same as Figure 5.4, for models A4 and A5.

where $\nabla_{\parallel} \equiv (\mathbf{B}/B) \cdot \nabla$. The relative strength between this anisotropic force and the usual Lorentz curvature force can be estimated from $\alpha \equiv (p_{\parallel} - p_{\perp})/(B^2/4\pi)$.

As a measure of the dynamical importance of the anisotropy, we calculated the average value of $|\alpha|$ for all the models of Table 5.1 and the values are listed in Tables 5.2, 5.3, and 5.4 for models A, B and C, respectively.

First let us consider the models with initial moderate magnetic field ($\beta_0 = 200$). For models A1, A6, A7, and A8 ($\nu_S = \infty$), the anisotropic force is non dominant: $\langle |\alpha| \rangle \approx 0.4$. For model A2 ($\nu_S = 0$), on the other hand, the anisotropic force is dominant, with $\langle |\alpha| \rangle \approx 5$. For the models A3, A4, and A5, with finite isotropization rate, the anisotropic force is comparable to the curvature force, being smaller for the higher isotropization rate: $\langle |\alpha| \rangle \approx 4$ for model A3 ($\nu_S = 10^1$) and $\langle |\alpha| \rangle \approx 1.5$ for model A5 ($\nu_S = 10^3$).

For model with strong magnetic field ($\beta_0 = 0.2$) B1, the anisotropic force is negligible

compared to the Lorentz curvature force: $\langle |\alpha| \rangle \approx 0.04$.

5.2.3 PDF of Density

Figure 5.6 shows the normalized histograms of $\log \rho$ for models A and B of Table 5.1 having different rates of anisotropy relaxation ν_S . The left panel shows models with initial moderate magnetic field intensity ($\beta_0 = 200$) and the right panel the model with initial strong magnetic field intensity ($\beta_0 = 0.2$). The corresponding collisional MHD models are also shown for comparison.

Examining the high β models in the top diagram, we note that all the models with anisotropy relaxation have similar distribution to the collisional model. Model A2, for which the anisotropy relaxation is null, has a much broader distribution, specially in the low density domain. This difference is due to the presence of strong mirror forces in the A2 model which expels the gas to outside of high magnetic field intensity regions, causing the formation of low density zones. Consistently, we can check this effect in the bi-histograms of density versus magnetic field intensity in Figure 5.7 for model A2 (the bi-histogram for the model Amhd is also shown for comparison). The lowest density points are correlated with high intensity magnetic fields for the model A2.

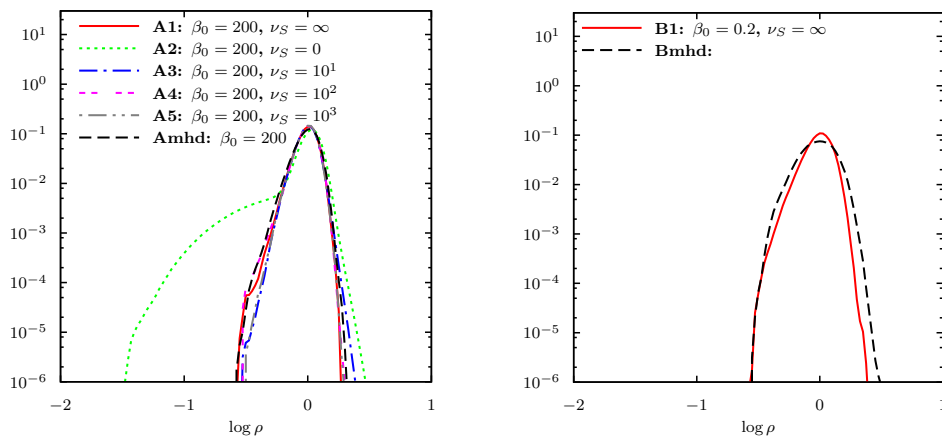


Figure 5.6: Normalized histogram of $\log \rho$. Left: models starting with $\beta_0 = 200$. Right: models starting with $\beta_0 = 0.2$. The histograms were calculated using one snapshot every $\Delta t = 1$, from $t = 2$ until the final time t_f indicated in Table 5.1.

The right panel of Figure 5.6 indicates that the low β , strong magnetic field model B1 has density distribution only slightly narrower than the collisional MHD model Bmhd, specially at the high density region. The slight difference with respect to the collisional model is possibly due to: (i) the sound speed parallel to the field lines is higher in the collisionless models: $c_{\parallel s} = \sqrt{3p_{\parallel}/\rho}$ for the collisionless model, while for the collisional model $c_s = \sqrt{5p/3\rho}$; and (ii) in the direction perpendicular to the magnetic field, the fast modes have characteristic speeds higher in the collisionless model: $c_f = \sqrt{B^2/4\pi\rho + 2p_{\perp}/\rho}$, while for the MHD model $c_f = \sqrt{B^2/4\pi\rho + 5p/3\rho}$. These larger speeds in the anisotropic model imply a larger resistance to compression and therefore, smaller density enhancements (at least for our transonic models).

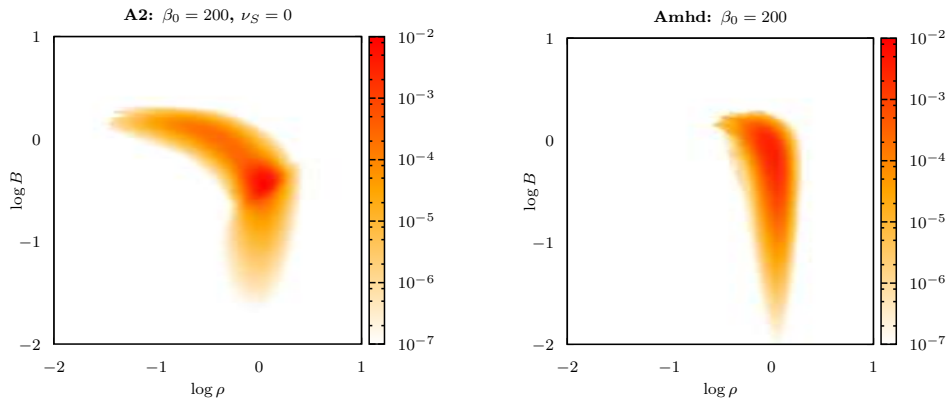


Figure 5.7: Two-dimensional normalized histograms of $\log \rho$ versus $\log B$. Left: collisionless model A2 with null anisotropy relaxation rate. Right: collisional MHD model Amhd. The histograms were calculated using snapshots every $\Delta t = 1$, from $t = 2$ until the final time t_f indicated in Table 5.1. See more details in Section 5.2.3.

5.2.4 The turbulence power spectra

Power spectrum is an important characteristic of turbulence. For MHD turbulence a substantial progress has been achieved recently as the Goldreich-Sridhar model has become acceptable. Recent numerical work has tried to resolve the controversies and confirmed the Kolmogorov $-5/3$ spectrum of Alfvénic turbulence predicted in the model (e.g. Beres-

nyak & Lazarian 2009a, 2010; Beresnyak 2011, 2012b). This spectrum corresponds to the Alfvénic mode of the compressible MHD turbulence (Cho & Lazarian 2002, 2003; Kowal & Lazarian 2010; Beresnyak & Lazarian 2013).

Our goal here is to determine the power spectrum of the turbulence in collisionless plasma in the presence of the feedback of plasma instabilities on scattering.

Figure 5.8 compares, for different models of Table 5.1, the power spectra of the velocity (top row), magnetic field (middle row) and density (bottom row). The models starting with moderate magnetic field and $\beta_0 = 200$ (A1, A2, A3, A4, A5, Amhd), for which the turbulence is super-Alfvénic, are in the left column, and the models starting with strong magnetic field and $\beta_0 = 0.2$ (B1, Bmhd), for which the turbulence is sub-Alfvénic are in the right column. Each power spectrum is multiplied by the factor $k^{5/3}$.

The velocity power spectrum $P_u(k)$ for the super-Alfvénic high beta collisional model Amhd (in the left top panel of Figure 5.8) is consistent with the Kolmogorov slope approximately in the interval $4 < k < 20$ and decays quickly for $k > 30$. The power spectra of the collisionless models A1, A3, A4, and A5 are similar, but show slightly less power in the interval $4 < k < 30$. In fact, in Table 5.2, we find that the average values of u^2 for these models are smaller than the model Amhd. Models A3 and A4 evidence more power at the smallest scales, already at the dissipation range. This is due to the acceleration of gas produced by the firehose instability (see Figure 5.2). Model A2 ($\nu_S = 0$), has a flatter velocity power spectrum than the collisional MHD model Amhd, and much more power at the smallest scales. This excess of power comes from the firehose and mirror instabilities and is consistent with the trend reported in the previous sections and also in Kowal et al. (2011a).

The sub-Alfvénic velocity power spectrum $P_u(k)$ of the collisional MHD model Bmhd (top right panel in Figure 5.8) has a narrower interval of wavenumbers consistent with the Kolmogorov slope. The power spectra $P_u(k)$ of the collisionless model B1 is almost identical which is in agreement with the small dynamical importance of the anisotropy forces compared to the magnetic forces (see Section 5.2.2).

The power spectrum related to the compressible component of the velocity field $P_C(k)$ is shown in Figure 5.9, where it is divided at each wavenumber by the total power of the

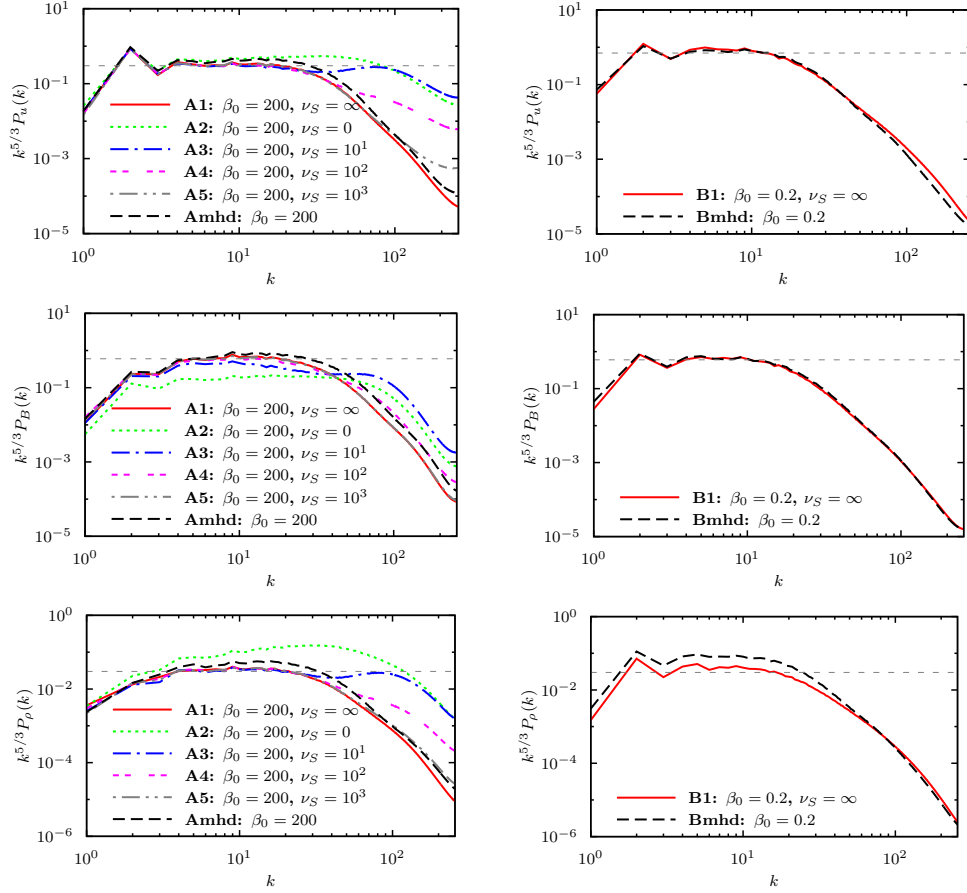


Figure 5.8: Power spectra of the velocity $P_u(k)$ (top row), magnetic field $P_B(k)$ (middle row), and density $P_\rho(k)$ (bottom row), multiplied by $k^{5/3}$. Left column: models A, with initial $\beta_0 = 200$. Right column: models B, with $\beta_0 = 0.2$. Each power spectrum was averaged in time considering snapshots every $\Delta t = 1$, from $t = 2$ to the final time step t_f indicated in Table 5.1.

velocity field. For the high beta models, the ratio $P_C(k)/P_u(k)$ for the collisionless models is similar to that of the collisional MHD model Amhd for almost every wavenumber k and is ≈ 0.15 . For the low beta model, however, the collisionless model has a ratio $P_C(k)/P_u(k)$ slightly higher than that of the collisional MHD model Bmhd for wavenumbers above $k \approx 10$. The fractional power in the compressible modes in the interval $2 < k < 20$ is smaller compared to the super-Alfvénic (high β) models, but at larger wavenumbers it becomes higher.

The anisotropy in the structure function of the velocity is shown in Figure 5.10. The

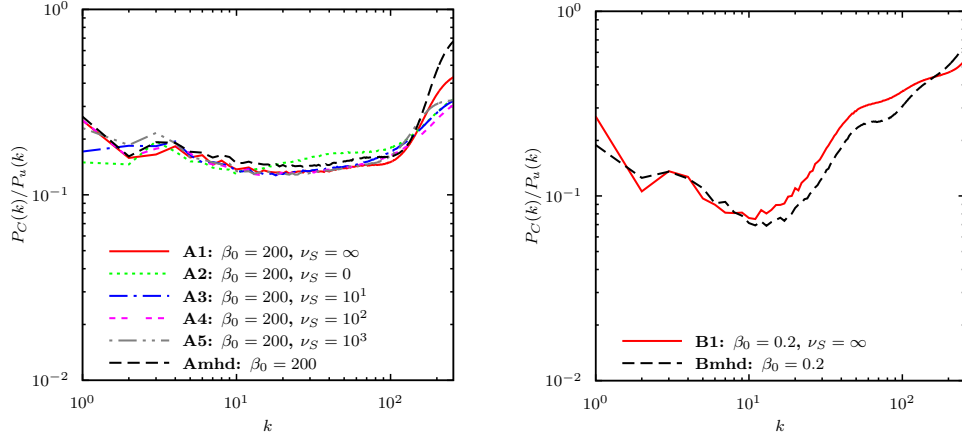


Figure 5.9: Ratio between the power spectrum of the compressible component $P_C(k)$ and the total velocity field $P_u(k)$, for the same models as in Figure 5.8 (see Table 5.1 and Section 5.2.4 for details).

structure function of the velocity S_2^u is defined by

$$S_2^u(l_{\parallel}, l_{\perp}) \equiv \langle |\mathbf{u}(\mathbf{r} + \mathbf{l}) - \mathbf{u}(\mathbf{r})|^2 \rangle, \quad (5.5)$$

where the displacement vector \mathbf{l} has the parallel and perpendicular components (relative to the local mean magnetic field) l_{\parallel} and l_{\perp} , respectively. The local mean magnetic field is defined by $(\mathbf{B}(\mathbf{r} + \mathbf{l}) + \mathbf{B}(\mathbf{r}))/2$ (like in Zrake & MacFadyen 2012). The GS95 theory predicts an anisotropy scale dependence of the velocity structures (eddies) of the form $l_{\parallel} \propto l_{\perp}^{2/3}$. The axis in Figure 5.10 are in cell units. The collisional MHD model Amhd is consistent with the GS95 scaling for the interval $10\Delta < l_{\perp} < 40\Delta$, where Δ is one cell unit in the computational grid. For the sub-Alfvénic model Bmhd, however, this scaling is less clear, although the anisotropy is clearly seen.

The collisionless models A1, A4, and A5 in Figure 5.10 evidence anisotropy in the velocity structures which is identical to that of the collisional MHD model Amhd. Models A2 and A3, on the other hand, have more isotropized structures at small values of l . This effect is due to the action of the instabilities and is also observed in the high beta models in Kowal et al. (2011a) for both the firehose and mirror instability regimes.

The magnetic field power spectra $P_B(k)$ of the collisional MHD models Amhd and Bmhd (middle row of Figure 5.8) show a power law consistent with the Kolmogorov slope

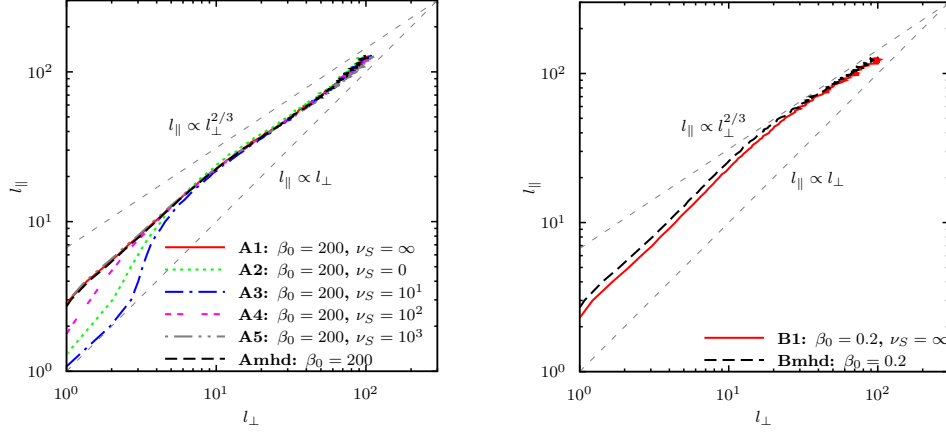


Figure 5.10: l_{\perp} vs l_{\parallel} obtained from the structure function of the velocity field (Eq. 5.5). The axes are scaled in cell units.

at the same intervals of the velocity power spectra. As in the velocity power spectrum, in the high beta, super-Alfvénic cases, the collisionless models A1, A3, A4, and A5 have similar $P_B(k)$ to the collisional model Amhd (although with slightly less power). Model A2 has a $P_B(k)$ much flatter than that of Amhd and has less power (by a factor of two) at the inertial range interval. In the smallest scales ($k > 50$), however, its power is above that of the Amhd model (this is also observed for model A3). As in the velocity power spectrum, these small-scale structures are due to the instabilities which are present in this model.

For the sub-Alfvénic, low beta models (B), the magnetic field power spectrum $P_B(k)$ of the collisionless model is again similar to the collisional MHD model Bmhd.

Figure 5.11 compares $P_B(k)$ and $P_u(k)$ for our models. For the super-Alfvénic, high beta models (A) which are in steady state, the magnetic field power spectrum is in super equipartition with the velocity power spectrum for $k > 3$ for all models, but the A2 model which has $P_B(k) < P_u(k)$ for all wavenumbers. Models A3, A4, and A5 show $P_B(k)/P_u(k)$ decreasing values for larger wavenumbers, being this effect more pronounced in model A3 which has smaller anisotropy relaxation rate. The sub-Alfvénic, low beta collisionless model B1 has the ratio $P_B(k)/P_u(k)$ slightly smaller than unity for all wavenumbers and slightly smaller than the collisional Bmhd model at large k values.

The anisotropy in the structure function for the magnetic field shows similar trend

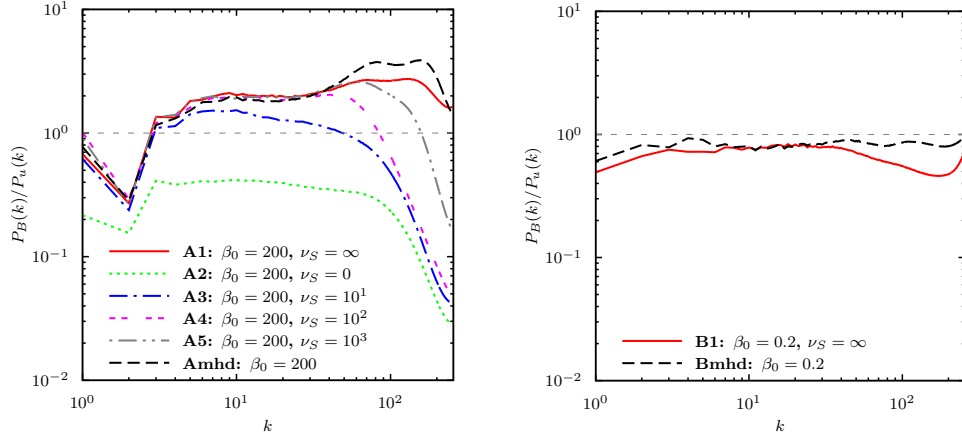


Figure 5.11: Ratio between the power spectrum of the magnetic field $P_B(k)$ and the velocity field $P_u(k)$ for the same models as in Figure 5.8 (see Table 5.1 and Section 5.2.4 for details).

to the velocity field in all models and is not presented here. Likewise, the density power spectra $P_\rho(k)$ for the super-Alfvénic, high beta models (bottom row in Figure 5.8) reveal the same trend of the velocity power spectra. For the sub-Alfvénic model, however, the smaller power in the larger scales compared to the collisional MHD model Bmhd is clearly evident, specially in the inertial range. This is consistent with the discussion following the presentation of the density distribution (Section 5.2.3), which evidenced that the collisionless models resist more to compression than the collisional model (see also Figure 5.9).

5.2.5 Turbulent amplification of seed magnetic fields

Figure 5.12 shows the magnetic energy evolution of the models having initially very weak magnetic (seed) field, models C1, C2, C3, C4, and Cmhd of Table 5.1. The kinetic energy of the models is not shown, but their values are approximately constant in time (after $t \approx 1$) and their average values (taken during the last $\Delta t = 10$ for each model) $\langle E_K \rangle$ are shown in Table 5.4. For each of these models, Figure 5.13 shows the power spectrum of the magnetic field, from $t = 2$ until the final time, for every $\Delta t = 2$ (dashed lines). The final magnetic field power spectrum is the continuous line. Also for comparison, it is

plotted the final velocity power spectrum (dash-dotted line).

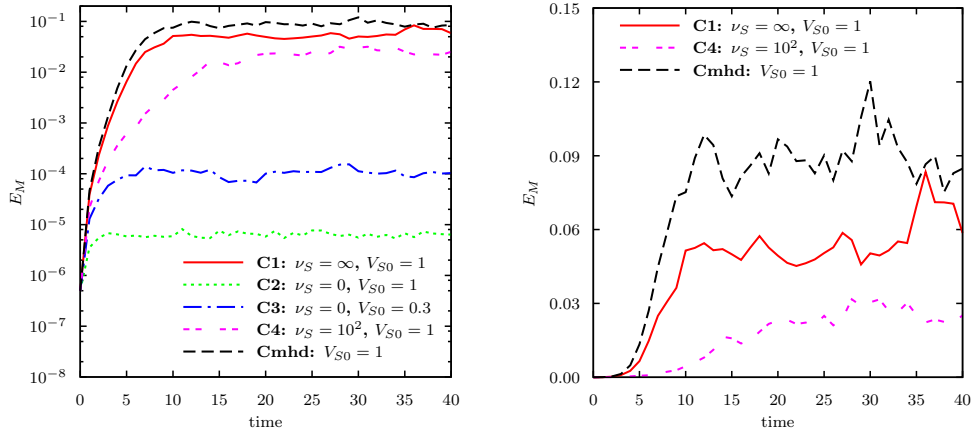


Figure 5.12: Time evolution of the magnetic energy $E_M = B^2/2$ for the models starting with a weak (seed) magnetic field, models C1, C2, C3, C4, and Cmhd, from Table 5.1. The left and right panels differ only in the scale of E_M . This is shown in a log scale in the top panel and in a linear scale in the bottom panel. The curves corresponding to models C2 and C3 are not visible in the right panel.

The collisional MHD model Cmhd shows an initial exponential growth of the magnetic energy until $t \approx 5$. In this interval, the average magnetic energy grows from $E_M = 5 \times 10^{-7}$ to $E_M \sim 10^{-2}$. After this, a slower (linear) growth rate of the magnetic energy takes place until $t \approx 10$, as can be seen in the right panel of Figure 5.12. This is consistent with studies of turbulent dynamo amplification of magnetic fields in collisional plasmas (see, e.g., Cho et al. 2009). At the final times, the magnetic energy achieves the value $E_M \approx 9.0 \times 10^{-2}$ which is approximately four times smaller than the average kinetic energy $E_K \approx 0.38$ (see Table 5.4). The bottom panel of Figure 5.13 shows that the final magnetic field power spectrum is peaked at $k \approx 20$ above which it is in super-equipartition with the velocity power spectrum.

The collisionless model C1 with instantaneous relaxation of the pressure anisotropy ($\nu_S = \infty$), has a turbulent amplification of the magnetic energy very similar to that of the collisional MHD model Cmhd (Figure 5.12). The initial exponential growth rates are nearly indistinguishable between the two models, but in the linear stage the growth rate

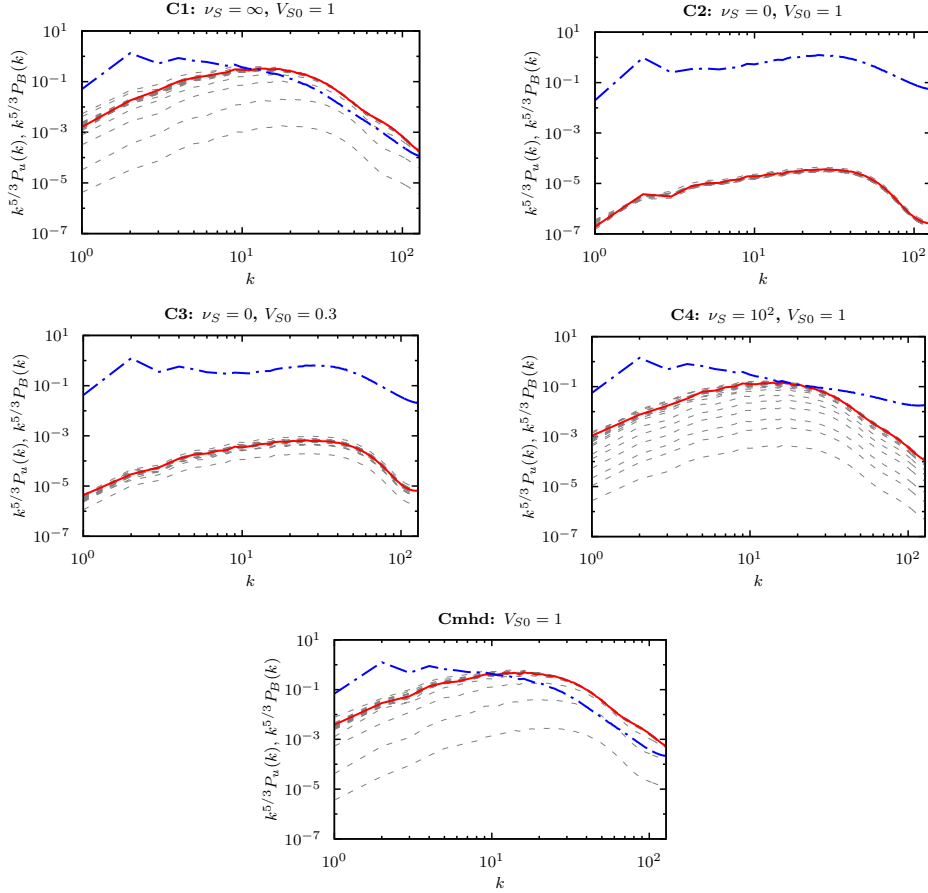


Figure 5.13: Magnetic field power spectrum multiplied by $k^{5/3}$ for the same models presented in Figure 5.12, from $t = 2$ at every $\Delta t = 2$ (dashed lines) until the final time indicated in Table 5.1 (solid lines). The velocity field power spectrum multiplied by $k^{5/3}$ at the final time is also depicted for comparison (dash-dotted line).

is slightly smaller in model C1 (see right panel of Figure 5.12) and also the final value of saturation of the magnetic energy: $E_M \approx 6.2 \times 10^{-2}$ (see Table 5.4). During the initial exponential growth of the magnetic energy, when the plasma still has high values of β , the pressure anisotropy relaxation due to the kinetic instabilities keeps the plasma mostly isotropic, explaining the similar behavior to the collisional MHD model. When β starts to decrease, the anisotropy A can increase (or decrease) spanning a range of A values in the stable zone (as in Figure 5.2 for model A1). Then, the anisotropic forces can start to have dynamical importance. At the final times, the value of $\langle |p_{\parallel} - p_{\perp}| / (B^2/4\pi) \rangle$, which

measures the dynamical importance of the anisotropic forces compared to the Lorentz curvature force (see Section 5.2.2) is ≈ 0.5 (Table 5.4). The magnetic field power spectrum has an identical shape to the model Cmhd, specially in the final time step.

The turbulent dynamo is also tested for a model with a finite anisotropy relaxation rate, model C4, which has $\nu_S = 10^2$. The growth rate of the magnetic energy (in the exponential and linear phases) is smaller compared to models Cmhd and C1 (left and right panels in Figure 5.12). In this case, the anisotropy $A > 1$ develops moderately during the magnetic energy amplification and gives the mirror forces some dynamical importance to change the usual collisional MHD dynamics. The value of the magnetic energy at the final time of the simulation is approximately one third of the value for the collisional MHD model. The final magnetic power spectrum has a shape similar to the collisional MHD model Cmhd, but below the equipartition with the velocity field power spectrum which has more power at the smallest scales due to the presence of the instabilities (Figure 5.13).

Model C2, a standard CGL model with no constraints on the growth of pressure anisotropy ($\nu_S = 0$) shows no evidence of a turbulent dynamo amplification of its magnetic energy which saturates at very low values already at $t \approx 5$ (Figure 5.12), when $E_M \approx 6.2 \times 10^{-6}$, while the kinetic energy is $E_K \approx 0.32$ (see Table 5.4). The reason is that the anisotropy A increases at the same time that the magnetic field is increased ($A \propto B^3/\rho^2$ in the CGL closure), giving rise to strong mirror forces along the field lines which increase their resistance against bending or stretching. For this model, $\langle |p_{\parallel} - p_{\perp}| / (B^2/4\pi) \rangle \sim 10^5$, that is, the anisotropic forces dominate over the Lorentz force. The magnetic field power spectrum (top right panel in Figure 5.13) is similar in shape (but not in intensity) to the Cmhd model, being peaked at $k \approx 40$.

The saturated value of the magnetic energy for models without anisotropy relaxation is, nevertheless, sensitive to the initial plasma β . Model C3 is similar to model C2, but starts with a lower sound speed ($V_{S0} = 0.3$) which makes β ten times smaller (see Table 5.1). Turbulence is supersonic in this case, rather than transonic. The magnetic energy evolution is similar to that of the model C2, but the magnetic energy saturates with a value about two orders of magnitude larger, although the anisotropic forces are

still dominant, with $\langle |p_{\parallel} - p_{\perp}| / (B^2/4\pi) \rangle \sim 10^4$ (see Table 5.4).

Table 5.2: Space and time averages (upper lines) and standard deviations (lower lines) for the models A which have moderate initial magnetic fields ($\beta_0 = 200$).

Quantity	A1	A2	A3	A4	A5	A6	A7	A8	Ahhhd
	$(\nu_S = \infty,$ $\nu_{th} = 5)$	$(\nu_S = 0,$ $\nu_{th} = 5)$	$(\nu_S = 10^1,$ $\nu_{th} = 5)$	$(\nu_S = 10^2,$ $\nu_{th} = 5)$	$(\nu_S = 10^3,$ $\nu_{th} = 5)$	$(\nu_S = \infty,$ $\nu_{th} = 0)$	$(\nu_S = \infty,$ $\nu_{th} = 0.5)$	$(\nu_S = \infty,$ $\nu_{th} = 50)$	$(\nu_{th} = 5)$
$\langle \log \rho \rangle$	-6.3×10^{-3} 7.5×10^{-2}	-2.4×10^{-2} 0.17	-6.0×10^{-3} 7.3×10^{-2}	-6.3×10^{-3} 7.5×10^{-2}	-5.9×10^{-3} 7.3×10^{-2}	-1.6×10^{-3} 3.8×10^{-2}	-2.6×10^{-3} 4.8×10^{-2}	-1.0×10^{-2} 9.5×10^{-2}	-8.0×10^{-3} 8.5×10^{-2}
$\langle u^2 \rangle$	0.48 0.40	0.59 0.54	0.49 0.42	0.46 0.39	0.47 0.39	0.46 0.40	0.48 0.41	0.50 0.41	0.55 0.48
$\langle E_K \rangle$	0.24 0.20	0.28 0.25	0.24 0.21	0.23 0.19	0.23 0.19	0.23 0.20	0.23 0.20	0.24 0.21	0.27 0.24
$\langle E_M \rangle$	0.25 0.16	0.12 0.17	0.20 0.13	0.24 0.16	0.25 0.16	0.25 0.18	0.25 0.17	0.24 0.15	0.29 0.23
$\langle E_I \rangle$	1.7 0.39	1.7 0.49	1.6 0.38	1.7 0.39	1.6 0.38	4.5 1.2	2.9 0.56	1.5 0.34	1.7 0.44
$\langle M_A \rangle$	1.2 1.5	1.8 1.3	1.2 1.3	1.2 1.6	1.2 1.5	1.3 1.7	1.2 1.6	1.2 1.5	1.3 1.5
$\langle M_S \rangle$	0.60 0.26	0.68 0.31	0.61 0.27	0.59 0.26	0.60 0.25	0.37 0.17	0.45 0.20	0.64 0.28	0.64 0.29
$\langle \log A \rangle$	1.8×10^{-2} 9.0×10^{-2}	0.45 0.64	2.7×10^{-2} 0.18	2.0×10^{-2} 0.10	1.6×10^{-2} 9.1×10^{-2}	4.2×10^{-3} 4.3×10^{-2}	6.0×10^{-3} 5.8×10^{-2}	1.9×10^{-2} 9.5×10^{-2}	- -
$\langle \log \beta_{ } \rangle$	0.74 0.47	0.70 1.0	0.79 0.45	0.77 0.49	0.75 0.47	1.2 0.50	1.0 0.47	0.71 0.46	0.75 0.52
$\langle \alpha \rangle^a$	0.37 0.25	5.5 7.2×10^2	4.2 4.8×10^2	3.6 1.0×10^3	1.4 8.5×10^2	0.44 0.26	0.41 0.26	0.37 0.25	- -

$$^a \alpha \equiv (p_{||} - p_{\perp}) / (B^2 / 4\pi)$$

Table 5.3: Space and time averages (upper lines) and standard deviations (lower lines) for models B which have initial strong magnetic field ($\beta = 0.2$).

Quantity	B1 ($\nu_S = \infty$)	Bmhd
$\langle \log \rho \rangle$	-1.0×10^{-2} 9.8×10^{-2}	-1.8×10^{-2} 0.12
$\langle u^2 \rangle$	0.90 0.79	0.86 0.73
$\langle E_K \rangle$	0.44 0.41	0.42 0.39
$\langle E_M \rangle$	4.8 0.80	4.8 0.90
$\langle E_I \rangle$	1.7 0.57	1.7 0.75
$\langle M_A \rangle$	0.28 0.13	0.27 0.13
$\langle M_S \rangle$	0.83 0.37	0.82 0.36
$\langle \log A \rangle$	5.5×10^{-2} 0.21	- -
$\langle \log \beta_{\parallel} \rangle$	-0.69 0.30	-0.66 0.21
$\langle \alpha \rangle^a$	4.1×10^{-2} 3.9×10^{-2}	- -

$$^a \alpha \equiv (p_{\parallel} - p_{\perp}) / (B^2 / 4\pi)$$

Table 5.4: Space and time averages (upper lines) and standard deviations (lower lines) for models C which have initial very weak (seed) magnetic field.

Quantity	C1 ($\nu_S = \infty$, $V_{S0} = 1$)	C2 ($\nu_S = 0$, $V_{S0} = 1$)	C3 ($\nu_S = 0$, $V_{S0} = 1$)	C4 ($\nu_S = 10^2$, $V_{S0} = 0.3$)	Cmhd ($V_{S0} = 1$)
$\langle \log \rho \rangle$	-8.5×10^{-3} 8.7×10^{-2}	-1.5×10^{-2} 0.12	-8.7×10^{-2} 0.28	-8.8×10^{-3} 8.9×10^{-2}	-9.1×10^{-3} 9.0×10^{-2}
$\langle u^2 \rangle$	0.79 0.63	0.70 0.73	0.79 0.64	0.80 0.63	0.79 0.63
$\langle E_K \rangle$	0.38 0.30	0.32 0.31	0.37 0.39	0.38 0.29	0.38 0.30
$\langle E_M \rangle$	6.2×10^{-2} 7.5×10^{-2}	6.2×10^{-6} 3.5×10^{-5}	1.0×10^{-4} 3.7×10^{-4}	2.6×10^{-2} 3.9×10^{-2}	9.0×10^{-2} 0.11
$\langle E_I \rangle$	1.7 0.49	1.7 0.44	0.33 0.28	1.6 0.49	1.7 0.51
$\langle M_A \rangle$	4.6 6.7	5.9×10^2 5.7×10^2	2.8×10^2 4.2×10^2	8.1 11	3.8 5.3
$\langle M_S \rangle$	0.78 0.34	0.74 0.38	2.1 1.0	0.79 0.34	0.78 0.34
$\langle \log A \rangle$	1.3×10^{-2} 3.2×10^{-2}	0.51 0.87	2.1 1.2	6.7×10^{-3} 8.6×10^{-2}	- -
$\langle \log \beta_{\parallel} \rangle$	1.5 0.64	5.5 1.4	2.0 2.1	2.0 0.70	1.4 0.62
$\langle \alpha \rangle^a$	0.52 0.25	8.8×10^5 7.1×10^7	5.5×10^4 1.7×10^7	1.5×10^2 6.7×10^4	- -

$$^a \alpha \equiv (p_{\parallel} - p_{\perp}) / (B^2 / 4\pi)$$

5.3 Discussion

The anisotropy in pressure created by the turbulent motions gives rise to new forces in the collisionless MHD description (see the momentum conservation equation in Eq. 2.51). These new forces gain dynamical importance when the anisotropy $A = p_{\perp}/p_{\parallel}$ deviates significantly from unity (depending on β) and give rise to instabilities. The standard CGL-MHD model is able to capture the correct linear behavior of the long wavelength limit of the firehose instability (which has scales much larger than the proton Larmor radius l_{cp}), but not of the mirror instability which is overstable (see the kinetic and CGL-MHD instability limits in the $A - \beta_{\parallel}$ plane in Figure 5.2). The correct linear threshold of the mirror instability can be obtained from higher order fluid models which evolve heat conduction (e.g. Snyder et al. 1997; Ramos 2003; Kuznetsov & Dzhalilov 2010) and results in substantial difference with regard to the CGL-MHD criterium (see the kinetic and CGL-MHD instability limits in the $A - \beta_{\parallel}$ plane in Figure 5.2).

These same (mirror and firehose) instabilities are known to constrain the (proton) pressure anisotropy growth to values close to the instability thresholds, via wave-particle interactions which obviously are not captured by any fluid model. Other kinetic instabilities driven by pressure/temperature anisotropy are also known to relax the anisotropy, such as the cyclotron instability (for protons) and whistler anisotropy instability (for electrons; see Gary 1993). Based on this phenomenology, we here imposed source terms on the standard CGL-MHD equations which relaxed the pressure anisotropy A to the marginally stable value (conserving the internal energy) at a rate ν_S , whenever A evolved to a value inside the unstable kinetic mirror or firehose zones.

As remarked before, there are several studies about the rate at which instabilities driven by pressure anisotropy relax the anisotropy itself. Using 2D particle simulations, Gary et al. (2000) studied the anisotropy relaxation rate for protons subject to cyclotron instability and found rates which are related to the growth rate of the fastest unstable mode $\sim 10^{-3} - 10^{-1}\Omega_p$ (where Ω_p is the proton gyrofrequency). Nishimura et al. (2002), also employing 2D particle simulations, found an analogous result for electrons subject to the whistler anisotropy instability with an anisotropy relaxation rate of a few percent

of the electron gyrofrequency. In both studies, part of the free energy of the instabilities is converted to magnetic energy. Recently, Yoon & Seough (2012) and Seough & Yoon (2012) studied the saturation of specific modes of the mirror and firehose instabilities via quasi-linear calculations, using the Vlasov-Maxwell dispersion relation. They also found that the temperature anisotropy relaxes to the marginal state after a few hundreds of the proton Larmor period and there is accumulation of magnetic fluctuations at the proton Larmor radius scales.

However, exactly what kinetic instabilities saturate the pressure anisotropy or the detailed processes involved are not fully understood yet and one cannot be sure to what extent the rates inferred in the studies above or those employed in the present analysis are applicable to the ICM plasma, specially with driven turbulence. In other words, the rate ν_S is subject to uncertainties and further forthcoming study involving particle-in-cell (PIC) simulations will be performed in order to investigate this issue in depth. In particular, in a very recent study about accretion disks, Riquelme et al. (2012) performed direct two-dimensional PIC shearing box simulations and found that for low beta values ($\beta < 0.3$), the pressure anisotropy is constrained by the ion-cyclotron instability threshold, while for large beta values the mirror instability threshold constrains the anisotropy, which is compatible with the present study. However, they have also found that in the low beta regime, initially the anisotropy can reach maximum values above the threshold due to the mirror instability. Nevertheless, they have attributed this behavior to the initial cyclotron frequency adopted for the particles which was small compared to the orbital frequency in order to save computation time.

We must add yet that here we have taken into account the isotropization feedback due to the firehose and mirror instabilities only, neglecting, for instance, the ion-cyclotron instability because this is more probably to be important in low β_{\parallel} regimes, which is not the case for ICM plasmas. We have considered that the anisotropy relaxation to the marginally stable value occurs at the rate of the fastest mode of the triggered instability (Equations 2.50), which is of the order of the proton gyrofrequency. As discussed above, for the typical parameters of the ICM, these relaxation times correspond to time scales which are extremely short compared to the shortest dynamical times one can solve. This

means that the plasma at least at the macroscopic scales is essentially always inside the stable region. This justifies why we adopted the simple approach of constraining the anisotropy by the marginal values of the instabilities, similarly to the *hardwall* constraints employed by Sharma et al. (2006). However, if one could resolve all the scales and frequencies of the system, one would probably detect some fraction of the plasma at the small scales lying in the unstable region. For the ICM, the scale of the fastest growing mode is $\sim 10^{10}$ cm, i.e., the proton Larmor radius.

5.3.1 Consequences of assuming one-temperature approximation for all species

Although the electrons have a larger collisional rate than the protons in the ICM ($\sim \sqrt{m_p/m_e}$), we have assumed in this study, for simplicity, that both species have the same anisotropy in pressure. Also, we assumed them to be in “thermal equilibrium”. A more precise approximation would be to consider the electrons only with an isotropic pressure. This would require another equation to evolve the electronic pressure and additional physical ingredients in our model, such as a prescription on how to share the turbulent energy converted into heat at the end of the turbulent cascade or how to quantify the thermalization of the free-energy released by the kinetic instabilities, as well as a description of the cooling for each of the species. The assumption of same temperature and pressure anisotropy for both species has resulted a force on the collisionless plasma due to the latter which is maximized. Nevertheless, since our results have shown that the dynamics of the turbulence when considering the relaxation of the anisotropy due to the instabilities feedback is similar to that of collisional MHD, we can conclude that if we had considered the electronic pressure to be already isotropic then, this similarity would be even greater.

Another relevant aspect that should be considered in future work regards the fact that the electron thermal speed achieves relativistic values for temperatures ~ 10 keV which are typical in the ICM. Thus a more consistent calculation would require a relativistic treatment (see for example Hazeltine & Mahajan 2002).

5.3.2 Limitations of the thermal relaxation model

Our model considers a thermal relaxation (Eq. 5.2) which ensures that the average temperature of the domain is maintained nearly constant, despite of the continuous dissipation of turbulent power. This simplification allowed us to avoid a detailed description of the radiative cooling and its influence on the temperature anisotropy. Even though, the rate $\nu_{th} = 5$ employed in most of our simulations is low enough to not perturb significantly the dispersion relation arising from the CGL-MHD equations. Time scales $\delta t \simeq \nu_{th}^{-1} = 0.2$ are much larger than the typical time-step of our simulations ($\sim 10^{-5}$). This means that the maximum characteristic speeds calculated via relations (2.45) and (2.46) were more than appropriate for the calculation of the fluxes in our numerical scheme (see Section 5.1.2).

In order to evaluate the effects of the rate of the thermal relaxation on the turbulence statistics, we also performed numerical simulations of three models with different rates ν_{th} (namely, models A6, A7, and A8 of Table 5.1). Model A6 has no thermal relaxation ($\nu_{th} = 0$), while model A7 has a slower rate than model A1, $\nu_{th} = 0.5$, and both, A6 and A7 systems undergo a continuous increase of the temperature as time evolves which increases β and reduces the sonic Mach number of the turbulence. Model A8, on the other hand, has a faster rate $\nu_{th} = 50$ and quickly converges to the isothermal limit. Despite of different averages and standard deviations in their internal energy, models A6, A7, and A8 presented overall behavior similar to model A1 (see Table 5.2).

We have also tested models without anisotropy relaxation (not shown here) which employed the CGL-MHD equations of state for calculating the pressure components parallel and perpendicular to the magnetic field (Equations 2.44 accompanied of homogeneous initial conditions, rather than evolving the two last equations in Eq. 2.51 for the anisotropy A and the internal energy, respectively). Although there are some intrinsic differences due to larger local values of the sound speeds, the overall behavior of these models was qualitatively similar to the models with $\nu_S = 0$ presented here.

In spite of the results above, a more accurate treatment of the energy evolution will be desirable in future work. For instance, as discussed earlier, the lack of a proper treatment for the heat conduction makes the linear behavior of the mirror instability in a fluid

description different from the kinetic theory leading to an overstability of the system. A higher order fluid model reproducing the kinetic linear behavior of the mirror instability (see Eq. 2.49) would enhance the effects of this instability in the models with finite ν_S , probably producing more small scale fluctuations compared to the present results (see Figures 5.4 and 5.5). The effects of the mirror instability on the turbulence statistics have been extensively discussed in Kowal et al. (2011a) (see also next section) where a double-isothermal closure was used. This closure is able to reproduce the threshold of the mirror instability given by kinetic derivation.

5.3.3 Comparison with previous studies

Kowal et al. (2011a) studied the statistics of the turbulence in collisionless MHD flows assuming fixed parallel and perpendicular temperatures in the so called double-isothermal approximation, but without taking into account the effects of anisotropy saturation due to the instabilities feedback. They explored different regimes of turbulence (considering different combinations of sonic and Alfvénic Mach numbers) and initially different (firehose or mirror) unstable regimes. They analyzed the power spectra of the density and velocity, and also the anisotropy of the structure function of these quantities and found that super-Alfvénic, supersonic turbulence in these double-isothermal collisionless models do not evidence significant differences compared to the collisional-MHD counterpart.

In the case of subsonic models, they have also detected an increase in the density and velocity power spectra at the smallest scales due to the growth of the instabilities at these scales, when compared to the collisional-MHD counterparts. They found elongation of the density and velocity structures along the magnetic field in mirror unstable simulations and isotropization of these structures in the firehose unstable models. In the present study, the closest to their models is the high β , super-Alfvénic model A2 which is without anisotropy relaxation. As in their subsonic sub-Alfvénic mirror unstable case, the instabilities accumulate power in the smallest scales of the density and velocity spectra. However, we should note that the density and velocity structures in our Model A2 become more isotropic at these scales probably because it is in a super-Alfvénic regime.

Our simulations starting with initial seed magnetic field have revealed the crucial role of the pressure anisotropy saturation (due to the mirror instability) for the dynamo turbulent amplification of the magnetic field, which in turn increases the anisotropy A . In our seed field simulations without anisotropy constraints (models C2 and C3), where the mirror forces dominate the dynamics, the turbulent flow is not able to stretch the field lines and therefore, there is no magnetic field amplification. This is consistent with earlier results presented in Santos-Lima et al. (2011) and de Gouveia Dal Pino et al. (2013), and also with the findings of de Lima et al. (2009), where the failure of the turbulent dynamo using a double-isothermal closure for $p_{\perp} > p_{\parallel}$ was reported. On the other hand, in model C1 where the pressure anisotropy growth is constrained by the instabilities, there is a dynamo amplification of the magnetic energy until nearly equipartition with the kinetic energy. This result is in agreement with 3D numerical simulations of magneto-rotational instability (MRI) turbulence performed by Sharma et al. (2006), where a collisionless fluid model taking into account the effects of heat conduction was employed in a shearing box. They have found that the anisotropic stress stabilizes the MRI when no bounds on the anisotropy are considered, making the magnetic lines stiff and avoiding its amplification. When using bounds on the anisotropy, however, they found that the MRI generated is similar (but with some small quantitative corrections) to the collisional-MHD case. Sharma et al. (2006), however, did not consider any cooling mechanism, so that the temperature increased continuously in their simulations. Besides, the simulations here presented have substantially larger resolution. Further, they have found that the system overall evolution is nearly insensitive to the adopted thresholds values for the anisotropy. We have also found little difference in the turbulence statistics between models with different non null values of the anisotropy relaxation rate.

Meng et al. (2012a) also employed a collisionless MHD model to investigate the Earth's magnetosphere by means of 3D global simulations. They employed the CGL closure, adding terms to constrain the anisotropy in the ion pressure only (the electronic pressure considered isotropic was neglected in their study). Using real data from the solar wind at the inflow boundary, they compared the outcome of the model in trajectories where data from space crafts (correlated to the inflow data) were available. Then, they repeated the

same calculation, but employing a collisional MHD model. They found better agreement with the collisionless MHD model in the trajectory passing by the bowshock region, where gas is compressed in the direction parallel to the radial magnetic field lines, producing a firehose ($A < 1$) unstable zone. However, in the trajectory passing by the magnetotail, the simulated data in the collisionless model were not found to be more precise than in the collisional case. In summary, the collisionless MHD description of the magnetosphere seems to differ little from the standard MHD model when the anisotropy is constrained. Even though, they have found quantitative differences in, for example, the thickness of the magnetosheath, which is augmented in the collisionless case, in better agreement with the observations. In the more homogeneous problem discussed here, in a domain with periodic boundaries and isotropic turbulence driving, we have found that both the evolution of the turbulence and the turbulent dynamo growth in the ICM under a collisionless-MHD description accounting for the anisotropy saturation due to the kinetic instabilities feedback, behave similarly (both qualitatively and quantitatively) to the collisional-MHD description. ³

Brunetti & Lazarian (2011) appealed to theoretical arguments about the decrease of the effective mean free path and related isotropization of the particle distribution to argue that the collisionless damping of compressible modes will be reduced in the ICM compared to the calculations in earlier papers (Brunetti & Lazarian 2007)⁴. These present calculations do not account for the collisionless damping of compressible motions, but similar to Brunetti & Lazarian (2011) we may argue that this type of damping is not important at least for the large scale compressions.

³We note, as remarked before, that while in the case of the ICM plasma the anisotropy relaxation rate is expected to be much larger than the dynamical rates of turbulent motions by several orders of magnitude, in the case of the solar wind the relaxation rate is only about ten times larger than the characteristic compression rates, so that in this case an instantaneous relaxation of the anisotropy is not always applicable (Meng et al. 2012a; Chandran et al. 2011).

⁴This happened to be important for cosmic ray acceleration by fast modes (see Yan & Lazarian 2002, 2004, 2008) that takes place in the ICM.

5.3.4 Implications of the present study

The dynamics of the ICM plasmas is important for understanding most of the ICM physics, including the formation of galaxy clusters and their evolution. The relaxation that we discussed in this paper explains how clusters can have magnetic field generation, as well as turbulent cascade present there. We showed that for sufficiently high rates of isotropization arising from the interaction of particles with magnetic fluctuations induced by plasma instabilities, the collisionless plasma becomes *effectively collisional* and can be described by ordinary MHD approach. This can serve as a justification for earlier MHD studies of the ICM dynamics and can motivate new ones.

In general, ICM studies face one major problem. The estimated Reynolds number for the ICM using the Coulomb cross-sections is small (~ 100 or less) so that one may even question the existence of turbulence in galaxy clusters. This is the problem that we deal with in the present paper and argue that the Reynolds numbers in the ICM may be much larger than the naive estimates above. The difference comes from the dramatic decrease of the mean free path of the particles due to the interaction of ions with fluctuations induced by plasma instabilities. In other words, our study shows that the collisional MHD approach may correctly represent properties of turbulence in the intracluster plasma. In particular, it indicates that MHD turbulence theory may be applicable to a variety of collisionless media. This is a big extension of the domain of applicability of the Goldreich & Sridhar (1995) theory of Alfvénic turbulence.

5.4 Summary and Conclusions

The plasma in the ICM is formally weakly collisional. Indeed, as far as Coulomb collisions are involved, the mean free paths of particles are comparable to size of galaxy clusters as a result of the high temperatures and low densities of the intracluster plasmas. Therefore, one might expect the plasmas to have high viscosity and not allow turbulent motions. At the same time, magnetic fields and turbulence are observed to be present there. The partial resolution of the paradox may be that even small magnetic fields can substantially

decrease the perpendicular viscosity of plasmas and enable Alfvénic turbulence that is weakly couple with the compressible modes (see also Lazarian 2006b). This present study indicates that the parallel viscosity of plasmas can also be reduced compared with the standard Braginskii values.

Aiming to understand the effects of the low collisionality on the turbulence statistics and on the turbulent magnetic field amplification in the ICM, both of which are commonly treated using a collisional-MHD description, we performed three-dimensional numerical simulations of forced turbulence employing a single-fluid collisionless-MHD model. We focused on models with trans-sonic turbulence and at the high β regime (where β is the ratio between the thermal and magnetic pressures), which are conditions appropriate to the ICM. We also considered a model with low β for comparison.

Our collisionless-MHD approach is based on the CGL-MHD model, the simplest fluid model for a collisionless plasma, which differs from the standard collisional-MHD by the presence of an anisotropic thermal pressure tensor. The new forces arising from this anisotropic pressure modify the MHD linear waves and produce the firehose and mirror instabilities. These instabilities in a macroscopic fluid can be viewed as the long wavelength limit of the corresponding kinetic instabilities driven by the temperature anisotropy for which the higher the β regime the faster the growth rate.

Considering the feedback of the kinetic instabilities on the pressure anisotropy, we adopted a plausible model of anisotropy relaxation and modified the CGL-MHD equations in order to take into account the effects of relaxation of the anisotropy arising from the scattering of individual ions by fluctuations induced by plasma instabilities. This model appeals to earlier observational and numerical studies in the context of the solar magnetosphere, as well as theoretical considerations discussed in earlier works. While the details of this isotropization feedback are difficult to quantify from first principles, the rate at which an initial anisotropy is relaxed is found (at least in 2D PIC simulations) to be a few percent of the ion Larmor frequency (Gary et al. 1997, 1998, 2000). The frequencies that we deal with in our numerical simulations are much larger than the ion Larmor frequency in the ICM (considering the scale of the computational domain ~ 100 kpc). This has motivated us to consider this anisotropy relaxation to be instantaneous.

Nevertheless, for completeness we also performed simulations with finite rates, in order to access their potential effects in the results.

The main results from our simulated models can be summarized as follows:

- Anisotropy in the collisionless fluid is naturally created by turbulent motions as a consequence of fluctuations of the magnetic field and gas densities. In all our models, the net increase of magnetic field intensity led to the predominance of the perpendicular pressure in most of the volume of the domain;
- In the high β regime with moderate initial magnetic field, the model without anisotropy relaxation (which is therefore, a “standard” CGL-MHD model; see Model A2 in Figures 5.1 and 5.2) has the PDF of the density broadened, specially in the low density tail, in comparison to the collisional-MHD model. This is a consequence of the action of the mirror instability which traps the gas in small cells of low magnetic field intensity. The density and velocity power spectra show excess of power specially at small scales, where the instabilities are stronger, although the magnetic field reveals less power. Consistently, the anisotropies in the structure functions of density, velocity, and magnetic field are reduced at the smallest scales in comparison to the collisional-MHD model;
- Models with anisotropy relaxation (either instantaneous, or with the finite rates 10^2 times or 10^3 times larger than the inverse of the turbulence turnover time t_{turb}) present density PDFs, power spectra, and anisotropy in structures which are very similar to the collisional MHD model. However, the model with the smallest anisotropy relaxation rate ($\sim 10t_{turb}^{-1}$) shows a little excess of power in density and velocity in the smallest scales, already in the dissipative range. This is consistent with the presence of instabilities in the smallest regions of the gas;
- Models starting with a very weak, seed magnetic field (i.e., with very high β), without any anisotropy relaxation, have the magnetic energy saturated at levels many orders of magnitude smaller than kinetic energy. The value of the magnetic

energy at this saturated state is shown to depend on the sonic Mach number of the turbulence, the smaller the sound speed the higher this saturation value;

- Models starting with a very weak, seed magnetic field, but with anisotropy relaxation (with instantaneous or finite rates) show an increase of the magnetic energy until values close those achieved by the collisional-MHD model. The growth rate of the magnetic energy for the model with instantaneous relaxation rate is similar to the collisional-MHD model, but this rate is a little smaller for the models with a finite rate of the anisotropy relaxation, as one should expect;
- In the low β regime, the strength of the injected turbulence (trans-sonic and sub-Alfvénic) is not able to produce anisotropy fluctuations which trigger instabilities. The statistics of the turbulence is very similar to the collisional-MHD case, in consistency with the fact that in this regime the pressure forces have minor importance.

All these results show that the applicability of the collisional-MHD approach for studying the dynamics of the ICM, especially in the turbulent dynamo amplification of the magnetic fields, is justified if the anisotropy relaxation rate provided by the kinetic instabilities is fast enough and the anisotropies are relaxed until the marginally stable values. As stressed before, the quantitative description of this process is still lacking, but if we assume that the results obtained for the anisotropy relaxation (usually studied in the context of the collisionless plasma of the solar wind) can be applied to the turbulent ICM, we should expect a relaxation rate much faster than the rates at which the anisotropies are created by the turbulence.

We intend in future work to investigate the kinetic instabilities feedback on the pressure anisotropy in the context of the turbulent ICM. To do this in a self-consistent way a kinetic approach is required. This can be done analytically and/or by the employment of PIC simulations.

We should emphasize that, even in the case of a good agreement between the collisional-MHD and collisionless-MHD results for the dynamics of the ICM, collisionless effects, like the kinetic instabilities themselves, can still be important for energetic processes in the

ICM, such as the acceleration of particles (Kowal et al. 2011b, 2012b), heating and conduction (Narayan & Medvedev 2001; Schekochihin et al. 2010; Kunz et al. 2011; Rosin 2011; Riquelme et al. 2012).

Chapter 6

Conclusions and Perspectives

We have presented in this thesis the results of our investigations on magnetic flux diffusion during different phases of star-formation in the interstellar medium (ISM) via the mechanism termed “turbulent reconnection diffusion” (TRD, Lazarian 2005), and on the turbulence and turbulent magnetic field amplification in the collisionless plasma of the intracluster medium (ICM) of galaxies. These studies were approached numerically by the use of three-dimensional simulations of collisional and collisionless-MHD models.

The two first Chapters presented the theoretical and observational motivation of the subjects we treated. In Chapter 2 we started presenting the collisional-MHD description for astrophysical plasmas and pointed its range of validity. Some fundamental concepts and results of recent theories on MHD turbulence were reviewed. We then exposed two open issues related to the diffusion of magnetic fields: the observational requirement of the transport of magnetic flux during the gravitational collapse of molecular clouds to allow star formation (the “magnetic flux problem”) and the formation of rotationally sustained protostellar discs in the presence of magnetic fields inside molecular cloud cores. Both problems challenge the frozen in condition of the magnetic fields, generally expected to be a good approximation in these environments. The diffusive mechanism (TRD) investigated in Chapters 3 and 4, based on fast magnetic reconnection induced by turbulence (Lazarian & Vishniac 1999) was then presented as an alternative to the one discussed in the literature, the ambipolar diffusion, which has been lately challenged both by ob-

servations and numerical simulation results. Next, we moved to intergalactic scales and revised the turbulent dynamo mechanism based on collisional MHD which is believed to be responsible for amplifying and sustaining the magnetic fields observed in the ICM. However, we pointed that a collisional-MHD treatment is loosely justified in this environment and described a more appropriate collisionless-MHD model for the ICM which was studied in Chapter 5.

In Chapter 3 (see also Santos-Lima et al. 2010), we presented our numerical simulations addressing the diffusion of magnetic flux via TRD. Using simple models injecting turbulence into molecular clouds with cylindrical geometry and periodic boundary conditions, we demonstrated the efficiency of the TRD in decorrelating the magnetic flux from the gas, enabling the infall of gas into the gravitational well while the field lines migrate to the outer regions of the cloud. This mechanism worked for clouds starting either in magnetohydrostatic equilibrium or for clouds initially out-of-equilibrium, in free-fall. We estimated the rates at which the TRD operates and found it to be faster when the central gravitational potential is higher¹. Besides, we found the diffusion rates to be consistent with the predictions of the theory. We also presented results of models without gravity and found that the TRD is equally able to remove the initial correlation between magnetic field and matter. An absence of correlation is observed in the diffuse interstellar medium. All the results in the models with gravity demonstrate that the TRD alone has the potential to solve the “magnetic flux problem”. Finally, we remark that the TRD efficiency depends only on the dynamic conditions of the medium, contrary to the ambipolar diffusion mechanism which depends on very stringent conditions of the molecular cloud composition for being efficient (Shu et al. 2006).

Advancing further in this research, recently Leão et al. (2012; see also de Gouveia Dal Pino et al. 2012) tested successfully the TRD during the collapse of molecular cloud cores employing more realistic initial conditions with a spherical gravitational potential representing embedded stars and including self-gravity. Their results confirm the trends

¹We remark that the setups were always controlled to not allow the system to be Parker-Rayleigh-Taylor unstable. This ensured that the gas and magnetic field decoupling were due to the effect of TRD only, rather than to the Parker-Rayleigh-Taylor instability.

presented in Chapter 3. Future work on this subject should explore the effects of the TRD in the evolution of initially starless clouds in order to assess the effects of self-gravity only upon the transport, without considering an external field. Also, our studies above have been performed considering isothermal clouds. This approximation actually mimics the effects of an efficient radiative cooling of the gas. However, in more realistic cases, a detailed treatment of non-equilibrium radiative cooling in the clouds (e.g., Melioli et al. 2005) is required, particularly in the late stages of the core formation. The effects of non-equilibrium radiative cooling will be also considered in these forthcoming studies. Besides, quantitative measurements of the effects of the gravity strength on the TRD diffusivity are also desirable.

In Chapter 4 (see also Santos-Lima et al. 2012, 2013a), we presented numerical simulations of protostellar disks formation. When considering realistic values of ambient magnetic fields, previous numerical simulations demonstrated that a disk rotationally sustained fails to form due to the extraction of the angular momentum from the gas in the plane of the developing disk by the torsioned field lines. These previous studies also showed that an enhanced microscopic diffusivity of about three orders of magnitude larger than the Ohmic diffusivity would be necessary to enable the formation of a rotationally supported disk. However, the nature of this enhanced diffusivity was not explained. Our numerical simulations of disk formation in the presence of turbulence demonstrated the plausibility of the TRD in providing the diffusion of the magnetic flux to the envelope of the protostar during the gravitational collapse, thus enabling the formation of rotationally supported disks of radius ~ 100 AU, in agreement with the observations (Santos-Lima et al. 2012). Afterwards, another group (Seifried et al. 2012) also appealing to turbulence during the gravitational collapse of a molecular cloud, argued that in their simulations the turbulence was not changing or removing the magnetic flux. They concluded that the rotationally supported disks were formed simply due to the action of turbulent shear. However, their assertive about the absence of magnetic flux diffusion was based on the evaluation of the mass-to-magnetic-flux ratio averaged over a volume much larger than the disk radius, which they found to be constant. In more recent work (Santos-Lima et al. 2013a), we demonstrated that their averaging of the mass-to-flux ratio over large volumes

is inappropriate as hinders the real increase of the magnetic-to-flux ratio occurring at the smaller scales where the disk is formed. We demonstrated that the magnetic flux diffusion is occurring in the inner envelope regions of the collapsing gas that is forming the disk. These conclusions were reinforced by new calculations with resolution twice as large as the resolution of our previous study (Santos-Lima et al. 2012) and confirmed that our results are robust and not product of numerical dissipation (Santos-Lima et al. 2013a).

Very recently, new simulations also confirmed the formation of rotationally supported disks and the diffusion of the magnetic flux when turbulence is present during the gravitational collapse of molecular clouds (Joo et al. 2013, Myers et al. 2013). Our investigation on this subject has still many possibilities of refinement. It would be interesting to repeat them varying the parameters of the turbulence and the mass of the proto-star as well, in order to explore the variations in the diffusion of the magnetic flux.

In Chapter 5 (see also Santos-Lima et al. 2013b), we have studied the turbulence statistics and turbulent dynamo amplification of magnetic fields using a collisionless-MHD model for exploring the plasma of the ICM. We performed simulations of transonic turbulence in a periodic box, assuming different initial values of the magnetic field intensity. We compared models with different rates of relaxation of the pressure anisotropy to the marginal stability condition, due to the feedback of the firehose and mirror instabilities. We showed that, in the high β plasma regime of the ICM where these kinetic instabilities are stronger, a faster anisotropy relaxation rate gives results closer to the collisional-MHD model in the description of the statistical properties of the turbulence (we analyzed the PDF of the density, the power spectra of density, velocity and magnetic field, and the anisotropy in the structure functions of these quantities). The growth rate of the magnetic energy by the turbulent dynamo when starting with a seed field, and the value of the magnetic energy at the saturated state are also similar to the values found for the collisional-MHD models, particularly when considering an instantaneous anisotropy relaxation. The models without any pressure anisotropy relaxation deviate significantly from the collisional-MHD results (in consistency with earlier results; e.g. Kowal et al. 2011), showing more power in small-scale fluctuations of the density and velocity field, in agreement with the strong presence of the kinetic instabilities at these scales; however,

the fluctuations in the magnetic field are mostly suppressed. In this case, the turbulent dynamo fails in amplifying seed magnetic fields, with the magnetic energy saturating at values several orders of magnitude below the kinetic energy.

It was suggested by previous studies of the collisionless plasma of the solar wind that the pressure anisotropy relaxation rate is of the order of a few percent of the ion gyrofrequency (Gary et al. 1997, 1998, 2000). The present analysis has shown that if this is also the case in the ICM, then the models which best represent the ICM are those with instantaneous anisotropy relaxation rate, i.e., the models which revealed a behavior very similar to the collisional-MHD description.

Nonetheless, this assumption applied to the ICM requires further investigation. In forthcoming work, we intend to investigate the details of the kinetic instabilities feedback on the pressure anisotropy in the context of the turbulent ICM. To do this in a self-consistent way, a kinetic approach, as for instance, the use of 3D particle simulations, will be required.

This is a new field and there are many topics to be studied yet about collisionless-MHD turbulence. The use of a model including the evolution of the heat conduction, for example, can help to represent more correctly the linear behavior of the mirror instability and to better capture the effects of this instability in comparison with the present study. Also the use of a two-temperature model, separating electrons and ions would be more realistic in the context of the ICM. These two ingredients, besides a realistic cooling treatment will probably shed new light on the comprehension of the energy distribution and structuring of the ICM and cold-core clusters as well.

Bibliography

- Allen A., Li Z.-Y., & Shu F. H., 2003, *ApJ*, 599, 363
- Armstrong J. W., Rickett B. J., & Spangler S. R., 1995, *ApJ*, 443, 209
- Bai, X.-N., & Stone, J. M. 2011, arXiv:1103.1380
- Balbus, S. A., & Hawley, J. F. 1991, *ApJ*, 376, 214
- Bale, S. D., Kasper, J. C., Howes, G. G., et al. 2009, *Physical Review Letters*, 103, 211101
- Ballesteros-Paredes, J., & Mac Low, M.-M. 2002, *ApJ*, 570, 734
- Basu, S., & Mouschovias, T. C. 1994, *ApJ*, 432, 720
- Basu, S., & Mouschovias, T. C. 1995, *ApJ*, 453, 271
- Batchelor, G. K. 1950, *Royal Society of London Proceedings Series A*, 201, 405
- Beresnyak, A., & Lazarian, A. 2006, *ApJ*, 640, L175
- Beresnyak, A., & Lazarian, A. 2009a, *ApJ*, 702, 1190
- Beresnyak, A., & Lazarian, A. 2009b, *ApJ*, 702, 460
- Beresnyak, A. & Lazarian, A. 2010 *ApJL*, 722, L110
- Beresnyak, A., & Lazarian, A. 2013, in *Magnetic Fields in Diffuse Media* (book) (submitted)
- Beresnyak, A. 2011, *PhRvL*, 106, 075001

Bibliography

- Beresnyak, A. 2012a, PhRvL, 108, 035002
- Beresnyak, A. 2012b, MNRAS, 422, 3495
- Bhattacharjee, A., & Hameiri, E. 1986, PhRvL, 57, 206
- Biskamp, D. 1986, Physics of Fluids, 29, 1520
- Boris, J. P., & Manheimer, W. 1977, Unknown
- Boldyrev, S. 2005, ApJ, 626, L37
- Boldyrev, S. 2006, PhRvL, 96, 115002
- Brandenburg, A., Nordlund, A., Stein, R. F., & Torkelsson, U. 1995, ApJ, 446, 741
- Brandenburg, A., & Subramanian, K. 2005, Phys. Rep., 417, 1
- Brandenburg, A., Sokoloff, D., & Subramanian, K. 2012, Space Sci. Rev., 169, 123
- Brunetti, G., & Lazarian, A. 2007, MNRAS, 378, 245
- Brunetti, G., & Lazarian, A. 2011, MNRAS, 412, 817
- Burkhart, B., Falceta-Gonçalves, D., Kowal, G., & Lazarian, A. 2009, ApJ, 693, 250
- Chandran, B. 2006, APS, Kinetic Dissipation of High-frequency MHD Turbulence, 48th Annual Meeting of the Division of Plasma Physics
- Chandran, B. D. G., Dennis, T. J., Quataert, E., & Bale, S. D. 2011, ApJ, 743, 197
- Chandrasekhar, S. 1960, Proc. Nat. Acad. Sci., 46, 53
- Chepurnov, A., & Lazarian, A. 2010, ApJ, 710, 853
- Chepurnov, A., Lazarian, A., Stanimirovic', S., Heiles, Carl, & Peek, J. E. G. 2010, ApJ, 714, 1398
- Chew, G. F., Goldberger, M. L., & Low, F. E. 1956, Royal Society of London Proceedings Series A, 236, 112

Bibliography

- Cho, J., & Lazarian, A. 2002, PhRvL, 88, 245001
- Cho, J., Lazarian, A. & Vishniac, E.T. 2002, ApJ, 564, 291
- Cho, J., & Lazarian, A. 2003, MNRAS, 345, 325
- Cho, J., Lazarian, A., Honein, A., Knaepen, B., Kassinis, S., & Moin, P. 2003a, ApJ, 589, L77
- Cho, J., Lazarian, A., & Vishniac, E. T. 2003b, ApJ, 595, 812
- Cho, J., Vishniac, E. T., Beresnyak, A., Lazarian, A., & Ryu, D. 2009, ApJ, 693, 1449
- Cho, J., & Vishniac, E.T. 2000 ApJ, 539, 273
- Crutcher, R. M. 2005, Massive Star Birth: A Crossroads of Astrophysics, 227, 98
- Dapp, W. B., & Basu, S. 2010, A&A, 521, L56
- de Gouveia Dal Pino, E.M., 1995, Plasmas em Astrofísica, Apostila do curso, IAG-USP
- de Gouveia Dal Pino E. M., Santos-Lima R., Lazarian A., Leão M. R. M., Falceta-Gonçalves D., & Kowal G., 2011, IAUS, 274, 333
- de Gouveia Dal Pino E. M., Leão M. R. M., Santos-Lima R., Guerrero G., Kowal G., & Lazarian A., 2012, PhysS, 86, 018401
- de Gouveia Dal Pino, E. M., Santos-Lima, R., Kowal, G., & Falceta-Gonçalves, D. 2013, arXiv:1301.0372
- de Lima, R. S., de Gouveia Dal Pino, E. M., Lazarian, A., & Falceta-Gonçalves, D. 2009, IAU Symposium, 259, 563
- Denton, R. E., Anderson, B. J., Gary, S. P., & Fuselier, S. A. 1994, J. Geophys. Res., 99, 11225
- Diamond, P. H., & Malkov, M. 2003, Physics of Plasmas, 10, 2322
- Dobrowolny, M., Mangeney, A., & Veltri, P. 1980, PhRvL, 45, 144

Bibliography

- Draine, B. T., & Lazarian, A. 1998, *ApJ*, 508, 157
- Duffin, D. F., & Pudritz, R. E. 2009, *ApJL*, 706, L46
- Elmegreen, B. G., & Scalo, J. 2004, *ARA&A*, 42, 211
- Esquivel, A., Benjamin, R. A., Lazarian, A., Cho, J., & Leitner, S. N. 2006, *ApJ*, 648, 1043
- Evans, C.R., & Hawley, J.F. 1988, *ApJ*, 332, 659E
- Eyink G. L., 2011, *PhRvE*, 83, 056405
- Eyink G. L., Lazarian A., & Vishniac E. T., 2011, *ApJ*, 743, 51
- Falceta-Gonçalves, D., Lazarian, A., & Kowal, G. 2008, *ApJ*, 679, 537
- Falceta-Gonçalves, D., de Gouveia Dal Pino, E. M., Gallagher, J.S., & Lazarian, A. 2010a
ApJL, 708, L57
- Falceta-Gonçalves, D., Caproni, A., Abraham, Z., Teixeira, D. M., & de Gouveia Dal
Pino, E.M. 2010b, *ApJL*, 713, L74
- Fatuzzo M., & Adams F. C., 2002, *ApJ*, 570, 210
- Federrath, C., Banerjee, R., Clark, P. C., & Klessen, R. S. 2010, *ApJ*, 713, 269
- Fiedler, R. A., & Mouschovias, T. C. 1992, *ApJ*, 391, 199
- Fiedler, R. A., & Mouschovias, T. C. 1993, *ApJ*, 415, 680
- Galli, D., Lizano, S., Shu, F. H., & Allen, A. 2006, *ApJ*, 647, 374
- Gary, S. P. 1993, *Theory of Space Plasma Microinstabilities*, Cambridge: University Press
- Gary, S. P., Wang, J., Winske, D., & Fuselier, S. A. 1997, *J. Geophys. Res.*, 102, 27159
- Gary, S. P., Li, H., O'Rourke, S., & Winske, D. 1998, *J. Geophys. Res.*, 103, 14567
- Gary, S. P., Yin, L., & Winske, D. 2000, *Geophys. Res. Lett.*, 27, 2457

- Goedbloed, J.P.H., & Poedts, S. 2004, *Principles of Magnetohydrodynamics*, Cambridge: University Press
- Giacalone, J., & Jokipii, J. R. 1999, *ApJ*, 520, 204
- Gogoberidze, G. 2007, *Phys. Plasmas*, 14, 022304
- Goldreich, P., & Sridhar, S. 1995, *ApJ*, 438, 763
- Goldreich, P., & Sridhar, S. 1997, *ApJ*, 485, 680
- Grasso, D., & Rubinstein, H. R. 2001, *Phys. Rep.*, 348, 163
- Hall, A. N. 1979, *Journal of Plasma Physics*, 21, 431
- Hall, A. N. 1980, *MNRAS*, 190, 371
- Hall, A. N. 1981, *MNRAS*, 195, 685
- Hellinger, P., Trávníček, P., Kasper, J. C., & Lazarus, A. J. 2006, *Geophys. Res. Lett.*, 33, 9101
- Hau, L.-N., & Wang, B.-J. 2007, *Nonlinear Processes in Geophysics*, 14, 557
- Hazeltine, R. D., & Mahajan, S. M. 2002, *ApJ*, 567, 1262
- Heitsch, F., Zweibel, E. G., Slyz, A. D., & Devriendt, J. E. G. 2004, *ApJ*, 603, 165
- Hennebelle P., & Fromang S., 2008, *A&A*, 477, 9
- Hennebelle, P., & Ciardi, A. 2009, *A&A*, 506, L29
- Higdon, J. C. 1984, *ApJ*, 285, 109
- Hosking, J. G., & Whitworth, A. P. 2004, *MNRAS*, 347, 994
- Inutsuka, S., Machida, M., & Matsumoto, M. 2010, *ApJ*, 718, L58
- Iroshnikov, P. S. 1963, *AZh*, 40, 742

- Joo, S.J., & Lee, Y.W. 2013, *ApJ*, 762, 18
- Käpylä, P. J., Korpi, M. J., & Brandenburg, A. 2008, *A&A*, 491, 353
- Kraichnan, R. H. 1965, *Phys. Fluids*, 8, 1385
- Krasnopolsky, R., & Königl, A. 2002, *ApJ*, 580, 987
- Krasnopolsky, R., Li, Z.-Y., & Shang, H. 2010, *ApJ*, 716, 1541
- Krasnopolsky, R., Li, Z.-Y., & Shang, H. 2011, *ApJ*, 733, 54
- Keiter, P. A. 1999, Ph.D. Thesis,
- Kotarba, H., Lesch, H., Dolag, K., et al. 2011, *MNRAS*, 415, 3189
- Kowal, G., Lazarian, A., & Beresnyak, A. 2007, *ApJ*, 658, 423
- Kowal, G., Lazarian, A., Vishniac, E. T., & Otmianowska-Mazur, K. 2009, *ApJ*, 700, 63
- Kowal, G., & Lazarian, A. 2010, *ApJ*, 720, 742
- Kowal, G., Falceta-Gonçalves, D. A., & Lazarian, A. 2011a, *New Journal of Physics*, 13, 053001
- Kowal, G., de Gouveia Dal Pino, E. M., & Lazarian, A. 2011b, *ApJ*, 735, 102
- Kowal G., Lazarian A., Vishniac E. T., & Otmianowska-Mazur K., 2012a, *Nonlinear Processes in Geophysics*, 19, 297
- Kowal, G., de Gouveia Dal Pino, E.M., & Lazarian, A. *PhRvL* 2012b, 24, 241102
- Kulpa-Dybel, K., Kowal, G., Otmianowska-Mazur, K., Lazarian, A., & Vishniac, E. 2010, *A&A*, 514, 26
- Kulsrud, R. M. 1983, *Basic Plasma Physics: Selected Chapters*, *Handbook of Plasma Physics*, Volume 1, 1

- Kunz, M. W., Schekochihin, A. A., Cowley, S. C., Binney, J. J., & Sanders, J. S. 2011, MNRAS, 410, 2446
- Kuznetsov, V. D., & Dzhililov, N. S. 2010, Plasma Physics Reports, 36, 788
- Landau, L. D., & Lifshitz, E. M. 1959, Fluid Mechanics, Course of theoretical physics, Oxford: Pergamon Press
- Landau, L. D., & Lifshitz, E. M. 1981, Physical Kinetics, Course of theoretical physics, Oxford: Pergamon Press
- Lazarian, A., & Vishniac, E. T. 1999, ApJ, 517, 700
- Lazarian, A., Vishniac, E. T., & Cho, J. 2004, ApJ, 603, 180
- Lazarian, A. 2005, in AIP Conf. Proc. 784, Magnetic Fields in the Universe: From Laboratory and Stars to Primordial Structures (Melville, NY: AIP), 42
- Lazarian, A. 2006a, Astronomische Nachrichten, 327, 609
- Lazarian, A. 2006b, ApJ, 645, L25
- Lazarian, A., & Beresnyak, A. 2006, MNRAS, 373, 1195
- Lazarian, A. 2009, Space Sci. Rev., 143, 357
- Lazarian, A., & Vishniac, E. T. 2009, RevMexAA, 36, 81
- Lazarian A., 2011, arXiv, arXiv:1111.0694
- Lazarian A., Esquivel A., & Crutcher R., 2012, ApJ, 757, 154
- Le, A., Egedal, J., Fox, W., et al. 2010, Physics of Plasmas, 17, 055703
- Leão, M. R. M., de Gouveia Dal Pino, E. M., Falceta-Gonçalves, D., Melioli, C. & Geraissate, F. G. 2009, MNRAS, 394, 157
- Leão, M. R. M., de Gouveia Dal Pino, E. M., Santos-Lima, R., & Lazarian, A. 2012, arXiv:1209.1846

- Lesieur, M. 1990, NASA STI/Recon Technical Report A, 91, 24106
- Li, P. S., McKee, C. F., Klein, R. I., & Fisher, R. T. 2008, ApJ, 684, 380
- Li, Z.-Y., Krasnopolsky, R., & Shang, H. 2011, ApJ, 738, 180
- Lizano, S., & Shu, F. H. 1989, ApJ, 342, 834
- Machida, M. N., Inutsuka, S.-i., & Matsumoto, T. 2010, ApJ, 724, 1006
- Machida, M. N., Inutsuka, S.-I., & Matsumoto, T. 2011, PASJ, 63, 555
- Maron, J., Cowley, S., & McWilliams, J. 2004, ApJ, 603, 569
- Maron, J., & Goldreich, P. 2001, ApJ, 554, 1175
- Marsch, E., Ao, X.-Z., & Tu, C.-Y. 2004, Journal of Geophysical Research (Space Physics), 109, 4102
- Marsch, E. 2006, Living Reviews in Solar Physics, 3, 1
- Maruca, B. A., Kasper, J. C., & Gary, S. P. 2012, ApJ, 748, 137
- Mason, J., Cattaneo, F., & Boldyrev, S. 2008, PhRvE, 77, 036403
- McKee, C. F., & Ostriker, E. C. 2007, ARA&A, 45, 565
- Melioli, C., de Gouveia Dal Pino, E. M., de La Reza, R., & Raga, A. 2006, MNRAS, 373, 811
- Mellon, R. R., & Li, Z.-Y. 2008, ApJ, 681, 1356
- Mellon, R. R., & Li, Z.-Y. 2009, ApJ, 698, 922
- Meng, X., Tóth, G., Liemohn, M. W., Gombosi, T. I., & Runov, A. 2012a, Journal of Geophysical Research (Space Physics), 117, 8216
- Meng, X., Tóth, G., Sokolov, I. V., & Gombosi, T. I. 2012b, Journal of Computational Physics, 231, 3610

Bibliography

- Mestel, L., & Spitzer, L., Jr. 1956, MNRAS, 116, 503
- Mestel, L., 1966, MNRAS, 133, 265
- Mestel, L., & Paris, R. B. 1984, A&A, 136, 98
- Mestel, L., & Ray, T. P. 1985, MNRAS, 212, 275
- Montgomery, D., & Turner, L. 1981, Physics of Fluids, 24, 825
- Mouschovias, T. C. 1976, ApJ, 207, 141
- Mouschovias, T. C. 1977, ApJ, 211, 147
- Mouschovias, T. C. 1979, ApJ, 228, 475
- Müller, W.C., Biskamp, D. & Grappin, R. 2003, PhRvE, 67, 066302
- Müller, W.C., & Grappin, R. 2005, PhRvL, 95, 114502
- Myers, A.T., McKee, C.F., Cunningham, A.J., Klein, R.I., & Krumholz, M.R. 2013, ApJ, 766, 18
- Nakano T., & Tadamaru E., 1972, ApJ, 173, 87
- Nakano, T., & Nakamura, T. 1978, PASJ, 30, 671
- Nakano, T., Nishi, R., & Umebayashi, T. 2002, ApJ, 573, 199
- Narayan, R., & Medvedev, M. V. 2001, ApJL, 562, L129
- Nishimura, K., Gary, S. P., & Li, H. 2002, Journal of Geophysical Research (Space Physics), 107, 1375
- Ng, C.S., & Bhattacharjee, A. 1997. Phys. Plasmas 4, 605
- Padoan, P., Jimenez, R., Juvela, M., & Nordlund, Å. 2004, ApJ, 604, L49
- Padoan, P., Juvela, M., Kritsuk, A., & Norman, M.L. 2009, ApJ, 707, L153

Bibliography

- Parker, E. N. 1958, *ApJ*, 128, 664
- Parker, E. N. 1966, *ApJ*, 145, 811
- Passot, T., & Vázquez-Semadeni, E. 2003, *A&A*, 398, 845
- Petschek, H. E. 1964, In *Procs. AAS-NASA Symposium, The Physics of Solar Flares*, Eds. W. N. Hess. Washington, NASA Special Publication, 1964, 50, 425
- Price, D. J., & Bate, M. R. 2007, *MNRAS*, 377, 77
- Press, W. H., Teukolsky, S. A., Vetterling, W. T., & Flannery, B. P. 1992, Cambridge: University Press
- Pudovkin, M. I., Besser, B. P., Lebedeva, V. V., Zaitseva, S. A., & Meister, C.-V. 1999, *Physics of Plasmas*, 6, 2887
- Qu, H., Lin, Z., & Chen, L. 2008, *Geophys. Res. Lett.*, 35, 10108
- Ramos, J. J. 2003, *Physics of Plasmas*, 10, 3601
- Richardson, L. F. 1926, *Proc. R. Soc. A*, 110, 709
- Riquelme, M. A., Quataert, E., Sharma, P., & Spitkovsky, A. 2012, *ApJ*, 755, 50
- Rosin, M.S., Schekochihin, A.A., Rincon, F., Cowley, S.C. 2011, *MNRAS*, 413, 7R
- Rothstein, D. M., & Lovelace, R. V. E. 2008, *ApJ*, 677, 1221
- Saito, S., Gary, S. P., Li, H., & Narita, Y. 2008, *Physics of Plasmas*, 15, 102305
- Samsonov, A. A., Alexandrova, O., Lacombe, C., Maksimovic, M., & Gary, S. P. 2007, *Annales Geophysicae*, 25, 1157
- Samsonov, A. A., Pudovkin, M. I., Gary, S. P., & Hubert, D. 2001, *J. Geophys. Res.*, 106, 21689
- Samsonov, A. A., & Pudovkin, M. I. 2000, *J. Geophys. Res.*, 105, 12859

Bibliography

- Santos-Lima, R., Lazarian, A., de Gouveia Dal Pino, E. M., & Cho, J. 2010, *ApJ*, 714, 442
- Santos-Lima, R., de Gouveia Dal Pino, E. M., Lazarian, A., Kowal, G., & Falceta-Gonçalves, D. 2011, *IAU Symposium*, 274, 482
- Santos-Lima R., de Gouveia Dal Pino E. M., & Lazarian A., 2012, *ApJ*, 747, 21
- Santos-Lima, R., de Gouveia Dal Pino, E. M., & Lazarian, A. 2013a, *MNRAS*, 429, 3371
- Santos-Lima, R., de Gouveia Dal Pino, E. M., Kowal, G., et al. 2013b, *arXiv:1305.5654*
- Schekochihin, A. A., Cowley, S. C., Taylor, S. F., Maron, J. L., & McWilliams, J. C. 2004, *ApJ*, 612, 276
- Schekochihin, A. A., Iskakov, A. B., Cowley, S. C., et al. 2007, *New Journal of Physics*, 9, 300
- Schekochihin, A.A., Cowley, S.C., Rincon, F., & Rosin, M.S. 2010, *MNRAS*, 405, 291
- Schlickeiser, R., & Skoda, T. 2010, *ApJ*, 716, 1596
- Schlickeiser, R., Lazar, M., & Skoda, T. 2011, *Physics of Plasmas*, 18, 012103
- Schlickeiser, R., Michno, M. J., Ibscher, D., Lazar, M., & Skoda, T. 2011, *PhRvL*, 107, 201102
- Seifried D., Banerjee R., Pudritz R. E., & Klessen R. S., 2012, *MNRAS*, 423, L40
- Seough, J., & Yoon, P. H. 2012, *Journal of Geophysical Research (Space Physics)*, 117, 8101
- Sharma, P., Hammett, G. W., Quataert, E., & Stone, J. M. 2006, *ApJ*, 637, 952
- Shay, M. A., Drake, J. F., Denton, R. E., & Biskamp, D. 1998, *J. Geophys. Res.*, 103, 9165
- Shay, M. A., Drake, J. F., Swisdak, M., & Rogers, B. N. 2004, *Phys. of Plasmas*, 11, 2199

Bibliography

- Shebalin, J. V., Matthaeus, W. H., & Montgomery, D. 1983, *J. Plasma Phys.*, 29, 525
- Shu, F. H. 1983, *ApJ*, 273, 202
- Shu, F. H., Galli, D., Lizano, S., & Cai, M. 2006, *ApJ*, 647, 382
- Shu, F. H., Galli, D., Lizano, S., Glassgold, A. E., & Diamond, P. H. 2007, *ApJ*, 665, 535
- Snyder, P. B., Hammett, G. W., & Dorland, W. 1997, *Physics of Plasmas*, 4, 3974
- Spitzer, L. 1968, *Diffuse Matter in Space*, New York: Interscience Publication
- Strauss, H.R. 1986, *PRL*, 57, 223
- Subramanian, K. 1998, *MNRAS*, 294, 718
- Subramanian, K., Shukurov, A., & Haugen, N. E. L. 2006, *MNRAS*, 366, 1437
- Sweet, P. A. 1958, *Electromagn. Phenom. Cosm. Phys.*, 6, 123
- Tajima, T., Mima, K., & Dawson, J. M. 1977, *PhRvL*, 39, 201
- Tanaka, M. 1993, *Journal of Computational Physics*, 107, 124
- Tassis, K., & Mouschovias, T. C. 2005, *ApJ*, 618, 769
- Treumann, R.A., & Baumjohann, W. 1997, *Advanced Space Plasma Physics*, London: Imperial College Press
- Troland, T. H., & Heiles, C. 1986, *ApJ*, 301, 339
- Troland, T. H., & Crutcher, R. M. 2008, *ApJ*, 680, 457
- Toro, E.F. 1999, *Riemann Solvers and Numerical Methods for Fluid Dynamics. A Practical Introduction*. Second edition. Berlin: Springer-Verlag
- Uzdensky, D. A., & Kulsrud, R. M. 2000, *Phys. of Plasmas*, 7, 4018
- Vainšhteĭn, S. I., & Zel'dovich, Y. B. 1972, *Soviet Physics Uspekhi*, 15, 159

Bibliography

- Vishniac, E. T., & Cho, J. 2001, *ApJ*, 550, 752
- Yamada, M., Ren, Y., Ji, H., Breslau, J., Gerhardt, S., Kulsrud, R., & Kuritsyn, A. 2006, *Phys. Plasmas*, 13, 052119
- Yan, H., & Lazarian, A. 2002, *Physical Review Letters*, 89, 1102
- Yan, H., & Lazarian, A. 2004, *ApJ*, 614, 757
- Yan, H., & Lazarian, A. 2008, *ApJ*, 673, 942
- Yan, H., & Lazarian, A. 2011, *ApJ*, 731, 35
- Yoon, P. H., & Seough, J. 2012, *Journal of Geophysical Research (Space Physics)*, 117, 8102
- Zrake, J., & MacFadyen, A. I. 2012, *ApJ*, 744, 32
- Zel'dovich, Y. B., Ruzmaikin, A. A., Molchanov, S. A., & Sokolov, D. D. 1984, *Journal of Fluid Mechanics*, 144, 1
- Zweibel, E. G. 2002, *ApJ*, 567, 962

Appendix A

Numerical MHD *Godunov* code

The three-dimensional numerical simulations presented in this thesis employed modified versions of the MHD *Godunov*¹ code which was originally built by Grzegorz Kowal (Kowal et al. 2007; 2009) and employed in several astrophysical studies², such as the investigation of MHD turbulence in the ISM and the ICM (e.g., Kowal et al. 2007; Falceta-Gonçalves et al. 2010a, 2010b); in molecular cloud core collapse (Leão et al. 2009; 2012; de Gouveia Dal Pino et al. 2012); in magnetic reconnection studies (Kowal et al. 2009; 2012a); in relativistic particle acceleration (Kowal et al. 2011b; 2012b); etc. Below, we present a brief description of our employed versions of the code.

A.1 Code units

The dimensionless units used in the code can be easily converted into physical ones with the employment of reference physical quantities as described below.

We arbitrarily choose three representative quantities from which all the other ones can be derived: a length scale l_* (which can be given, e.g., by the dimension of the system), a density ρ_* (usually given by the initial ambient density of the system), and a velocity v_* (which can be given by the sound speed of the medium). For instance, with

¹A public version of this code is available in the website <http://www.amunocode.org> under the GNU licence terms (more details in the website of the code).

²An updated list of publications using the code can be found in its website.

such representative quantities the physical time scale is given by the time in code units multiplied by l_*/v_* ; the physical energy density is obtained from the energy value in code units times $\rho_*v_*^2$, and so on. The magnetic field in code units is already divided by $\sqrt{4\pi}$, thus to obtain the magnetic field in physical units one has to multiply the value in code units by $v_*\sqrt{4\pi\rho_*}$.

A.2 MHD equations in conservative form

Our code is an unsplit, second-order Godunov code able to evolve the collisional or collisionless MHD equations on a three-dimensional, cartesian, uniform grid. The code solves the equations in the conservative form. Let us consider the basic scheme for solving the following set of ideal MHD equations, already in code units:

$$\frac{\partial \rho}{\partial t} + \nabla \cdot (\rho \mathbf{v}) = 0, \quad (\text{A.1})$$

$$\rho \left(\frac{\partial}{\partial t} + \mathbf{v} \cdot \nabla \right) \mathbf{v} = -\nabla p + (\nabla \times \mathbf{B}) \times \mathbf{B} \quad (\text{A.2})$$

$$\frac{\partial \mathbf{B}}{\partial t} = \nabla \times (\mathbf{v} \times \mathbf{B}), \quad (\text{A.3})$$

$$\frac{\partial e}{\partial t} + \nabla \cdot \{ (e + p + B^2/2) \mathbf{u} + (\mathbf{u} \cdot \mathbf{B}) \mathbf{B} \} = 0 \quad (\text{A.4})$$

where ρ , \mathbf{u} , \mathbf{B} , p are the primitive variables density, velocity, magnetic field, and thermal pressure, respectively $e = w + \rho u^2/2 + B^2/2$ is the total energy density, with w being the internal energy of the gas. This set of equations is closed by an adiabatic equation-of-state:

$$p = (\gamma - 1)w, \quad (\text{A.5})$$

where γ is the adiabatic index given by the ratio between the specific heats.

The above set of equations can be written in the following flux conservative form

$$\frac{\partial \mathbf{U}}{\partial t} = - \sum_{l=x,y,z} \frac{\partial \mathbf{F}_l}{\partial l}, \quad (\text{A.6})$$

with the vector of conservative variables \mathbf{U} and fluxes \mathbf{F}_l

$$\mathbf{U} = \begin{bmatrix} \rho \\ \rho u_d \\ B_d \\ e \end{bmatrix}, \quad \mathbf{F}_l = \begin{bmatrix} \rho u_l \\ \rho u_d u_l - B_d B_l + \delta_{kl}(p + B^2/2) \\ B_d u_l - B_l u_d \\ (e + p + B^2/2)u_l - (\mathbf{u} \cdot \mathbf{B})B_l \end{bmatrix}, \quad (\text{A.7})$$

where the different components x, y, z are represented by the label d .

Our code solves the MHD equations discretized in the finite-volume approach. Integrating (A.6) over the volume of each cell (i, j, k) of sizes $\Delta x, \Delta y, \Delta z$ in the cartesian grid gives

$$\begin{aligned} \frac{\partial \mathbf{U}^{i,j,k}}{\partial t} = & - \frac{1}{\Delta x} \left(\hat{\mathbf{F}}_x^{i+1/2,j,k} - \hat{\mathbf{F}}_x^{i-1/2,j,k} \right) \\ & - \frac{1}{\Delta y} \left(\hat{\mathbf{F}}_y^{i,j+1/2,k} - \hat{\mathbf{F}}_y^{i,j-1/2,k} \right) \\ & - \frac{1}{\Delta z} \left(\hat{\mathbf{F}}_z^{i,j,k+1/2} - \hat{\mathbf{F}}_z^{i,j,k-1/2} \right) \end{aligned} \quad (\text{A.8})$$

where $\mathbf{U}^{i,j,k}$ are the average values of \mathbf{U} in the cell (the values evolved numerically), and $\hat{\mathbf{F}}_l$ are the fluxes across the surfaces of the cell. The fluxes $\hat{\mathbf{F}}_l$ are calculated by means of a Riemann solver (e.g. Toro 1999). In the simulations presented in this thesis, we employed the approximated Riemann solver HLL, which is fast and robust.

For performing time integration, we used the second-order Runge-Kutta scheme (RK2, see e.g. Press et al. 1992). Represented by $\mathcal{L}(\mathbf{U})$ on the rhs of Equation (A.8), the advancing of the solution from the initial condition $\mathbf{U}(t^n) \equiv \mathbf{U}^n$ (omiting now the indices i, j, k) up to the time t^{n+1} through the RK2 scheme is given by

$$\begin{aligned} \mathbf{U}^* &= \mathbf{U}^n + \Delta t \mathcal{L}(\mathbf{U}^n), \\ \mathbf{U}^{n+1} &= \frac{1}{2}(\mathbf{U}^n + \mathbf{U}^*) + \frac{1}{2} \Delta t \mathcal{L}(\mathbf{U}^*), \end{aligned} \quad (\text{A.9})$$

where $\Delta t = t^{n+1} - t^n$.

The numerical algorithm has to obey the Courant-Friedrichs-Lewy (CFL) stability condition, which states that the fluid is not allowed to flow more than one cell within one

time-step. In order to fulfill this condition the maximum allowed time-step to advance the solution must be given by:

$$\Delta t_C = \frac{\min(\Delta x, \Delta y, \Delta z)}{V_{\max}^n} \quad (\text{A.10})$$

where V_{\max}^n is the maximum signal speed in the flow at the earlier state t^n . This maximum signal speed is the maximum value of $\{|\mathbf{u}| + \max(c_A, c_s, c_f)\}$ in the domain (c_A, c_s, c_f are the speed of the Alfvén, slow, and fast waves of the linear modes, respectively).

In practice, Δt_C is multiplied by a safety factor $C < 1$, to make $\Delta t = C\Delta t_C$. The simulations presented in this thesis use $C = 0.3$.

In Chapters 3 and 4 we presented simulations employing the collisional MHD equations above considering an isothermal equation-of-state. The only modification was to drop the last component of the vector of conserved variables \mathbf{U} (and of the fluxes \mathbf{F}_l) which corresponds to the total energy density. The pressure term in the momentum equation is simply given by

$$p = c_s^2 \rho, \quad (\text{A.11})$$

where c_s^2 is the fixed sound speed of the gas.

A.3 The collisionless MHD equations

As stressed before, our code also solves the collisionless-MHD set of equations. For the simulations of the collisionless MHD presented in Chapter 5, the vector of conserved variables \mathbf{U} and fluxes \mathbf{F}_l in the numerical scheme (Eq. A.6) are modified to

$$\mathbf{U} = \begin{bmatrix} \rho \\ \rho u_d \\ B_d \\ e \\ A(\rho^3/B^3) \end{bmatrix}, \quad \mathbf{F}_l = \begin{bmatrix} \rho u_l \\ \rho u_d u_l - B_d B_l - (p_{\parallel} - p_{\perp}) b_d b_l + \delta_{kl}(p_{\perp} + B^2/2) \\ B_d u_l - B_l u_d \\ (e + p_{\perp} + B^2/2) u_l - (\mathbf{u} \cdot \mathbf{B}) B_l - (p_{\parallel} - p_{\perp})(\mathbf{u} \cdot \mathbf{b}) b_l \\ A(\rho^3/B^3) u_l \end{bmatrix}, \quad (\text{A.12})$$

where $p_{\perp,\parallel}$ are the thermal pressures perpendicular/parallel to the local magnetic field; $e = (p_{\perp} + p_{\parallel}/2 + \rho u^2/2 + B^2/2)$ is total energy density, $b_l = B_l/B$, and $A = p_{\perp}/p_{\parallel}$ is the anisotropy in the pressure (see more details in Chapter 5).

To prevent negative values of the anisotropy A due to precision errors during the numerical integration, we used an equivalent logarithmic formulation for the conservative variable $[A(\rho^3/B^3)]$, which is replaced by $[\rho \log(A\rho^2/B^3)]$ (and the corresponding flux becomes $[\rho \log(A\rho^2/B^3)\mathbf{u}]$).

With this set of equations, in order to evaluate V_{max} in the CFL stability condition (Eq. A.10), we take into account both the real and the imaginary wave speeds of the linear modes (see Eqs. 2.45 and 2.46).

A.4 Magnetic field divergence

The code stores each magnetic field components at the center of the cell interface perpendicular to the component. The divergence of the magnetic field calculated at the cell centers is given by

$$\begin{aligned}
 (\nabla \cdot \mathbf{B})^{i,j,k} = & \frac{1}{\Delta x} (B_x^{i+1/2,j,k} - B_x^{i-1/2,j,k}) \\
 & + \frac{1}{\Delta y} (B_y^{i,j+1/2,k} - B_y^{i,j-1/2,k}) \\
 & + \frac{1}{\Delta z} (B_z^{i,j,k+1/2} - B_z^{i,j,k-1/2}),
 \end{aligned} \tag{A.13}$$

is kept null (to the machine precision) using the constrained transport method (CT) (Evans & Hawley 1988). The code also offers an equivalent formulation, where the induction equation is replaced by its ‘‘uncurled’’ form. With this formulation, the potential vector stored at the cell corners is evolved and used for calculating the magnetic field.

A.5 Source terms

The simulations presented in Chapters 3 and 4 have the basic collisional MHD equations modified by following source terms: an external gravity force and magnetic diffusivity.

Their effect in the method is simply to add a vector of source terms $\mathbf{S}(\mathbf{U})$ is the rhs of the Equation (A.6). However, they also add constraints in the time-step Δt of the integration. Besides the CFL condition, the external gravity and the magnetic diffusivity imposes the following maximum time-step to advance the solution:

$$\Delta t_G = \left(\frac{\min(\Delta x, \Delta y, \Delta z)}{a_{\max}} \right)^{1/2}, \quad (\text{A.14})$$

$$\Delta t_\eta = \frac{\min(\Delta x^2, \Delta y^2, \Delta z^2)}{\eta} \quad (\text{A.15})$$

where a_{\max} is the maximum gravity acceleration in the grid and η the magnetic diffusivity.

Additionally, in the simulations presented in Chapter 4 we have employed the technique of sink particles. Its implementation in our code version followed the recipe provided in Federrath et al. (2010).

In Chapter 5, we have also presented numerical calculations of the collisionless-MHD equations which have been modified by source terms. These are described in detail in Chapter 5 and so their effects which are explained in Section 5.2.1.

A.6 Turbulence injection

In all numerical simulations presented in this thesis, the turbulence in the code is driven by adding a solenoidal velocity field to the domain at the end of each time-step. This velocity field is calculated in the Fourier space with a random (but solenoidal) distribution in directions and sharply centered in a chosen value k_f (being the injection scale $l_{inj} = L/k_f$, where L is the size of the cubic domain). The forcing is approximately delta correlated in time.

Appendix B

Diffusion of magnetic field and
removal of magnetic flux from clouds
via turbulent reconnection

Appendix C

The role of turbulent magnetic reconnection in the formation of rotationally supported protostellar disks

Appendix D

Disc formation in turbulent cloud
cores: is magnetic flux loss necessary
to stop the magnetic braking
catastrophe or not?

Appendix E

Magnetic field amplification and
evolution in turbulent collisionless
MHD: an application to the
intracluster medium